

Impact resistant ultra-high performance fibre reinforced concrete: materials, components and properties

Peipeng Li

Bouwstenen

282

Impact resistant ultra-high performance fibre reinforced concrete: materials, components and properties

PROEFSCHRIFT

ter verkrijging van de graad van doctor
aan de Technische Universiteit Eindhoven,
op gezag van de rector magnificus, prof.dr.ir. F.P.T. Baaijens,
voor een commissie aangewezen door het College voor Promoties,
in het openbaar te verdedigen op dinsdag 17 december 2019 om 13:30 uur

door

Peipeng Li

geboren te Hubei, China



CIP-DATA LIBRARY TECHNISCHE UNIVERSITEIT EINDHOVEN

Impact resistant ultra-high performance fibre reinforced concrete: materials, components and properties / by Peipeng Li

A catalogue record is available from the Eindhoven University of Technology Library

ISBN: 978-90-386-4952-8

Bouwstenen 282

NUR 955

Copyright © 2019 by Peipeng Li

Ph.D. thesis, Eindhoven University of Technology, the Netherlands

Cover design: Xing Zheng & Xuan Ling

All rights reserved. No part of this publication may be reproduced in any form or by any means without permission in writing form from the author.

Dit proefschrift is goedgekeurd door de promotoren en de samenstelling van de promotiecommissie is als volgt:

Voorzitter: prof.dr.ir. T.A.M. Salet
Promotor: prof.dr.ir. H.J.H. Brouwers
Copromotor: dr. Q.L. Yu
Leden: prof.dr. W. Chen (Wuhan University of Technology)
prof.dr. H. Justnes (Norwegian University of Science and Technology)
prof.ir. S.N.M. Wijte
prof.dr.-ing. P.M. Teuffel
Adviseur: dr.dipl.-ing. G. Hüsken (Bundesanstalt für Materialforschung und -prüfung)

Het onderzoek of ontwerp dat in dit proefschrift wordt beschreven is uitgevoerd in overeenstemming met de TU/e Gedragscode Wetenschapsbeoefening.

Dedicated to:

My family

Teachers in life

Contents

1	Introduction.....	1
1.1	Ultra-high Performance Fibre reinforced Concrete	1
1.2	Research motivation	2
1.3	Research aim and strategy	3
1.3.1	Research aim.....	3
1.3.2	Strategy	4
1.4	Outline of this thesis	4
2	Effect of superplasticizer on early-age behaviour of UHPC.....	7
2.1	Introduction.....	8
2.2	Materials and experiments	9
2.2.1	Materials and proportions	9
2.2.2	Testing methods.....	11
2.3	Results and discussion	13
2.3.1	Dispersing ability of SP	13
2.3.2	Slump life and fluid-retaining ability.....	17
2.3.3	Retardation effect.....	19
2.3.4	Physical and chemical process effects	22
2.4	Conclusions.....	25
3	Binder optimization for UHPC by using mineral admixtures.....	27
3.1	Introduction.....	28
3.2	Optimization of high-volume limestone in UHPC	30
3.2.1	Materials and mixtures.....	30
3.2.2	Experimental methods	31
3.2.3	Experimental results	32
3.2.4	Discussion and summary	40
3.3	Development of UHPC paste with quaternary blends	43
3.3.1	Materials and mixtures.....	43
3.3.2	Experimental methods	45
3.3.3	Results and discussion	46
3.3.4	Summary.....	56
3.4	Conclusions.....	56
4	Introduction of coarse aggregate in UHPC system	59
4.1	Introduction.....	60
4.2	Utilizing coarse aggregates by normal mixing	61

4.2.1	Materials	61
4.2.2	Mix design by a packing model	62
4.2.3	Testing methods	63
4.2.4	Results and discussion	64
4.2.5	Summary	68
4.3	Two-stage UHPC with high-volume coarse aggregate	68
4.3.1	Materials and mixtures	68
4.3.2	Casting procedure and testing methods	70
4.3.3	Results and discussion	71
4.3.4	Summary	81
4.4	Conclusions	82
5	Application of steel fibres in UHPC	83
5.1	Introduction	84
5.2	Materials and experiments	85
5.2.1	Materials	85
5.2.2	Mix design	85
5.2.3	Testing methods	86
5.3	Results and discussion	87
5.3.1	Compressive and tensile splitting strengths	87
5.3.2	Flexural behaviour	89
5.3.3	Synergistic effect between aggregate and fibre	92
5.4	Conclusions	93
6	Functionally graded UHPC beams	95
6.1	Introduction	96
6.2	Materials and experiments	97
6.2.1	Materials	97
6.2.2	Fabrication of FGCB	97
6.2.3	Experimental methods	99
6.3	Results and discussion	100
6.3.1	Fresh and hardened properties of slurry	100
6.3.2	Flexural Load-deflection curves	100
6.3.3	Damage pattern and bond characteristic	102
6.3.4	Fibre utilization efficiency	103
6.4	Conclusions	105
7	Pendulum and drop-weight impact resistance of UHPFRC	107
7.1	Introduction	108
7.2	Specimens and impact methods	109

7.2.1	Pendulum impact test.....	109
7.2.2	Drop-weight impact test.....	110
7.3	Results of pendulum impact tests	111
7.3.1	Synergistic effect of steel fibres and coarse aggregates.....	111
7.3.2	Post-impact properties of UHPFRC beams	113
7.4	Results of drop-weight impact tests.....	120
7.5	Predicting low-velocity impact resistance by static properties.....	121
7.6	Conclusions.....	123
8	Bullet impact resistance of UHPFRC	125
8.1	Introduction.....	126
8.2	Materials and testing methods	127
8.2.1	Materials and mix design.....	127
8.2.2	Specimens preparation	128
8.2.3	Testing methods.....	129
8.3	Results and discussion	130
8.3.1	Effect of matrix strength	130
8.3.2	Effect of steel fibre type and content	132
8.3.3	Effect of coarse aggregates	134
8.3.4	Effect of target thickness	136
8.4	Conclusions.....	138
9	Conclusions and recommendations.....	141
9.1	Conclusions.....	141
9.1.1	Superplasticizer effect on early-age behaviour.....	141
9.1.2	Binder optimization towards low clinker content.....	142
9.1.3	Introduction of coarse aggregates	142
9.1.4	Efficient utilization of steel fibres.....	143
9.1.5	Resistance under low and high-velocity impact loadings.....	143
9.2	Recommendations for future research	144
10	Bibliography	145
11	Abbreviations and symbols	159
12	Acknowledgements	163
13	Summary	165
14	List of publications	167
15	Curriculum vitae.....	169

Chapter 1

Introduction

1.1 Ultra-high Performance Fibre reinforced Concrete

- **Development**

Concrete or cementitious materials are among the most widely used artificial construction and building materials since hundreds of years ago. During the past decade, ultra-high performance fibre reinforced concrete (UHPFRC) has drawn great attention from both researchers and engineers. Richard et al. [1] developed the reactive powder concrete (RPC) in 1993, which was characterized by a large amount of reactive powder, fine quartz powder, without any coarse aggregates, a very low water content and a high superplasticizer dosage, utilization of steel fibres and special treatment (pre-setting pressurization and heat-treating). RPC showed a dense microstructure, excellent toughness and ultra-high strength over 150 MPa. A few years later, De Larrard [2] extended this material concept and proposed the term of ‘ultra-high performance concrete (UHPC)’ with high packing density. Currently, the terms of this kind of material are designated slightly different, such as ‘Ultrahochfester Beton’ in German, ‘High Performance Concrete’ by the Federal Highway Administration in US, ‘Ductal’ in France, or ‘UHPFRC’ to distinguish UHPC with fibres by some researchers. In this thesis, the terms of grout/slurry, UHPC and UHPFRC are utilized to describe the ultra-high performance paste, plain concrete and fibre reinforced concrete, respectively, which should be characterized by excellent strength, workability and durability.

- **Characteristics of mix design**

The superior properties and wide range of applications of UHPFRC is greatly dependent on raw materials and mix design methods, such as water-to-binder (w/b) ratio, mineral admixture condition, powder content, aggregate size and content, and fibre type and dosage. The following characteristics of UHPFRC mixtures have been widely accepted [3]:

- Unconfined compressive strength usually in the range of 150 – 250 MPa,
- Direct tensile strength higher than 7 MPa,
- w/b ratio typically between 0.16 and 0.2, at least lower than 0.25,
- High content of binder, which leads to the reduction of capillary porosity,
- Fibres utilization to ensure a ductile behaviour.

Besides, the following principles also should be considered [4]:

- Utilizing a relatively high dosage of superplasticizer to achieve a desired workability,
- Eliminating coarse aggregates to ensure the homogeneity,
- Optimizing the granular distribution to enhance the packing density,
- Probably using post-set pressure and thermal treatments to enhance microstructure.

Followed by the above mentioned characteristics and design principles, UHPFRC mixtures should greatly differ from normal concrete, e.g. they are more complex and expensive for both recipe and mixing. Table 1.1 shows an example of a UHPFRC recipe based on the average composition by 75 UHPFRC compositions [5].

Table 1.1: Composition of UHPFRC mixture.

Materials	Cement	Reactive powders	Inert powders	Silica sand, gravel	Steel fibres	PP fibres	Super-plasticizer	Water
Mass (kg/m ³)	752	173	169	887	242	2	31	184

- **Properties**

Based on the characteristics and design principles, the desired fresh and hardened properties of UHPFRC mixtures could be acquired. The addition of new generation superplasticizers (e.g. polycarboxylic ethers (PCE) polymers) could greatly reduce the water amount and improve the fresh behaviour, such as spread flow, V-funnel time, fluid-retaining ability, etc. Normally, the UHPFRC should possess self-compacting or self-consolidating ability. The hydration kinetics of cement in UHPFRC is similar to that in ordinary concrete, however less amorphous phases are observed due to the pozzolanic reactions by adding reactive powders, e.g. silica fume, slag or fly ash. It means that relatively high C-S-H is formed by consuming CH, which then fills the voids and refines the microstructures. Furthermore, the relatively high powder and low water-to-powder ratio (w/p) ratio contributes to less remaining free water after hydration, which lowers the porosity and densifies the pore structure. Because of the densified microstructure and stable hydration products, the hardened properties of UHPFRC are much more superior compared to conventional concrete, such as ultra-high strength (several or tens of times), enhanced crack resistance, long service life or good durability, improved energy absorption and both low and high velocity impact resistance, and even fire resistance. As one of the most critical properties, the compressive, tensile and flexural strengths of UHPFRC could easily be more than 150 MPa, 25 MPa, and 30 MPa, respectively [6]. The excellent strength contributes to developing thin, long span, spatial, light components and structures. The superior durability, e.g. low water permeability, ions or gas penetration, high freezing-thawing or thermal resistance, etc. make it suitable to bear extreme service conditions or loadings, as well as enlarging service life and diminishing maintenance costs. The high energy dissipation and toughness of UHPFRC results in impact resistant applications and protective elements and structures, both in civil and defence engineering. To sum up, UHPFRC has excellent fresh and hardened properties due to its special design principles, improved hydration products and microstructure, and which possesses wide application potentials.

1.2 Research motivation

Besides application in common buildings, concrete is also applied in sensitive objects which need to be resistant against incidental events under both low and high velocity impact loadings. The enormous extreme conditions or accidental loadings surrounding our human life have attracted more and more public attention, such as explosive or ballistic impact in

terrorist attack, natural earthquake or hurricane disaster, vehicle impact in traffic accidents, ship collisions on offshore structure or bridge pillars, and falling object impact on concrete slabs [7,8]. And the impact properties of concrete (e.g. penetration depth, perforation, crack propagation) are always an important concern. Among the diverse types of concretes, UHPFRC has great potential for protective and military applications, owing to its superior workability, mechanical strength, toughness and energy absorption capacity [6,9–13]. However, the responses and properties of UHPFRC shows great difference compared to the normal concrete. Furthermore, the phase composition, microstructure and response behave very differently under impact loadings compared to the static ones [14–17]. Additionally, the dynamic properties and damage patterns exhibit large differences when subjected to different impact loadings, such as drop-weight or pendulum impact, seismic action, projectile impact and explosions [7,18]. Hence, the material or even structural design principles should differ based on the specific loading type, instead of simply considering static performance. Therefore, it is necessary to develop impact resistant UHPFRC, and investigate its impact resistance under both low and high velocity impact loadings.

As mentioned above, UHPFRC is a new generation of construction and building material. It has great potential in wide applications, e.g. protective and defence engineering. However, it still has some disadvantages and needs be further optimized. Firstly, the large amounts of superplasticizer and binder or cement consumption in UHPFRC lead to high costs and environmental burden. Generally, commercial UHPFRC is usually twenty times more expensive than conventional concrete, and three times greater in terms of the cement consumption [19]. Therefore, the chemical utilization and mineral addition in binder should be optimized to achieve environmentally sustainability and cost-efficiency. Secondly, conventional UHPFRC is designed without using coarse aggregate to ensure homogeneity. But, introducing coarse aggregates could reduce the powder content and cost, and improve the volume stability and penetration impact resistance, etc. Hence, the use of appropriate type and content of coarse aggregates has great significance, without sacrificing performance. Thirdly, high strength steel fibres are much more expensive compared to other solid raw materials in UHPFRC, although they considerably improve the mechanical and impact properties. And, the reinforcement degree is significantly influenced by fibre characteristics, such as fibre content [20,21], shape [22,23], orientation [24,25] and hybridization [26]. Thus, an appropriate type of steel fibre and a suitable structural design of components should be carefully researched to achieve an optimal utilization efficiency. To sum up, the mix design of UHPFRC should be optimized before using if as impact resistant material, including chemicals, binders, coarse aggregates, steel fibres and even component design.

1.3 Research aim and strategy

1.3.1 Research aim

As described above, UHPFRC has great potential as impact resistant material and in structures in both civil and protective engineering. While, the mix design of UHPFRC should be further optimized to make it more environmentally sustainable, cost-efficient and more impact resistant. Thus, the aim of this research is to design impact resistant UHPFRC under

ambient temperature curing without special treatment, and investigate its dynamic response and impact properties under both low-velocity and high-velocity impact loadings.

1.3.2 Strategy

To design and achieve a better understanding of impact resistant UHPFRC, the following objectives and strategy are taken into consideration in this study: understanding the superplasticizer and water on early-age behaviour; optimizing the fines with mineral addition towards low powder, thus low cost; studying the aggregates fraction effect to reduce powder content and increase the impact resistance without sacrificing the strength; applying steel fibres appropriately to enhance the fibre utilization efficiency and performance; evaluating impact resistance by low-velocity pendulum and drop-weight impact, and high-velocity in-service bullet impact. The schematic description of the research objectives and strategy are illustrated in Figure 1.1.

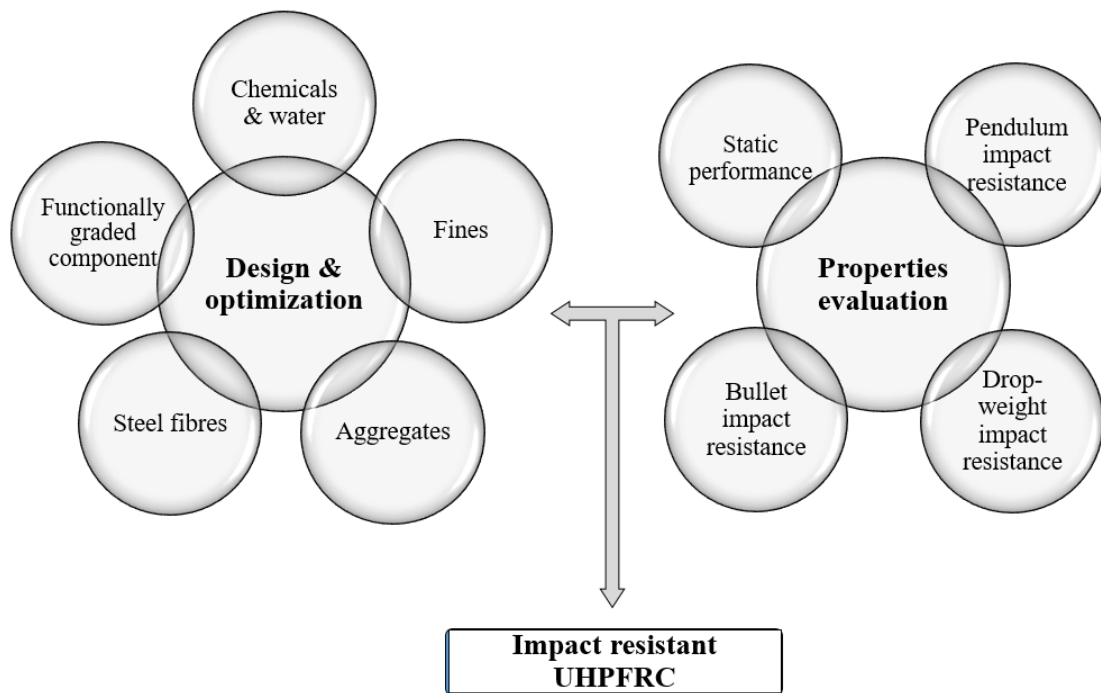


Figure 1.1: Schematic description of the research objectives and strategy.

1.4 Outline of this thesis

The framework of this thesis is presented in Figure 1.2. The contents of each chapter are explained in the following paragraphs.

In Chapter 2, the effect of PCE-type superplasticizer on early-age behaviour of UHPC is studied. The dispersing, fluid-retaining and retardation effects of the PCE polymers in UHPC systems are addressed, and the physical and chemical process of UHPC are discussed. The zeta potential of particles, spread flow, hydration kinetics, setting time, autogenous shrinkage and chemical shrinkage of UHPC pastes are measured, as well as the spread flow, slump life and early-age strength development of UHPC.

In Chapter 3, the binder is optimized for UHPC system with low cement clinker consumption, by applying mineral admixtures, for environmentally sustainable and cost-efficient purposes. Two methods are proposed, namely utilizing high-volume limestone powder to replace cement and developing quaternary binders containing cement-slag-limestone-silica. The roles of limestone powder on sustainability, plasticization effect, hydration kinetics, microstructure and hardened properties are investigated, as well as the synergistic effect of quaternary blends with cement-slag-limestone-silica.

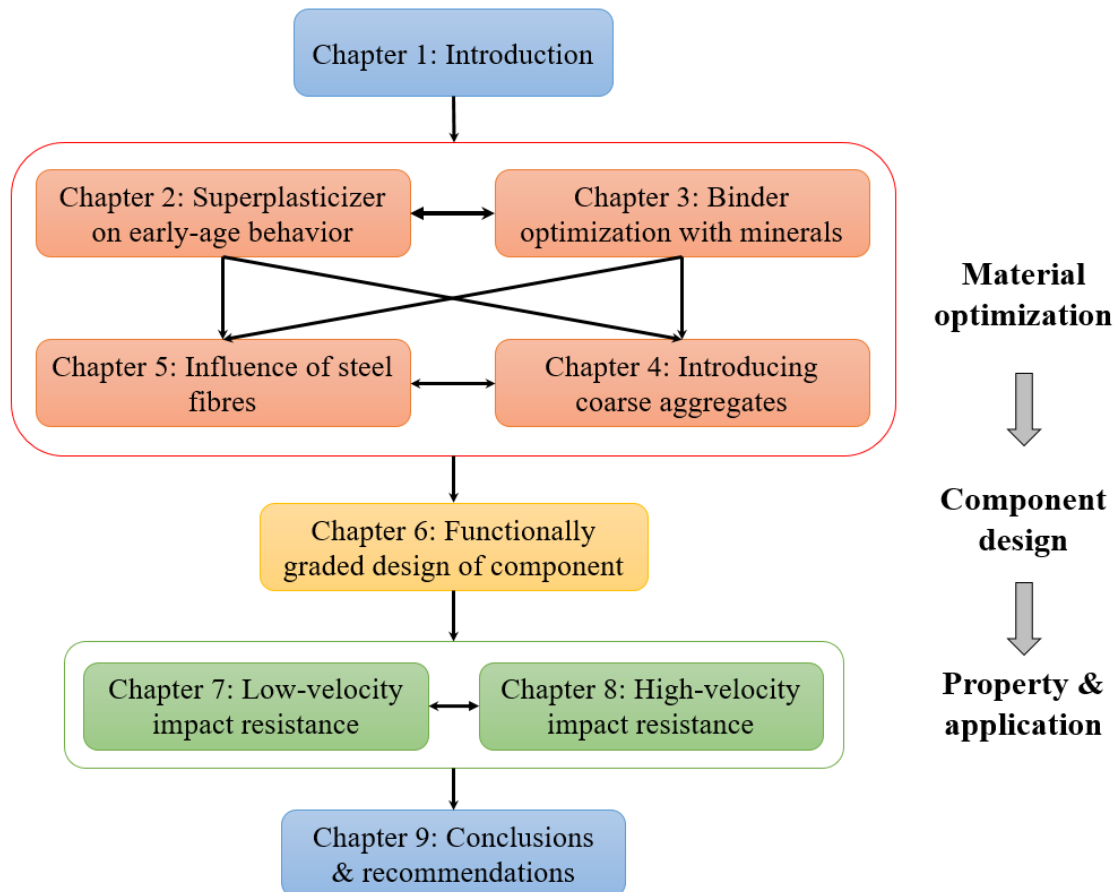


Figure 1.2: Outline of this thesis.

In Chapter 4, coarse basalt aggregates are introduced in the UHPC system to reduce the powder content and cost, improve the volume stability and penetration impact resistance, etc. Firstly, UHPC mixtures applying coarse basalt aggregate with the maximum particle size D_{\max} of 16 mm is designed by using a particle packing model and considering an optimal powder proportion. The basalt aggregate size effect, powder content effect and fibre reinforcing effect are analysed and discussed by evaluating the mechanical strengths. Secondly, the novel concept of two-stage UHPC (TS-UHPC) is proposed for maximum volume of coarse aggregate utilization and ultra-low binder consumption. The fresh and hardened properties of grout, mechanical strengths of TS-UHPC, compatibility between grouts and aggregates are researched.

In Chapter 5, the influences of steel fibres on the properties of UHPC in the presence of coarse aggregates are explored. UHPFRC matrices with a low cement content and maximum aggregate sizes of 8 mm and 25 mm are designed by making use of a particle packing model.

Three types of steel fibres (13 mm short straight, 30 mm medium hook-ended and 60 mm long 5D) are studied in terms of the utilization efficiencies.

In Chapter 6, functionally graded ultra-high performance cementitious composite beams are developed by applying the composite concepts of UHPC, Two-stage Concrete (TSC) and Slurry-infiltrated Fibrous Concrete (SIFCON). The functionally graded composite beam (FGCB) is fabricated with a bottom layer of SIFCON and top layer of TSC, and the two layers are synchronously cast by using UHPC slurry. The fresh and hardened properties of UHPC slurry, flexural properties of FGCB are evaluated to demonstrate the superior properties, namely excellent flexural bearing capacity and impact resistance, low cement consumption and a high steel fibre utilization efficiency.

In Chapter 7, the low-velocity impact resistances of designed UHPFRC materials and components are investigated under pendulum and drop-weight impacts. The effects of steel fibres and coarse aggregates, damage development and post-impact properties, and superiority of functionally graded composite component are analysed.

In Chapter 8, the influences of key parameters on high-velocity impact resistance of UHPFRC slabs by using in-service bullets are studied, in order to achieve optimized and enhanced protective materials. The effects of steel fibre type and dosage, matrix strength, coarse basalt aggregate, and target thickness are researched by subjected to a 7.62 mm bullet shot with velocities of 843-926 m/s.

In Chapter 9, comprehensive conclusions of the present work are drawn and summarized, and recommendations for future research are proposed.

Chapter 2

Effect of superplasticizer on early-age behaviour of UHPC

This chapter investigates the dispersing, fluid-retaining and retardation effects of the indispensable chemical additive (i.e. superplasticizer, SP) in the UHPC system, and discusses the physical and chemical process of UHPC. The zeta potential of particles, spread flow, hydration kinetics, setting time, autogenous shrinkage and chemical shrinkage of UHPC pastes are measured, as well as the spread flow, slump life and early-age strength development of UHPC. The results show that the dispersing ability of PCE-type SP is determined by its chemical structure, which shows an exponential relationship between the flow ability of pastes and SP dosages. The fluid-retaining abilities of UHPC mixtures are sensitive to the water-to-powder ratio, while the further addition of SP will not enhance the slump life after exceeding the saturation dosage. Both the adsorbed PCE and the PCE remaining in the aqueous phase contribute to retardation effect. A linear correlation between the final setting time (t_{final}) and the time of maximum heat flow rate ($t_{\dot{Q}=max}$) is derived. The types and dosages of SP primarily influence the absolute chemical shrinkage of pastes within 1 day, but have a great effect on the autogenous shrinkage due to different coagulation and hydration rates.

This chapter is partially published elsewhere:

P.P. Li, Q.L. Yu, H.J.H. Brouwers. Effect of PCE-type superplasticizer on early-age behaviour of ultra-high performance concrete (UHPC). *Construction and Building Materials*. 153 (2017) 740-750.

2.1 Introduction

The excellent material properties of UHPC can be achieved by different methods, such as eliminating the coarse aggregate and using high content of powders to increase the homogeneity [1], optimizing the grain-size distribution of the raw materials to improve the compactness [27], utilizing special heat curing or compressing treatments [28], adding high strength fibre [11], etc. Besides those principles, limiting the porosity by using low water-to-powder ratio (w/p) for concretes is probably the most convenient and efficient way to realize those superior material properties. Nevertheless, too low water addition causes the fluidity problem for the fresh concrete.

Plasticizers are used to increase the fluidity of concrete with a relatively low addition of water. Since introduction of application in the 1930s, they have been used as critical chemical admixtures for modern concrete [29]. The molecules are adsorbed onto particles, which are then physically separated by opposing their attractive forces with steric and/or electrostatic forces [30,31]. As the first generation water reducer, the lignosulfonates can limit the water content by about 10% [29]. The polymelamine sulfonate and sulfonated melamine formaldehyde condensate have been produced as the second generation dispersant since 1960s, with a water-reduction ability of about 20-30% [32]. The polycarboxylic ethers (PCEs) based superplasticizers, developed as the new generation in 1980s, can achieve up to 40% water reduction [33]. Until now, more and more researchers focus on the investigation on the mechanism of PCE-type SPs because of their excellent water reduction ability compared to other types of SP [33]. Some mechanisms and effect of PCE-type SP on fresh behaviours of cementitious materials have been revealed, such as chemical structure, adsorption, rheological behaviour and retardation effect [29,34]. However, systematic studies on the effect of PCEs on early-age behaviour of UHPC are still very limited and needed because of the complex influential parameters of those PCE polymers, such as chemistry and length of the backbone, number and length of the side chains, amount of anionic and ionic groups, bond type between backbone and side chain, and overall charge density [29,35–37]. Meanwhile, most researches just focus on cement paste or self-compacting concrete under relatively high water-to-powder ratios. But large amount of powders and very low water contents are usually used in UHPC. Therefore, it is necessary to study the effect of PCEs on early-age behaviours of UHPC under very low w/p. To better understand the influence of PCEs, the early-age behaviours should be researched from particle to paste, and then to concrete.

Generally, the early-age behaviour of UHPC can be interpreted by the following parameters: charge characteristic, workability, hydration kinetics, setting time, chemical and autogenous shrinkage, strength development [38]. The workability of UHPC can be described by the initial spread flow and fluid-retaining ability (slump life), mainly determined by dispersing ability and retention of superplasticizers [33,39,40], and mineral admixtures [41–46]. The retardation effect is generally defined as the delay of hydration, which can be changed with the different adsorption amounts on particles, concentrations of carboxylic in the aqueous phase, and charge characteristics of SP [33,35,47]. The setting time is usually described as a percolation process in forming hydration products to connect the isolated or weakly bound

particles [48,49]. This stiffening process is greatly influenced by cement size and w/p, as well as stability of bond between backbone and side chain of SP at alkaline environment [39,50,51]. The chemical shrinkage occurs during the cement hydration because of the smaller volume of the hydration products than that of the raw materials. When concrete is sealed, the autogenous shrinkage is resulting from internal consumption of moisture due to hydration [52,53]. The chemical and autogenous shrinkages are particularly high at early ages of UHPC, due to the usage of low w/p and high content of fine cementitious materials. However, the early-age properties are often discussed on its own, the investigation on the correlation between the early-age properties is very limited. Therefore, it is necessary to analyse the correlation between different features.

The objective of this chapter is to investigate and understand the effect and mechanism of PCE superplasticizer's type and dosage on the early-age behaviours of UHPC. The dispersing ability, fluid-retaining ability and retardation effect of PCEs, as well as physical coagulation and chemical process with PCEs are discussed by using zeta potential, spread flow, water demand, slump life, hydration kinetics, setting time, shrinkages, and early-age strength development. Furthermore, influential factors on superplasticizer's action effects and dispersing effectiveness are illustrated and analysed, such as fine aggregate with clay, water-to-powder ratio, content of nano-material, etc.

2.2 Materials and experiments

2.2.1 Materials and proportions

The raw materials used in this study are Portland Cement CEM I 52.5 R (PC), limestone powder (LP), nano-silica (nS), micro-sand 0-1 (MS), sand 0-2 (S), water (W) and superplasticizers (SP). The particle size distributions of the used materials are measured by the sieve and laser diffraction analyses using Malvern Mastersizer 2000®, shown in Figure 2.1. The chemical compositions of used powders are tested by X-ray Fluorescence (XRF), shown in Table 2.1.

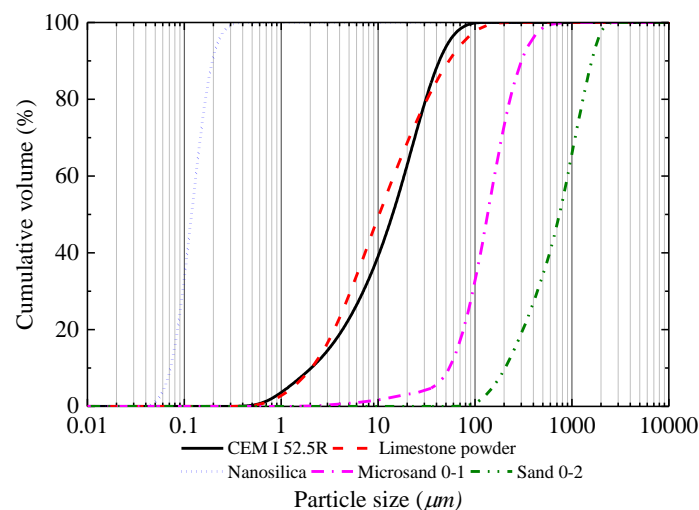


Figure 2.1: Particle size distribution of raw materials.

Table 2.1: Chemical composition of powders.

Substance (%)	CaO	SiO ₂	Al ₂ O ₃	Fe ₂ O ₃	K ₂ O	Na ₂ O	SO ₃	MgO	TiO ₂	Mn ₃ O ₄
PC	64.60	20.08	4.98	3.24	0.53	0.27	3.13	1.98	0.30	0.10
LP	89.56	4.36	1.00	1.60	0.34	0.21	-	1.01	0.06	1.61
nS	0.08	98.68	0.37	-	0.35	0.32	-	-	0.01	-

Four PCE-type superplasticizers with different dispersing and retarding abilities are used in the pastes and UHPC, which are provided by different producers. SP1 is synthesized with long side chains. SP2 has a rapid absorption to the cement particles and covers less surface, which ensures a large surface of cement particles to react with water and then accelerates the cement hydration. SP3 can be used to get a very high fluidity and long retention of rheology, even at low water-to-cement ratio. SP4 is suitable for UHPC, which adsorbs on the cement particle with long flexible side chains. The product information (from datasheet) and molecular weight (measured by gel permeation chromatography, GPC) of the superplasticizers are shown in Table 2.2.

Table 2.2: Product information and molecular weight of superplasticizers.

No.	Dry matter	Colour/shape	Density (g/cm ³)	pH	Chloride content	Alkali content	molecular weight M_w (g/mol)	PDI (M_w/M_n)
SP1	35%	Amber/liquid	1.11	5.9	≤ 0.1%	≤ 3%	49500	2.27
SP2	25%	Light brown/liquid	1.05	5.2	≤ 0.1%	≤ 1.5%	87600	2.22
SP3	35%	Translucent yellowish/liquid	1.07	4.2	≤ 0.1%	≤ 0.5%	59700	2.27
SP4	40%	Yellowish/liquid	1.09	4.1	≤ 0.1%	≤ 1%	40700	1.96

Fourier transform infrared spectroscopy (FTIR) tests are performed to characterize the chemical structures instrument with the wavenumbers ranging from 4000 to 400 cm⁻¹ at a resolution of 1 cm⁻¹, shown in Figure 2.2. The FTIR spectrum of the four PCEs are very similar in both wavenumber and intensity, which indicates that the mainly functional groups of the PCEs are same. The O–H stretching vibration is evidently shown around 3200 - 3400 cm⁻¹. The other common absorption peaks respectively appear around 2920 cm⁻¹ (C–H stretching), 2880 cm⁻¹ (C–H stretching), 1640 cm⁻¹ (C=O stretching), 1460 cm⁻¹ (C–H bending), 1350 cm⁻¹ (C–H bending), 1250 cm⁻¹ (C–O stretching), 1080 cm⁻¹ (C–O–C stretching) and 950 cm⁻¹ (=C–H bending). While, the SP1 also shows some different infrared absorption peaks around 1550 cm⁻¹ (C=C stretching) and 1410 cm⁻¹ (C–H bending).

The mass proportion of paste and UHPC reference admixture in this study is shown in Table 2.3, following previous research [27]. The nano-silica to binder mass ratio and limestone-to-powder mass ratio is fixed at 4% and 30% respectively in all mixtures. The micro-sand to powder ratio and sand-to-powder ratio is fixed at 0.25 and 1.2 respectively for all UHPC mixtures. The research parameter of the reference mixture includes the SP type and dosage and w/p. The totally used water includes the water in the nano-silica slurry and SP, and the added tap water. The w/p is fixed at 0.2 for the study of spread flow, slump life, hydration kinetic, setting time, shrinkage and strength. While, to evaluate water content sensitivity on

slump life, the w/p ratio of 0.22 at SP dosage of 2.2% is also investigated. The dosages of SP are determined by the dry matter weight, based on the total mass of all powders.

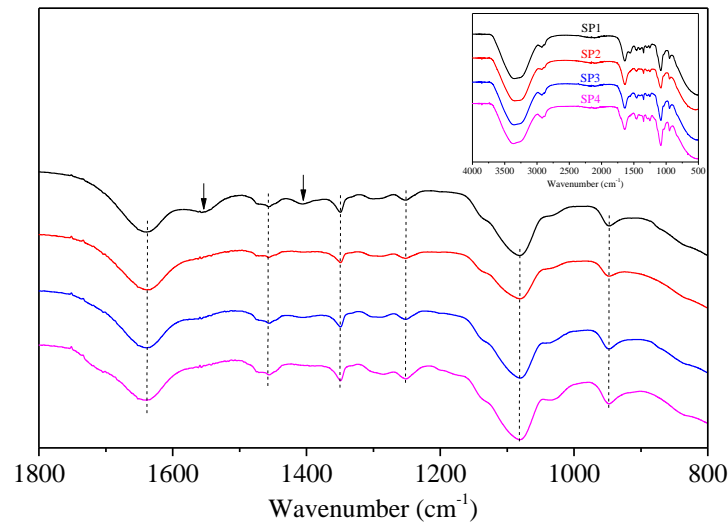


Figure 2.2: FTIR spectra of PCEs.

Table 2.3: Mass proportion of paste and UHPC reference mixtures.

Mixtures	PC	LP	MS	S	nS
Paste	1.000	0.4464	0	0	0.0417
UHPC	1.000	0.4464	0.3720	1.7857	0.0417

The mixing time of pastes lasts about 5 min using a 5-liter Hobart mixer, following the procedure: dry mixing (cement and limestone) for 30 s at the low speed, sequentially adding nano-silica slurry, 80% water, and remaining water incorporated with SP for about total 2 min at the low speed, followed by mixing the paste for 2 min at the low speed and 30 s at the medium speed. The adding order of components in mixing procedure of UHPC is similar to that of paste, whereas the total time is about 8 min (30 s for dry mixing, 180 s for adding slurries and water, another 150 s at the low speed and 120 s at the medium speed).

2.2.2 Testing methods

- **Zeta potential**

To study the charge characteristics of the suspended particles and determine the adsorption of the PCE-type SPs, zeta potential measurement is conducted by using a Malvern Zetasizer at the set temperature of 25 °C. Diluted slurries are prepared by dissolving 0.1 g of powder (PC, LP, nS) in 100 mL deionized water with SP1 and SP3 at different concentrations. All samples are mixed manually and vibrated for about 8 min before test. Furthermore, the correlation between zeta potential and pH is determined.

- **Flow ability and slump life**

The spread flow of pastes and UHPCs are measured by using a truncated conical mould (Hägermann cone: height 60 mm, top diameter 70 mm, bottom diameter 100 mm) without jolting, in accordance with EN 1015-3: 2007. The pastes are utilized with four different SPs at the dosage varying from 0.4% to 2.0%, while the UHPCs incorporate the SPs with the

dosage from 1.0% to 3.0%. It should be pointed out that the samples are mixed with tap water at w/p ratio of 0.2, and the water temperature has slight variation at different seasons. So, this may have an influence on the spread flow [54].

To evaluate the fluid-retaining ability and slump life of UHPC, the spread flow of UHPCs are measured till 4 hours after the sample preparation. The samples are stored at room temperature of 20 ± 1 °C and a plastic film is covered on the mixing bowl to prevent moisture loss after each measurement. The measurement is performed with a regular time interval, and the UHPC is mixed for about 20 s before each measurement. To analyse the SP dosage effect, UHPC samples are tested at SP dosages of 2.2% and 2.6% respectively, with a w/p ratio of 0.2. Then, to evaluate the water content sensitivity, the w/p ratios are increased to 0.22 at the SP dosage of 2.2%.

- **Reaction kinetics**

To analyse the effect of superplasticizer on the hydration kinetics, an isothermal calorimeter (TAM Air, Thermometric) is employed to measure the heat evolution of UHPC pastes, with the set temperature of 20 °C. The samples are mixed manually, and then vibrated to ensure a good homogeneity. The prepared pastes are filled into an ampoule which is then loaded to the calorimeter, which means that the sampling time (4~6 mins) is not recorded. The samples are fixed at w/p ratios of 0.2, and added four different types of SP at the dosage of 0.4%, 0.8%, 1.2%, 1.6% and 2.0%, respectively.

- **Setting time**

The setting times of pastes are evaluated by using the Vicat apparatus based on EN 196-3: 2005. The w/p ratios for all pastes are fixed at 0.2. The PCE-type SPs are added to the pastes at the dosage of 0.4%, 0.8% and 1.2%, respectively. The setting time is tested under the room temperature of approximately 20 ± 1 °C.

- **Chemical and autogenous shrinkage**

The chemical shrinkage of pastes is tested by a vial-capillary setup based on ASTM C 1608-05, completely filled by paraffin oil without water in the capillary tube in order to keep the w/p ratio at constant of 0.2. The autogenous shrinkage of pastes is obtained by using the digital dilatometer bench and sealing corrugated tubes following ASTM C 1698-09, while the zero-time of measurement is defined as the final setting time. The samples are firstly tested under different SP types with a constant dosage of 0.8%, then the samples containing SP3 with different dosages (0.4% and 1.2%) are measured. All the specimens are stored at room temperature 20 ± 1 °C and data is collected for 72 h.

- **Strength**

The fresh UHPC is cast into plastic moulds ($40 \times 40 \times 160$ mm³), and covered with plastic film to prevent moisture loss. All the samples are demoulded approximately 24 h after casting and then cured in water under room temperature of 20 ± 1 °C. The compressive and flexural strength of UHPC samples are tested after 1 day, 3 days, and 7 days respectively, based on EN 196-1: 2005. To investigate the SP type effect on the early age strength, the UHPCs are

cast with all SPs under dosage of 2.2% (close to saturation dosages). Then, the UHPCs are also prepared using SP3 with a dosage of 1.8%, 2.6% and 3.0%, respectively.

2.3 Results and discussion

2.3.1 Dispersing ability of SP

- **Zeta potential**

The zeta potential measurement has been proven to be an effective method to characterise the interaction between powder particles and PCEs [31,55–58]. Figure 2.3 shows the pH and zeta potential of the particles in water and organic solvent (2-propanol). The cement suspension in water shows a high pH, and is slightly acidic in 2-propanol. The zeta potential changes from -1.42 mV to 0.91 mV. The limestone powder and nano-silica have a similar pH and zeta potential in water, approximately 9 and -23 mV, respectively. The limestone powder in 2-propanol shows a comparable result to cement, about 6.1 (pH) and 3.1 mV (zeta potential). The pure cement particles in water without PCE shows a negative zeta potential, which is in line with the reported researches [55,56,58,59]. Nevertheless, some researchers reported a positive zeta potential for cement pastes without SP, and then it changes from positive to negative with the addition of SP [30,33,57]. These differences may be caused by the particle concentration, chemical composition, conductivity, ion characteristic and pH value of suspension, and testing methods. Normally, higher magnitudes of zeta potential values occur at higher cement concentrations [56,60]. Lower zeta potentials could be caused by high pH and high clinker phases of C_3S and C_2S , while higher contents of Ca^{2+} , C_3A and C_4AF lead to relatively higher zeta potentials [55,61]. The limestone powder and nano-silica have higher negative zeta potentials than cement in water, which may indicate that they generate more anions in water. As a similar explanation, it was also pointed out that a great amount of silica powder could produce a large amount of dissociated silanol site $[SiO^-]$, which results in higher negative zeta potentials [55].

Figure 2.4 presents the zeta potential of different powder suspensions with SP1 and SP3. With the addition of SP, the zeta potential of cement suspension decreases sharply, due to the adsorption of carboxylic acids groups on cement particles. Conversely, the zeta potential values of limestone powder and nano-silica suspension have a rapid increase. These increases are probably caused by the better adsorption ability and lower charge density of PCE molecules than the previous anions on the particles. A similar hypothesis was used to explain the relationship between zeta potential of synthesized ettringite and PCE concentration [62]. With the continuous increase of SP, all suspensions tend to be stable beyond SP concentrations of 0.05 g/L, which confirms the existence of saturation dosages. Because no further PCE molecules are adsorbed on particles above the saturation dosage, which contributes to unchanged zeta potential.

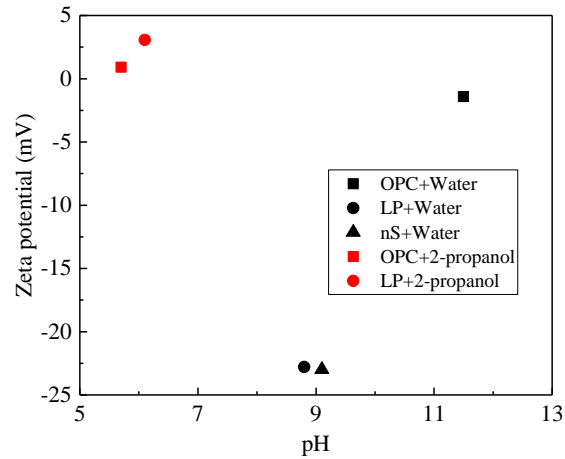


Figure 2.3: Zeta potential of particles without SP.

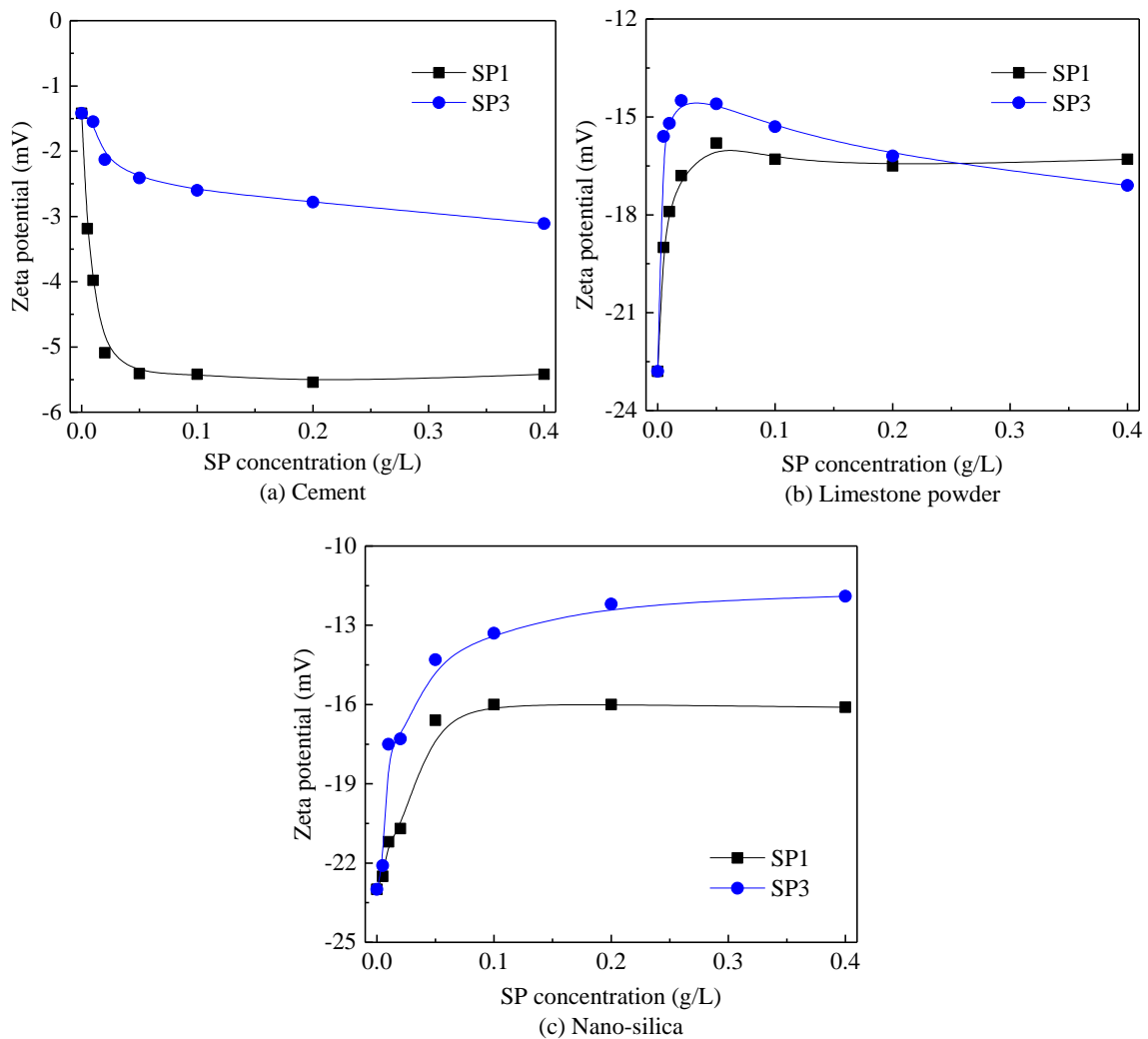


Figure 2.4: Zeta potential of particles with SPs.

- **Spread flow and water demand of paste**

The critical dosage of SP can be defined as the dosage that begins to provide obvious dispersing effect, while the saturation dosage means that the fluidity will not or just change very slightly beyond this dosage [29]. Figure 2.5(a) depicts the spread flow of pastes

incorporating different types and dosages of SP. The relationship between the flow ability of pastes and SP dosages shows an exponential trend in this study, which means the spread flow diameters have a rapid increase at relatively low dosages of SP, and then typical plateaus occur after the saturation dosages. It shows that the maximum flow diameters of pastes with different SP types are approximately 35 cm. The critical (saturation) dosages of SP1, SP2, SP3 and SP4 for paste are approximately 0.6% (1.4%), 0.4% (0.8%), 0.6% (1.2%) and 0.4% (1.2%), respectively. It can be concluded that SP2 and SP3 have a much higher dispersing ability for pastes with dosages ranging from 0.4% to 1.2%. However, with the increase of SP dosages, the dispersing ability of SP3 and SP4 are only a bit higher than that of SP2 and SP1.

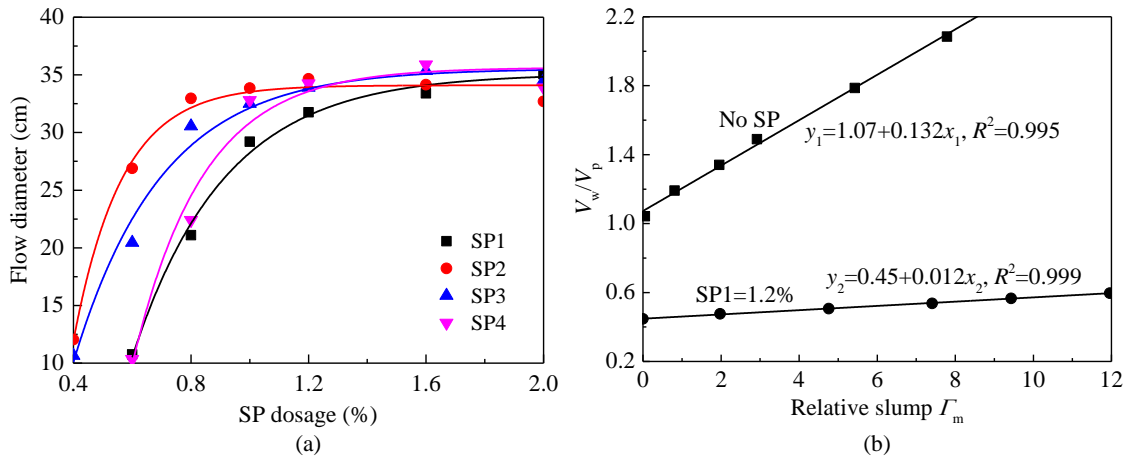


Figure 2.5: Spread flow and water demand of pastes

To reduce the porosity, it is necessary to limit the w/p for a fluid paste at a certain dosage of SP. To investigate the effect of SP on the water demand of UHPC paste, the relative slump Γ_p was calculated according to Okamura and Ozawa [63,64]:

$$\Gamma_p = \left(\frac{d}{d_0}\right)^2 - 1; d = \frac{d_1 + d_2}{2} \quad (2.1)$$

where d_1 and d_2 are the perpendicular diameters of the spread flow, d_0 is the cone base diameter (100 mm). The relative slump can be plotted versus w/p and a linear trend line can be plotted thus [65,66]:

$$\frac{V_w}{V_p} = \beta_p + E_p \Gamma_p \quad (2.2)$$

where V_w and V_p presents the volume of water and powder. β_p is as water demand and represents the minimum water content to assure a fluid paste. The deformation coefficient (E_p) is derived from the slope of the linear regression line, which indicates the sensitivity of the materials on the water demand for a specified workability. In this research, Figure 2.5(b) shows that water demand of UHPC paste reduces from 1.07 (without SP) to 0.45 (with enough SP), which means the water reduction of demand water is approximately 58%. It also shows a very small deformation coefficient when using sufficient dosage of SP, which indicates that the relative slump is very sensitive to w/p and will increase dramatically with

a further addition of water. Thus, all four PCE-type SPs have a good water reduction ability and it is possible to utilize it to achieve a very low w/p ratio for UHPC.

- **Spread flow of UHPC**

Figure 2.6 presents the spread flows of UHPC incorporating different types and dosages of SP. The spread flows of UHPC with SP2, SP3 and SP4 show a typical plateau at high dosages, which are similar to that of pastes. However, the SP1 presents more like a linear increase, which indicates that SP1 increases the flow ability very slowly at the investigated dosage range. The critical dosages of SP2, SP3 and SP4 for UHPC are similar, about 1.0%, meanwhile the saturation dosages are about 2.2%. The critical dosage of SP1 for UHPC is approximately 1.0%, but it does not show a clear saturation dosage till 3.0%. Generally, SP3 and SP4 have a higher dispersing ability than SP1 and SP2 for UHPC.

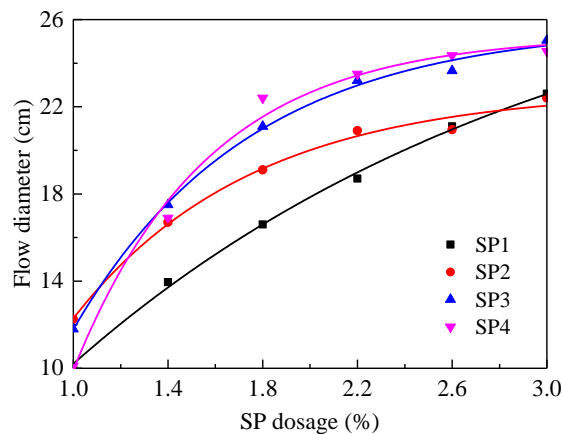


Figure 2.6: Spread flow of UHPCs versus SP dosage.

It shows a lower flow diameter of UHPCs than that of pastes at the same dosage of SP, the reduction is particularly high for SP1 and SP2 at the saturation dosage. SP3 shows excellent effect on spread flow in both pastes and concrete. On the contrary, the SP2 presents a good ability on spread flow in pastes, but cannot keep this ability in UHPCs when aggregates are used as well.

- **Dispersing mechanisms**

It is believed that the dispersing forces between particles are generated by steric hindrance and electrostatic force after adsorption of PCE-type SP molecules [30,33]. Some researchers noted that the PCE-type SP begins to disperse the particles when it causes the zeta-potential of the pastes to change [58]. A larger magnitude negative value of zeta potential means a higher electrostatic repulsion, which may contribute to a higher fluidity [57]. Obviously, the suspensions of all powders with SP1 have more negative zeta potentials than that of SP3 (see Figure 2.4), which means that SP1 has a larger electrostatic repulsion force than SP3. However, SP1 has a worse dispersing ability than SP3, as seen in Figure 2.5 and Figure 2.6. Thus, the dispersing ability of PCE-type SP is more dependent on the steric hindrance of adsorbed molecules rather than the electrostatic repulsion force.

The amount of adsorbed molecules depends on their structure and dosages, and a higher adsorption on particle surface usually occurs with a higher molecular weight, lower side chain density and shorter side chains [31,36]. The typical plateau occurs after the saturation

dosage as shown in Figure 2.5, whose existence is confirmed by the results of zeta potential of particles (see Figure 2.4). This typical plateau at high dosages can be also observed from the relationships between the SP adsorption on particles and SP dosages [29,33,36,67]. It manifests that SP works only after the adsorption on the particles, which corresponds to the surface coverage [29,68]. When the used SP reaches the saturation dosage, a complete surface coverage will be obtained. Then the dispersing ability of SP will not increase anymore, which results in the occurrence of the typical plateau at high dosages.

Figure 2.6 shows considerably lower flow diameters at the same dosage usage of all SPs compared to the results shown in Figure 2.5(a), owing to the addition of aggregates. The decrease tendency of flow is possibly due to the high content of clay inside the used micro-sand by X-ray diffraction analysis, which can occur as an impurity in aggregates [69]. The clay can absorb SP and free water, and then the spread flow is reduced. The negative influence of clay on flow ability might originate from the following aspects: 1) the clay can absorb the free water and reduce the spread flow; 2) some clays (e.g. kaolinite clay) reduce the dispersing effectiveness of SP due to strong electrostatic interaction or formation of clay-PCE “network” via hydrogen bonding [43]; 3) some clays (e.g. montmorillonite clay) exhibit much higher affinity for PCE than cement, which means the adsorption of SP on powders will be decreased [45,46]. Some researchers suggested modifying the polyethylene oxide side chain to obtain a more clay tolerant PCE [44]. It is worth to point out that SP2 possesses the best dispersing ability for paste below the saturation dosage, but has a relatively weak dispersing ability for UHPC. It indicates that SP2 has a poor adsorption effect on UHPC than on paste, which indicates that SP2 is incompatible with the micro-sand in this study.

2.3.2 Slump life and fluid-retaining ability

Fresh concrete is well known to lose its workability with time, which is called “slump flow loss” [32,70,71]. Figure 2.7(a) presents the slump life of the fresh UHPC in 4 hours. It shows that the UHPCs with SP1 and SP2 have a short slump life, which have a linear decrease relationship between the flow and elapsed time. The UHPC with SP4 can only keep a good slump life for about 1 h, then the spread flow decreases quickly. UHPC with SP3 presents the best slump life, nearly without any slump flow loss in the testing period of 4 h.

Figure 2.7(b) shows the spread flow of the UHPCs within 4 hours above the saturation dosages. Compared to the results shown in Figure 2.7(a), the fluid-retaining abilities are not improved or just have a slight increase for SP4 after 2 h, which indicates that the further addition of PCEs cannot increase the slump life. Beyond the saturation dosages of SPs, the completed surface coverage of particles has already been produced and it will not adsorb the PCEs anymore, which results in the same fluid-retaining ability. It also indicates that the slump life is mainly dependent on the adsorbed PCEs rather than PCEs in aqueous solution. Nevertheless, the retention effects can be enhanced greatly when a slightly more amount of water is added, as shown in Figure 2.7(c), indicating a very sensitive role of water in UHPC. More alite hydrates and more Ca^{2+} ions are generated, and lime saturation in the pore solution increases, which will retard the hydration and then enhance the fluidity retention [32].

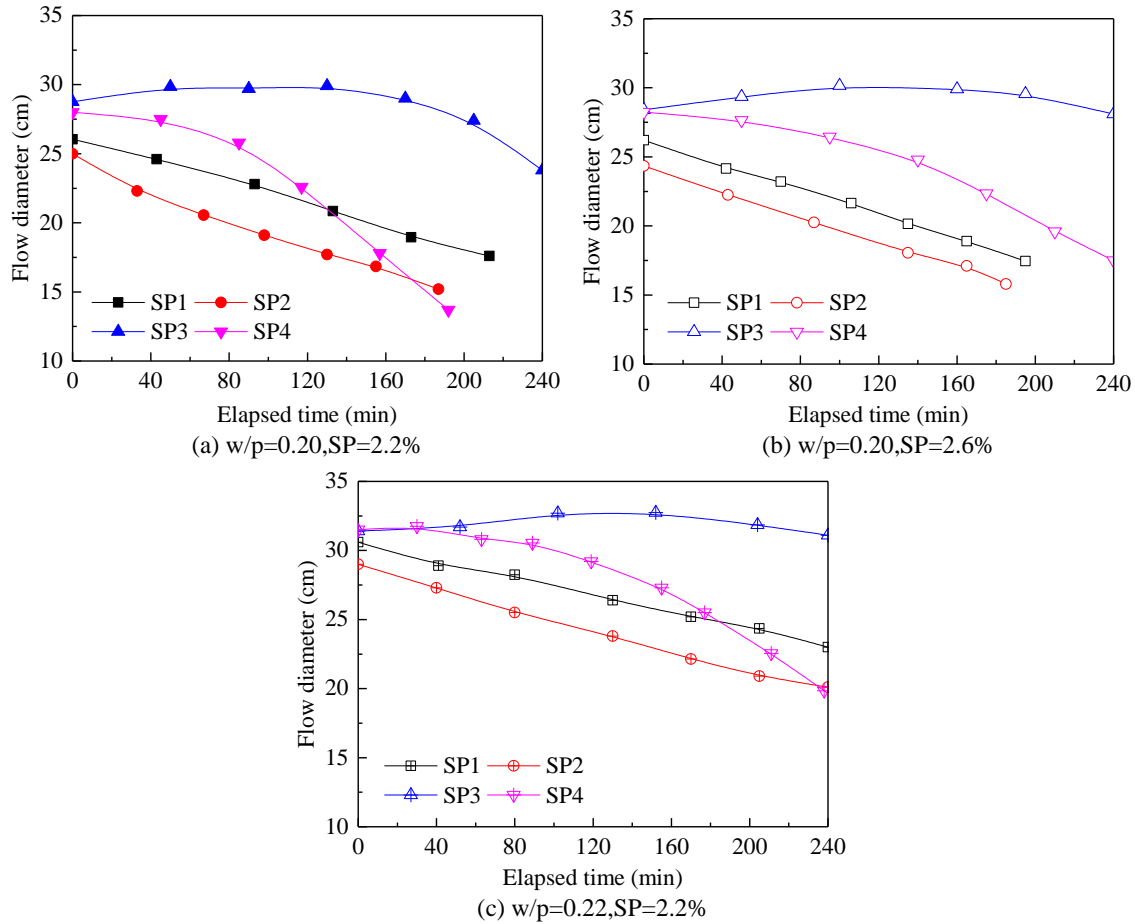


Figure 2.7: Spread flow of UHPCs versus time.

The fluid-retaining ability is an important index to describe the workability of concrete, which is usually measured by slump flow loss. The previous researches imply that slump flow loss involves chemical and physical processes [32], which is mainly attributed to the w/p ratio, type and dosage of SP, as well as SO_3 , alkali content, C-S-H formation, charge characteristic, C_3S/C_2S ratio [32,72,73]. UHPC with SP1 has the shortest slump life, even though SP1 shows the highest retardation effect on the paste setting. The possible reason is that SP1 has a low adsorption ability, which induces an uncompleted surface coverage. Uncompleted surface coverage (below saturation dosage) results in a rapid stiffening of the concrete [29]. UHPC with SP2 has a poor slump life probably due to its weak retardation effect on paste hydration and uncompleted surface coverage. The UHPC with SP3 shows an excellent slump life in the whole testing time (4 h) because of good adsorption ability. UHPC with SP4 can maintain a good slump life up to 1 h, which then experiences a sharp decrease after that time. The fluid-retaining ability is mainly determined by the adsorbed PCEs rather than the PCEs in the aqueous solution, which is similar to the dispersing ability.

2.3.3 Retardation effect

- Hydration kinetics of paste

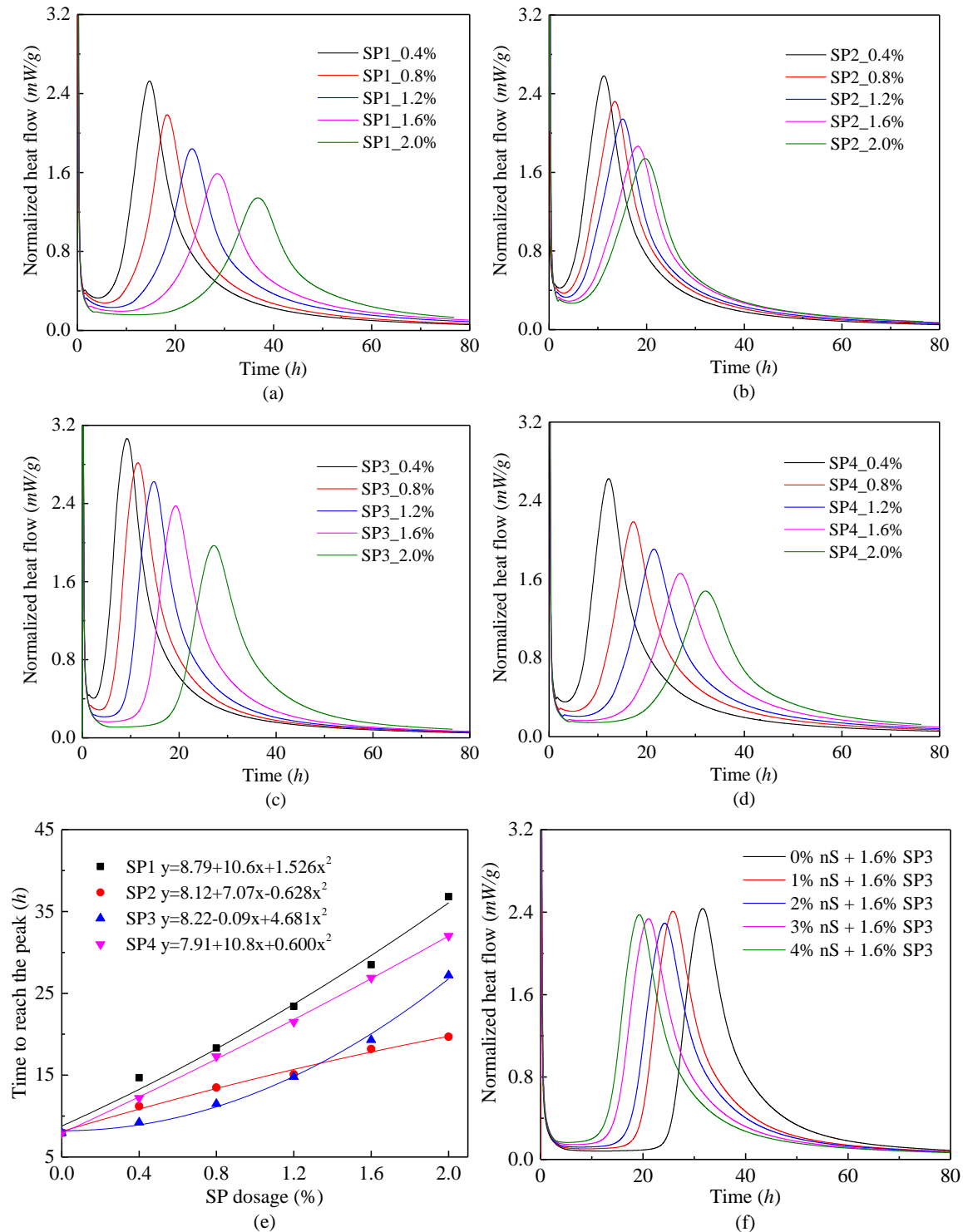


Figure 2.8: Calorimetry test results of pastes.

Figure 2.8(f) gives the normalized heat flow of pastes using different contents of nano-silica. The normalized heat flow curves indicate the time to reach the peak reduces from about 40 h to 20 h, with the increase of nano-silica addition from 0 to 4%. Nano-silica can act as nucleation sites for the precipitation of hydration products, thus accelerating the hydration

reactions of cement [65]. Thus, it is feasible to add an appropriate content of nano-materials to decrease the retardation effect when a high dosage of PCE is used. In this study, 3% of nano-silica is observed to be the optimal content on providing accelerating effect on the hydration process.

- **Setting time of paste**

Figure 2.9 presents the initial and final setting times of pastes incorporating SP1, SP2, SP3 and SP4. It is obvious that the setting times are affected by both SP types and dosages. For all those four SPs, high dosages always increase the setting times. It is also clear that pastes with SP1 have the longest setting times, reaching at about 7.8 h of initial and 11.2 h of final setting time at a dosage of 1.2%. The pastes with SP2 show the shortest setting times, which are approximately 4.25 h (6.5 h) of initial (final) setting time at the dosage of 1.2%. Compared with SP1 and SP2, medium setting times are observed for the pastes containing SP3 and SP4.

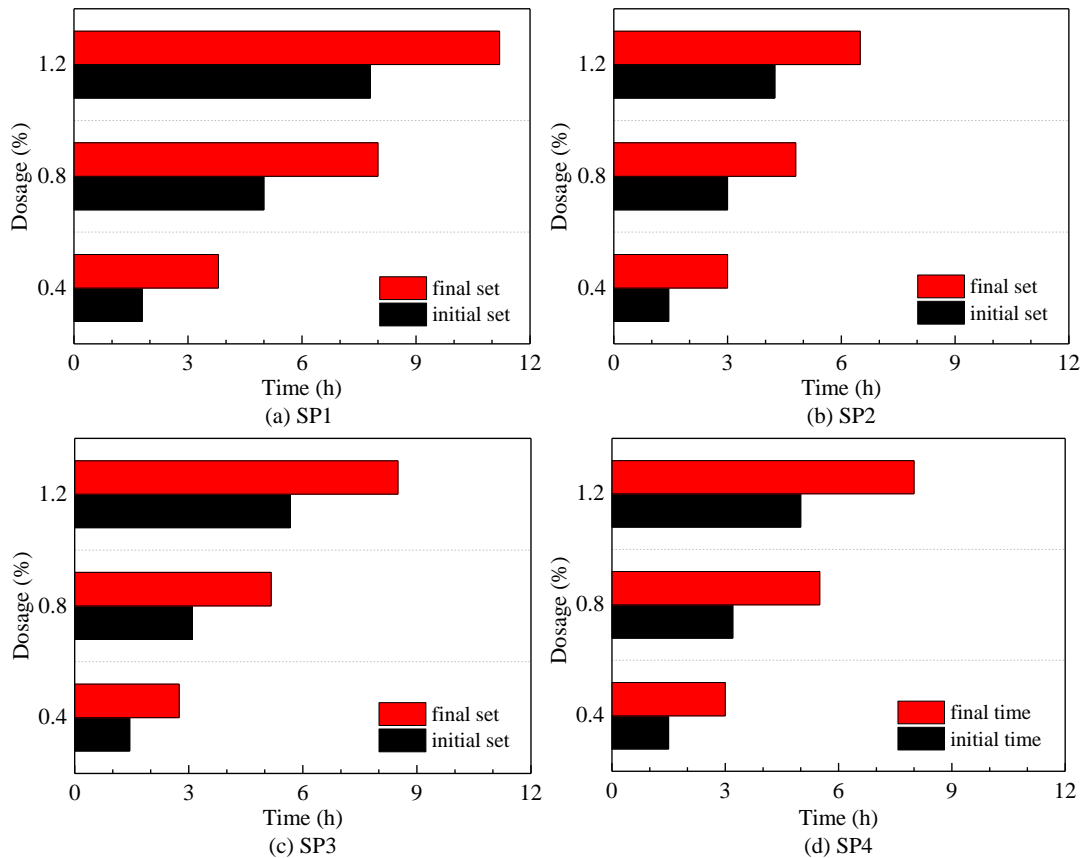


Figure 2.9: Setting time of pastes.

- **Early-age strength of UHPC**

The retardation effect of PCE polymers leads to the delay of the hydration process, which would consequently lead to a slower development of early-age strength of UHPC. Figure 2.10(a) presents the compressive strengths of UHPC with different SPs at a fixed dosage of 2.2%. The 1-day compressive strengths of the UHPCs containing different types of SPs are about 3.2 MPa, 71.1 MPa, 70.9 MPa, and 46.6 MPa, respectively. The 3-day and 7-day compressive strengths are approximately close to 80.9 MPa and 93.3 MPa, respectively.

Figure 2.10(b) shows the compressive strength of UHPC with SP3 at different dosages. With the increase of SP3 dosage, the 1-day compressive strengths sharply decrease from 75.8 MPa to 1.1 MPa. While the 3-day compressive strengths have a smaller difference, changing from 82.0 MPa to 68.3 MPa. The 7-day compressive strengths are near to 91.8 MPa. It can be concluded that different types and dosages of SPs contribute to a large different early-age strength development, especially for 1-day strength. The differences become smaller after 3 days, and comparative strengths are obtained after 7 days.

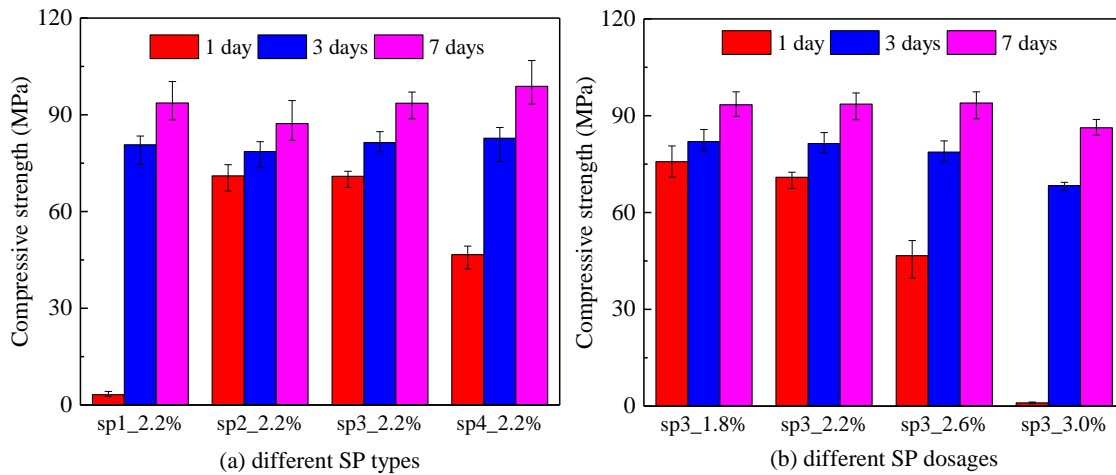


Figure 2.10: Compressive strength of UHPCs.

- **Retardation mechanisms**

The retardation effect of SP can be observed and reflected by the hydration kinetics and setting of pastes, as well as flow retention and early-age strength development of concretes. Some researchers described the retardation effect of PCEs as following: adding PCEs prevents solid phase nucleation and hydration products growths, then leads to retardation of cement hydration [31].

The results of hydration kinetics of pastes show that the retardation effects of PCEs on hydration are greatly attributed by types and dosages of PCEs. It should be noted that the normalized heat flow of all pastes (approximately 1.2%) is still delayed after saturation dosage (Figure 2.8). It indicates the retardation effect is not only affected by the adsorbed PCEs but also the PCEs in the aqueous phase, which is different from the mechanism of fluid-retaining effect. Generally, a larger retardation effect is probably resulted from a shorter side chain [44], higher concentrations of the carboxylic groups in the aqueous phase, higher adsorption amount of PCE on cement particle, and different charge characteristics of SP molecules ($-\text{COO}^- > -\text{SO}_3^- > \equiv\text{N}^+$ [47]). Some researchers illustrated the retarding effect of PCEs to three aspects [33,74]: 1) hindering the diffusion of water and ions at the particle-solution interface by adsorbed polymer layers; 2) inhibiting the nucleation and precipitation of hydrates through chelating the Ca^{2+} ions in the aqueous solution by $-\text{COO}^-$ groups in PCE molecules; 3) changing the growth kinetics and morphology of hydrate phases by better dispersion of particle grains.

From the results of setting time of pastes, it indicates that those PCEs have a retardation effect on the setting of pastes, and the retardation effect is higher with the increase of SP

dosages. The results indicate that SP1 is not suitable to obtain a high early age strength for paste or concrete due to the high retardation effect, which is confirmed by the strength results as shown in Figure 2.10. The low retardation effect of SP2 makes it possible to achieve a relatively high early age strength for paste or concrete.

From the early-age strength development of view, it is obvious to observe the retardation effect of PCEs on the development of strength during the early curing age. The retardation effect on the early-age strength of UHPC is in line with the results from hydration kinetics and setting times of paste. A higher dosage always shows a lower strength before 3 days, and the differences turn to be smaller with the increasing curing time. From Figure 2.10, it also indicates that the retardation effect has limited influence on the strength development after 3 days.

2.3.4 Physical and chemical process effects

- **Correlation between final setting and hydration**

Some researchers pointed out that the final setting time of paste (t_{final}) is closest to the inflection point of the heat flow curve in the accelerating stage, which means the correlation coefficient is close to 1.0 [75]. To analyse the correlation and understand the physical meaning of the inflection point, the first derivative $\ddot{Q}(t)$ of the heat flow curve $\dot{Q}(t)$ is calculated by:

$$\ddot{Q}(t) = \frac{\partial \dot{Q}(t)}{\partial t} \quad (2.3)$$

where $\ddot{Q}(t)$ is the heat flow rate [J/s^2], $\dot{Q}(t)$ is the heat flow [J/s], t is the time [s]. As shown in Figure 2.11, these heat flow rate curves can be interpreted as the energy acceleration curves. The vertical lines present the times $t_{\ddot{Q}=max}$ under the maximum heat flow rates (inflection points of the accelerated heat flow curves).

The relationship between t_{final} and $t_{\ddot{Q}=max}$ of all pastes are shown in Figure 2.11(c). Linear relationships for all PCEs under different dosages are observed, which means that there is a good correlation between t_{final} and $t_{\ddot{Q}=max}$. Meanwhile, the four linear trend lines cross the same point at (4.6, 0.9), which represents the theoretical value of t_{final} versus $t_{\ddot{Q}=max}$ of paste without SP. A time difference between t_{final} and $t_{\ddot{Q}=max}$ clearly exists, which changes with different type and dosage of PCE. These differences occur due to different mechanisms for setting and hydration kinetics of pastes. Namely, hydration is mainly affected by chemical processes, while the setting time is determined by both chemical process and physical coagulation, especially under the use of PCEs. The physical coagulation effect makes the t_{final} smaller than $t_{\ddot{Q}=max}$, and a larger time difference indicates a higher physical coagulation effect. A smaller slope of the trend line indicates that the SP has a larger delay effect on the chemical process than the physical coagulation.

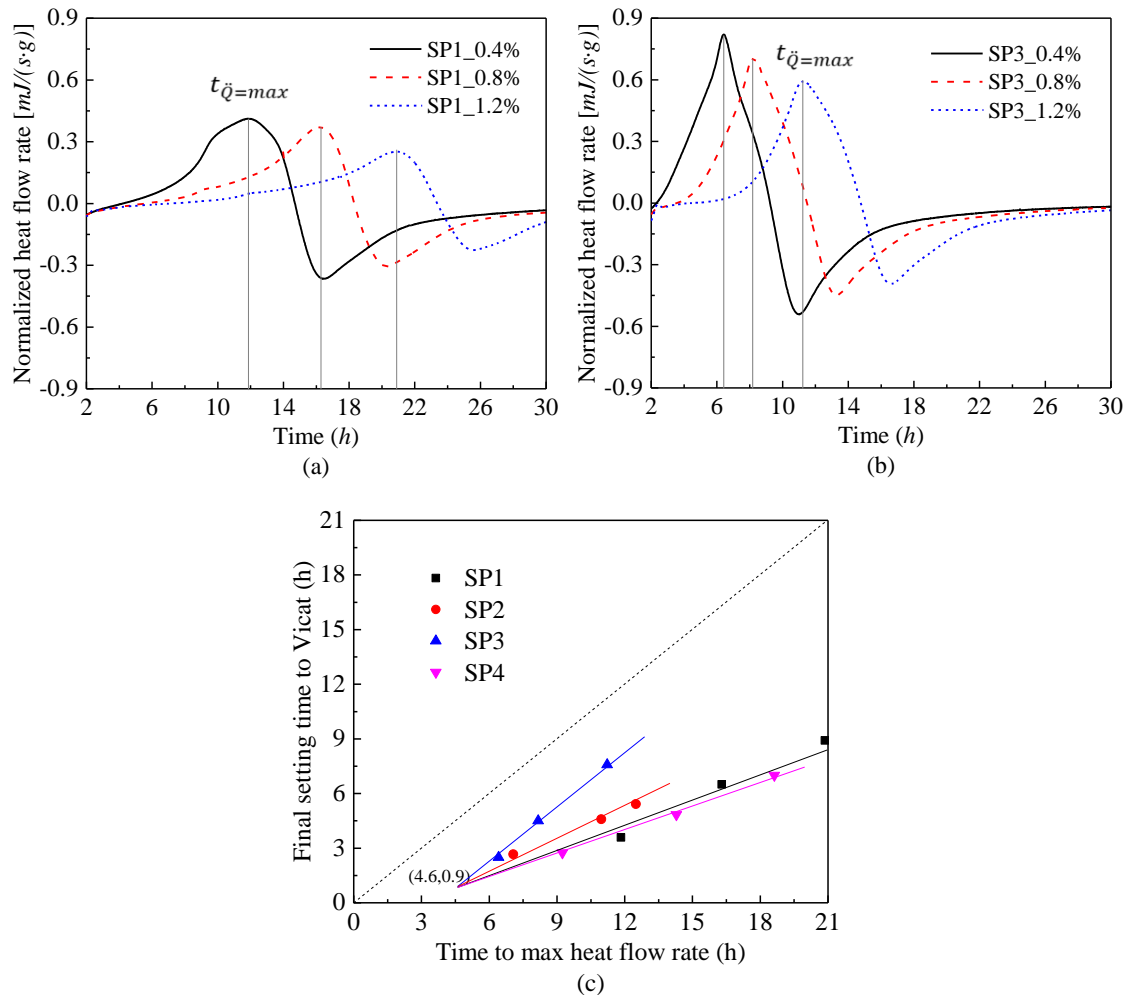


Figure 2.11: Normalized heat flow rates and t_{final} versus $t_{\dot{Q}=max}$.

- **Correlation between shrinkage and retardation**

The early-age shrinkages of UHPC, including the chemical and autogenous shrinkage, are particularly high because of the low w/p and large amount of powders [76,77]. Those shrinkages producing early-age cracks have been important issues for structural concretes, especially for their long-term durability, which are mainly resulted from moisture loss and self-desiccation [38,78]. Usually, the chemical and autogenous shrinkage of cement is considered as an internal (absolute) and external (apparent) volume reduction, respectively. Some researchers believe that the initial cracking may already exist due to autogenous shrinkage [77]. If it is free, the autogenous shrinkage deformation increases as hydration progresses after the final setting. If it is restrained, significant tensile stress and cracks may arise.

Figure 2.12(a) shows the chemical shrinkages of pastes with different SP types, while Figure 2.12(b) presents the chemical shrinkages of pastes incorporating different dosages of SP3. It is obvious that different types of PCE mainly influence the chemical shrinkage development rate before 24 h, after that they are almost the same. Incorporating a higher dosage of PCE, the paste shows a slower developing rate of chemical shrinkage before 24 h.

Figure 2.13(a) and Figure 2.13(b) present the autogenous shrinkage of pastes with different SP types and dosages, respectively. It can be concluded that SP3 and SP4 contribute to a smaller absolute value of autogenous shrinkage than that of SP1 and SP2. The absolute value of autogenous shrinkage decreases continuously from 0.4% to 1.2% of SP3.

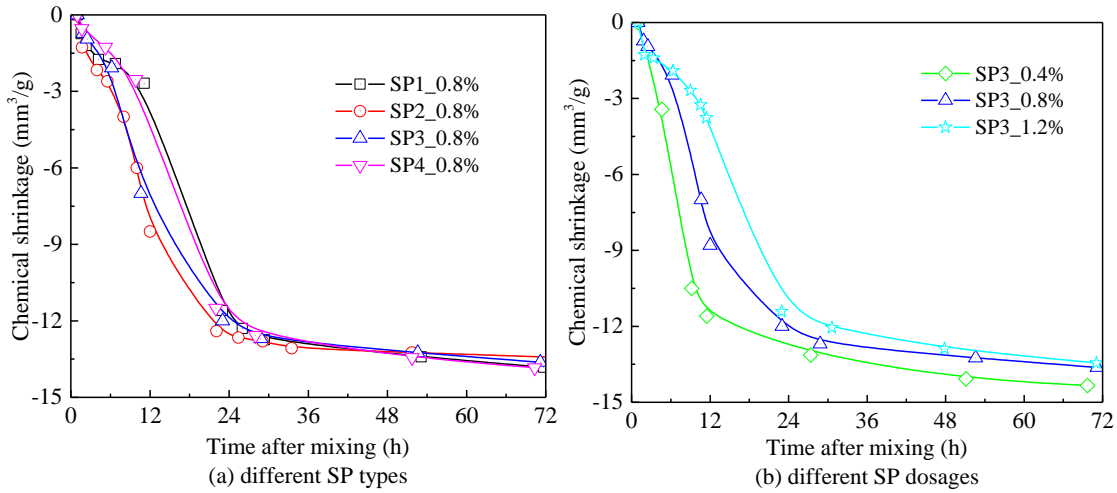


Figure 2.12: Chemical shrinkage of pastes.

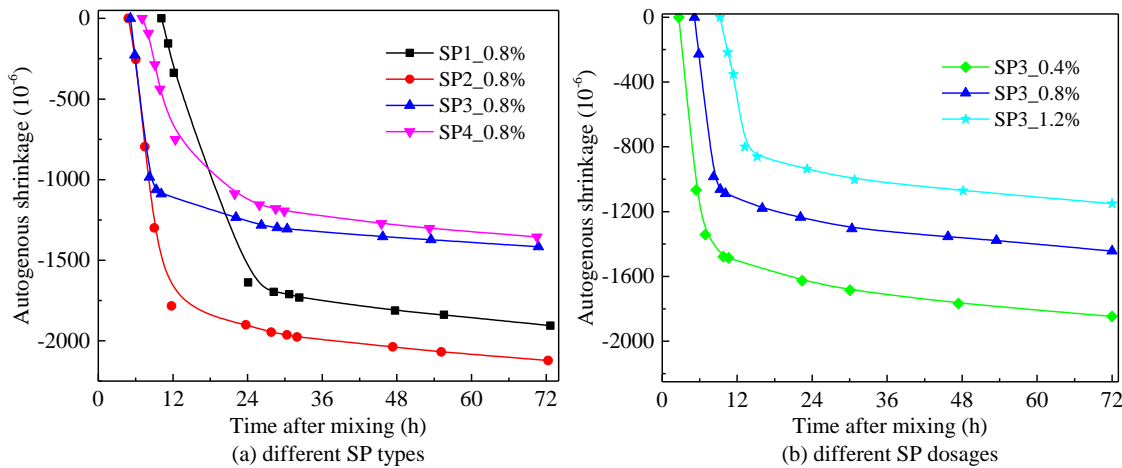


Figure 2.13: Autogenous shrinkage of pastes.

The chemical shrinkage of paste is generated by the absolute volume change during the hydration. Therefore, it should be influenced by the retardation effect of PCEs on the hydration of paste, which is mainly determined by chemical process. Comparing the results shown in Figure 2.8 and Figure 2.12, there is a correlation between chemical shrinkage and hydration delay, a longer delay results in a faster developing rate of chemical shrinkage before about 24 h. After that, the chemical shrinkages are almost the same, which indicates that the retardation of PCEs mainly affects the hydration rate in the early age, and possesses little influence on the final total hydration, which is consistent with the findings of the early-age strength development of UHPC.

The autogenous shrinkage of pastes was measured based on the final setting time, which was considered as the zero time of autogenous shrinkage. Hence, the autogenous shrinkage results are affected by the retardation effect of PCEs on the setting of paste, namely, both

chemical process and physical coagulation. For the pastes with the same type of PCEs, the absolute autogenous shrinkage value can be reduced with the increase of SP dosage, as seen from Figure 2.13(b), which means a slower physical coagulation and chemical process within a certain period could result in a smaller autogenous shrinkage. However, there is no obvious correlation between autogenous shrinkage and setting with the addition of different type of PCEs from Figure 2.13(a). This is probably because the physical coagulation and chemical process have different influence on the final setting time and autogenous shrinkage.

2.4 Conclusions

This chapter investigates the effect of PCE-type SP on the early-age behaviour of UHPC. Zeta potential of powder suspensions, setting, hydration kinetics, early-age shrinkages, spread flow and water demand of pastes, spread flow, slump life and early-age strength development of UHPC are measured. The dispersing and fluid-retaining ability, retardation effect of PCEs, as well as physical coagulation and chemical process with PCEs are analysed and discussed. The results indicate that appropriate types and dosages of PCE-type SP should be carefully selected for the design of UHPC. Based on the obtained results, the following conclusions can be drawn:

- The zeta potential of different powder suspension shows large difference under the addition of PCE-type SP. It proves the existence of the saturation dosages and shows steric hindrance as the main influence factor on the dispersing ability of PCE-type SP.
- The dispersing ability of PCE-type SP is greatly dependent on its chemical structure and adsorption ability on particles. The flow ability of paste increases continuously from critical dosage to saturation dosage and will not increase after obtaining a complete surface coverage of particles above the saturation dosage.
- The fluid-retaining ability is mainly determined by the adsorbed PCEs and it will not increase after saturation dosages of SPs due to the complete coverage of particles, but the water content plays a very sensitive role on the fluid-retaining ability of UHPC.
- Both the adsorbed PCEs and the PCEs remaining in the aqueous phase contribute to the retardation effect. The retardation effect mainly influences the early-age strength before 3 days. 3% of nano-silica as cement replacement is found as the optimal content to reduce the retardation effect.
- A linear correlation between t_{final} and $t_{\dot{q}=max}$ is observed. The $t_{\dot{q}=max}$ is mainly resulting from hydration, while the t_{final} can be influenced by both coagulation and hydration rates.
- The chemical shrinkage of paste is mainly generated by chemical process, which only influences the chemical shrinkage developing rate for about 1 day with PCEs. But autogenous shrinkage is affected by both coagulation and hydration rates.

Chapter 3

Binder optimization for UHPC by using mineral admixtures

This chapter aims to optimize the binder by mineral admixtures addition to the UHPC system to reduce cement content, for environmentally sustainable and cost-efficient purposes. Two methods are proposed, namely utilizing high-volume limestone powder to replace cement and developing quaternary binders with cement-slag-limestone-silica. The roles of limestone powder on sustainability, plasticization effect, hydration kinetics, microstructure and hardened properties are investigated, as well as the synergistic effect of quaternary blends with cement-slag-limestone-silica. Results show that limestone powder shows a positive mineral plasticization effect that should be considered in designing UHPC. The degree of secondary pozzolanic hydration is more intensive than C_3S/C_2S hydration, which can enhance the later-age strength development potential. The optimum content of limestone powder appears to be 50 vol.% of the total powder content in UHPC, and contribute to a higher strength, denser pore structure, diminished total free shrinkage and higher sustainability efficiency. Quaternary blends with cement-slag-limestone-silica in UHPC pastes have considerable advantage of reducing embodied energy and improving sustainability efficiency. Furthermore, positive synergies in term of strength, fibre-to-matrix bond and total free shrinkage are observed in UHPC pastes with quaternary binders compared to binary and ternary ones.

This chapter is partially published elsewhere:

P.P. Li, H.J.H. Brouwers, W. Chen, Qingliang Yu. Optimization and characterization of high-volume limestone powder in sustainable ultra-high performance concrete. Submitted.

P.P. Li, Y.Y.Y. Cao, H.J.H. Brouwers, W. Chen, Q.L. Yu. Development and properties evaluation of sustainable ultra-high performance pastes with quaternary blends. *Journal Cleaner Production*. 240 (2019) 118124.

3.1 Introduction

UHPC is an advanced and promising construction material with excellent fresh and hardened properties [6,10,79,80], characterized by a very low water amount and a high binder content [28]. Although the structures made by UHPC are sustainable when considering the less concrete demand and longer service life due to the higher strength and better durability, the binder or cement consumption in UHPC itself is often more than 900 kg/m^3 , e.g. 37.9% by the total mass as illustrated in Figure 3.1 [5], which is approximately three times as that in normal strength concrete [81]. Generally, commercial UHPC is usually twenty times more expensive than the normal strength concrete, and three times greater in terms of the cement consumption [19]. Those drawbacks of large environmental footprint and high cost currently limit the use of UHPC. Therefore, it is motivated to develop eco-friendly and low-cost UHPC for greater acceptance and wider engineering application.

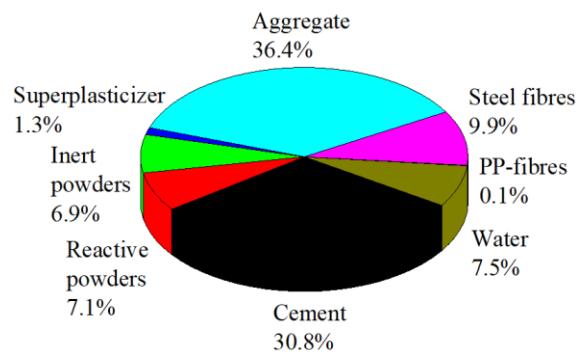


Figure 3.1: Average composition (by mass) of UHPC from 75 references [5].

Currently, attempts have been made to reduce the cost and embodied energy by using less expensive and locally available eco-friendly constituents. Limestone powder shows great potential due to its very low embodied energy, abundant reserve on earth and low cost [82]. Furthermore, an appropriate content of limestone powder can provide some positive influence on the properties of concrete as filler, nucleation and chemical effects, as well as improving workability [83]. However, both roles and optimum content of limestone powder still need further study in UHPC systems with relatively low water-to-binder ratio and high superplasticizer dosage. For example, researches have already indicated that limestone powder has a positive effect on workability and mixing time [84,85], but some minerals addition could cause incompatibility problem in a UHPC system with low water and high PCE superplasticizer content [42,46]. The compatibility and synergic effect between limestone powder addition and superplasticizer and/or water amount is very rarely investigated. The mechanism of the mineral plasticization effect of limestone powder is not systematically researched. Since the compactness and porosity of UHPC are very sensitive to the water amount and superplasticizer dosage, how to make full use of this positive effect and reduce water addition is of great significance. Besides, the substitution content of cement by limestone powder in normal concrete is usually less than 30% without sacrificing too much of the hardened properties [86–88]. Limestone powder was suggested to replace cement up to 15% or 100% of silica powder in UHPC [84], and it was also used to replace quartz powder in UHPC without any negative impact on strength or dimensional stability

[89]. Furthermore, limits or allowable contents of limestone powder in cement have a large difference based on different standards, such as 35% in European standard (EN 197-1: 2000), 15% in Canadian standard (CSA A3001: 2010), 25% in Chinese standard (JC/T 600: 2010) and 15% in American standard (ASTM C595: 2012). It was pointed out that a reasonable range should be considered during the utilization of limestone powder [82]. However, the optimum amount of limestone powder in UHPC is still not determined yet.

Furthermore, some researches on developing sustainable UHPC, through substituting Portland cement by some supplementary cementitious materials (SCMs), are mainly concentrating on binary and ternary blends [90–93]. Positive synergistic effects of ternary binder with cement-silica fume-slag has been demonstrated on workability and early-age strength due to the accelerated hydration by silica fume and low water demand of slag, but shows negative synergistic effects on porosity and later-age strength because of dilution effect [90]. It showed that ternary binder with cement-silica-limestone has great potential to benefit sustainability and strength of UHPC mixtures by replacing some cement and silica powder, because of pozzolanic effect of silica, and filler effect and high sustainability of limestone powder [84]. Several researchers also reported benefits of quaternary binders in ordinary mortar and concrete, such as positive effect on strength and chloride resistance with cement-fly ash-silica fume-metakaolin/slag/limestone by optimum composition combination [94,95]; good sulfuric acid resistance under drying-immersion cycles with cement-slag-limestone-pozzolana by reducing portlandite and degradation of hydrated compounds of cement, attributed to the dilution effect of limestone and pozzolanic reactions by slag and pozzolana [96,97], improvement on shrinkage and permeability in hot climate with cement-fly ash-slag-silica fume by accelerating the hydration process [98]. Nevertheless, there is no study yet on quaternary system by adding cement-slag-limestone-micro/nano silica in UHPC. The probable positive or negative synergy of quaternary binder with cement-slag-limestone-silica is not clear in the special system of UHPC characterized with low water and high superplasticizer amount. In addition, most of the studies on environmental sustainability evaluation of concrete applying supplementary cementitious materials were performed by comparing only one or two materials [99] and a sound analysis of whole binding materials on environmental sustainability is of highly significance.

Therefore, this chapter aims to optimize high-volume limestone powder content and understand the synergistic effect of quaternary binders with cement-slag-limestone-micro/nano silica in developing sustainable UHPC system. The roles of limestone powder on plasticization, hydration process and hardened properties of UHPC are analysed by investigating the fluidity, phase composition, pore structure, compressive strength and shrinkage. The positive synergies in terms of strength, bond and shrinkage are assessed to demonstrate the reasonability of quaternary blends in sustainable UHPC instead of binary or ternary ones.

3.2 Optimization of high-volume limestone in UHPC

3.2.1 Materials and mixtures

The mixtures are designed including following materials, Portland cement CEM I 52.5 R (PC), micro-silica, limestone powder (LP), fine sand (S), water (W) and PCE-type superplasticizer (SP) with the solid content of 35% (SP3 from Chapter 2 is used). To avoid any large difference of physical packing density by the size effect, in this research, the particle sizes (Blaine surface area of around 570 m²/kg) and morphology of limestone powder are similar and/or comparable to those of cement (Blaine surface area of around 520 m²/kg), as shown in Figure 3.2.

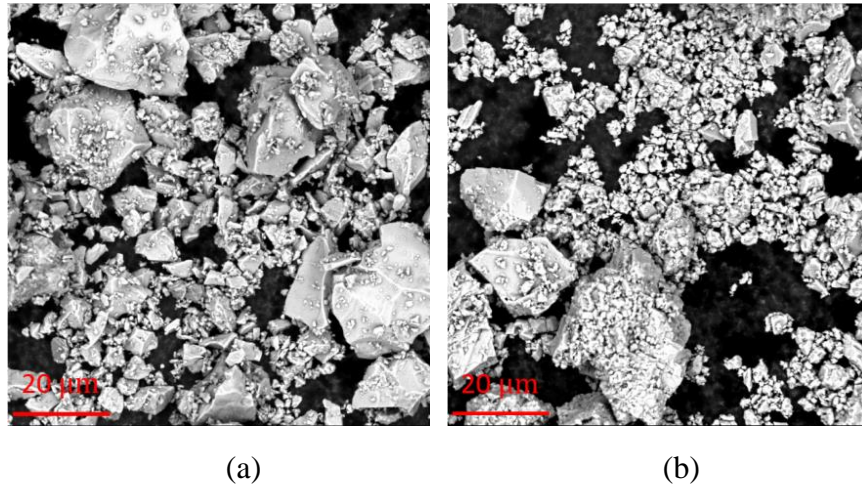


Figure 3.2: Particle morphologies of (a) cement and (b) limestone powder by SEM.

Table 3.1: Proportion of ingredients for designed UHPC.

Mix	Powder (P)			S/P	W/P	SP/P	PC	mS	LP	S	W	SP
	PC	mS	LP									
	(by volume)			(kg/m ³)								
M0	86.9%	13.1%	0%	0.85	0.67	0.042	1072	119	0.0	885	261	19.6
M20	69.5%	10.5%	20%	0.85	0.63	0.037	871	97	216	899	251	17.4
M40	52.1%	7.9%	40%	0.85	0.60	0.031	664	74	439	914	241	15.2
M60	34.8%	5.2%	60%	0.85	0.57	0.026	448	50	666	925	234	12.8
M80	17.4%	2.6%	80%	0.85	0.55	0.021	227	25	898	936	227	10.4

Note: In this study, the total of PC and mS is considered as binder, while the powder includes binder and LP.

A total of 5 UHPC mixtures are designed in this study, and the detailed mix proportions can be seen in Table 3.1. Utilizing the key components' proportions by volume instead of by mass is more reasonable and useful in mix design [64,100]. The content of micro-silica is fixed at 13.1% by the total volume of binders (cement plus micro-silica in this study), as 10% by mass. The volume of sand-to-powder ratio is fixed at 0.846. The volume substitution of binder by limestone powder ranges from 0 to 80 vol.%, with an increment frequency of 20 vol.%. The water including water in superplasticizer and externally added tap water, and solid superplasticizer dosage by volume of powder (bvop), are adjusted to achieve a mini-slump spread flow of 30 ± 2 cm, which meets self-compacting property without having too

much surplus fluidity [100,101]. The determining method on minimum required water content and superplasticizer dosage will be discussed and described in Section 3.2.3.

3.2.2 Experimental methods

The isothermal calorimetry, spread flow and free shrinkage are tested based on the methods as mentioned in Section 2.2.2. Other experimental methods are described below.

- **Thermal gravimetry**

In order to research the effect of limestone powder on the cement hydration degree, the thermal gravimetric (TG) and differential thermal gravimetric (DTG) results of the 5 hardened UHPC at the age of 28 days are recorded by a Netzsch simultaneous analyser (model STA 449 C). The heating rate during this measurement is 10 °C/min, from 20 °C to 1000 °C under the flowing nitrogen environment. The hardened UHPC is first ground. Then, the powder is collected by using a 63 μm sieve and used for the thermal gravimetric test.

- **Water-permeable porosity**

The water permeable porosity of the designed UHPC is measured by using the vacuum-saturation technique [102]. The samples are cut from the 50 mm \times 50 mm \times 50 mm cubic specimens after 28 days with a thickness of about 20 mm. The water permeable porosity φ (%) can be calculated as,

$$\varphi = \frac{m_s - m_d}{m_s - m_w} \times 100 \quad (3.1)$$

where m_s , m_d and m_w are the masses of sample measured in air after water saturation by vacuum condition, in air after oven drying, in water after water saturation by vacuum condition, respectively.

- **Mercury intrusion porosimetry**

The pore size distributions are measured by mercury intrusion porosimetry (MIP, Micromeritics AutoPore IV). The hardened specimens are crushed into small pieces of 2 - 4 mm, and approximately 1.5 g dried samples are used for measurement. The intrusion pressure changed from 0 to 227 MPa, with an Hg surface tension of 485 dynes/cm and contact angle of 130 degrees.

- **Nitrogen sorption**

To further analyse the gel pores in the designed UHPC, nitrogen sorption analysis is carried out with a micromeritics instrument, TriStar II 3020, at the boiling temperature of liquid nitrogen (77 K). After 28 days water curing, the hardened UHPC is crushed into small pieces with diameter less than 1 mm, following oven drying at 40 °C for 3 days [103]. The specific surface area can be measured by the Brunauer-Emmett-Teller (BET) method [104]. Meanwhile, the pore size distribution can be calculated by the Barrett-Joyner-Hallenda (BJH) method [105] from the desorption isotherm [106].

- **Compressive strength**

The compressive strength of UHPC is tested after 7 and 28 days in accordance with [107], by 50 mm × 50 mm × 50 mm cubic samples. The fresh UHPC mixtures are poured into steel mould, then covered by plastic film to keep moisture for approximately 24 hours under room temperature around 20 °C. After that, all samples are demoulded and cured in water.

3.2.3 Experimental results

- **Plasticization effect of limestone powder**

To explore the mineral plasticization effect of limestone powder in the UHPC system, characterized with low water-to-powder ratio and relatively high superplasticizer dosage utilization, the spread flow of cement-limestone paste is investigated under different superplasticizer dosages and limestone powder contents, as shown in Figure 3.3. With the continuous addition of PCE-type superplasticizer, the mini-slump flow diameters of cement-limestone pastes firstly increase rapidly at relatively low dosages, up to the maximum values at saturation dosages (i.e. saturation point shown in Figure 3.3), subsequently typical plateaus occur. This trend is attributed to the adsorption of PCE molecules that disperse the solid particles by steric and/or electrostatic forces, thus releasing free water and strengthening fluidity [33]. After achieving the saturation adsorption, extra superplasticizer only remains in free water and does not enhance fluidity anymore [108].

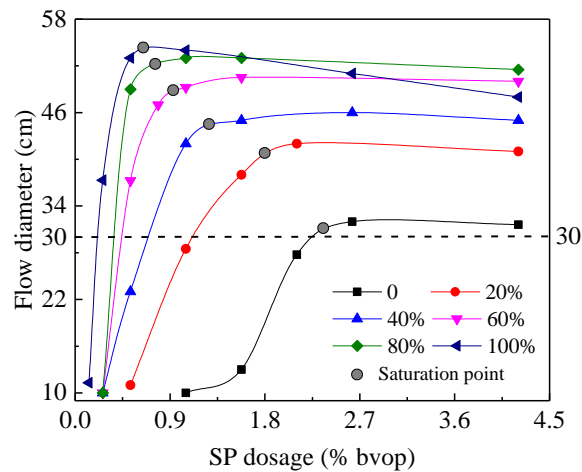


Figure 3.3: Spread flow of cement-limestone pastes.

The saturation dosage of superplasticizer has a great application significance in UHPC, which can achieve the best workability with the lowest superplasticizer addition at a fixed water amount, or the lowest water utilization for a desired workability. With the replacement of cement by limestone powder from 0 to 100 vol.% in the cement-limestone pastes, the superplasticizer saturation dosage diminishes from approximately 2.5% to 0.6% by the volume of total powder (bvop), as shown in Figure 3.4. The correlation between limestone powder content and superplasticizer saturation dosage indicates that less superplasticizer can be used in UHPC system in the presence of limestone powder, resulting in environmental and economic benefits. For example, the SP demand decreases from 2.2% to 0.2% for a desired mini slump flow of 30 cm, as shown in Figure 3.4. Although a less superplasticizer

saturation dosage is needed, the maximum flow diameter (at saturation dosage of superplasticizer) improved from about 31.2 cm to 53.5 cm, as shown in Figure 3.5. The correlation between limestone powder content and maximum flow diameter indicates that introducing limestone powder can improve the potential of workability in UHPC system. On the other hand, the mini slump flow between 24 cm to 26 cm already meets the requirement of self-compacting property [100,101]. Hence, the fluidity could probably be surplus when a high volume of binder is replaced by limestone powder. In other words, the water content could be further reduced, which certainly tends to improve the hardened properties of UHPC, such as the compactness, pore structure, strength, shrinkage, etc.

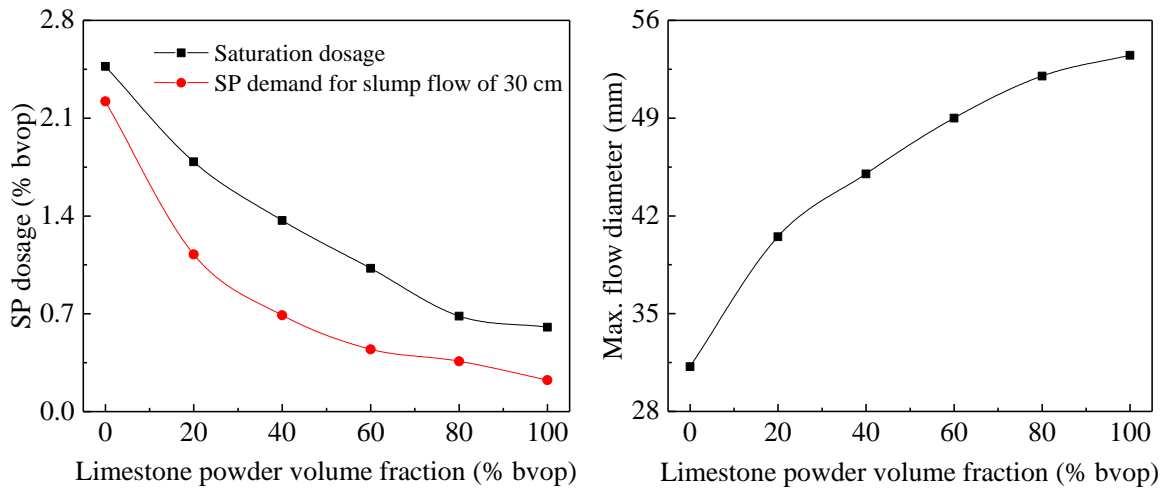


Figure 3.4: SP at saturation and demand dosages. Figure 3.5: Maximum flow diameter.

Based on the observation on fluidity of cement-limestone pastes, limestone powder can be regarded as a mineral plasticizer that improves the fluidity of UHPC system. The plasticization effect is mainly attributed to the following factors: (a) nucleation and chemical effects of limestone powder with comparable particle sizes to binders are quite limited or will occur after several hours of hydration [82], thus reducing the inter-particles fraction and resulting in very limited negative effect on the workability compared to reactive binders; (b) limestone powder is characterized as a neutral surface with Ca^{2+} and CO_3^{2-} ions, and OH^- groups tend to localize over the Ca^{2+} surface [86,109], which contributes to electrostatic repulsion between particles, then decreasing particle flocculation and increasing the fluidity; (c) limestone powder has weaker adsorption ability than cement and micro-silica because of a lower solubility and lower surface charge, leading to a reduced adsorption of PCE molecules and consequently reduced superplasticizer saturation dosages, as shown in Figure 3.4, which is in line with the observation by [110] and [111].

Therefore, it is recommended to make full use of the positive plasticization effect of limestone powder on workability in the mix design of UHPC incorporating limestone powder, namely, using a lower water amount and superplasticizer dosage with the increase of limestone powder amount. Hence, in the mix design of UHPC with different limestone powder contents in this study, the water content and superplasticizer dosage are adjusted to achieve a comparable fluidity, in accordance with the following method: (a) predefine the mini-slump flow at 30 ± 2 cm as a precondition that is derived based on our preliminary tests,

which can meet the self-compacting property without having too much surplus fluidity; (b) set initial superplasticizer dosage at relatively large value of 5% bovp (\geq saturation dosage), then add the water content up to W_i to reach the predefined flow as the lowest water demand; (c) prepare another mixture with W_i and add the superplasticizer dosage gradually from zero to SP_i to reach the predefined flow again. By this suggested method, the lowest water amount (W_i) and corresponding most efficient superplasticizer dosage (SP_i) can be obtained for a specific UHPC with the desirable fluidity.

- **Thermogravimetric analysis**

Figure 3.6 shows the TG and DTG results of the designed UHPC with different limestone powder contents. Three dominant peaks can be observed in Figure 3.6(b), which are in accordance with the three drastic decrease of TG curves in Figure 3.6(a). They are respectively related to the free water loss, dehydration of ettringite, AFm and some C-S-H (30 - 200 °C); portlandite (CH) decomposition (400 - 500 °C; mainly during 400 - 450 °C); calcium carbonate ($CaCO_3$) decarbonation (600 - 800 °C)[112,113]. The first and second peaks tend to be weaker and narrower with the increase of limestone powder amount, because of the dilution effect of limestone powder on the active binders. While, the third peak tends to be stronger and broader, attributed to the limestone powder addition.

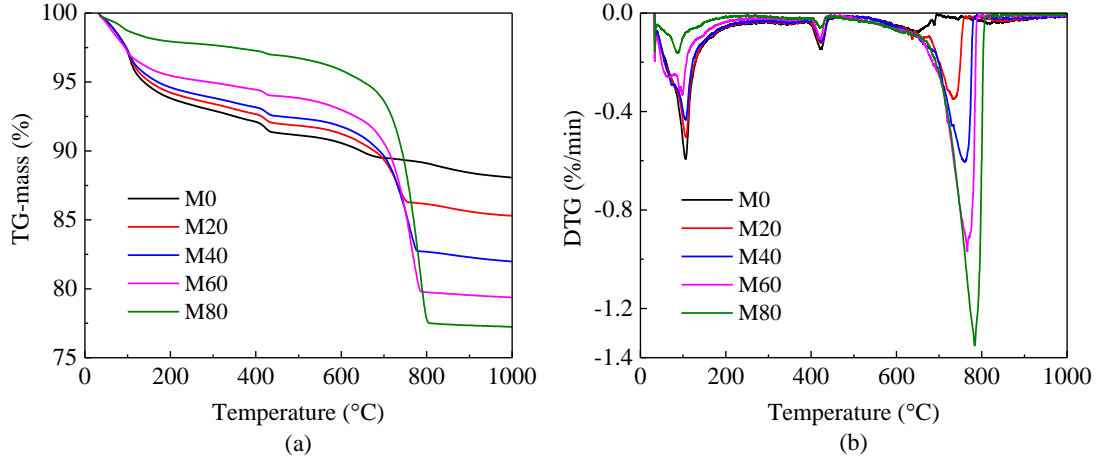
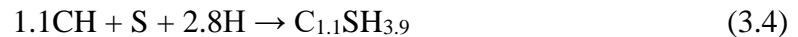


Figure 3.6: TG results of UHPC.

To further determine the hydration products and hydration degree of binders in the presence of limestone powder, the C-S-H and CH are calculated and analysed based on the TG curves. The C-S-H and CH are mainly formed from the hydration of C_3S and C_2S , and secondary (pozzolanic) reaction between CH and SiO_2 [114]:



Then, the C-S-H and CH contents can be estimated as [114],

$$C-S-H(\%) = M_{C-S-H} \div (2.1M_H) \times \Delta m_{C-S-H}(\%) \quad (3.5)$$

$$CH(\%) = M_{CH} \div M_H \times \Delta m_{CH}(\%) \quad (3.6)$$

where M_{C-S-H} , M_H , and M_{CH} are the molar masses of C-S-H gel, water and calcium hydroxide, respectively. Δm_{C-S-H} and Δm_{CH} are the TG mass loss during 400 - 450 °C and 150 - 400 °C. The water content in C-S-H gel greatly depends on mineral condition, relative humidity and temperature [115–117], and the stoichiometric amount of water in this study is taken as 2.1 in Eq. (3.5), as suggested in [115], because some water of the 4 moles has already been lost below 150 °C.

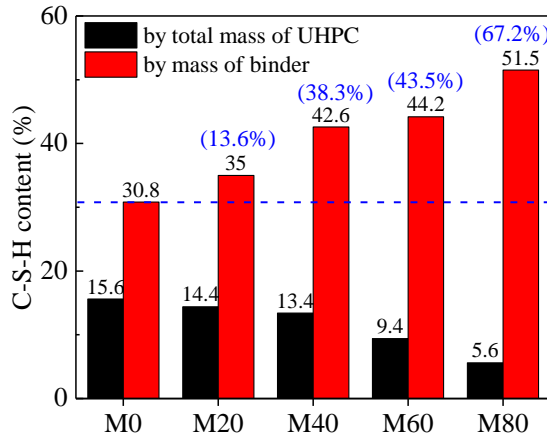


Figure 3.7: C-S-H contents of UHPC.

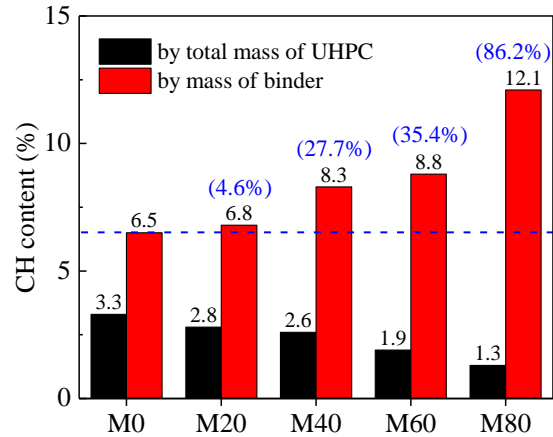


Figure 3.8: CH contents of UHPC.

The total contents of both C-S-H and CH in the designed UHPC are gradually reduced from 15.6% to 5.6% and 3.3% to 1.3%, respectively, with the increase of limestone powder amount from 0 to 80 vol.%, as shown in Figure 3.7 and Figure 3.8. Those diminished hydration products are due to the dilution effect of reactive binders by limestone powder. However, it is remarkable that the normalized C-S-H and CH contents by mass of binders show continuous increases from 30.8% to 51.5% and from 6.5% to 12.1%, respectively. It means that the hydration degree of binders in UHPC system is considerably improved by the volume substitution of binders by limestone powder due to the increased water-to-binders, consequently enhancing binder efficiency and decreasing the environmental and economic impact. Furthermore, in the presence of limestone powder below 60 vol.%, the increase ratios of normalized C-S-H contents (13.6%, 38.3% and 43.5%) in designed UHPC compared to the reference mixture (M0) are larger than those of CH (4.6%, 27.7% and 35.4%), which imply that the hydration degree of secondary (pozzolanic) reaction in Eq. (3.4) is larger than that of C_3S and C_2S hydration in Eqs. (3.2) - (3.3), resulting in more formation of C-S-H rather than CH. The much higher hydration degree of secondary reaction is probably attributed to preferable formation of pozzolanic products under relatively higher water-to-binder ratio and nucleation effect of limestone powder. However, UHPC with too much limestone powder content, e.g. 80 vol.%, shows a lower hydration degree of secondary reaction, due to the overlarge dilution of CH and mS by limestone powder, consequently making them difficult to contact to each other.

- **Pore structure analysis**

To understand the substitution effect of binder by limestone powder on pore structure in sustainable UHPC, three experimental methods are jointly employed, including vacuum-saturation porosity, MIP and BJH pore size distributions. The vacuum-saturation method is

a relatively easy way to determine the total water-permeable “open porosity”, as shown in Figure 3.9. With the increase of limestone powder content from 0 to 80 vol.%, water-permeable porosity is firstly improved from 6.87% to 4.87%, after reaching to the lowest porosity of 4.52% at M40, a slight increase occurs at M60, afterwards experiences a sharp increase up to 12.15% at M80. Although the absolute intensity of hydration products is diluted by limestone powder, as confirmed in Figure 3.6 & 3.7, an appropriate limestone powder volume substitution (20 - 60 vol.%) shows a positive effect on the water-permeable porosity of the UHPC. It proves that the negative dilution can be compensated by reducing the water amount and enhancing the compactness by utilizing the mineral plasticization of limestone powder, as analysed above. Other researchers also pointed out that water reduction was an efficient way to decrease porosity of UHPC [28]. Furthermore, the higher hydration degree of UHPC with limestone powder addition can also provide some positive compensation. However, too much limestone powder addition in UHPC, more than 60 vol.%, leads to significantly increased water-permeable porosity that cannot be completely compensated, which certainly weakens the macro-scope properties in hardened UHPC, such as mechanical properties and durability.

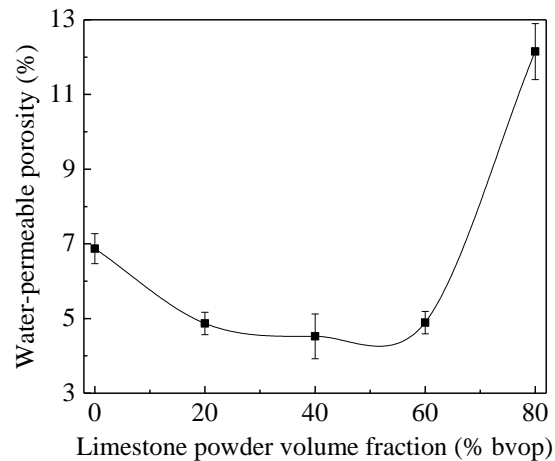


Figure 3.9: Water-permeable porosity of UHPC.

The MIP and BJH methods can further characterize the differential pore size distribution and cumulative pore volume, which cover pore sizes between 5 nm and 100 μm as shown in Figure 3.10, and those between 3 nm to 100 nm as shown in Figure 3.11. The critical pore diameter is defined as when the pore achieves the highest rate of mercury intrusion and begins to penetrate the interior of sample [112,118], illustrated by the peak in the differential pore size distribution curves. The first critical pore diameters and intensities by MIP shown in Figure 3.10(a) are very similar when the limestone powder content is less than 40 vol.%. As the limestone powder volume substitution ratio further increases up to 80 vol.%, the first critical peak tends to be broader and more intensive, shifting from around 13.7 nm to 26.3 nm. The cumulative pore volume by MIP is first improved at M20 and then slightly weakened at M40 and M60, followed an almost triple pore volume at M80, compared to the UHPC without limestone powder. The second critical peaks of the 5 mixtures by BJH in Figure 3.11(a) share the same pore diameter at around 3.9 nm, only the intensities differ, first decreasing from M0 to M40 and subsequently increasing considerably till M80. The

cumulative pore volume by BJH has a similar change tendency to that by MIP when increasing the limestone powder volume substitution. While, the BJH method usually possesses a larger cumulative pore volume due to more efficient to detect gel pores, which occupy a large part of the total pores in UHPC.

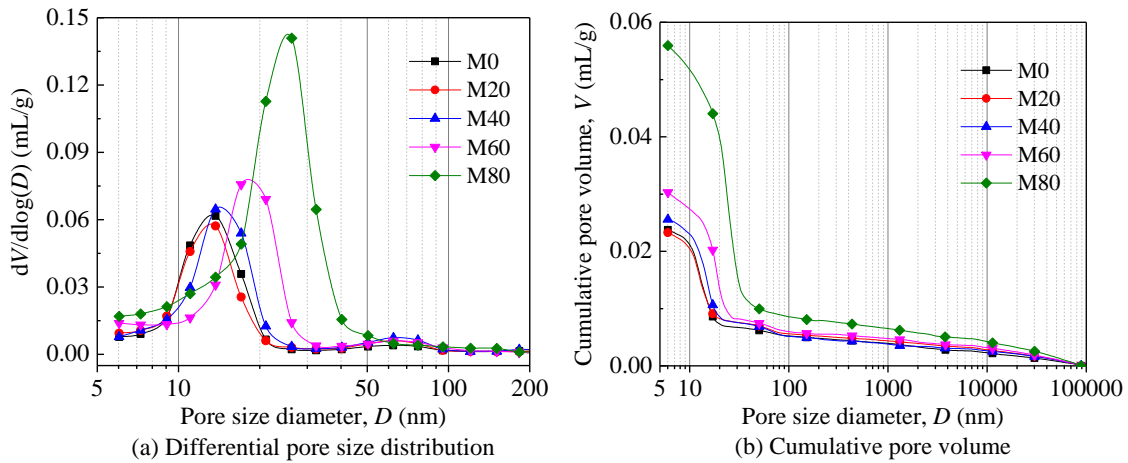


Figure 3.10: Pore structure by MIP of different mixes (Table 3.1).

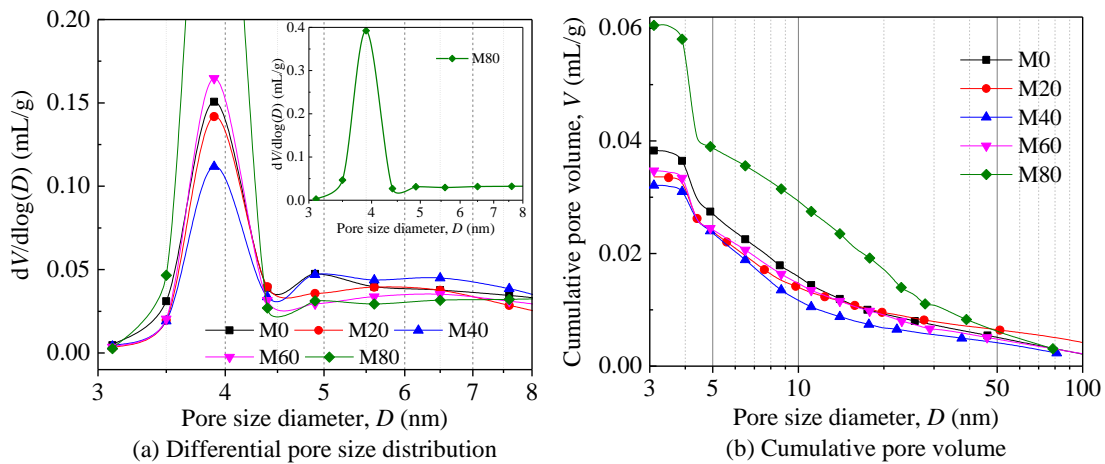


Figure 3.11: Pore structure by BJH of different mixes (Table 3.1).

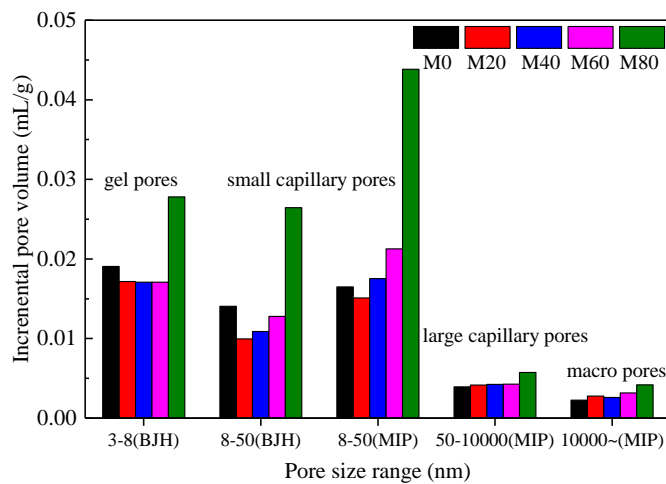


Figure 3.12: Pore volume and classification of different mixes (Table 3.1).

Different pore types in cementitious materials affect different macro properties, which usually are summarized into slightly different categories by different researchers [106,119–123]. The total pores in UHPC can be classified and suggested into four categories as illustrated in Figure 3.12: (a) gel pores from 2 nm to 8 nm, intrinsic to internal porosity of reaction products, e.g. C-S-H gel phase [121]; (b) small capillary pores from 8 nm to 50 nm, mainly controlled by the water amount and hydration products [106]; (c) large capillary pores from 50 nm to 10 μm , corresponding to evaporable bulk water [119]; (d) macro pores larger than 10 μm , linked to entrained air voids and initial defects [122]. With the volume replacement of binders by limestone powder within 20 - 60 vol.%, whereas the second critical peaks vary in Figure 3.11(a), the total gel pores are almost the same at 0.0171 mL/g, which is a slight improvement compared to the reference UHPC without limestone powder. The reduced total gel pores are attributed to the decreased hydration products, confirmed by Figure 3.7 and Figure 3.8. However, the M80 shows significantly more gel pores in Figure 3.12, but less C-S-H gel phase in Figure 3.7, which indicates that more low-density and porous C-S-H gel are preferably formed in the presence of large contents of limestone powder. The MIP method usually acquires more small capillary pores than the BJH method, especially for the UHPC incorporating limestone powder. The small capillary pores of UHPC with limestone powder less than 60 vol.% can be slightly decreased based on the BJH analysis, while they are increased by the MIP method. The pores larger than 50 nm in the five UHPC mixtures are comparable to each other, accounting for about 10% of total pore volume.

- **Compressive strength and binder efficiency**

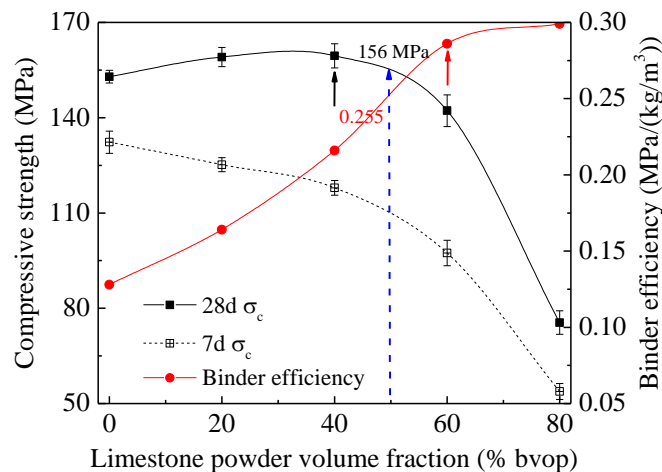


Figure 3.13: Compressive strength and binder efficiency.

Figure 3.13 presents the compressive strength of UHPC with different limestone powder contents after 7 and 28 days, as well as binder efficiencies. The 7 days compressive strength shows a continuous reduction from 132.3 MPa to 53.8 MPa with the limestone powder substitution ratio changing from 0 to 80 vol.%, mainly due to the dilution effect instead of the filler or nucleation effects. The 28 days compressive strength firstly shows a slight increase from 152.9 MPa at M0 to 159.5 MPa at M40, then sharply decreases to 75.5 MPa at M80. UHPC without limestone powder shows relatively high early-age strength, but an appropriate limestone powder content (less than 60 vol.%) contributes to a larger strength

development potential at a later age. The higher secondary (pozzolanic) reaction of UHPC incorporating limestone powder, as analysed by ghermogravimetric results, contributes to C-S-H formation at later ages and then improves the mentioned strength development potential. Figure 3.13 also indicates that ultra-high strength more than 150 MPa can be achieved in eco-friendly and low-cost UHPC incorporating high-volume of limestone powder. Normally, common sustainable UHPC needs special curing regimes or extra chemical activators [124], which certainly cause extra environmental and economic impacts. The binder efficiency is defined as normalized compressive strength (σ_c) after 28 days by binder mass (m_{binder}),

$$X = \sigma_c / m_{binder} \quad (3.7)$$

It is greatly improved in the presence of limestone powder, from 0.128 MPa/(kg/m³) at M0 to 0.286 MPa/(kg/m³) at M60, afterwards keeping at a stable level till M80. Based on the results shown in Figure 3.10, the maximum compressive strength occurs at 40 vol.%, while the largest binder efficiency is achieved at 60 vol.%. Hence, 50 vol.% is suggested as optimum content for limestone powder in UHPC, considering both compressive strength and binder efficiency, namely around 156 MPa and 0.255 MPa/(kg/m³), respectively.

The compressive strength of cementitious material is greatly dependent on the porosity, which can be significantly improved by controlling the porosity under 30% [122]. The correlations between compressive strength and porosities by the three different methods are presented in Figure 3.14. Linear trends are observed, which is in line with other researches [123]. The quality of the line fit is assessed by the coefficient of determination (R^2), and the porosity determined by MIP shows the best correlation to compressive strength with the maximum coefficient value of 0.983. In addition, the water-permeable porosity is usually lower than that measured by BJH or MIP.

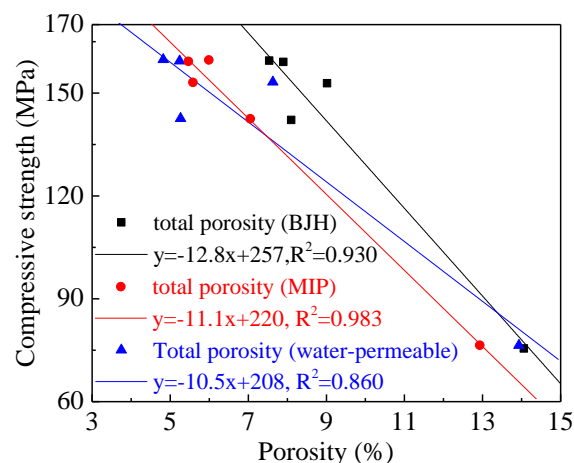


Figure 3.14: Correlation between compressive strength and porosity.

- **Total free shrinkage**

The total free shrinkage is attributed to synergetic effect of both self-desiccation induced autogenous shrinkage caused by binder hydration and water-loss induced drying shrinkage. Figure 3.15 presents the total free shrinkage and water loss in UHPC within 56 days with different limestone powder contents. At relatively early age, Figure 3.15(a) shows a slower

total free shrinkage development for UHPC with more limestone powder, due to a smaller absolute amount of hydration products formation and hence smaller autogenous shrinkage generation. However, at later ages, e.g. 56 days, M20 and M40 have enlarged total free shrinkages than M0 without limestone powder, while M60 and M80 tend to have diminished total free shrinkages. Because the water-to-binder ratio in UHPC with more limestone powder is higher, e.g. 0.9 in the mixture of M80, which is far more than the water needed for complete cement hydration. More free water remains in the pores and tends to evaporate in the drying environment, as shown in Figure 3.15(b), consequently leading to larger water-loss induced drying shrinkage at later ages. Hence, UHPC with more limestone powder shows diminished autogenous shrinkage but enlarged drying shrinkage, and the total free shrinkage can be decreased or just slightly increased by using limestone powder.

Our previous study showed that mass replacement of cement by 20% limestone powder has a considerably negative effect on UHPC paste at a fixed water-to-powder ratio [125]. However, the presence of limestone powder in this study shows comparable or even diminished total free shrinkage, which is due to the decreased absolute water amount with increased limestone powder content (see Table 3.1), thus improving the volumetric stability of UHPC [87]. It indicates that simply replacing binders by limestone powder with a fixed absolute water amount is not reasonable and negative to the total free shrinkage. While, the designed UHPC system in this study can overcome this shortage by using less water and superplasticizer amount to achieve a comparable fluidity as the precondition. It is concluded that the mineral plasticization effect of limestone powder should be considered in the mix design of UHPC based on evaluation of shrinkage, rather than simple mass substitution at a fixed water-to-binder ratio.

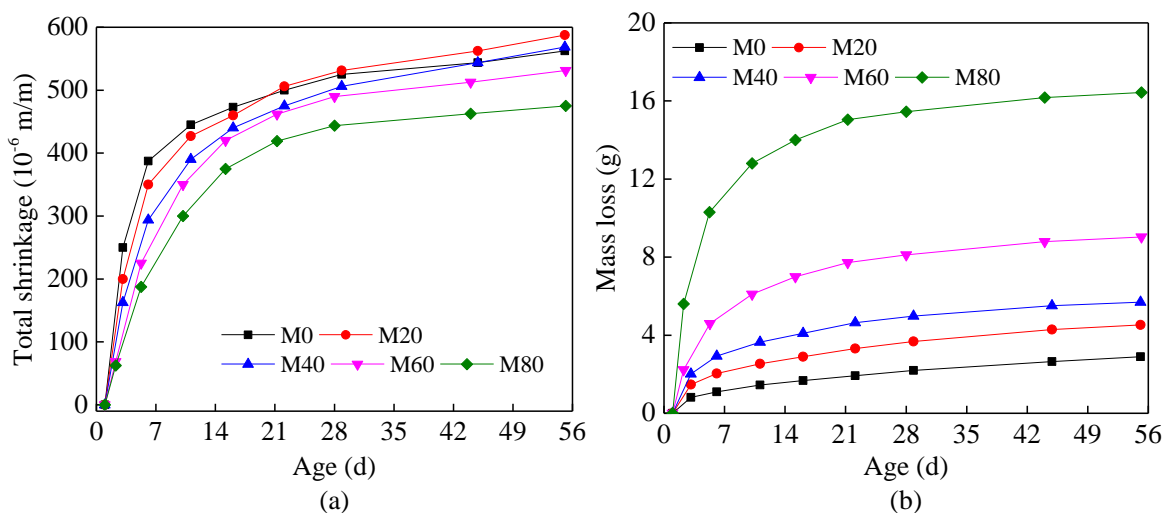


Figure 3.15: Total free shrinkage and mass loss.

3.2.4 Discussion and summary

- **Role of limestone powder in UHPC**

Based on the results and analysis above, the role of limestone powder in UHPC can be summarized from three main aspects, namely fresh behaviour, hydration kinetics and hardened properties. The fluidity of UHPC should be considered during comparative studies,

because it influences the pore structure in the hardened state [102]. Insufficient or over use of superplasticizer could lead to enlarged macro porosity, lower compactness, segregation problems [6]. Limestone powder contributes to enhanced fluidity by reducing inter-particles fraction due to limited chemical interaction, increasing inter-particle electrostatic repulsion due to OH⁻ groups' localization over the Ca²⁺ surface, and lowering adsorption and consumption of PCE molecules of superplasticizer due to lower surface charge. Thus, the mineral plasticization effect of limestone powder should not be neglected in the mix design of UHPC. Namely, using a lower water content and superplasticizer dosage to achieve a comparable fluidity (30 ± 2 cm) as precondition is proposed.

Even through there exists a dilution effect on hydration process of a reactive binder by limestone powder that results in less formation of hydration products, its positive functions can partly compensate or even overcome the negative dilution effect. The dilution conversely increases the water-to-binder ratio in the UHPC system where generally rather low water content is applied, which is beneficial to improve the hydration degree. In addition, the results in this study also show that hydration degree of the secondary (pozzolanic) reaction with micro-silica is more intensive than C₃S and C₂S hydration in the presence of limestone powder, which means more CH is consumed to form C-S-H gel. Furthermore, the filler and nucleation effect of limestone powder could also show certain positive significances, which tend to accelerate the hydration kinetics and generate more C-S-H gel. Meanwhile, the limestone powder can be somewhat soluble and conduce to preferably form the carboaluminate rather than monosulfate [82,86].

The hardened properties, e.g. pore structure, strength, shrinkage of UHPC with limestone powder are intrinsic to the fresh behaviour and hydration process. Generally, the dilution effect of limestone powder plays the main negative influence on the hardened properties of UHPC because of less hydration products. While, the improved pozzolanic reaction degree, formation of more and stiffer carboaluminate, filler and nucleation effects by limestone powder can provide certain extent positive effects on pore structure and compressive strength, especially in the situation of a relatively low volume replacement. Furthermore, the reduced absolute water amount can improve the compactness of UHPC, which is beneficial to the hardened properties. Generally, the hardened properties of UHPC can be enhanced with limestone powder up to 60 vol.%.

- **Sustainability evaluation**

To better understand the sustainability of the designed sustainable UHPC, environmental and economic significances are evaluated by comparing the embedded CO₂ emission and unit cost of designed UHPC. The embedded CO₂ emission of raw materials are referred to [126] and [127], and prices are based on European market provided by ENCI. without the inclusion of transportation cost, as shown in Table 3.2. The incorporated limestone powder in UHPC can reduce the consumption of cement and superplasticizer, which occupy the two largest unit embedded CO₂ emission, thus contributing to considerable reduction of total embedded CO₂ emission of UHPC. As shown in Figure 3.16, the total embedded CO₂ emission of UHPC linearly decreases from 1011 to 234 kg/m³ with the limestone powder increasing from 0 to 80 vol.%. The eco-efficiency, defined as 28 days compressive strength

normalized by CO₂ emission, is in line with the binder efficiency in Figure 3.13. It increases continually at relatively low limestone powder content till 60 vol.%, then staying at a stable level. The total cost of UHPC is mainly dependent on the price of powders. Due to the large variations in different countries/areas and time-dependent characteristics, only prices of cement and limestone powder are compared to illustrate the economic significance of the designed UHPC. The unit price of cement is twice as that of limestone powder, which means the total cost of UHPC could be greatly reduced with incorporating high-volume of limestone powder. For example, UHPC with around 50 vol.% limestone powder can decrease 47% of the embedded CO₂ emission (474 kg/m³), and reduce the cost by about 25.5 €/m³ without sacrificing the macro performance. Hence, eco-friendly and low-cost UHPC can be successfully developed by incorporating high-volume limestone powder contents.

Table 3.2: Embedded CO₂ emission and price of raw materials.

Raw materials	PC	mS	LP	S	W	SP
CO ₂ emission (kg/ton)	930	28	17	4	0	378
Price (€/kg)	0.090	-	0.045	-	0	-

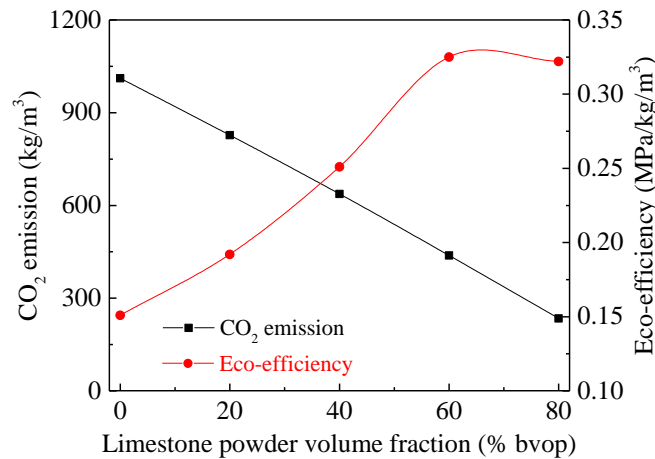


Figure 3.16: Environmental significance.

- **Optimum content of limestone powder**

Even though limestone powder has been extensively applied in concrete, the optimum content of limestone powder has rarely been investigated, especially in the UHPC system with relatively low water-to-binder ratio and high superplasticizer dosage. Furthermore, the content limit of limestone powder by mass is suggested varying from 15% to 35%, based on different standards [82,128].

A higher content of limestone powder in UHPC shows improved fluidity (or less water demand to a comparable fluidity), an increased hydration degree of the binder and a diminished self-desiccation induced autogenous shrinkage caused by binder hydration, but reduced absolute hydration products and enlarged water loss. 20 vol.% replacement of binder by limestone powder in UHPC can slightly improve the pore structure, compressive strength, binder efficiency, but slightly enlarge the total free shrinkage. 40 vol.% of limestone powder can further strengthen compressive strength and binder efficiency with comparable pore

structure and total free shrinkage. 60 vol.% of limestone powder tends to weaken both pore structure and strength, but decrease total free shrinkage. 80 vol.% of limestone powder contributes to a further decrease of total free shrinkage without any further improvement of binder efficiency, but the UHPC gets a rather weak pore structure and cannot meet the demand of high strength (75.5 MPa).

To sum up, considering the main roles of limestone powder on fresh behaviour, hydration, hardened properties, as well as sustainability, 50 vol.% is suggested as the optimum content of limestone powder in UHPC, achieving compressive strength of 153 MPa with the significantly low cement content of 560 kg/m³.

- **Summary**

- Limestone powder shows a mineral plasticization effect in UHPC by reducing inter-particles fraction due to limited chemical reaction, increasing inter-particle electrostatic repulsion due to OH⁻ groups' localization over the Ca²⁺ surface, and lowering adsorption and consumption of PCE molecules of superplasticizer due to lower surface charge.
- Although less absolute hydration products are formed due to dilution effect by limestone powder, positive effects simultaneously work to compensate or even overcome its negative influence, including enlarged hydration degree, increased formation of stiffer carboaluminates, and promoted C-S-H gel by the filler and nucleation effect. The degree of secondary pozzolanic hydration with micro-silica is more intensive than C₃S/C₂S hydration, which enhances the later-age strength development potential.
- An appropriate limestone powder content contributes to a denser pore structures, enhanced strengths and comparable total free shrinkages. 50 vol.% is suggested as the optimum content for the limestone powder with comparable size and morphology to cement, by considering both performance and sustainability.
- UHPC incorporating the suggested optimum limestone powder content (50 vol.%) can reduce 47% of the embedded CO₂ emission (474 kg/m³) and the cost by about 25.5 €/m³, with 28 days compressive strength of 153 MPa and a low cement content of 560 kg/m³.

3.3 Development of UHPC paste with quaternary blends

3.3.1 Materials and mixtures

Several initial materials are used, including cement CEM I 52.5 R (PC), ground granulated blast furnace slag (GGBS) cement CEM III/A 52.5 N (SC) with 50% of slag by mass, limestone powder (LP), densified micro-silica from Elkem Grade 920E D (mS), aqueous dispersion of colloidal nano-silica (nS), water, PCE-based superplasticizer (SP3 from Chapter 2 is used). Both Portland cement and slag cement are from the same manufacturer (ENCI), and slag cement is chosen as binary binder considering its already optimized particle size distribution and homogeneous mixing during the manufacture instead of blending GGBS into the Portland cement by ourselves. The particle size distributions of powders are shown in Figure 3.17, except for mS due to the densified process makes it difficult to be measured. A 3D hook ended steel fibre (Dramix RC-80/30-BP) is used to research the fibre-to-matrix bonding effect by single fibre pull-out test. Table 3.3 shows the chemical and physical properties of powders, respectively.

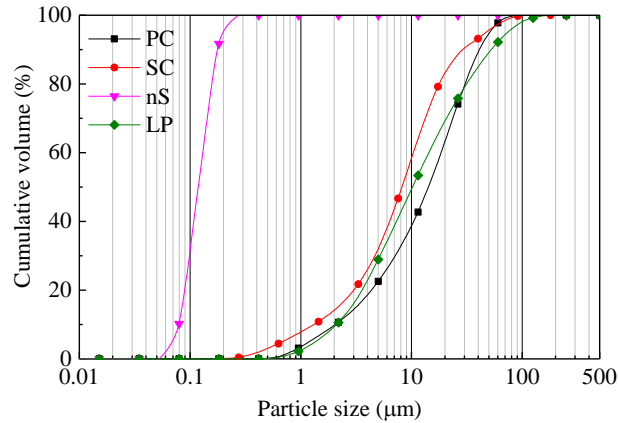


Figure 3.17: Particle size distribution of powders.

Table 3.3: Chemical and physical properties of the PC, SC, ms, nS, LP.

Substituent (%)	PC	SC	mS	nS	LP
CaO	64.60	54.54	0.90	0.08	97.21
SiO ₂	20.08	22.27	93.06	98.68	0.87
Al ₂ O ₃	4.98	7.64	-	0.37	0.17
Fe ₂ O ₃	3.24	1.61	2.06	-	0.13
K ₂ O	0.53	0.42	1.15	0.35	-
Na ₂ O	0.27	-	0.63	0.32	-
SO ₃	3.13	5.52	1.28	-	0.11
MgO	1.98	5.35	0.70	-	1.17
TiO ₂	0.30	0.83	-	0.01	0.01
MnO	0.10	0.19	0.07	-	0.01
Specific density (g/cm ³)	3.15	3.03	2.32	2.22	2.71
BET surface area (m ² /kg)	1420	1590	18400	22700	1080

A total of 14 pastes with a low water-to-powder ratio of 0.2 are produced to simulate the UHPC system, and the water-to-powder ratio is chosen based on the previous research [108,125]. The pure PC is applied as the reference binder, while the remaining binders are binary (SC), ternary (PC + mS/nS + LP) and quaternary (SC + mS/nS + LP) cementitious blends. The SC contains 50% GGBS which is therefore regarded as binary binder. The replacement levels for LP are 10%, 20% and 30% by the total mass of powders, while those of mS and nS are 5% and 3%, respectively, based on the previous studies [102,125]. The difference between the dosage of nano-silica and micro-silica is caused by the higher pozzolanic, filler and nucleation effects with clearly finer particle size and larger specific surface area of nano-silica. In addition, excessive nano-silica addition would cause significant issues on water demand and resulting workability. A polycarboxylic ether type superplasticizer (SP3 in Chapter 2) with a solid content of 35% is applied with a fixed content (1% by mass of powders) to adjust the flow ability of the mixtures. The mixture proportions are summarized in Table 3.4. The mixing procedure of UHPC pastes is illustrated in Figure 3.18. For hardened properties assessment, samples are cast and demoulded after 24 hours and then cured in water under ambient conditions (20 ± 1 °C) till the testing age.

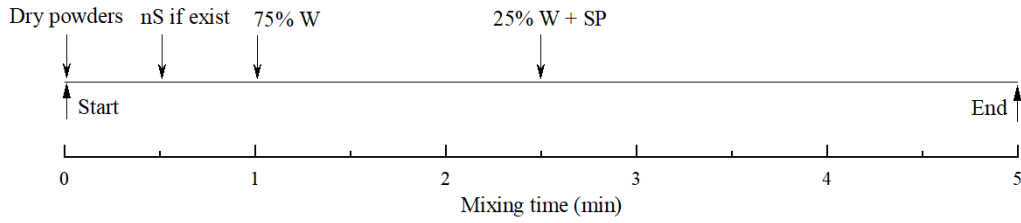


Figure 3.18. Mixing procedure of mixtures.

Table 3.4: Mix proportions of UHPC pastes (w/p=0.2, SP 1%).

Mix	Note	PC (%)	SC (%)	mS (%)	nS (%)	LP (%)
M1	PC	100	-	-	-	-
M2	PC5mS10LP	85	-	5	-	10
M3	PC5mS20LP	75	-	5	-	20
M4	PC5mS30LP	65	-	5	-	30
M5	PC3nS20LP	87	-	-	3	10
M6	PC3nS20LP	77	-	-	3	20
M7	PC3nS20LP	67	-	-	3	30
M8	SC	-	100	-	-	-
M9	SC5mS10LP	-	85	5	-	10
M10	SC5mS20LP	-	75	5	-	20
M11	SC5mS30LP	-	65	5	-	30
M12	SC3nS20LP	-	87	-	3	10
M13	SC3nS20LP	-	77	-	3	20
M14	SC3nS20LP	-	67	-	3	30

3.3.2 Experimental methods

The isothermal calorimetry, mercury intrusion porosimetry, spread flow, compressive strength, free shrinkage are tested based on the methods as mentioned in Sections 2.2.2 and 3.2.2. Other experimental methods are described below.

- **Wet packing density**

The fresh sample is filled in a container with a known volume to determine its fresh density ρ . Most packing densities are measured under dry condition based on codified test methods [129,130], which cannot reflect the real compactness in the real wet condition, especially in the presence of superplasticizer in UHPC. In order to research the compactness under real wet condition, a wet packing density is proposed and described by the solid concentration [130], as,

$$\phi_p = \frac{V_{solids}}{V_{container}} = \frac{\sum_i^n \frac{r_i}{\rho_i} m \frac{1}{(1 + w/p)}}{V_{container}} = \sum_i^n \frac{r_i}{\rho_i} \frac{\rho}{(1 + w/p)} \quad (3.8)$$

where ϕ_p is the wet packing density, V_{solids} is the solid volume of the particles, $V_{container}$ is the volume of testing container (bulk volume of mixture), m is the mass of paste, r_i and ρ_i are the mass fraction and density of powder i , w/p is the water-to-powder ratio as 0.2 in this study.

- **Fibre-to-matrix bond**

Dog-bone shape moulds following the standard ASTM C307-03 [131] are used to cast the specimens for carrying out the steel fibre pull-out tests. A piece of hard foam is put in the middle of the mould, separating the mould into two parts. A half-length embedded hooked-end steel fibre is held by the hard foam in Figure 3.19(a), then the fresh paste is poured into one half of the mould, shown in Figure 3.19(b). Similar curing regime is applied as that in compressive strength tests. The pull-out tests are performed after 56 days, under the displacement control (0.5 mm/min) with a 30 kN load cell, illustrated in Figure 3.19(c).

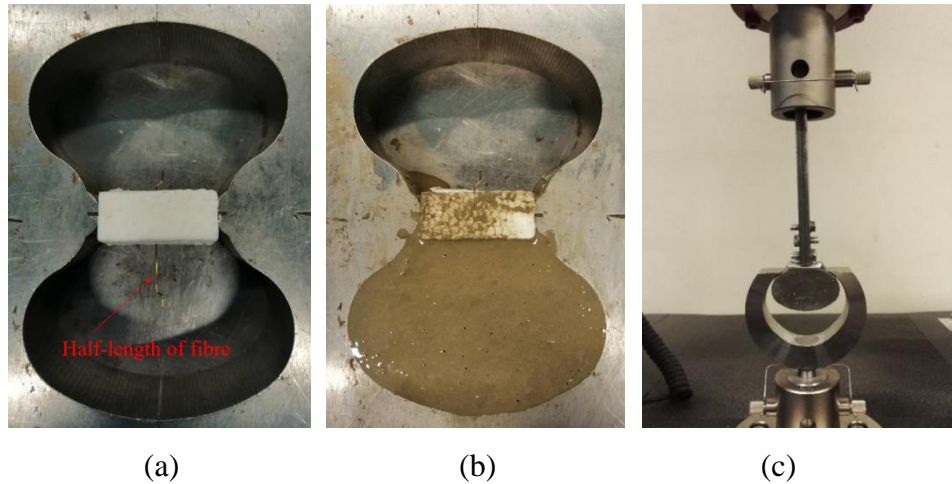


Figure 3.19: (a) fixed steel fibre, (b) sample and (c) set-up for fibre pull-out test.

3.3.3 Results and discussion

- **Hydration kinetics and pore structures**

Figure 3.20 shows the influence of different blends on the hydration kinetics of UHPC pastes. The heat flow is characterized by the time to reach the maximum peak (TRMP) and the maximum heat flow (MHF). The pure PC paste has the longest TRMP (17 h) and highest MHF (3.7 mW/g). More LP addition shows a slightly faster hydration but lower normalized heat flow and normalized total heat when comparing the mixtures of M2 and M4, which indicates that LP addition mainly shows dilution effect on the cement clinker, but as well as somewhat acceleration effect due to nucleation sites for hydration products. While, the normalized total heat by cement before the 7 days of M4 is much larger than that of M2, which means the hydration degree of cement can be improved with more LP addition. The mixtures of M7 and M14 show much earlier TRMP compared to the M4 and M11, which is attributed to the higher surface area and increased number of nucleation sites by 3% nS than the 5% mS. The GGBS in SC further enlarges the dilution effect on hydration, as confirmed by the much lower normalized heat flow and total heat of M11 and M14 compared to the M4 and M7.

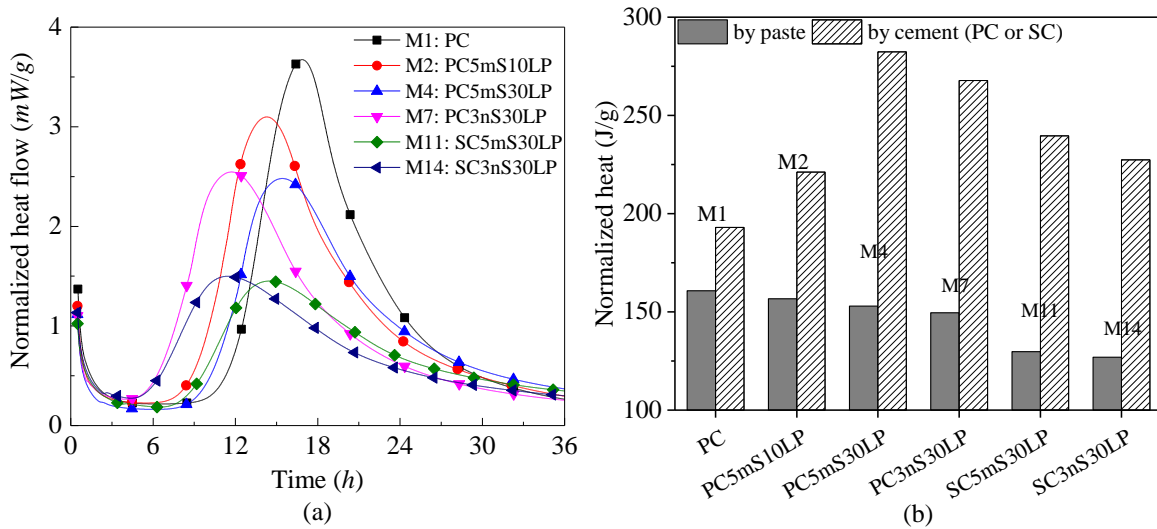


Figure 3.20: (a) normalized heat flow and (b) normalized heat of mixes (Table 3.4).

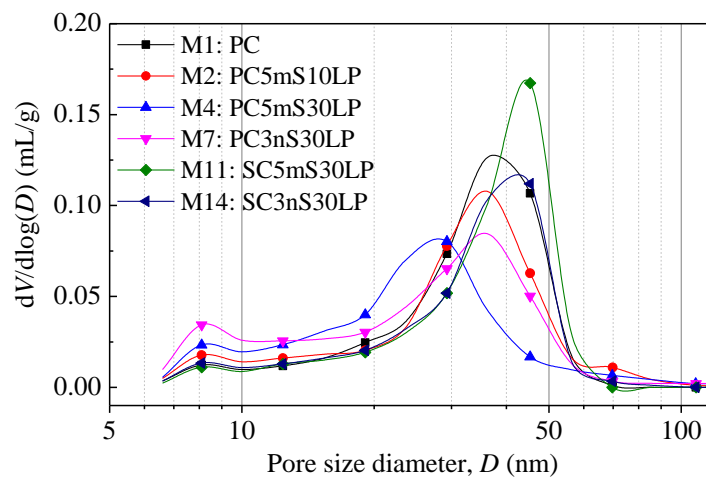


Figure 3.21: Differential pore size distribution of mixes (Table 3.4).

Figure 3.21 presents the pore size distribution of the designed hardened pastes after 56 days. This study mainly focuses on the pore sizes ranging from 5 nm to 100 nm, because the pore size distributions of all designed mixtures between 100 nm to 100 μm are very low and similar to each other. The critical pore diameters (the peak in the differential pore size distribution curve) of the designed mixtures range between 30 nm and 50 nm. With the inclusion of 5% mS and 10% LP in PC, the pore structure of M2 with ternary binder is densified compared to M1, especially for pore sizes between 30 nm and 60 nm. While, more addition of LP up to 30% (M4) results in a shift of the critical pore diameter to a smaller size and causes a large amount smaller pores, which is due to the dilution effect and generates low-density and porous C-S-H gel phases [120]. When the PC is replaced by the SC, the pore size distribution of M11 with quaternary binder tends to a shift towards larger diameters and the pore volume is enlarged compared to M7 with ternary binder. While, the pore structure of mixture with quaternary binder can be considerably improved by using 3% nS instead of 5% mS, namely extending M11 to M14.

- **Fresh behaviour**

The spread flow and wet packing density results are summarized in Figure 3.22. According to our previous study, the PCE-type superplasticizer (SP) is one of the most important factors and has a great influence on the fresh behaviours of UHPC [108]. Both water and superplasticizer contents have very important effect on the particle packing of matrix under real wet conditions [130]. In this study, SP with a dosage of 1% can provide the system with an excellent workability and self-compacting characteristics, namely mini slump flow more than 35 mm. The excellent fresh behaviour is due to the adsorption of PCE molecules on particles and consequently dispersing the particles by mainly electrostatic repulsion and steric effect. Furthermore, our previous study confirmed that the saturation dosage of UHPC paste is around 1% with water-to-powder ratio of 0.2. the spread flow cannot be further improved beyond the saturation dosage [108].

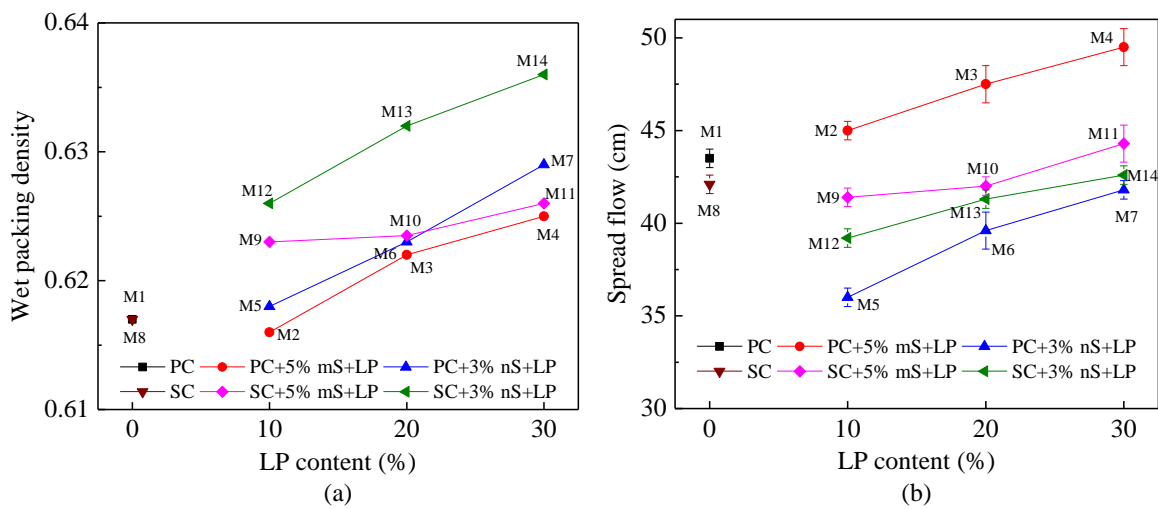


Figure 3.22: Fresh behaviour of UHPC pastes.

The quaternary binder tends to possess large wet packing density, with a maximum value of 0.636 in the case of M14. Mixtures with Portland cement (M1) and Slag cement (M8) result in similar wet packing densities, around 0.617. LP contributes to an increased compactness, probably due to better fresh behaviour and particle size distribution. A good fresh behaviour means a sufficient free water to fill the voids in the bulk volume of the matrix that avoids entrapping air in the voids, which efficiently decreases the larger pores. Furthermore, it is hypothesized that cement incorporating limestone powder can optimized the total particle size distribution and increase the compactness compared to the pure cement [84,132]. As seen in Figure 3.22, 3% nS leads to a better compactness than 5% mS under the same other conditions, because of its finer particle size and better filling effect.

The SC pastes (M8) have a slightly smaller spread flow compared to PC pastes (M1), 42.1 cm vs. 43.5 cm. It indicates that the SC shares similar overall integrated effects by water demand and adsorption ability of PCE-type superplasticizer as PC clinker. With the increase of LP from 10% to 30%, the spread flow of mixtures is improved significantly, e.g. 36 cm (M5) to 41.2 cm (M7). The LP is mainly composed of Ca^{2+} and CO_3^{2-} ions, which result in a neutral surface. In aqueous solution, the OH^- groups preferably concentrate on the Ca^{2+}

surface, resulting in electrostatic repulsion between particles, which consequently improves the fluidity and decreases particle flocculation [109]. Moreover, the lower water demand of LP than those of PC, GGBS and mS/nS benefits better fluidity of UHPC pastes [125,133]. Normally, the mS and nS have negative effects on the fresh behaviour of cementitious materials [102,125]. They have quite high water demand and consume large amount of superplasticizer, leading to the reduction of effective lubricating water content between the particle voids [42]. As seen in Figure 3.22, the spread flow of pastes with nS is always worse than that of similar mixtures with mS, e.g. with spread flow from M2 of 45 cm to M5 of 36 cm, because of the higher fineness and pozzolanic effect, which enlarges the inter-particles friction [134].

- **Compressive strength**

The compressive strength of UHPC pastes, measured after 28 days and 56 days, are shown in Figure 3.23. At 28 days, the compressive strengths vary between 131.3 MPa and 153.8 MPa. 20% LP addition to the system shows a positive contribution on the 28 days compressive strength of mixtures with PC. The strengths further increase up to the range from 137.2 MPa to 181.8 MPa, with the maximum strength at pure PC paste (M1), at the curing age of 56 days.

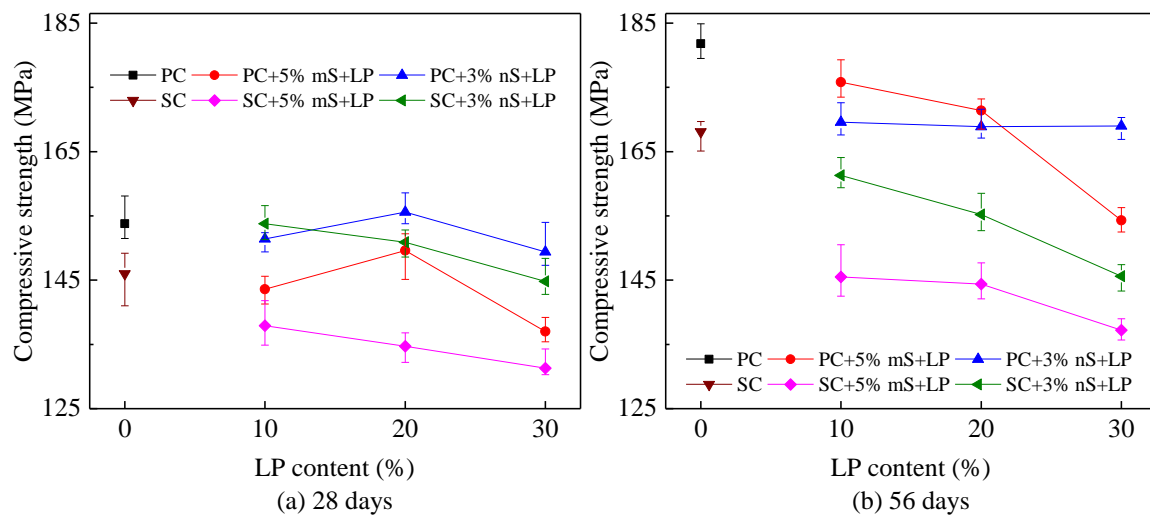


Figure 3.23: Compressive strengths of UHPC pastes.

The mixtures without GGBS (M1~M7), but with the same amount of mS/nS and LP, show slightly higher compressive strength than the mixtures with GGBS (M8~M14) at both 28 days and 56 days, which indicates that GGBS results in lower strength development potential for UHPC pastes. However, ordinary strength concrete incorporates GGBS often shows a better compressive strength at later age due to the formation of C-S-H by consuming portlandite, even for UHPC with GGBS substitution rate of 25% [90]. When adding a high amount of GGBS in low water-to-binder system, such as 50% in this study, 30% and 60% in [135], 50% in [90], and 31% in [136], the later age (e.g. 56 or 90 days) strengths are lower than those of mixtures without GGBS. This is probably attributed to the low water amount and dilution effect (as seen in Figure 3.20) of clinker by the high amount of GGBS, then the produced portlandite from PC and free water to solute portlandite are quite limited. Thus, no

saturated calcium hydration solution can contact and activate the GGBS, which results in lower strength development potential at later age [90]. Some researchers also attributed this phenomenon of lower later strength to the special UHPC system with a high superplasticizer content and low water amount [136], which might significantly affect the pozzolanic reaction and cause slow increase of strength development.

LP leads to lower compressive strength of UHPC paste due to dilution effect, leading to weaker bonding force and less hydration products, as confirmed in Figure 3.20. But the decrease is quite limited in the presence of mS/nS in this study, especially for the ternary mixtures (M2~M7). Because LP also shows some benefits, such as increased water-to-clinker ratio and then enhanced hydration potential of reactive binder (as illustrated by the normalized heat by cement in Figure 3.20(b)), enlarged nucleation sites for the hydration products of cement [137], preferably generated more stable carboaluminate hydrate [86,138]. In addition, the application of LP can also improve the flow ability and packing density under real wet condition, which means decreased larger pores [130].

Due to the decrease of compressive strength by introducing LP and GGBS, it is wise to compensate it adding more reactive pozzolans such as mS and/or nS. Because mS and nS can strengthen the compressive strength of the mixtures attributed to their high pozzolanic effect on consuming $\text{Ca}(\text{OH})_2$ to form C-S-H, filling internal pores with finer particle, and nucleation effect [90,139]. In this paper, 5% mS and 3% nS are utilized by considering their efficiency [102,125] and agglomeration issue [134,140]. Based on the results in Figure 3.23, 5% mS contributes higher strength than 3% nS for the mixtures containing PC, e.g. with compressive strength from M2 of 175.8 MPa to M5 of 169.6 MPa after 56 days. While this trend reverses for the mixture incorporating SC (M9~M14), e.g. with compressive strength from M9 of 145.5 MPa to M12 of 161.3 MPa after 56 days. This is probably due to two factors, namely different Ca/Si ratios with the different cementitious material blends and the different fineness of silica powders [141]. The appropriate Ca/Si ratio has been reported to be around 1.30 [142]. And both more silica amount (5%) and finer particle size (nS) promote higher strength. Therefore, the PC with a higher Ca/Si ratio needs more silica (5% mS) even coarser particle size, and the SC with a lower Ca/Si ratio are preferred to a lower amount but more reactive and finer silica, i.e. better fineness (3% nS). It can be concluded that 5% mS is more effective on Portland cement for the ternary binders (PC-mS-LP), while 3% nS on slag cement for the quaternary (SC-nS-LP) binders.

- **Fibre-to-matrix bond characteristics**

The fibre-to-matrix bond is also characterized in the present study considering the fact that steel fibres are usually utilized in the UHPC system. Therefore, the bonding behaviour contributes to the understanding of the investigated blended binders from the UHPC matrix point of view. Two different responses are observed during the fibre pull-out tests, namely, complete fibre pull-out and fibre breakage at the hook end, and the related two force-displacement curves are plotted in Figure 3.24(a). The curve representing the complete fibre pull-out procedure can be divided into five phases [143]. In the initial phase P₁, the response of the curve is almost during elastic stage until fibre debonding. Thereafter, debonding phase P₂ takes place and the adhesion bond fails continuously. After the complete debonding of

the fibre, anchorage phase P₃ is activated, during which bending of the hook occurs. Plastic hinges are formed due to the bending effects on the hook, inducing additional anchorage that significantly amplifies the pull-out force. As the pull-out process continues, the force reaches its maximum values, then the hook undergoes a straightening phase P₄. In the last phase (P₅), the fully straightened fibre slips along the tunnel, the pull-out behaviour of which is determined by the frictional force. The pull-out load reduces gradually with the decrease of the remained embedded length.

In the pull-out tests, fibre breakage occurs frequently thanks to the strong bond between the fibres and the designed UHPC pastes. Examples of the steel fibre before pull-out, after complete pull-out and experienced fibre breakage are illustrated in Figure 3.24(b). The fibre breaks at a location near the hook, which has more serious stress concentrations compared to the straight part of the fibre. The critical pull-out force for the fibre breakage is approximately 290-300 N in this study, which indicates the full utilization of the fibre tensile capacity. As suggested by Robins et al. [144], the fibres breakage can be attributed to the inter-crystal slippage in the material. At the hooked end, the localized stresses remarkably accelerate the inter-crystal slip process. Consequently, the hook part reaches the yield condition first and fibre breakage occurs.

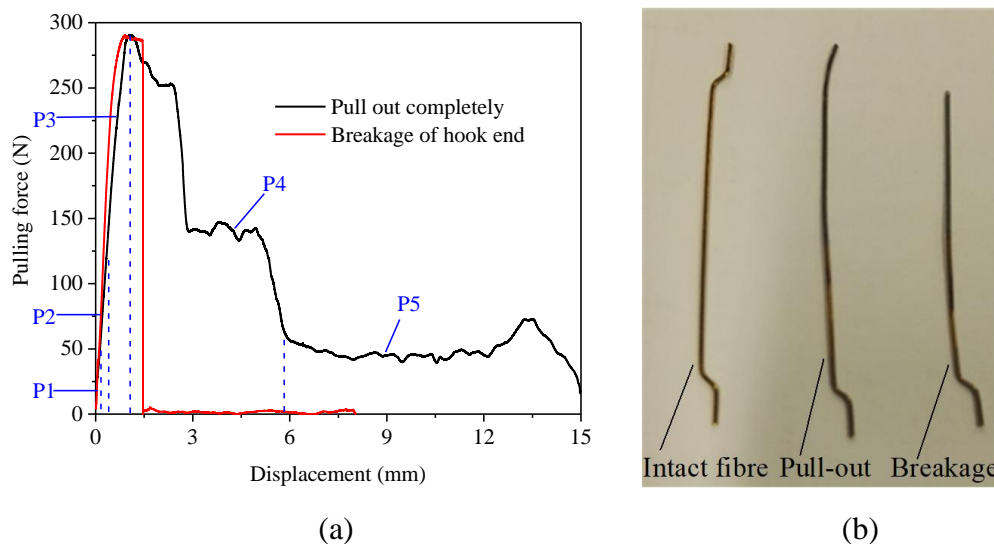


Figure 3.24: Typical force-displacement curves (a) and failure patterns of steel fibre (b).

Figure 3.25 summarizes the maximum pull-out forces of the designed UHPC matrices. It can be obtained from the figure that the ternary binder pastes (M2~M7) has a higher maximum pull-out force than that of the quaternary binder ones (M9~M14). This observation can be related to the higher compressive strength of former groups (M2~M7), resulting in a stronger fibre-matrix interface [145]. Moreover, the substitution of LP seems to have no significant or just slight fluctuation on the bond properties. On the one hand, replacing cement by LP can result in a weaker matrix strength in the interface zone due to dilution effect of reactive clinker and thus a reduced bond force; on the other hand, the enlarged shrinkage provides a confinement around the fibre [146] and formation of calcium carboaluminate [82] in the presence of LP, which in turn improves the frictional resistance during the fibre pull-out. Furthermore, the filling effects of the mS or nS between the

interfaces also help to compensate the bond-strength reduction due to the LP. In addition, the pozzolanic reactions of the mS and nS can further improve the fibre-matrix bond strength by replacing calcium-hydroxide crystals with higher strength calcium silicate gels in the interface zone [113]. In this study, 3% nS has limited difference in bonding effect compared to 5% mS.

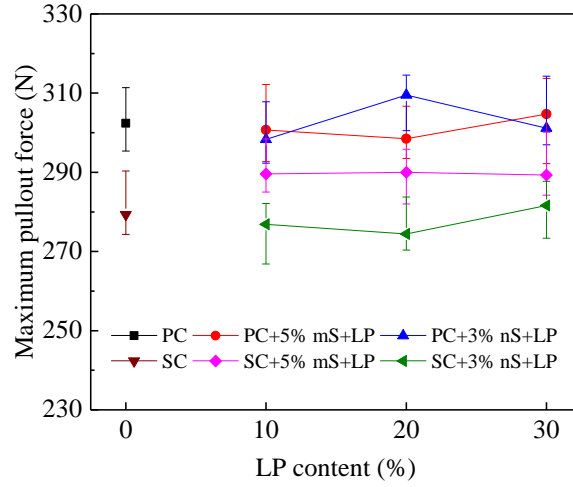


Figure 3.25: Maximum pull-out force.

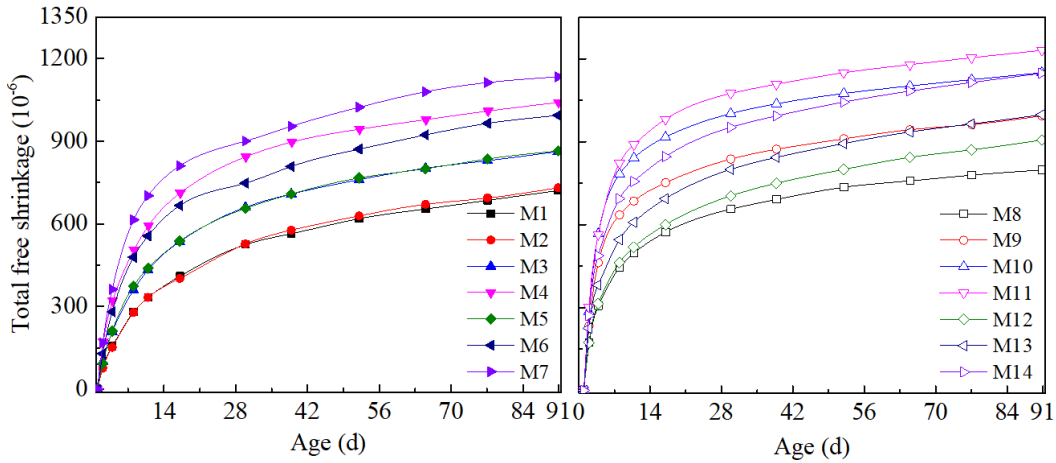


Figure 3.26: Total free shrinkage of pastes.

- **Total free shrinkage**

The total free shrinkage is defined as the contracting of a sample due to both chemical process of hydration (autogenous shrinkage) and loss of capillary water (drying shrinkage), which is related to crack resistance and durability especially in arid and desert regions [147–149]. Based on Mackenzie [150] and Kelvin-Laplace equation [38], the shrinkage strain is given as:

$$\varepsilon_p = \sigma_{cap} \left(\frac{1}{3K} - \frac{1}{K_s} \right) \quad (3.9)$$

$$\sigma_{cap} = \frac{2\gamma \cos \alpha}{r} = \frac{-\ln(RH) \rho R T}{M} \quad (3.10)$$

where K and K_s bulk modulus of the whole matrix and solid material, respectively. σ_{cap} is the capillary tensile stress. M and ρ are molar weight and density of water, respectively. RH is the relative humidity. R is ideal gas constant. T is absolute temperature. According to Eqs. (3.8) and (3.9), the quaternary blends effect on drying shrinkage is mainly influenced by the different abilities of capillary water loss in different mixtures. The total free shrinkages of 14 mixtures are shown in Figure 3.26, ranging from about 720×10^{-6} (M1) to 1230×10^{-6} (M11).

Compared to that of PC paste, the total free shrinkage of SC paste grows faster at the first week due to more free water loss and more capillary pores between 30 nm and 50 nm (drying shrinkage) caused by dilution effect of PC clinker by GGBS. At later age, the total free shrinkage of PC paste develops faster or with a comparable rate to SC paste, probably due to higher further hydration process (autogenous shrinkage), which is in line with the strength development. Normally, the LP generates an enlarged shrinkage due to increased water-to-clinker ratio (see Table 3.4) and dilution of reactive binder (illustrated in Figure 3.20), which results in less hydration product to fill the small pores (see Figure 3.21) and higher free water content is left in the pores. It makes the relative humidity easily loss, consequently increasing the capillary tensile stress and drying shrinkage. Hence, it is wise to apply mS or nS to restrict the shrinkage development in the presence of LP utilization, by generation of more C-S-H gel by pozzolanic reaction with calcium hydroxide and better pore structure refinement [151]. It is clear that, the total free shrinkages increase rather limited with relatively low LP contents under the condition of 5% mS or 3% nS addition. For example, the increase of total free shrinkages of M2, M3, M5 are 1.5%, 19.8% and 20.1%, respectively, compared with that of PC paste at the age of 91 days. While M9, M12, M13 show increase proportions of 24.5%, 13.6% and 25.1%, respectively, compared with that of SC paste at the age of 91 days. It should be noted that an addition of 5% mS is better for inhibiting the shrinkage of ternary binder mixtures (PC + mS/nS + LP), while 3% mS is better for the quaternary binder mixtures (SC + mS/nS + LP). This preferential combination of PC-mS and SC-nS is in accordance with the results of compressive strength.

- **Environmental sustainability**

Life cycle assessment (LCA) has been widely investigated and applied in construction industry to evaluate the environmental sustainability of consumer products. A small scale evaluation of materials level is appropriate to compare the different environmental sustainability of concrete mixtures [152]. The total embedded CO₂ emission for each UHPC paste, based on 1 m³, is first calculated including all components as,

$$m_{CO_2} = \sum_{i=1}^{i=n} r(i) \cdot m_{CO_2}(i) \quad (3.11)$$

where $r(i)$ represents the mass fraction of powder i , $m_{CO_2}(i)$ is the embodied CO₂ of powder i based on [126,127,136] as presented in Table 3.5. The embedded CO₂ emissions of the 14 UHPC pastes are shown in Table 3.6. With the addition of 50% GGBS in SC, its embedded CO₂ emission has a significant decrease to 1092 kg/m³, compared to the value of PC (1797 kg/m³). The environmental sustainability is further improved with the increasing content of

LP, till 731 kg/m³ in the case of quaternary mixture of M14 with a reduction of 59% based on the pure PC.

Table 3.5: Embedded CO₂ emission of ingredients.

Material	Portland cement	GGBS	Silica powder	Limestone powder
CO ₂ emission (kg/ton)	930	52	28	32

As shown in Figure 3.23 and Table 3.6, UHPC paste with a higher compressive strength normally corresponds to a larger embedded CO₂ emission. Hence, it is not comprehensive to evaluate the environmental sustainability by only the absolute embedded CO₂ emission. One significant importance in environmental sustainability assessment is therefore the definition of the functional unit. A good indicator is widely accepted that uses the normalized strength by CO₂ emission [153], which is adopted in the present study, as

$$\beta_{CO_2} = \sigma_c / m_{CO_2} \quad (3.12)$$

where β_{CO_2} is the binder sustainability efficiency based on strength (MPa/(kg/m³)), a larger value indicates a higher environmental sustainability efficiency. σ_c is the compressive strength of UHPC paste after 28 days (MPa). The binder environmental sustainability efficiencies of UHPC pastes are shown in Table 3.6. UHPC pastes with higher compressive strength usually have relatively lower environmental sustainability efficiency. This is linked to the relatively low hydration degree and cement efficiency when the cement amount is relatively high at relatively low water-to-binder ratio. With the utilization of GGBS and LP, the sustainability efficiency β_{CO_2} is enhanced, from approximately 0.086 MPa/(kg/m³) at mixture M1 to 0.198 MPa/(kg/m³) at mixture M14, with improvement of 130%.

Table 3.6: Embedded CO₂ emission and sustainability efficiency.

Mix	Note	CO ₂ emission (kg/m ³)	β_{CO_2} (MPa/(kg/m ³))
M1	PC	1797	0.086
M2	PC5mS10LP	1505	0.095
M3	PC5mS20LP	1322	0.113
M4	PC5mS30LP	1143	0.120
M5	PC3nS10LP	1546	0.098
M6	PC3nS20LP	1362	0.114
M7	PC3nS30LP	1181	0.127
M8	SC	1092	0.134
M9	PC5mS10LP	921	0.150
M10	PC5mS20LP	814	0.165
M11	PC5mS30LP	708	0.185
M12	PC3nS10LP	945	0.163
M13	PC3nS20LP	837	0.180
M14	PC3nS30LP	731	0.198

To sum up, the values of embedded CO₂ emission and binder efficiency of UHPC pastes with blended binders are significantly improved compared to the PC pastes, with maximum improvements of 59% reduction and 130% respectively, which means the sustainable binder

with quaternary blends has a lower environmental impact and higher sustainability efficiency.

- **Synergy of quaternary blends**

As illustrated above, the quaternary binders with cement-slag-limestone-silica can greatly reduce the embedded CO₂ emission and sustainability efficiency in UHPC system. However, it also should be noted that binders including slag or limestone powder tend to dilute Portland cement and show certain negative influence on compressive strength, fibre-to-matrix bond and total free shrinkage. It is critical to calculate synergy to quantify if there has some positive or negative combined effect in hybrid mixes [154,155]. Thus, it is important to understand if the quaternary blends show diminished or enlarged negative dilution influence. In this study, a synergy calculation method is adopted to assess the hybridization of quaternary blends compared to binary (cement-slag) and ternary binders (cement-silica-limestone), based on the following formula:

$$synergy = \frac{(X_{ref} - X_B) + (X_{ref} - X_T)}{X_{ref} - X_Q} - 1 \quad (3.13)$$

where X represents the properties of UHPC pastes, namely compressive strength, fibre-to-matrix bond and shrinkage in this study. To be specific, X_{ref} , X_B , X_T , X_Q are the property in reference (cement), binary binder (cement-slag), ternary binder (cement-silica-limestone) and quaternary binder (cement-slag-silica-limestone), respectively. A positive synergy (>0) indicates that quaternary blends has less adverse influence than binary and ternary blends. A negative synergy with a value between -1 and 0 represents the adverse influence is enlarged.

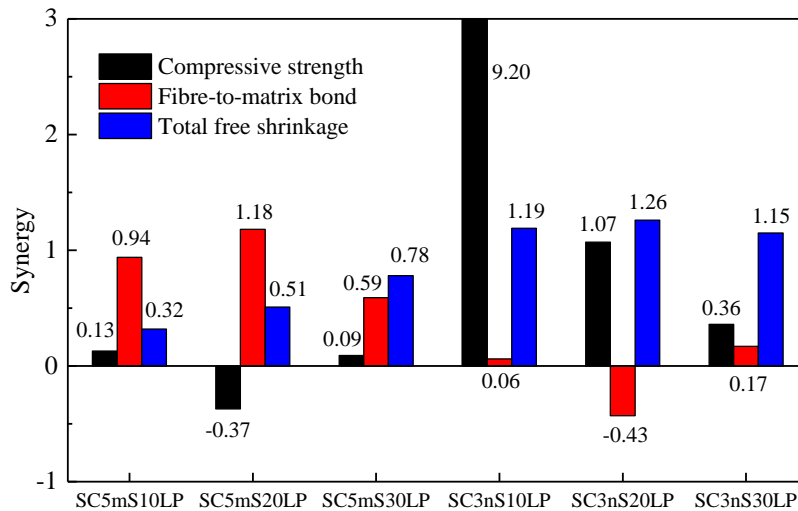


Figure 3.27: Synergy of quaternary binders compared to binary and ternary ones.

Figure 3.27 presents the synergies in terms of 28 days compressive strengths, fibre-to-matrix bond and total free shrinkage calculated by Eq. (3.13). The synergy values in the quaternary UHPC pastes are in general positive, except for only a few negative values. There exists positive synergy in quaternary binders to compensate the negative dilution effect, compared to binary or ternary ones. The quaternary blends probably optimize the total particle size distribution [132] and then enhance the compactness that is confirmed by the wet packing density in Figure 3.22, which contributes to the positive synergy values. Furthermore,

compared to the binary blends (slag cement), introducing limestone powder into the quaternary blends can increase the water-to-reactive binder ratio and improve the hydration degree of both cement and slag. Incorporating slag into ternary blends (cement-silica-limestone) tends to optimize the Ca/Si ratio. Hence, it is reasonable to develop sustainable UHPC pastes with quaternary blends instead of binary or ternary ones. In short, considering fresh and hardened properties, environmental sustainability and synergy, the quaternary binders of SC3nS10LP and SC3nS20LP are suggested for developing sustainable UHPC.

3.3.4 Summary

- Quaternary blends with cement-slag-silica-limestone have considerable advantage of environmental sustainability for UHPC pastes compared to the pure Portland cement, with maximum improvements of 59% CO₂ emission reduction and 130% sustainability efficiency based on strength.
- The designed quaternary binders in general slightly accelerate the hydration process and dilute the heat flow and total heat, but significantly improves the hydration degree and efficiency of cement in UHPC pastes. Furthermore, the pore structures of UHPC pastes with quaternary binders are densified compared to the mixture with pure Portland cement.
- Limestone powder contributes to better environmental sustainability, spread flow and wet packing density, but causes enlarged total free shrinkage and diminished strength of UHPC pastes due to dilution effect, while application of silica powder is an effective counter measure to overcome those disadvantages due to nucleation, pozzolanic and filling effects.
- Slag cement possessing a relatively lower Ca/Si ratio is preferred to a lower amount but finer silica in the presence of limestone powder to achieve enhanced hardened properties (3% nano silica for the quaternary binders), compared to the Portland cement with a higher Ca/Si that needs more silica even with coarser particle size (5% micro silica for the ternary binders).
- Positive synergies in term of strength, fibre-to-matrix bond and total free shrinkage can be observed in UHPC pastes with quaternary binders (cement-slag-silica-limestone) compared to binary (cement-slag) and ternary (cement-silica-limestone) ones. It demonstrates the reasonability of quaternary blends for developing sustainable UHPC system instead of binary or ternary ones.

3.4 Conclusions

This chapter aims to optimize the binder by mineral admixtures addition with low cement clinker consumption for UHPC system, towards environmentally sustainable and cost-efficient purposes. First, the roles and optimum content of limestone powder in eco-friendly and low-cost UHPC are investigated. Then, the sustainable quaternary binder cement-slag-limestone-micro/nano silica are developed.

- Limestone powder shows a positive mineral plasticization effect that should be considered in designing UHPC. The degree of secondary pozzolanic hydration is more

intensive than C_3S/C_2S hydration, which can enhance the later-age strength development potential.

- The optimum content of limestone powder appears to be 50 vol.% of the total powder content in UHPC, and contribute to a higher strength, denser pore structure, diminished total free shrinkage and higher sustainability efficiency.
- Quaternary blends with cement-slag-limestone-silica in UHPC pastes have considerable advantage of reducing embedded CO_2 emission and improving sustainability efficiency.
- Positive synergies in term of strength, fibre-to-matrix bond and total free shrinkage are observed in UHPC pastes with quaternary binders compared to binary and ternary ones.

Chapter 4

Introduction of coarse aggregate in UHPC system

Currently, most UHPC mixtures are designed without coarse aggregates to ensure the homogeneity. This chapter attempts to introduce coarse aggregates into the UHPC system, in order to reduce the powder content and costs, improve the volume stability and penetration impact resistance, etc. Firstly, UHPC applying coarse basalt aggregates with a maximum particle size D_{\max} of 16 mm are designed by using a particle packing model and considering optimal powder proportion. The basalt aggregate size effect, powder content effect and fibre reinforcing effect are analysed and discussed. The coarse basalt aggregates have limited reducing effect on the mechanical strength of UHPC. The optimal powder content of about 800 kg/m^3 and 700 kg/m^3 is found for UHPC when the D_{\max} is 8 mm and 16 mm, respectively. Furthermore, a distribution modulus q of 0.19 for the modified Andreasen and Andersen packing model is recommended for designing UHPC with coarse aggregates. Secondly, a novel concept of two-stage UHPC (TS-UHPC) is proposed towards maximum volume of coarse aggregate utilization and ultra-low binder consumption. Results show that TS-UHPC has a low binder amount (e.g. 364 kg/m^3) and high binder efficiency (e.g. $0.417 \text{ MPa}\cdot\text{m}^3/\text{kg}$), possessing an excellent compressive strength of up to 151.8 MPa at 91 days. New formulas are proposed to describe correlation between compressive and splitting tensile strength of TS-UHPC, and to predict the strength of TS-UHPC by grout strength.

This chapter is partially published elsewhere:

P.P. Li, Q.L. Yu, H.J.H. Brouwers. Effect of coarse basalt aggregates on the properties of Ultra-high Performance Concrete (UHPC). *Construction and Building Materials*. 170 (2018) 649-659.

P.P. Li, Q.L. Yu, H.J.H. Brouwers, W. Chen. Conceptual design and performance evaluation of two-stage ultra-low binder ultra-high performance concrete. *Cement and Concrete Research*. 125 (2019) 105858.

4.1 Introduction

To avoid the drawbacks of limited intrinsic strength of coarse aggregates, overcome the inherent weakness between coarse aggregates and paste matrix, increase the homogeneity and eliminate stress concentration at the contact points between those aggregates, most UHPCs are designed by using only fine aggregates or refined aggregates [1,79,156]. However, concrete containing appropriate type and content of coarse aggregates can possess certain advantages. Rozalija and Darwin [157] reported that high-strength concrete containing basalt aggregates yields higher mechanical properties than high-strength concrete containing limestone, which is attributed by the intrinsic strength of the rock. Ma et al. [158] reported that coarse aggregates can improve the elastic modulus and alter the workability of UHPC more easily, as well as reduce the cost. Some researchers presented that an addition of coarse aggregates does not reduce or even exhibits a slightly higher compressive strength [159,160]. With the utilization of coarse aggregates, the autogenous shrinkage was reduced by approximately 40% [79]. Peng et al. [161] suggested to use coarse basalt aggregates to improve the penetration impact resistance. Tai et al. [162] presented that at higher loading rates (impact loading), the cracks form quickly and can propagate through the aggregates, consequently increasing the impact resistance. Both the disadvantages and advantages are very considerable for concrete incorporating coarse aggregates. To utilize coarse aggregates in UHPC, these contradictions should be well balanced. Hence, it is of importance to study the aggregate size effect in UHPC. In this study, basalt aggregates are used to match the high strength of paste matrix of UHPC.

Currently, most UHPCs are designed with a high content of powder, which leads to poor economic benefit and low efficiency [102]. On the other hand, a relatively high content of powder is needed to fill the voids between the aggregates to reduce the contact stress concentration and obtain a homogenous stress distribution through the matrix [163]. Normally, the powder volume fraction in UHPC containing coarse aggregates is lower than that without coarse aggregates [158]. Some investigations show that the compressive strength of self-compacting concrete (SCC) increases noticeably with the increase of powder content, especially at lower water-to-cement ratios [164]. But Domone [165] pointed out that there was no discernible trend of variation on the mechanical properties of SCC when increasing the powder contents. Therefore, it is necessary to further understand the powder content effect and find an optimal amount for UHPC when coarse basalt aggregates are utilized. Steel fibre is a critical ingredient because of its considerable reinforcement on mechanical properties, especially for tensile strength, ductility and energy dissipation. The interaction effect between coarse aggregates and steel fibres is also researched on the UHPCs with different powder contents in the present study, as well as the discussion of fibre length for UHPC with coarser aggregates.

However, some attempts only used limited volume replacement levels (e.g. 25% by the volume of UHPC matrix [166]) and maximum particle sizes (e.g. 5.2 mm [167]) of coarse aggregates, and the powder contents are still quite large (e.g. 770 - 1100 kg/m³ [168]). Besides, coarse aggregates with low density and strength is not compatible with the relatively high strength of UHPC matrix. While high strength coarse aggregates usually have

dense structure and high density, which more easily causes segregation problem in the UHPC system. Hence, how to further increase the volume and size of coarse aggregates and reduce the binder consumption in UHPC systems is still an issue and potential research subject.

Two-stage (preplaced aggregate) concrete (TSC) is an effective way to extend the utilization of coarse aggregates, which is produced by first preplacing aggregates in a formwork and subsequently injecting grout [169,170]. High volumes of large size aggregates can be easily used, due to its fabrication methodology without any segregation concerns [170]. A higher volume (e.g. 53% - 59% [169,171]) means a much lower binder consumption. A larger maximum particle size of the aggregates (e.g. 40 mm [172]) indicates a better resistance against bullet or projectile impact [168]. TSC has already been successfully used in applications including underwater concrete construction, massive concrete structure, casting concrete in areas with narrowly spaced reinforcement, concrete repair, heavyweight concrete and low-shrinkage concrete. Nevertheless, the strength of current TSC is relatively low, usually ranging between 10 MPa to 60 MPa [169–175], which is probably attributed to low intrinsic strength of coarse aggregates, relatively low strength of the grout, weak homogeneity, stress concentration at the contact points between aggregates, inherent weakness between coarse aggregates and paste matrix. To sum up, UHPC and TSC have some complementary characteristics on coarse aggregate utilization, binder consumption and mechanical properties. Hence, there is potential to design a novel building material to make full use of advantages of TSC and UHPC and overcome their individual shortcomings.

The objective of this chapter is to investigate the effect of coarse aggregates and the consequent alteration of powder content on the properties of UHPC. The basalt aggregate size effect on mechanical strength is measured and analysed. The powder content effect on compactness and strength of UHPC with coarse basalt aggregates is analysed and discussed, and the optimum powder content and corresponding value of distribution modulus q are suggested. Furthermore, two-stage UHPC as a novel building material is developed, including fabrication methodology, excellent mechanical properties, high volume coarse aggregates and very low binder consumption, possessing widely potential application, e.g. impact resistant, underwater, massive, repaired, heavyweight, low-shrinkage and narrowly spaced reinforced concrete. The compatibility between grout and aggregates is analysed by assessing the interfacial transition zone (ITZ). New models are proposed and validated to correlate the compressive strength and tensile splitting strength of TS-UHPC, and compressive strength of TS-UHPC and grout. The proposed TS-UHPC concept further contributes to sustainability development of advanced concrete materials and the proposed models can be applied to predict the materials property.

4.2 Utilizing coarse aggregates by normal mixing

4.2.1 Materials

The raw materials used in this study are Portland Cement CEM I 52.5 R (PC), micro-silica (mS), limestone powder (LP), sand 0-2 (S), basalts aggregate (BA), water (W), PCE-type superplasticizer (SP3 from Chapter 2 is used). The steel fibre (SF) (length = 13 mm, diameter

= 0.2 mm, tensile strength = 1100 MPa) is utilized to investigate the reinforcement ratio for UHPC under different powder contents. The dosage of steel fibre is 2 vol.% of the UHPC, which is proven to be an appropriate dosage for UHPC [7,156]. The specific densities of those ingredients are measured by a gas pycnometer (AccuPyc 1340 II Pycnometer), shown in Table 4.1. The particle size distributions (PSD) of the used materials are measured by the sieve and laser diffraction analyses (Malvern Mastersizer 2000[®]), respectively, shown in Figure 4.1. The particle morphologies and the chemical compositions of the used powders can be seen in Sections 3.2.1 and 3.3.1.

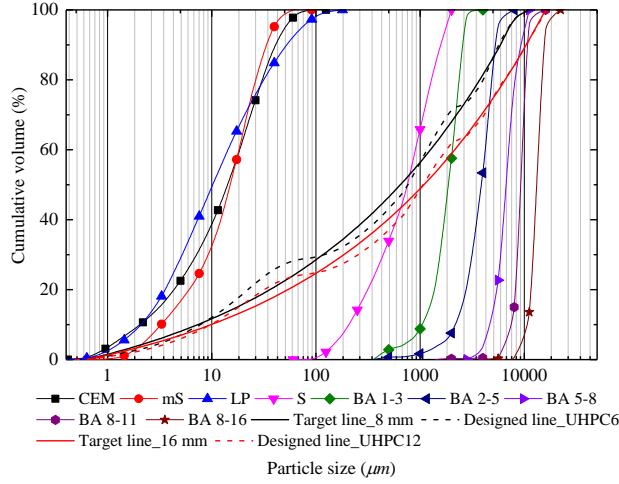


Figure 4.1: The PSDs of raw materials and mixtures.

Table 4.1: Specific densities of raw materials.

Materials	CEM	mS	LP	S	BA 8-11	BA 8-16	BA others	W	SP	SF
Specific density (g/cm ³)	3.15	2.32	2.71	2.72	2.89	2.71	3.05	1.00	1.07	7.85

4.2.2 Mix design by a packing model

The recipes of UHPCs are shown in Table 4.2. The mS and LP are fixed at 5% and 20% by mass of total powder, respectively. To research the effect of basalt aggregate size on the strength of UHPC, the powder content of UHPC is fixed at 900 kg/m³, considering that most UHPC incorporates powder more than 900 kg/m³ [90,176–181]. To investigate the effect of powder content on the compactness and strength of UHPC, the powder contents are changed from 900 kg/m³ to 650 kg/m³. The fraction of the basalt aggregates are calculated by using the modified Andreasen and Andersen model as follows [64,65,182–184]:

$$P(D) = \frac{D^q - D_{min}^q}{D_{max}^q - D_{min}^q} \quad (4.1)$$

$$RSS = \sum_{i=1}^n [P_{mix}(D_i^{i+1}) - P_{tar}(D_i^{i+1})]^2 \rightarrow \min \quad (4.2)$$

in which D is the particle size, D_{min} and D_{max} represent the minimum and maximum particle size, respectively; $P(D)$ is the cumulative fraction of the total solids being smaller than size D ; q is the distribution modulus, and 0.22 is used in this study as recommended [185,186],

P_{mix} is the designed mix, and the P_{tar} is the target grading calculated from Eq. (4.1). The proportions of each basalt aggregate size fraction in the designed mixture are adjusted until an optimum fit between $P_{mix}(D)$ and $P_{tar}(D)$, using an optimization algorithm based on the Least Squares Method, as presented in Eq. (4.2). It should be pointed out that 750 kg/m^3 and 650 kg/m^3 are the optimum powder content for the UHPC with the maximum aggregate size of 8 mm and 16 mm, respectively, based on the modified Andreasen and Andersen model without any fixed condition of powder content. Examples of the PSDs of the target and designed curve of UHPCs are shown in Figure 4.1. The quality of fit between the designed and target lines is evaluated by the coefficient of determination,

$$R^2 = 1 - \frac{\sum_{i=1}^n [P_{mix}(D_i^{i+1}) - P_{tar}(D_i^{i+1})]^2}{\sum_{i=1}^n [P_{mix}(D_i^{i+1}) - \frac{1}{n} \sum_{i=1}^n P_{mix}(D_i^{i+1})]^2} \quad (4.3)$$

To research the interaction between coarse aggregate and steel fibre, ultra-high performance fibre reinforced concretes (UHPRFCs) are designed, based on the designed UHPCs (in Table 4.2) with reinforcement by 2 vol. % steel fibres.

Table 4.2: Recipes of UHPCs with different basalt sizes and powder contents (kg/m^3).

No.	Note a-b	PC	m S	LP	S	BA 1-3	BA 2-5	BA 5-8	BA 8-11	BA 8-16	W	SP
UHPC1	3-900	675	45	180	865	576	0	0	0	0	180	10.8
UHPC2	8-900	675	45	180	588	179	403	314	0	0	180	10.8
UHPC3	16-900	675	45	180	305	308	307	248	121	206	180	10.8
UHPC4	8-850	638	43	170	700	101	436	310	0	0	170	10.2
UHPC5	8-800	600	40	160	812	22	468	307	0	0	160	9.6
UHPC6	8-750	563	38	150	904	0	319	454	0	0	150	9.0
UHPC7	16-900	675	45	180	243	339	279	252	110	201	207	5.4
UHPC8	16-850	638	43	170	355	259	315	239	118	203	196	5.1
UHPC9	16-800	600	40	160	467	180	352	225	126	205	184	4.8
UHPC10	16-750	563	38	150	579	100	389	212	135	208	173	5.3
UHPC11	16-700	525	35	140	699	0.6	445	187	148	210	161	4.9
UHPC12	16-650	488	33	130	783	0.0	407	222	136	214	150	4.6

a and b means the maximum particle size of used basalt and powder content, respectively. The water-to-powder ratio of No. UHPC1 - UHPC6 is fixed at 0.2, while the water-to-powder ratio of No. UHPC7 - UHPC12 is fixed at 0.23.

4.2.3 Testing methods

The fresh UHPCs are casted into steel cubic moulds ($100 \times 100 \times 100 \text{ mm}^3$). All samples are covered with polyethylene film to prevent the moisture loss. They are demoulded approximately 24 h after casting and then cured in water under room temperature of $20 \pm 1 \text{ }^\circ\text{C}$. The compressive and tensile splitting strength of UHPC samples are measured after 28 days, based on EN 12390-3 [107] and EN 12390-6 [187].

4.2.4 Results and discussion

- **Basalt aggregate size effect**

Figure 4.2 presents the compressive and tensile splitting strengths of UHPCs versus the maximum size of basalt after 7 days and 28 days, respectively. The results show that the 7 days compressive strength of UHPCs do not have an obvious difference, namely at about 122 MPa, while the tensile splitting strength of UHPCs has a linear decrease from 9.1 MPa to 6.1 MPa. At 28 days, the compressive strength has a linear decrease trend from 144 MPa to 132 MPa, while the tensile splitting strength shows a slight decrease from 9.8 MPa to 8.2 MPa, with the maximum basalt size changing from 3 mm to 16 mm.

The decrease tendency of strength caused by the larger basalt aggregate size fraction can probably be attributed to the following reasons: some aggregates with lower strength than paste, weaker interfacial transition zone (ITZ) between the aggregate and paste, and stress concentration at the contact points between those aggregates. Nevertheless, the decrease degree by basalt aggregate size effect is rather limited, which is similar to other researches on reactive powder concrete with addition of graded natural aggregates (max size 8 mm) [159]. It was even reported that the addition of coarse aggregates exhibits a slightly higher compressive strength [160]. In this case, the intrinsic strength of basalt aggregates is higher than ordinary aggregates, dense basalt can easily get a compressive strength more than 150 MPa. Besides, the ITZ between coarse basalt aggregates and paste can be stronger after optimization of powder content. Furthermore, with an appropriate powder content, the stress concentration can be improved by reducing contact points between the coarse aggregates. It can be concluded that it is possible to design UHPC with inclusion of coarse basalt aggregates.

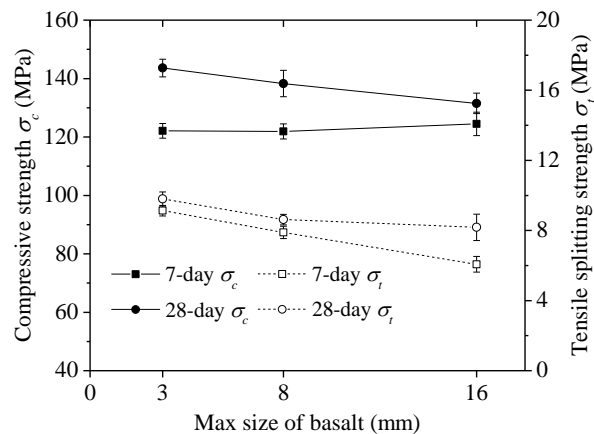


Figure 4.2: Strength of UHPCs with different basalt sizes.

- **Powder content effect**

Packing density is defined as the ratio of the solid volume to bulk volume. Several models can be utilized to describe the packing density, such as Furnas Model, Toufar Model, Dewar Model, Linear Packing Density Model, Compressible Packing Model, etc. [188]. The Compressible Packing Model can present the compactness of a mixture via the virtual packing density β [189,190], calculated from:

$$\beta = \min \left\{ \frac{\beta_i}{1 - \sum_{j=1}^{i-1} [1 - \beta_i + b_{ij}\beta_i(1 - 1/\beta_j)]r_j - \sum_{j=i+1}^n (1 - a_{ij}\beta_i/\beta_j)r_j} \right\} \quad (4.4)$$

$$\beta_j = (1 + 1/K_r)\alpha_j \quad (4.5)$$

$$a_{ij} = \sqrt{1 - (1 - d_j/d_i)^{1.02}} \quad (4.6)$$

$$b_{ij} = 1 - (1 - d_i/d_j)^{1.50} \quad (4.7)$$

in which a_{ij} and b_{ij} are interaction coefficients representing loosening effect and wall effect, respectively [189]; d_j is average particle diameter of j -class particle and arranged in a sequence $d_j > d_{j+1}$; β_j is the virtual packing density of the j -class particle; α_j is the experimentally determined packing density of j -class particle based on the EN 1097-3 [129]; K_r is the compaction index to determine the real packing density, the K_r value equal to 4.1 is used in this study, indicating no compaction is applied; r_j the volume fraction of j -class particle.

The size class with the lowest β is called the dominant size class. In this study, the dominant grain is found always to be the cement grain based on the calculation by Eq. (4.4), where the packing density of individual ingredient is experimentally acquired. This also indicates that the cement consumes more space than the interstitials available between the large particles. Because the fractions of micro-silica and limestone powder are fixed based on the cement in this study, it can be concluded that the powder content is the dominant factor which greatly influences the compactness of the designed UHPC. The packing densities of the designed UHPCs with basalt aggregates of 8 mm and 16 mm are shown in Figure 4.3. In this study, a lower powder content contributes to a better compactness, which indicates a lower powder content is preferably used to design UHPC incorporating coarse aggregates.

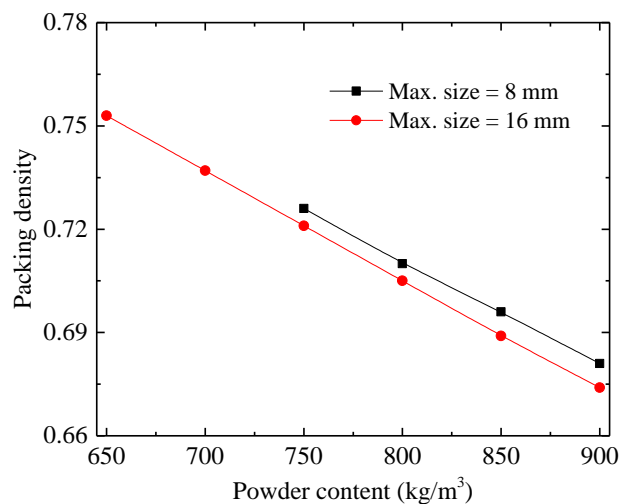


Figure 4.3: Packing densities of UHPCs with different powder contents.

The above analysis shows great influence of powder content on the compactness of UHPC with coarse basalt aggregates. Hence, it is of great significance to investigate the powder content effect on the mechanical strength of UHPC. Figure 4.4 shows the 28-day strength of UHPCs with different powder contents, using the maximum basalt size of 8 mm and 16 mm.

Figure 4.4(a) presents the strength of UHPCs with maximum basalt size of 8 mm. With the increase of powder content from 750 kg/m^3 to 900 kg/m^3 , the compressive strength of UHPC first increases and then decreases, reaching the maximum value of 143 MPa at the powder content of 800 kg/m^3 . The tensile splitting strength only has a slight fluctuation between 8.4 MPa and 9.1 MPa. Figure 4.4(b) presents the strength of UHPCs with the maximum basalt size of 16 mm, which has a similar tendency to Figure 4.4(a). The maximum compressive strength of 140 MPa occurs at the powder content of 700 kg/m^3 , and the tensile splitting strength fluctuates between 6.5 MPa and 8.7 MPa.

The results indicate that the powder content effect has a greater influence on compressive strength rather than tensile strength of the designed UHPC. The optimal powder content occurs at a moderate value, rather than the highest content (900 kg/m^3) or the lowest content based on the modified Andreasen and Andersen model. It indicates that the optimized mix design of UHPC with coarse basalt aggregates should incorporate an appropriate amount of powder to fill into the gaps between aggregates and avoid the possible stress concentration. The optimal powder content of UHPC is reducing from 800 kg/m^3 to 700 kg/m^3 , with the maximum basalt size changing from 8 mm to 16 mm. It indicates that a lower powder dosage is requested to design UHPC when coarser aggregates is applied, which is in accordance with the results in Figure 4.3.

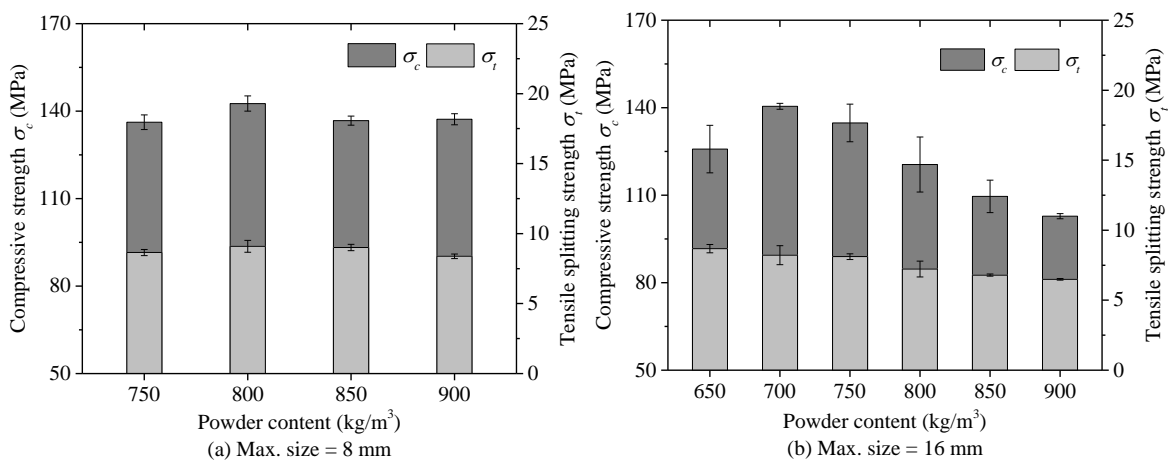


Figure 4.4. Strength of UHPCs with different powder contents.

- **Distribution modulus q**

The modified Andreasen and Andersen model has already been successfully employed in the optimization design for UHPC without coarse aggregates [186]. Different types of concrete can be designed using Eq. (4.1) by different values of distribution modulus q , which determines the proportion between fine and coarse particles. A smaller value of q contributes to a mixture rich in fine particles. Brouwers theoretically demonstrated the q value ranging of 0 - 0.28 [191], Hunger [185] and Yu [186] recommended using q in the range of 0.22 - 0.25 to design self-compacting concrete and UHPC with fine aggregates. However, an appropriate q value has not been investigated for the UHPC incorporating coarse aggregates.

In this study, an initial q value of 0.22 is used to design UHPC with basalt aggregates. The PSD of the target and designed curves of UHPCs are shown in Figure 4.5 (with the detailed

mix proportion information in Table 4.2), according to Eq. (4.1). Based on the modified Andreasen and Andersen model with q value of 0.22, the optimum powder contents can be computed, around 750 kg/m^3 and 650 kg/m^3 for the designed UHPC with basalt aggregates of 8 mm and 16 mm, respectively, as shown in Figure 4.5. However, the maximum strengths occur at the powder contents of 800 kg/m^3 and 700 kg/m^3 , respectively, which indicates that the chosen q value of 0.22 is slightly too high in this study. In order to get appropriate powder contents (800 kg/m^3 and 700 kg/m^3) for excellent mechanical strength of UHPCs with coarse basalt aggregates, a lower distribution modulus q , is requested, yielding 0.19.

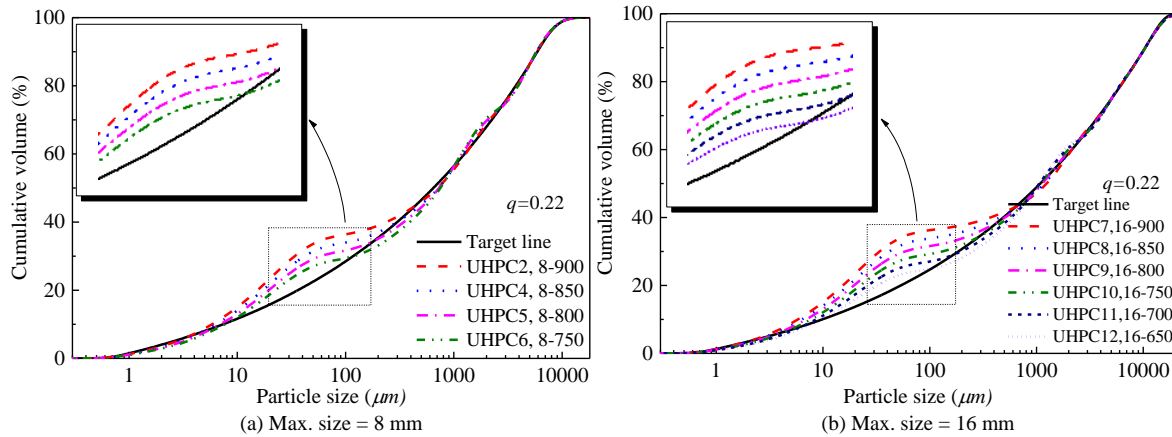


Figure 4.5: PSDs of the target and designed curve of UHPCs.

- **Steel fibre reinforcement**

Steel fibre is a critical parameter in designing UHPC because of its considerable reinforcement of mechanical properties. The strength of designed UHPFRCs, reinforced by 2 vol. % steel fibre, are shown in Figure 4.6.

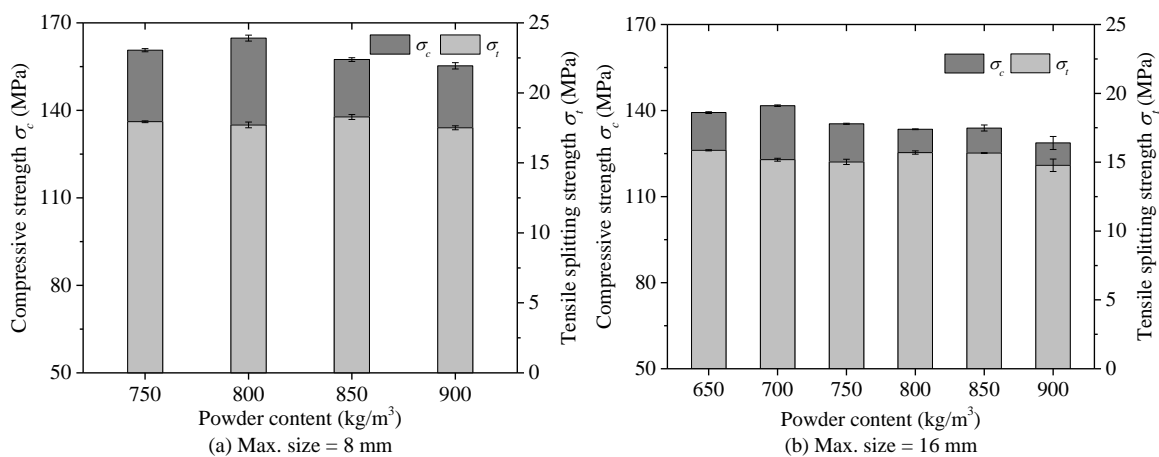


Figure 4.6: Strength of UHPFRCs with different powder contents.

The steel fibre reinforcement is researched on UHPFRCs with different powder contents. Compared the results in Figure 4.4 with those in Figure 4.6, the powder content has a similar effect on mechanical strength, with and without 2 vol.% steel fibre. The optimum powder contents still occur at 800 kg/m^3 and 700 kg/m^3 , respectively. The increase of compressive strength of UHPCs by the steel fibres are less than 25%. But, the increase ratios of tensile splitting strength are considerable, due to the bridging effect of steel fibres [192], between

83% and 131%. Figure 4.7 shows the strength improvement ratios of UHPCs at a favourable powder content, 700 kg/m^3 and 800 kg/m^3 . The strength improvement ratio of the mixture UHPC5 is always higher than that of the mixture UHPC11. A lower utilization efficiency of the 13 mm long steel fibre is observed for the UHPC containing coarser basalt aggregates, which indicates that the fibre-bridging stress interlock between fibres and coarse aggregates becomes worse. The steel fibre cannot completely overlay too large aggregate, subsequently the combined effect between steel fibres and bigger aggregates is weaker. Hence, steel fibres with a proper length is suggested when designing UHPC with inclusion of relatively big aggregates.

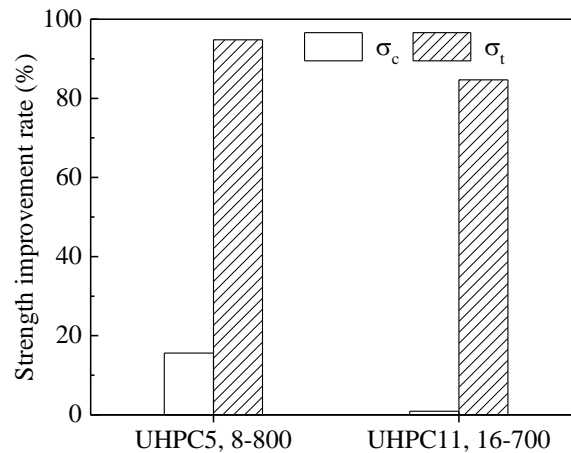


Figure 4.7: Strength improvement rate by steel fibres.

4.2.5 Summary

- The coarse basalt aggregates result in a decrease on mechanical strength, but the decrease degree is rather limited. With the increase of particle size of basalt aggregate, both compressive and tensile splitting strengths tend to decrease, from 144 MPa to 132 MPa and 9.8 MPa to 8.2 MPa at 28 days, respectively.
- A reduced powder content is required to design UHPC when coarser aggregates are applied. The optimal powder content of UHPC in this study is about 800 kg/m^3 and 700 kg/m^3 with the maximum basalt aggregate of 8 mm and 16 mm, respectively. In addition, a distribution modulus q of 0.19 is recommended in the modified Andreasen and Andersen model.
- The optimal powder contents are the same for UHPCs without and with 2 vol.% steel fibre. The reinforcement effect is more pronounced on tensile strength than compressive strength, ranging from 83% and 131%. Fibres with appropriate lengths should be considered when designing UHPC with coarser aggregate.

4.3 Two-stage UHPC with high-volume coarse aggregate

4.3.1 Materials and mixtures

- **Materials**

The raw materials include Portland cement CEM I 52.5 R (PC), densified micro-silica of Elkem Grade 920E D (mS), limestone powder (LP), fine silica sand (S), coarse basalt

aggregates (BA), PCE-based superplasticizer (SP3 from Chapter 2 is used) and tap water (W). Figure 4.8 shows the particle size distribution of raw materials. The specific and bulk densities are shown in Table 4.3.

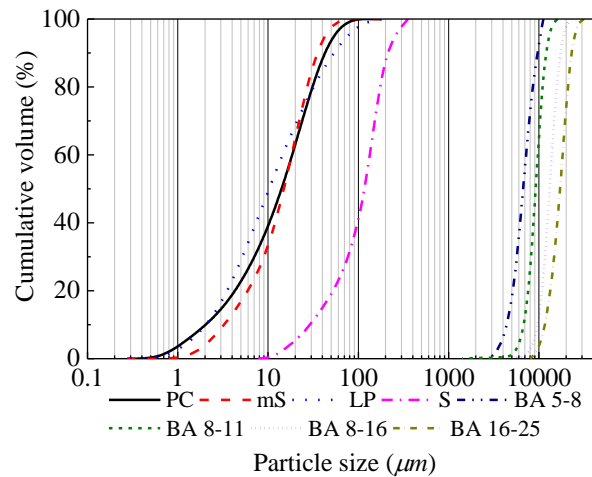


Figure 4.8: The PSDs of raw materials.

Table 4.3: Specific densities of raw materials.

Materials	PC	mS	LP	S	W	SP	BA 5-8	BA 8-11	BA 8-16	BA 16-25
Specific density (kg/m ³)	3150	2320	2710	2670	1000	1200	3050	2890	2710	3050
Bulk density (kg/m ³)	-	-	-	-	-	-	1715	1582	1514	1563

- **Mix design of grout and TS-UHPC**

The properties of TS-UHPC are mainly determined by the two ingredients: grout and aggregates. In this study, three ultra-high performance grouts are designed with relatively low water-to-powder ratios, with different fine sand-to-powder ratios at 0, 0.5, and 1.0. The proportion of powders is optimized at 5% of micro-silica and 20% of limestone powder by mass of the total powder [125]. The water content and superplasticizer dosage are adjusted to achieve a comparably desirable fluidity, with spread flow approximately between 35 cm and 40 cm by using a Hägermann cone [108]. The detailed recipes for the designed grouts are shown in Table 4.4.

Table 4.4: Recipes of designed grouts.

Mix	PC	mS	LP	S	water	SP	PC	mS	LP	S	water	SP
	Mass proportion						(kg/m ³)					
G1	0.75	0.05	0.20	0	0.200	1.3%	1378.0	91.9	367.5	0.0	367.5	23.9
G2	0.75	0.05	0.20	0.50	0.215	1.7%	1000.2	66.7	266.7	666.8	286.7	22.7
G3	0.75	0.05	0.20	1.00	0.240	2.0%	777.5	51.8	207.3	1036.6	248.8	20.7

Four coarse basalt aggregates with different sizes are utilized to produce TS-UHPC, as shown in Figure 4.9. To pre-estimate the ingredient consumption of designed TS-UHPC before concrete casting, the bulk densities of basalt aggregates are first measured in

accordance with EN 1097-3 [129], shown in Table 4.3. Then the masses of ingredients can be calculated as,

$$m_{BA} = \rho_{bulk} \times 1m^3 \quad (4.8)$$

$$m_i = m_{i_grout} \left(1 - \frac{\rho_{bulk}}{\rho_{specific}}\right) \quad (4.9)$$

where m_{BA} is the mass of basalt aggregates in TS-UHPC (kg/m^3), m_i and m_{i_grout} are the masses of other raw material i in TS-UHPC and the used grout (kg/m^3), respectively. ρ_{bulk} and $\rho_{specific}$ are the bulk and specific densities of used basalt aggregates (kg/m^3). The actual raw material consumptions for 1 cubic meter during the tests are shown in Table 4.5. The mix 1-4 contain grout of G2, and basalt aggregates of 5-8 mm, 8-11 mm, 8-16 mm and 16-25 mm, respectively. Mix 5 and mix 6 include basalt aggregates of 8-16 mm, and grout of G1 and G3, respectively. It should be noted that the volumes of coarse aggregates are around 55%, which is much higher than that in normal concrete. While, the total volume of fine sands and coarse aggregates varies from about 55% to 73%.

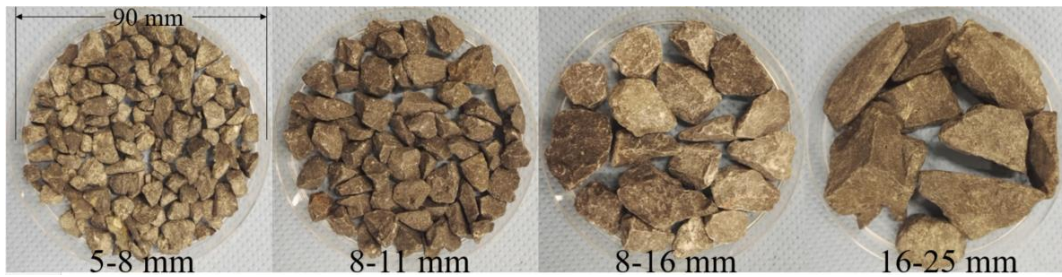


Figure 4.9: The coarse basalt aggregates.

Table 4.5: Recipes of designed TS-UHPC (kg/m^3).

Mix No.	Note	PC	mS	LP	S	BA	water	SP	Density
1	G2A8	430.9	28.7	114.9	287.2	1715	123.5	9.8	2710
2	G2A11	450.8	30.1	120.2	300.5	1582	129.2	10.2	2623
3	G2A16	426.1	28.4	113.6	284.1	1514	122.1	9.7	2498
4	G2A25	478.9	31.9	127.7	319.3	1563	137.3	10.9	2669
5	G1A16	625.7	41.7	166.9	0.0	1514	166.9	10.8	2526
6	G3A16	341.5	22.8	91.1	455.3	1514	109.3	9.1	2543

4.3.2 Casting procedure and testing methods

- **Casting procedure**

The coarse basalt aggregates are preplaced in a steel mould first. Then, the ultra-high performance grout is prepared following the procedure: drying mixing (PC+mS+LP+S) for 2 min, adding 80% water and mixing for 3 min, sequentially adding remaining water incorporated with SP and followed by mixing for about another 5 min. After that, the fresh ultra-high performance grout is poured into the preplaced coarse basalt aggregates. Several injecting methods can be found in literature, such as covering the top of moulds with a perforated plate and pumping grout into moulds from the bottom (need extra pumping device and energy) [193], pouring the grout from the top of aggregates by gravity effect (difficult

to observe any possible honeycombed problem at bottom for finer aggregates) [172], injecting grout from bottom through a pipe by gravity effect (easy to adjust the injecting pressure by different height) [170], or even scattng-filling coarse aggregate process [194]. Using an injecting pipe by gravity effect is chosen in this paper by considering quality control, convenience of casting and economic benefit. The detail casting procedure for TS-UHPC is illustrated in Figure 4.10(a). One example of the cross-section of hardened concretes ($100 \times 100 \text{ mm}^2$) by this casting procedure is shown in Figure 4.10(b), which presents very homogeneous distribution of coarse basalt aggregates and densified matrix.

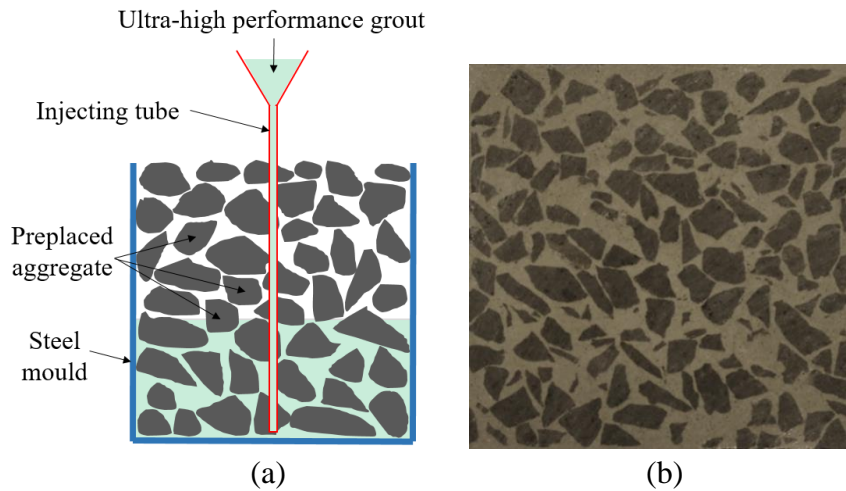


Figure 4.10: (a) casting procedure and (b) cross-section of TS-UHPC.

- **Testing methods**

The spread flow, wet packing density, isothermal calorimetry, thermal gravimetry, mercury intrusion porosimetry, mechanical strength and water permeable porosity are measured based on the methods as mentioned in Sections 2.2.2, 3.2.2 and 3.3.2. The cube sizes for grout and TS-UHPC are $50 \times 50 \times 50 \text{ mm}^3$ and $100 \times 100 \times 100 \text{ mm}^3$, respectively.

4.3.3 Results and discussion

- **Properties of grout**

Table 4.6: Fresh behaviour of grouts.

Mix	Flow (cm)	$T_{v\text{-funnel}}$ (s)	Fresh density (kg/m^3)	Wet packing density	Air content
G1	41	5.5	2197	0.611	1.4%
G2	38	9.2	2253	0.684	2.4%
G3	36	9.7	2281	0.721	2.6%

The casting method and quality control of TS-UHPC are dependent on the excellent fresh behaviour of ultra-high performance grout. The fresh behaviour of the three designed grouts is shown in Table 4.6. The mini slump flow ranges from 41 cm to 36 cm, while the mini V-funnel flow time changes from 5.5 s to 9.7 s, by adjusting the water content and SP dosage to meet the required self-compacting properties (slump flow of 24 to 26 cm and V-funnel time of 7 to 11 s) [100,101]. The fresh behaviour of the grouts is sufficient to fill the voids between aggregates, by checking the apparent and cross-section, as shown in Figure 4.10(b).

It also should be pointed out that the mini slump flow above 35 cm is appropriate for ultra-high performance grout to fill the voids of aggregates in this study. The wet packing density continuously increases from 0.611 to 0.721, which means an improved compactness in fresh state for ultra-high performance grout with the addition of an appropriate fine sand content. The air content of the grouts determined based on [102] vary from 1.4% to 2.6%.

To understand the hydration and pore structure of the designed grouts, normalized heat flow, TG-mass loss and pore size distribution are measured. Figure 4.11 shows the time-dependent normalized heat flow of ultra-high performance grouts with different sand contents, water amounts and PCE-type SP dosages. As seen from Table 4.4, the water proportion and SP dosage continuously increase with the increase of the sand content from 0 to 1.0 (sand-to-powder ratio), even though their absolute masses decrease. Compared to G1 without any sand, G2 (0.5) exhibits a shorter time to reach the peak of heat flow curve and releases more normalized heat, which is probably due to the nucleation effect of the very fine particles of sand that accelerate the hydration of binders. However, with further increasing the water-to-binder ratio and SP dosage, G3 (1.0) shows a longer time to reach the peak, which indicates a larger retardation effect due to a higher PCE-type SP dosage and a higher water-to-binder ratio in UHPC system [33,47,108]. This retardation effect is dominant in the hydration of binders, instead of the acceleration effect by the fine sand particles.

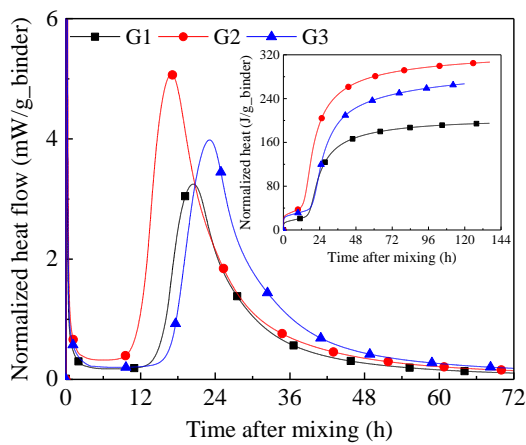


Figure 4.11: Calorimetric results of grouts.

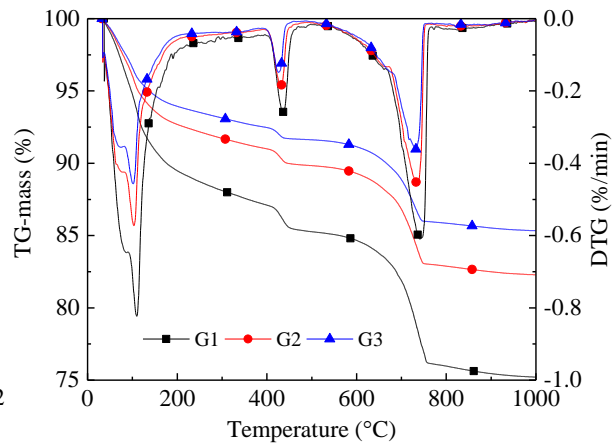


Figure 4.12: TG results of grouts.

Figure 4.12 presents the thermogravimetric results with TG and DTG curves. Three dominant peaks can be observed, which are respectively linked to the water loss from free water, C-S-H, ettringite and AFm dehydration (30 - 200 °C); decomposition of portlandite (CH) (400 - 500 °C); decarbonation of CaCO_3 (600 - 800 °C)[112,113]. All the three peaks tend to be weaker and sharper with the increased amount of fine sand, which indicates the dilution effect of fine sand on active binders. The contents of C-S-H and CH, calculated from Eqs. (3.5)-(3.6), are shown in Figure 4.13 and Figure 4.14, respectively. Even though the absolute C-S-H (by total grout) decreases with the increasing sand content, the C-S-H content by the mass of binder (PC+mS) keeps almost the same at around 34% from G1 to G2, and finally reaches up to 37.7% for G3. It indicates a higher hydration degree of active binder for G3 compared to G1, due to a higher water-to-binder ratio in G3. The higher hydration degree of G3 can also be directly observed by the amount of unreactive cement grains from the SEM observation that will be discussed in the following section. G3

possessing a higher hydration degree at a higher water-to-binder ratio should also generate more CH content by the mass of binder. However, a continuous decrease of CH content by the mass of binder is observed from G1 of 10% to G3 of 8.1%. It can probably be attributed to a better pozzolanic effect of micro-silica in UHPC system with a higher water-to-binder ratio and consumes more CH to form C-S-H gel.

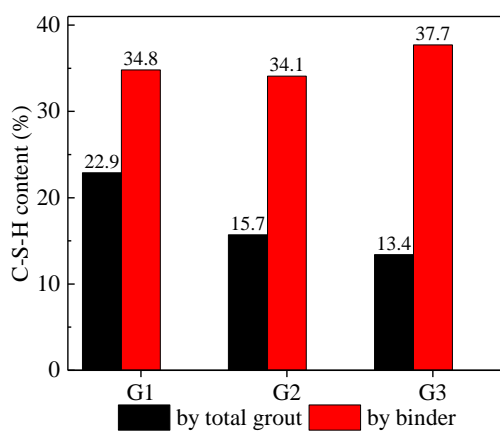


Figure 4.13: C-S-H contents of grouts.

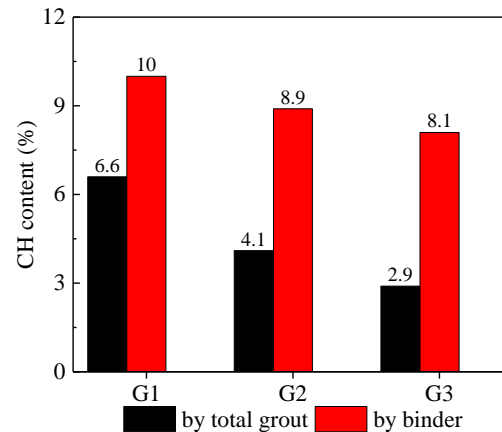
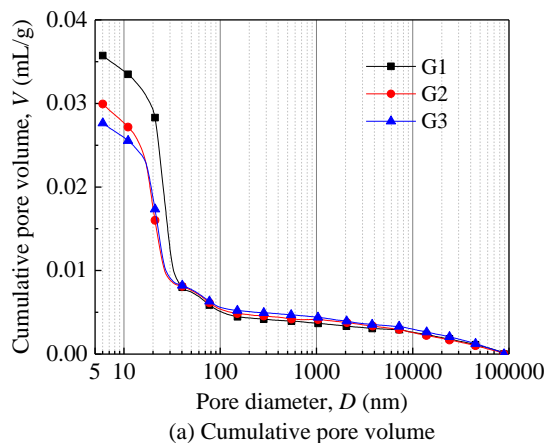
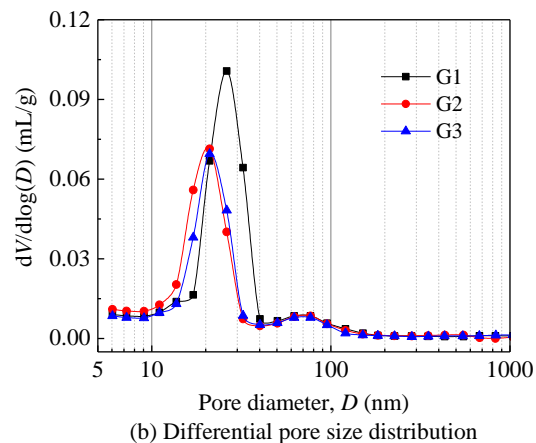


Figure 4.14: CH contents of grouts.



(a) Cumulative pore volume



(b) Differential pore size distribution

Figure 4.15: Pore structure of grouts.

Figure 4.15 shows the cumulative pore volume and differential pore size distribution of the grouts, which includes the pore size from 5 nm to 100 μm . It is clear that grout with a larger fine sand-to-powder ratio (up to 1.0 in this study) has a lower cumulative pore volume, namely a lower porosity. The critical or threshold pore diameter (the peak on the pore size distribution curve in Figure 4.15(b)), defined as the pore when achieving the highest rate of mercury intrusion and beginning to penetrate the interior of sample [112,118], decreases from around 26 nm of G1 to 21 nm of G2 with the increase of fine sand addition, and further keeps at 21 nm till G3. In this study, the pore size can be categorized into three parts as: (I) large pore more than 40 nm (air pore and partly capillary pore), (II) medium pore from around 20 nm to 40 nm (capillary pore), and (III) small pore from around 5 nm to 20 nm (partly gel pores and capillary pores [120]). The three grouts share comparable pore volumes from 40 nm to 100 nm, as shown in Figure 4.15(a). While, with the addition of fine sand as filler, the grout of G2 (0.5), have a considerable decrease of the pores between 20 nm and 40 nm compared to that of G1, which can be attributed to the better compactness and reduced

amount of the paste. As can be seen in Table 4.6, although G2 has a higher water-to-powder ratio that increases the capillary pores in the paste, G2 has a clearly lower amount of paste. Further addition of fine sand (G3) does not obviously increase the wet packing density, and cannot further improve the pore size distribution from 20 nm and 40 nm. G2 has a higher pore volume from 5 nm to 20 nm compared to G3, which can be explained by the relatively high C-S-H gel content in the grout (see Figure 4.12). The G2 and G3 have more pores from 5 nm to 20 nm compared to G1, but less C-S-H gel (see Figure 4.12), which indicates that more low-density and more porous C-S-H gels are preferably generated in G2 and G3 with higher water-to-powder ratios [120]. In overall, grout with a higher sand-to-powder ratio, 1.0 in this study, has a denser microstructure.

Figure 4.16 shows the compressive strength development of grouts. The early age strengths are very high, ranging between 66-100 MPa at 1 day, and then around 125 MPa at 7 days. The strength reaches between 142 MPa and 148 MPa at 28 days, and even higher at 91 days between 162 MPa and 173 MPa. These results confirm that ultra-high performance grouts can be successfully developed by applying the concept of UHPC, with both high early and later age strength. They could be used to design the TS-UHPC, and to predict the strength by that of grout (analysed below). Grout with less fine sand possesses a higher early age strength before 7 days, which is due to higher amount of active binders and hydration product, as can be seen in Table 4.4 and Figure 4.13. After a longer curing time, all the grouts reach comparable compressive strengths at 7 days. Later the grouts with more fine sand tend to surpass, e.g. 6.8% higher for G3 compared to G1. Two main factors contribute to those higher later compressive strengths, including better compactness and relatively higher hydration degree of binders. In overall, adding an appropriate amount of fine sand in ultra-high performance grout can improve its strength and reduce the binder consumption, which obviously contributes to the sustainability development of advanced concrete materials.

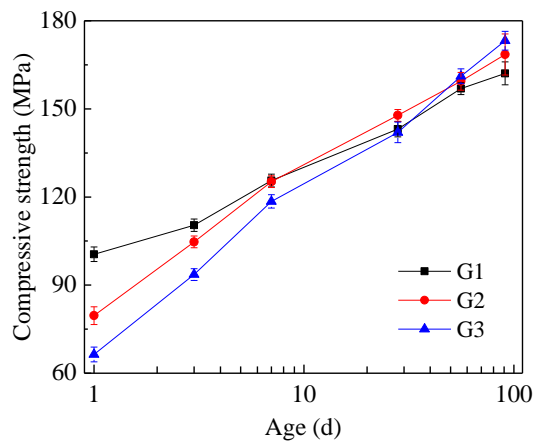


Figure 4.16: Compressive strength of grouts.

- **Properties of TS-UHPC**

Table 4.7 summarizes the compressive strength (σ_c) and splitting tensile strength (σ_t) of the designed TS-UHPC. The size effect of basalt aggregate, grout type effect, correlation between compressive and splitting tensile strength of TS-UHPC, and binder efficiency compared to normal TSC and UHPC will be discussed in the following sections.

Table 4.7: Strength of TS-UHPC (MPa).

Mix	Compressive strength σ_c						Splitting tensile strength σ_t					
	1d	3d	7d	28d	56d	91d	1d	3d	7d	28d	56d	91d
G2A8	-	-	-	142.1	-	-	-	-	-	7.4	-	-
G2A11	-	-	-	131.0	-	-	-	-	-	7.1	-	-
G2A16	80.5	105.3	114.1	116.2	124.0	140.1	4.0	5.9	6.3	6.6	6.9	7.5
G2A25	-	-	-	121.8	-	-	-	-	-	6.5	-	-
G1A16	87.4	109.5	111.3	113.0	118.1	127.6	4.5	5.3	5.6	5.9	6.1	6.6
G3A16	71.1	103.2	114.2	121.1	133.9	151.8	4.2	6.1	6.8	7.2	7.8	8.8

To analyse the size effect of coarse basalt aggregate, the mechanical strengths of TS-UHPC incorporated with G2 and different aggregate sizes are measured at 28 days, as shown in Figure 4.17. It should be noted that currently most UHPCs are designed without applying any coarse aggregates to improve homogeneity and eliminate intrinsic weakness [79,156,177,195]. However, introduction of coarse aggregates in normal concretes has shown advantages, including decrease of powders, economic benefits, high impact resistance [161,162] and low shrinkage [194,196]. The utilized powder contents of TS-UHPC are very low compared to normal UHPC because the preplaced coarse basalt aggregates already occupy rather large volume (around 55%). Although the coarser aggregates are easily for grout to fill into the voids, the demanded powder contents are comparable for coarse aggregates with different sizes. Figure 4.17 indicates a continuous decrease of both compressive and splitting tensile strength of TS-UHPC when increasing the maximum size of basalt aggregates, from 142.1 MPa to 121.8 MPa for compressive strength and 7.4 MPa to 6.5 MPa for splitting tensile strength. Because the volume of basalt aggregates are very similar, this reduction is mainly determined by the size effect of the basalt aggregates. However, the reduction is not significant, about 14.3% and 12.2% respectively, with the maximum size from 8 mm to 25 mm. This limited decreasing tendency is in line with the conventional UHPC in Section 4.2. The compressive damage pattern of the designed TS-UHPC usually shows an “explosive failure” as described in EN 12390-3: 2009 [107], which is similar to that of high strength concrete or plain UHPC.

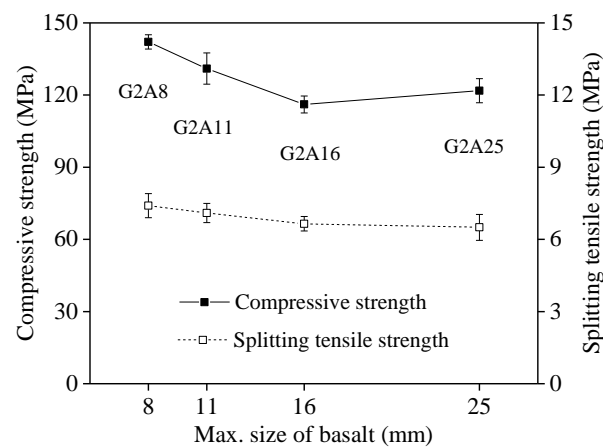


Figure 4.17: Strength of TS-UHPC with different aggregate sizes at the age of 28 days.

Figure 4.18 shows the strength development of TS-UHPC with different types of grouts at the maximum basalt size of 16 mm. The strength development of TS-UHPC follows the similar trend as that of ultra-high performance grout, namely smaller early strengths before 7 days, and surpassed at later strengths, with higher fine sand contents. The development rates of compressive and splitting tensile strength are not synchronized. TS-UHPC with more fine sand develops a faster splitting tensile strength, which indicates that splitting tensile strength is more positively sensitive to fine aggregates. The increase rate of tensile strength is approximately 33% from 6.6 MPa (G1A16) to 8.8 MPa (G3A16) at 91 days, while 19% for compressive strength from 127.6 MPa to 151.8 MPa.

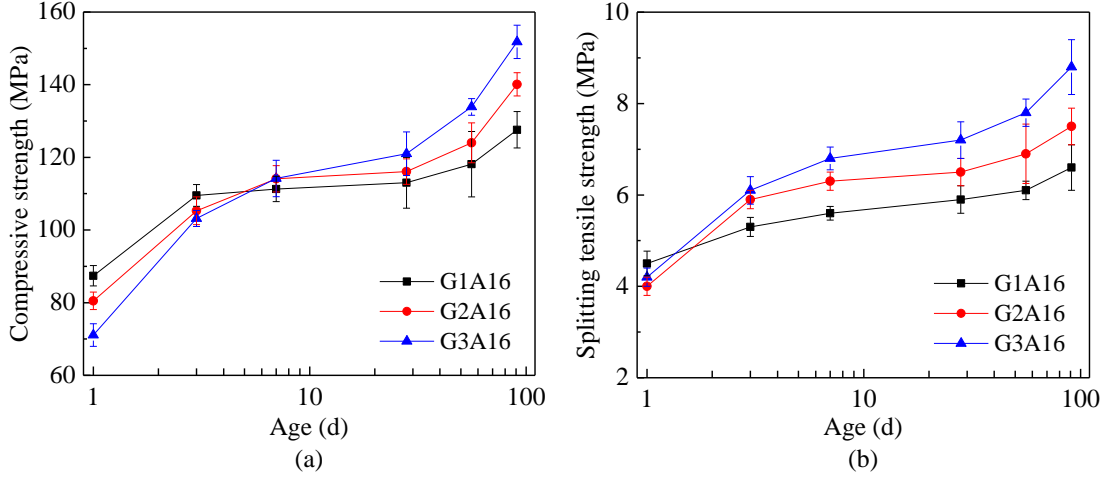


Figure 4.18: Strength of TS-UHPC with different grouts.

For certain engineering applications, both compressive strength and tensile strength are of interest, such as the design of highway and airfield slabs, and cracking resistant component. Normally, a TSC possessing a higher compressive strength has a larger splitting tensile strength. Several empirical equations have been established to present the correlation between the compressive strength ($\sigma_{c_concrete}$) and splitting tensile strength ($\sigma_{t_concrete}$) of conventional TSC, such as Abdelgader and Ben-Zeitun [197], Rajabi and Omid-Moaf. [173], respectively, as,

$$\sigma_{t_concrete} = 0.768 \cdot \sigma_{c_concrete}^{0.441} \quad (4.10)$$

$$\sigma_{t_concrete} = 0.638 \cdot \sigma_{c_concrete}^{0.460} \quad (4.11)$$

Successful applications of those empirical equations have been confirmed by properties of conventional TSC with relatively low strength. The empirical formulas usually follow the type of $\sigma_{t_concrete} = k \cdot \sigma_{c_concrete}^n$, where k and n are coefficients. Values of n for normal concrete have been suggested below 0.75 by e.g. American Concrete Institute and Euro Code, which indicates that $\sigma_{t_concrete}$ -to- $\sigma_{c_concrete}$ ratio decreases with an increase in $\sigma_{c_concrete}$ [198]. However, those empirical predicting models are not appropriate for the TS-UHPC developed in this study, as shown in Figure 4.19. Hence, a new model following the same format is proposed to describe the correlation between compressive strength and splitting tensile strength of TS-UHPC, yielding

$$\sigma_{t_concrete} = 0.029 \cdot \sigma_{c_concrete}^{1.129} \quad (R^2 = 0.81) \quad (4.12)$$

Figure 4.19 shows a successful prediction on relationship between compressive and splitting tensile strength of TS-UHPC, where the R^2 value is 0.81. It can be seen that the experimental results of the designed TS-UHPC are usually above the empirical curves of Eqs. (4.10) - (4.11), especially when the compressive strength surpasses 120 MPa. The coefficient n is 1.129 (slightly larger than 1), which means that $\sigma_{t_concrete-t0}-\sigma_{c_concrete}$ ratio slightly increases with an increase in $\sigma_{c_concrete}$. It is concluded that the designed TS-UHPC has a higher $\sigma_{t_concrete-t0}-\sigma_{c_concrete}$ ratio compared to the conventional TSC, indicating a wider engineering application potential thanks to the higher splitting tensile strength. The relatively higher $\sigma_{t_concrete-t0}-\sigma_{c_concrete}$ ratio of TS-UHPC is probably attributed to the less shrinkage-induced micro-cracks due to very low binder utilization, and the high intrinsic strength of basalt that provides an aggregate bridging effect on tensile strength [199].

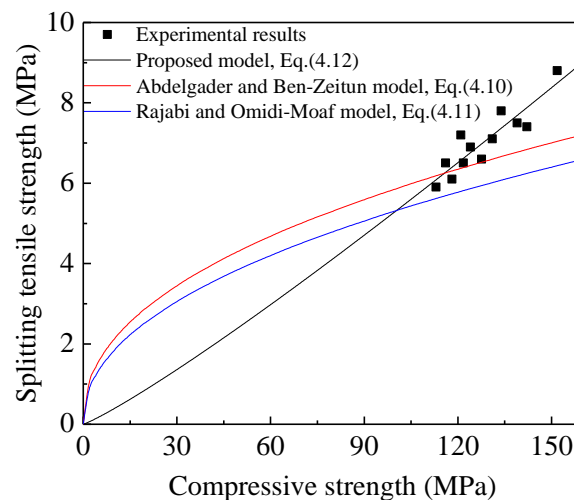


Figure 4.19: Compressive versus splitting tensile strength of TS-UHPC.

As can be seen in Table 4.7, the designed TS-UHPC has low binder consumption, ranging between 364 kg/m^3 and 667 kg/m^3 , which is significantly lower compared to conventional UHPC mixtures (usually more than 900 kg/m^3) [5]. To further analyse the advantage of binder consumption and economic benefit of designed TS-UHPC, the binder efficiency X is applied as in Eq. (3.7). In this study the binder efficiency after 91 days is also calculated. m_{binder} is the total mass of binders (kg/m^3), namely cement and micro-silica in this study. Figure 4.20 shows the binder efficiencies of designed TS-UHPC compared to other reported UHPC [10,156,186,200–202] and TSC [101] under similar curing condition. It indicates that the designed TS-UHPC has a comparable compressive strength compared to other conventional UHPC in literatures, but very low binder amount (as low as 364 kg/m^3) and high binder efficiency (as high as 0.417). The designed TS-UHPC shows similar low or even lower binder consumption compared to normal TSC, approximately $350 - 700 \text{ kg/m}^3$, which can be attributed to the high volume coarse aggregates utilization. However, the designed TS-UHPC can greatly overcome the relatively low strength of ordinary TSC (usually less than 70 MPa), and results in a much higher binder efficiency. The high binder efficiency of the designed TS-UHPC is attributed to very low water amount, pozzolanic addition and high-strength basalt aggregates. In overall, TS-UHPC is successfully developed combined with the advantages of both TSC and UHPC, namely very low binder amount, high binder efficiency, high volume of coarse aggregate, and ultra-high strength.

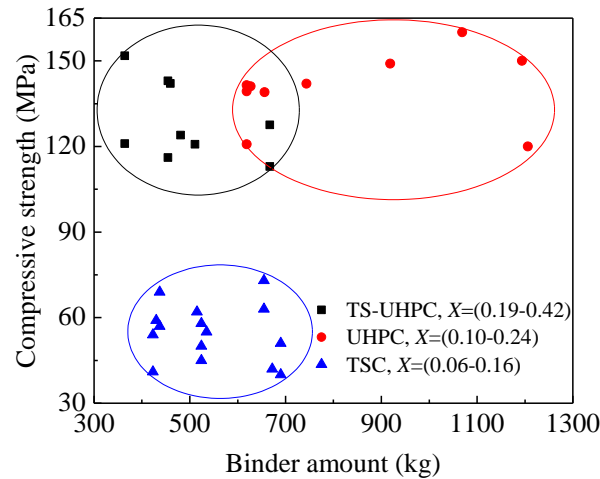


Figure 4.20: Binder efficiency of the designed TS-UHPC.

- **Compatibility between grout and aggregate**

The mechanical properties of the developed concrete are determined by the inherent property of the three phases: aggregates, grout and interfacial transition zone (ITZ). Normally, the ITZ is regarded as the weakest part of matrix and has a great influence on the mechanical and transport properties [139,203]. The ITZ is originally induced by water films around the aggregates and normally characterized by a higher porosity and larger pores compared to the paste, massive portlandite crystals precipitation, higher amount of porous ettringite and low-density C-S-H [139,203,204]. The ITZ of the designed TS-UHPC can be observed by SEM images, as shown in Figure 4.21. Obviously, all the three ultra-high performance grouts can contribute to a very tight ITZ with coarse basalt aggregates, compared to the ITZ in normal TSC [174]. The very dense ITZ is probably due to the very low water-to-binder ratios and excellent workability of the designed ultra-high performance grouts, which contribute to low porosities for both hardened ITZ and paste.

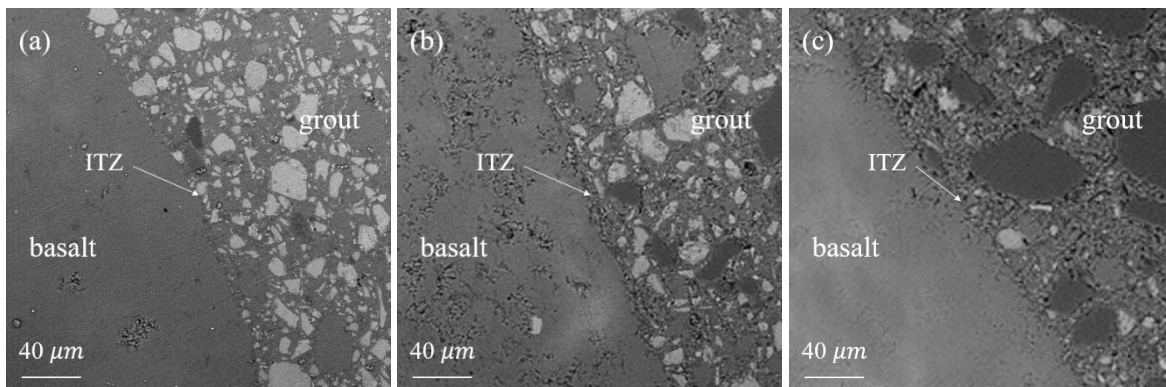


Figure 4.21: SEM images of TS-UHPC, (a) G1A16, (b) G2A16, (c) G3A16.

Besides the SEM observation, some quantitative methods are also used to directly analyse the ITZ, e.g. the statistical nano-indentation technique. However, they are usually complex and rely on expensive testing device [205,206]. In this study, a simple quantitative method, the water permeable porosity method, is utilized to further describe and analyse the ITZ. If the water permeable porosity of basalt aggregate is regarded as zero, the part of water permeable porosities in TS-UHPC caused by the ITZ can be deduced as,

$$\varphi_{ITZ-induced} = \varphi_{concrete} - \varphi_{grout} \times r_{grout} \quad (4.13)$$

where $\varphi_{ITZ-induced}$ is the ITZ-induced water permeable porosity; $\varphi_{concrete}$ and φ_{grout} are the water permeable porosities of TS-UHPC and grout, respectively; r_{grout} is the volume fraction of grout in TS-UHPC. The $\varphi_{ITZ-induced}$, $\varphi_{concrete}$ and φ_{grout} at 91 days are shown in Figure 4.23, respectively. Both grout and TS-UHPC have a diminished water permeable porosities with the increasing content of fine sand, from 16.06% to 8.47% and 8.00% to 4.98%, respectively, which are in line with the trends to wet packing densities and mechanical strengths. The water permeable porosities of TS-UHPC can be greatly improved in comparison with the corresponding grouts, due to the high content of aggregate utilization. However, the ITZ-induced water permeable porosities have a converse trend, increasing from G1A16 of 0.91% to G3A16 of 1.25%. The ITZ-induced porosity in the designed TS-UHPC (0.91% - 1.25%) is much smaller compared to the normal concrete (1.7% - 2.8%) with a comparable aggregate volume content (55%) [203], which demonstrates that the quality of the ITZ is very good. The relatively low ITZ-induced water permeable porosities are attributed to the designed ultra-high performance grouts with superior fluidity to avoid entraining air void, relatively low water amount to reduce the water films around aggregates, addition of extra pozzolanic material (5% of micro silica in this paper) in the grouts to enhance the C-S-H generation.

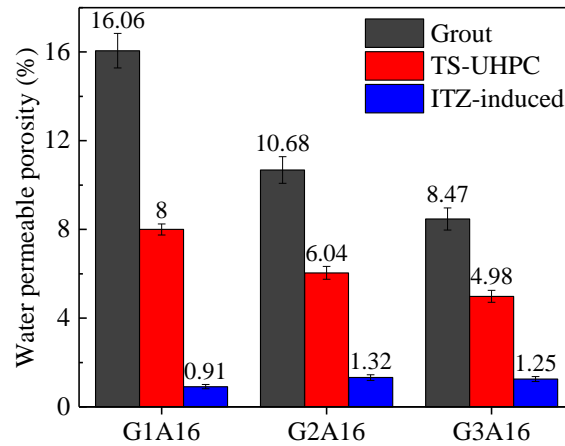


Figure 4.23: Water-permeable porosity of grout, TS-UHPC and ITZ-induced.

To further analyse the influence of the ITZ-induced porosity (0.91% - 1.32%) on mechanical properties of the designed TS-UHPC, the correlations between water-permeable porosity and compressive strength are compared with the existing results from literature [136], as shown in Figure 4.24. It can be found that the compressive strength of TS-UHPC has almost a linear decrease with the increase of water-permeable porosity. Compared to the correlation in conventional UHPC, the designed TS-UHPC has a lower water-permeable porosity owing to the high volume of coarse aggregate utilization. Furthermore, all the experimental results in this study are above the trend line of conventional UHPC, which means the water-permeable porosity has relatively lower negative effect on compressive strength of TS-UHPC compared to that of conventional UHPC. It also indicates the additional porosity caused by the ITZ has rather limited negative effect on mechanical properties of TS-UHPC. Those phenomena are probably due to the high intrinsic strength or bonding ability of the basalt aggregates.

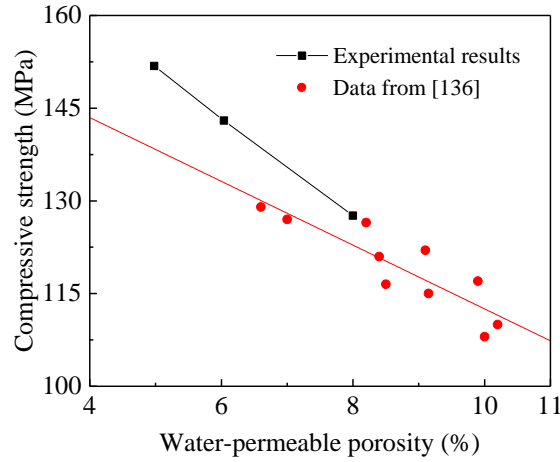


Figure 4.24: Correlation between water-permeable porosity and compressive strength.

For a practical engineering application, it is wise to propose a model to predict the strength of TS-UHPC by a simple and reliable formula. Except for ITZ, the aggregates and grout are the other critical phases in concrete. Hence, the strength of aggregates and grout should be compatible and match with each other. The compressive strength of TS-UHPC can continuously increase when increasing the strength of grouts, which indicates that the limit of inherent strength of basalt aggregates is not reached in this study, with the maximum strength of grout at around 180 MPa. Some researchers reported that the strength of basalt is usually more than 200 MPa [161,207]. Hence, we can conclude that basalt aggregate is a good choice to produce TS-UHPC, which can match the strength of ultra-high performance grout. It has to be noted that the strength of TS-UHPC is always lower than the corresponding grout, due to the weakness of ITZ and the strength concentration by point-to-point contacts between aggregates [170].

The strengths of both grout (σ_{c_grout} , MPa) and TSC ($\sigma_{c_concrete}$, MPa) depend on similar key factors, including quality of mixing, binder amount, water content and fluidity [169], as well as fine sand addition and SP dosage. This dependence has been investigated by Abdelgader [169] as,

$$\sigma_{c_concrete} = 6.70 + 0.42 \cdot \sigma_{c_grout}^{1.07} \quad (4.14)$$

The empirical relationship offers a potential method to estimate TSC strength by primary grout strength. However, this empirical equation underestimates the compressive strength of the designed TS-UHPC, which is due to the utilized UHPC grouts and high-strength of basalt aggregates. Because the volumes of used grouts are in a very narrow range, around 45%, the compressive strength is mostly determined by the strength of grouts and the particle size of coarse aggregates. A new formula is proposed by considering both the effects of the used ultra-high performance cement grouts and the maximum coarse aggregates size (D_{max} , mm), applying the regression analysis of the present results to predict the compressive strength of TS-UHPC as,

$$\sigma_{c_concrete} = (5.8 - 0.05D_{max}) \cdot \sigma_{c_grout}^{0.64} \quad (R^2 = 0.85) \quad (4.15)$$

It can be seen from Eq. (4.15) that the compressive strength of TS-UHPC is mainly dependent on the compressive strength of used grout, while the particle size (ranging from

5 mm to 25 mm) also has slightly adverse influence. As shown in Figure 4.25, the experimental results fit to the predicting results very well, confirming the validity of the proposed model. Therefore, this model can be effectively applied to choose the proper grout and aggregates to design TS-UHPC with a desired strength class. Nevertheless, further studies are needed to take different aggregate types into consideration.

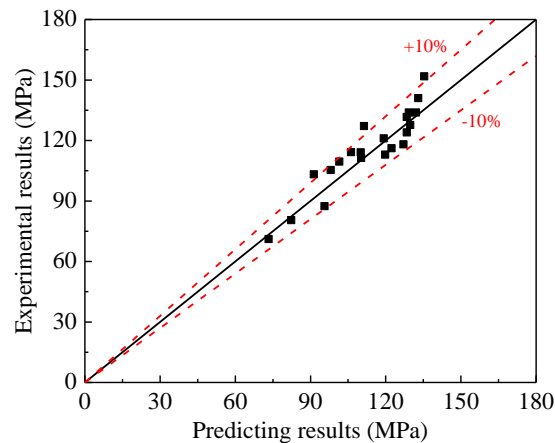


Figure 4.25: Validation of predicting model.

4.3.4 Summary

- TS-UHPC is a pioneering material concept with very low binder amount (down to 364 kg/m^3), a high volume of coarse aggregates and a high binder efficiency, according to two-stage (preplaced aggregate) method and high performance grout, with a compressive strength up to 151.8 MPa at the age of 91 days.
- When increasing the fine sand-to-powder ratio from 0 to 1.0, the grout tends to acquire a higher binder hydration degree, denser pore structure and compactness, increased later age strength and binder efficiency, and comparable fluidity.
- Coarser basalt aggregate tends to slightly lower the compressive and splitting tensile strength, around 14.3% and 12.2% reduction with the maximum size from 8 mm to 25 mm, respectively. Basalt aggregates with maximum size of 25 mm are suggested in TS-UHPC, due to the easier and faster grout injection during casting process, even though it needs a slightly higher binder content and has a lower strength.
- The compatibility between grout and aggregate is analysed based on ITZ and correlation between the strength of grout and TS-UHPC. The designed TS-UHPC has an excellent ITZ quality, with low ITZ-induced porosity around 0.91% - 1.32% compared to 1.7% - 2.8% in normal concrete.
- New formulas are proposed to describe the relationship between the compressive and splitting tensile strength of TS-UHPC designed by ultra-high performance grouts and basalt aggregates, and to predict the compressive strength of TS-UHPC by the applied grout's strength and aggregates' size. The compressive of TS-UHPC is mainly determined by the used grout, while the aggregate size also has slightly adverse influence.

4.4 Conclusions

This chapter attempts to introduce the coarse aggregate into UHPC system, in order to reduce the powder content and cost, improve the volume stability and penetration impact resistance, etc. Two methods are developed, i.e. utilizing coarse aggregate by normal mixing and proposing two-stage UHPC with high-volume coarse aggregate. The following conclusions can be drawn:

- Coarse basalt aggregates are successfully introduced in UHPC systems by applying the modified Andreasen and Andersen model with the normal mixing method. The utilization volume of coarse basalt aggregates is up to 35% with a reduced powder content.
- With the increase of particle size of basalt aggregates, the mechanical strengths tend to decrease. And the maximum decrease degrees of compressive and tensile strengths are very limited, namely 8.3% and 16.3%, respectively.
- The optimal powder content of UHPC in this study is about 800 kg/m^3 and 700 kg/m^3 with the maximum basalt aggregate of 8 mm and 16 mm, respectively. In addition, a distribution modulus q of 0.19 is recommended for the modified Andreasen and Andersen model.
- The new concept of TS-UHPC with coarse basalt volume around 55% has a low binder amount (e.g. 364 kg/m^3) and high binder efficiency (e.g. $0.417 \text{ MPa}\cdot\text{m}^3/\text{kg}$), possessing excellent compressive strength of up to 151.8 MPa at 91 days.
- New formulas are proposed to describe correlation between compressive and splitting tensile strength of TS-UHPC, and to predict strength of TS-UHPC by grout strength.

Chapter 5

Application of steel fibres in UHPC

This chapter investigates the effect of steel fibres on the properties of ultra-high performance fibre reinforced concrete (UHPFRC) in the presence of coarse aggregates. UHPFRC matrices with a low cement content and maximum aggregate sizes of 8 mm and 25 mm are designed by making use of a particle packing model. Three types of steel fibres (13 mm short straight, 30 mm medium hook-ended and 60 mm long 5D) are studied in terms of the utilization efficiencies. The results show that UHPFRC with coarser aggregates tends to have a lower cement consumption but slightly weaker mechanical strength, and the largest aggregate size is suggested to be 25 mm considering the reduction on mechanical strength and flexural toughness. The medium and long fibres contribute to an excellent deflection/strain hardening behaviour instead of short ones. A preferential synergistic effect on flexural properties is observed between the medium fibres and the finer aggregates, while the longer fibres are more compatible to the coarser aggregates. The length of steel fibre is recommended between 2 and 5 times the maximum aggregate size.

This chapter is partially published elsewhere:

P.P. Li, Y.Y.Y. Cao, M.J.C. Sluijsmans, H.J.H. Brouwers, Qingliang Yu. Synergistic effect of steel fibres and coarse aggregates on impact properties of ultra-high performance fibre reinforced concrete. Submitted.

5.1 Introduction

Ultra-high performance fibre reinforced concrete (UHPFRC) possesses superior properties [6,9–11,208] due to its special mix design methods and utilized raw ingredients, usually incorporating high steel fibre content and large amount of cement [1,28]. Chapter 4 has demonstrated that high-strength coarse aggregates, e.g. basalt aggregates, can be successfully introduced into a UHPC system, which greatly reduce the cement amount and cost [10,125]. Furthermore, concrete incorporating coarse aggregates can also enhance volume stability [209], improve projectile impact resistance [161], achieve better workability, sometimes even a higher strength [159,160], and increase the transition point of stress-strain curves under confined conditions [210]. In this study, coarse aggregates with the maximum size (D_{max}) from 8 mm to 25 mm are utilized to investigate the influence of steel fibres on the mechanical properties of UHPFRC.

Steel fibres are considerably efficient to improve the mechanical properties of UHPFRC, especially for enhancing the stress transfer capability beyond elastic state and then strengthening the toughness and energy absorption capacity [7,211]. Nevertheless, high strength steel fibres are much more expensive compared to the other solid ingredients in UHPFRC. Furthermore, the reinforcement degree is significantly influenced by fibre characteristics, such as fibre content [20,21], shape [22,23], orientation [24,25] and hybridization [26]. Therefore, the appropriate type and content of steel fibre should be carefully researched to achieve an optimal utilization efficiency. As previously reported [7,212,213], two methods are well-known to enhance the flexural properties and energy absorption ability, namely utilizing hook-ended or twisted steel fibres, and enlarging the length of steel fibres. However, relevant research in UHPFRC also incorporating coarse aggregates are very scarce.

The reinforcement of steel fibres is dependent on not only the fibre characteristics but also matrix properties (e.g. particle size, strength, shrinkage) and fibre-to-matrix bond. The presence of coarse aggregates in concrete has considerable effects on fibre distribution, dispersion and interfacial bonds, consequently influencing the fibre utilization efficiency [214]. Coarser aggregates tend to need longer steel fibres to overlay and provide enough bridging effect between them [215]. But, too long fibres conversely cause mixing and casting problems, as well as disturbance in compactness of the granular skeleton [186]. However, how to use appropriate fibres to outbalance those benefits and drawbacks is very important but still not clear, especially for the UHPFRC incorporating coarse aggregates. It is therefore very important to research the synergistic effect between steel fibres and coarse aggregates in UHPFRC systems for making full use of their potential.

The objective of this chapter is to explore the synergistic effect between steel fibres and coarse aggregates on the mechanical properties of UHPFRC. The effect of the D_{max} from 8 mm to 25 mm, steel fibre type (short straight, medium hook-ended and long 5D), and interaction between coarse aggregates and steel fibres are analysed. Based on the results of strengths and flexural behaviour, appropriate sizes of coarse aggregates and corresponding suitable lengths of steel fibres are suggested.

5.2 Materials and experiments

5.2.1 Materials

The ingredients of UHPFRC mixtures include Portland cement (PC), limestone powder (LP), micro-silica (mS), normal sand (S), coarse basalt aggregates (BA) with different sizes, steel fibres with different types (SF), superplasticizer (SP3 from Chapter 2 is used) and tap water (W). The physical and chemical properties of powders can be found in Sections 3.2.1, 3.3.1 and 4.2.1. Figure 5.1 shows the utilized six coarse basalt aggregates with different particle size fractions. Three different steel fibres are used, namely 13 mm (short) straight fibre, 30 mm (medium) hook-ended fibre and 60 mm (long) 5D fibre. Table 5.1 and Figure 5.2 present the characteristics and shapes of steel fibres.



Figure 5.1: The basalt aggregates.

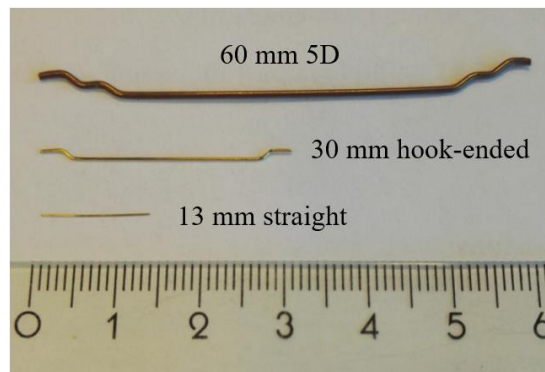


Figure 5.2: The steel fibres.

Table 5.1: Characteristics of steel fibres.

Length, L (mm)	Fibre shape	Diameter, d_f (mm)	Aspect ratio, L/d_f	Density (kg/m^3)	Tensile strength (MPa)	Elastic modulus (GPa)	Number of fibres per kg
13	Short straight	0.21	62	7850	2750	200	27000
30	Medium hook- ended	0.38	79	7850	2300	210	3600
60	Long 5D	0.9	65	7850	2300	210	2300

5.2.2 Mix design

Table 5.2 presents the recipes of UHPFRC matrices, Table 5.3 shows the research variables including basalt aggregate sizes and steel fibres type used in UHPFRC. The limestone powder and micro-silica contents are 20% and 5% of total powders' mass, following our previous study in Chapter 4. 900 kg/m^3 powder are used in the mixtures incorporating the maximum basalt size of 8 mm. While, the powder content is reduced to 700 kg/m^3 for UHPFRC with coarser basalt aggregates (maximum size of 25 mm), considering the fact that coarse aggregates contribute to less powders in concrete [125,209,216]. The contents of aggregates are calculated based on the particle packing model, as described in Section 4.2.2. The key parameter in this model is the distribution modulus q , and a small q value of 0.19 is proposed and utilized for UHPFRC mixtures with inclusion of coarse aggregates and low

powder contents, based on Chapter 4. The PSD curves of the designed and target UHPFRC matrices are shown in Figure 5.3. The water and superplasticizer amounts are adjusted to achieve self-compacting. The dosages of different steel fibres are fixed at 2 vol.%.

Table 5.2: Recipes of designed UHPFRC matrixes (kg/m³).

Mix No.	PC	mS	LP	S 0-2	BA 1-3	BA 2-5	BA 5-8	BA 8-11	BA 8-16	BA 16-25	W	SP
A8F0	675	45	180	640	198	403	194	0	0	0	174.2	5.8
A25F0	525	35	140	667	0	367	173	121	64	365	154.7	4.9

Table 5.3: Research variables for UHPFRC.

Mix No.	Short straight fibre (13 mm)	Medium hook ended fibre (30 mm)	Long 5D fibre (60 mm)	Max. size of aggregate, D (mm)	L/D_{max}
A8F0					0
A8F13	2 vol.%			8	1.625
A8F30		2 vol.%			3.75
A8F60			2 vol.%		7.5
A25F0					0
A25F13	2 vol.%			25	0.52
A25F30		2 vol.%			1.2
A25F60			2 vol.%		2.4

Note: the values in Mix No. respectively represent the maximum size of aggregate and the length of steel fibre used in the designed UHPFRC, and 0 means plain UHPFRC without steel fibre.

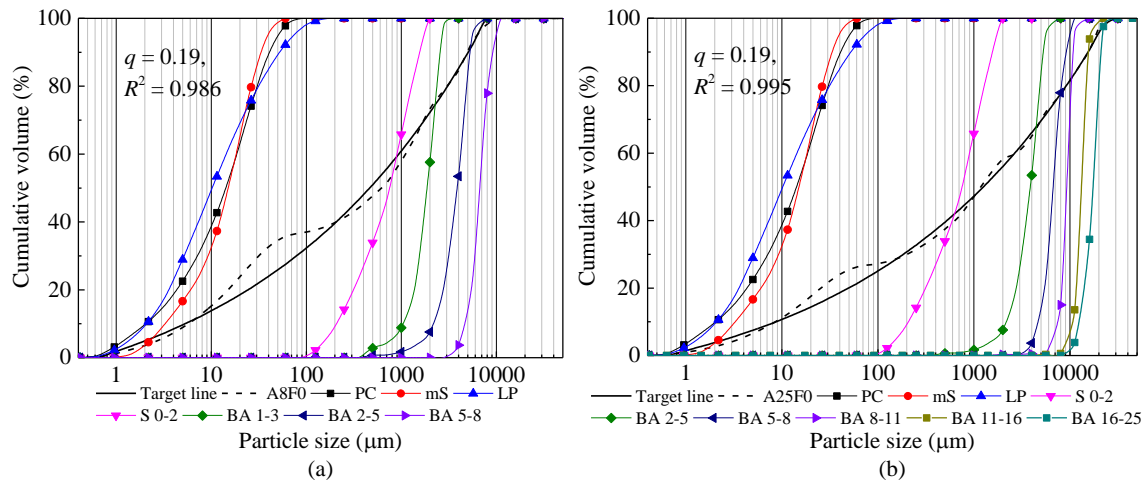


Figure 5.3: The PSDs of ingredients and UHPFRC matrixes.

5.2.3 Testing methods

- **Compressive and tensile splitting test**

The tensile splitting and compressive strengths of concrete samples are tested, in accordance with EN 12390-6: 2009 [187] and EN 12390-3: 2009 [107], respectively. Fresh concrete is cast into moulds (150 × 150 × 150 mm³) and demoulded after 1 day. After that, the samples

are cured in water (around 20 °C) for another 27 days before testing. The hardboard packing strips in EN 12390-6: 2009 cannot withstand UHPFRC and are replaced by steel ones. The specimens and set-ups are shown in Figure 5.4.



Figure 5.4: Specimens and set-ups of (a) compressive and (b) tensile splitting tests.

- **Central point flexural test**

The central point flexural tests are conducted for UHPFRC beams ($150 \times 150 \times 550 \text{ mm}^3$) with the span (l) of 450 mm, in accordance with EN 12390-5: 2009 [217], as shown in Figure 5.5(a). Based on the central point flexural tests, the load-deflection curves and corresponding key parameters can be obtained, as illustrated in Figure 5.5(b), such as first crack load and deflection, peak load and deflection, and toughness, as well as three stages (elastic stage, deflection/strain hardening stage, deflection/strain softening stage).

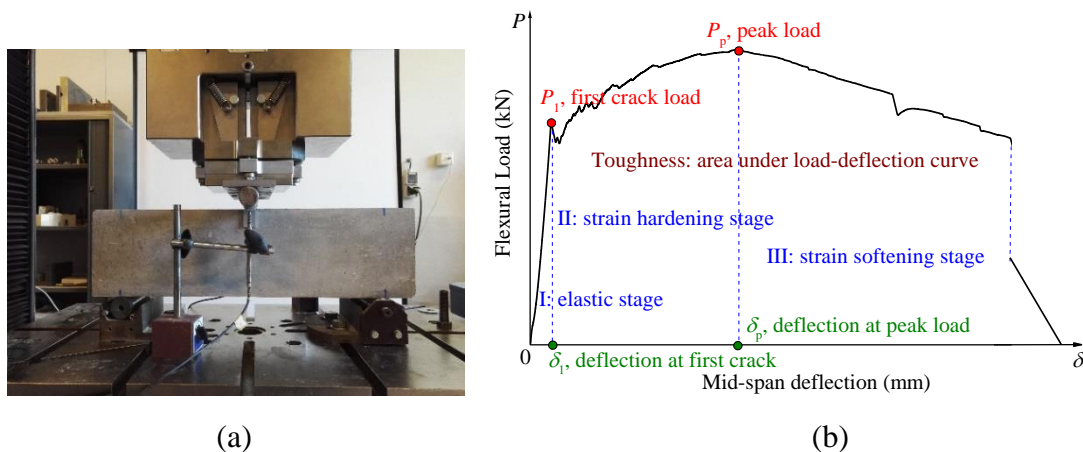


Figure 5.5: (a) flexural test device and (b) key parameters.

5.3 Results and discussion

5.3.1 Compressive and tensile splitting strengths

Figure 5.6 presents the compressive strength of the designed UHPFRC after 28 days. With increasing the maximum size of coarse aggregate from 8 mm to 25 mm, the compressive strength of the plain concrete reduces from 137.2 MPa to 124.3 MPa. Although the compressive strength has a decrease trend because of the coarse aggregates, the decrease degree is less than 10%, which is in line with results in Chapter 4. In addition, the UHPFRC matrix with coarser basalt aggregates tends to have a lower powder demand with even a better quality of fit, namely, powder content of 700 kg/m^3 and a R^2 of 0.995 for the mixture

A25F0, compared to 900 kg/m³ and 0.986 for the mixture A8F0. Furthermore, the binder efficiency, defined as 28 days compressive strength normalized by binder amount, can be greatly improved from 0.152 MPa/(kg/m³) at the mixture A8F0 up to 0.178 MPa/(kg/m³) at the mixture A25F0. With the inclusion of 2 vol.% steel fibres in the matrix ($D_{max} = 8$ mm), the compressive strength can be enhanced in the range between 10.4% to 15.7%. The 30 mm medium hook-ended steel fibres show the best reinforcement, possessing slightly larger compressive strength than the 13 mm short straight fibres, followed by the 60 mm long 5D fibres. The reinforcement ratio in UHPFRC with coarser aggregates ($D_{max} = 25$ mm) ranges between 6.2% and 22.5%. Smaller steel fibres tend to contribute to a higher compressive strength, probably due to their more homogenous distribution inside the concrete matrix.

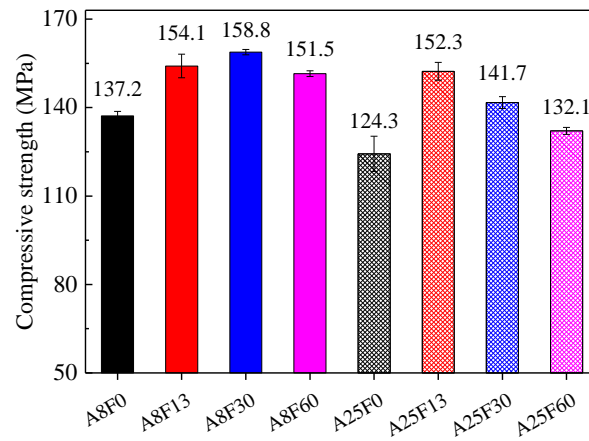


Figure 5.6: Compressive strength of mixes in Table 5.3.

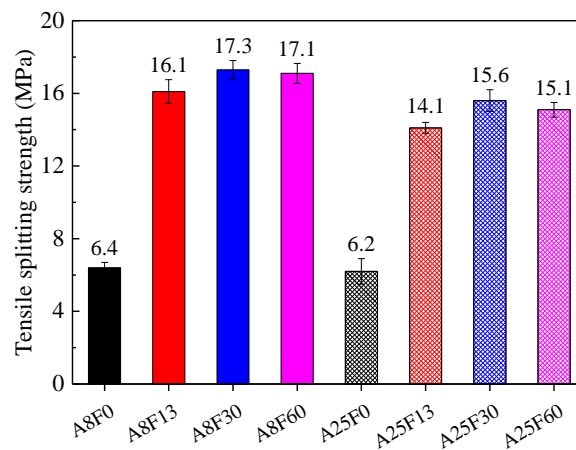


Figure 5.7: Tensile splitting strength of mixes in Table 5.3.

Figure 5.7 shows the tensile strength of the designed UHPFRC after 28 days. The coarse aggregates have a limited negative effect on the tensile strength, from 6.4 MPa to 6.2 MPa, which is similar to that of the compressive strength. After incorporating 2 vol.% steel fibres, the tensile strength is improved considerably, with increase ratios between 127% and 170%, due to the bridging effect of steel fibres. However, the effects of reinforcement on tensile strength between different fibre types are not very obvious in the same UHPFRC matrix. The 30 mm medium hook-ended steel fibres show the best reinforcement, followed by the 60 mm long 5D fibres and the 13 mm short straight ones.

5.3.2 Flexural behaviour

- **Load-deflection curves**

The flexural behaviour of UHPFRC is illustrated by the load-deflection curves or stress-normalized deflection curves in Figure 5.8. As illustrated in Figure 5.5(b), all the load-deflection curves experience three stages, namely elastic stage from zero point to the first crack point, deflection or strain hardening stage from the first crack point to the peak point, deflection or strain softening stage after peak point. The main key parameters in flexural tests are summarized in Table 5.4. The slopes (respecting elastic modulus), loads and deflections at the first cracks in the curves without or with different types of steel fibres are very similar, which indicates that the elastic stages are mainly dependent on the UHPFRC matrix instead of the steel fibres. With the inclusion of 2 vol.% steel fibres, all the UHPFRC beams exhibit strain hardening behaviours, although it is not obvious in the case of 13 mm short straight fibres. The peak deflection can be greatly enlarged from about 0.244 mm (A8F0) up to 2.246 mm (A8F60), therefore the ductility of UHPFRC is greatly improved. All the curves of the designed UHPFRC mixtures have long tails during the strain softening stages, revealing the high residual strength and energy absorption ability of the designed UHPFRC.

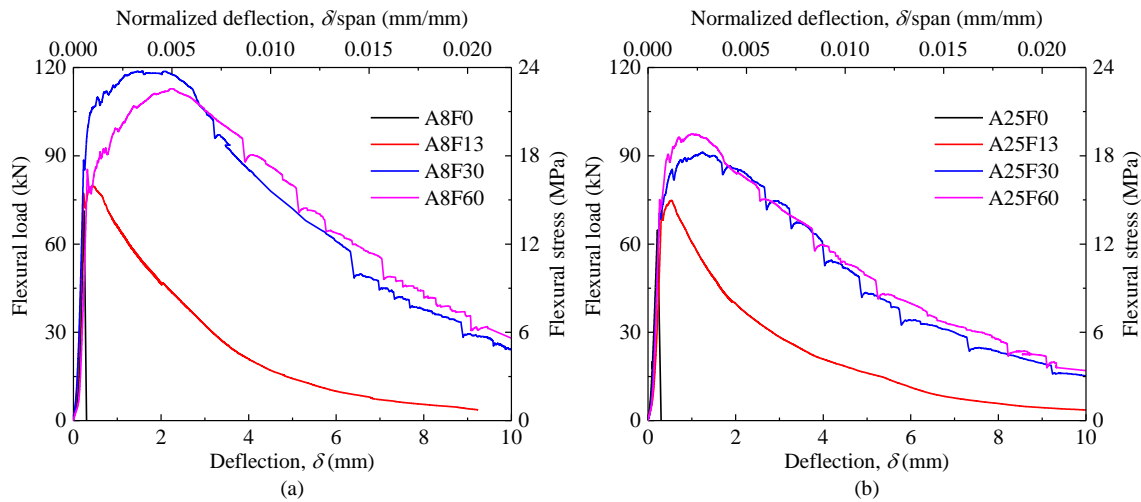


Figure 5.8: Flexural load vs. deflection curves.

Table 5.4: Key parameters of UHPFRC (shown in Table 5.3) in flexural test.

Mix No.	First crack load, P_1 (kN)	First crack stress, σ_1 (MPa)	Peak Load, P_p (kN)	Peak stress, σ_p (MPa)	Toughness, T_f (J)
A8F0	71.2	14.2	71.2	14.2	8.3
A8F13	77.3	15.5	79.6	15.9	235.4
A8F30	88.6	17.7	118.8	23.8	716.1
A8F60	85.4	17.1	112.8	22.6	718.1
A25F0	64.8	13.0	64.8	13.0	7.2
A25F13	70.5	14.1	74.8	15.0	219.3
A25F30	71.3	14.3	91.2	18.2	489.4
A25F60	75.1	15.0	97.4	19.5	516.1

- **Coarse aggregate effect**

When coarse aggregates are introduced into UHPFRC systems, the interfaces around the coarse aggregates could become the weakest part and be the inherent flaws [218]. Therefore, the effect of coarse aggregates on flexural properties should be very carefully evaluated. As mentioned above, in this study, the coarse basalt aggregates bring economic benefit by decreasing the powder content and increasing the binder efficiency, without significantly sacrificing the compressive and tensile strength. Figure 5.9 presents the size effect of coarse basalt on the flexural strength and toughness of UHPFRC beams. The decrease ratios of flexural strength are 8.5%, 5.7%, 23.5% and 13.7%, respectively, when increasing the D_{max} from 8 mm to 25 mm. Considering the benefits brought by coarse aggregates, the negative effect of coarse aggregates is tolerable. While, the decrease ratios of flexural toughness are 13.3%, 6.8%, 31.7% and 28.1%, respectively. It indicates that the negative effect of coarse aggregates size on toughness is more sensitive than the strength, which is probably attributed to a faster damage development and lower residual flexural strength for an UHPFRC beam with coarser aggregates. It should be noted that the decrease caused by coarse aggregates on both flexural strength and toughness are simultaneously influenced by the types of steel fibres, which will be discussed in the following sections.

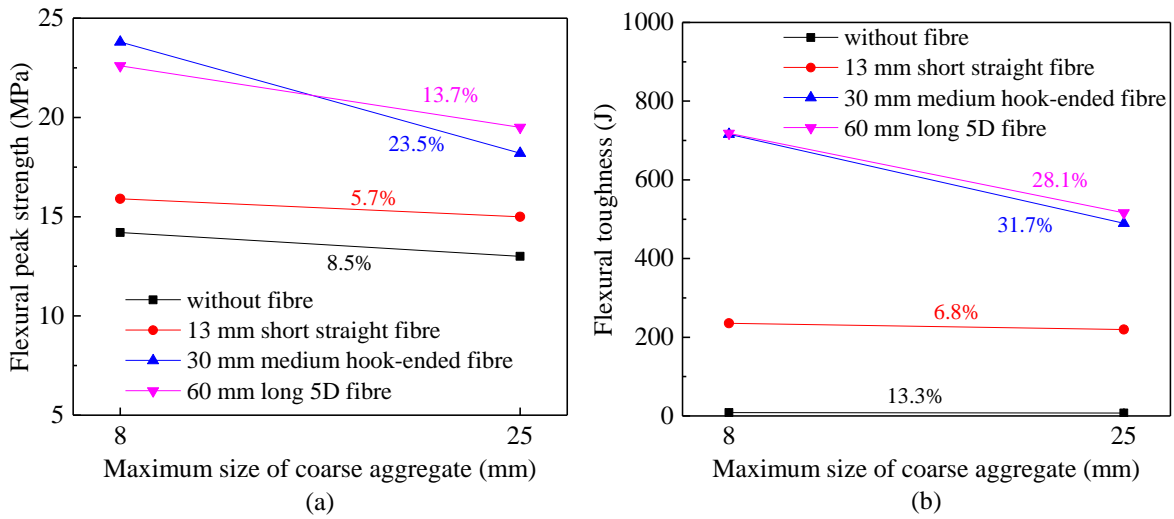


Figure 5.9: Aggregate size effect on flexural (a) strength and (b) toughness.

- **Steel fibre effect**

As mentioned above, the type of steel fibre is another key factor on flexural behaviour of UHPFRC beam. In this section, the effects of three different steel fibres are discussed with a fixed dosage of 2 vol.%. Normally, the reinforcement of steel fibres is dependent on the geometric and mechanical characters, utilized dosage and fibre-to-matrix bond. To assess the overall effects of the three different steel fibres on flexural properties, a reinforcing factor is introduced,

$$\eta = \frac{X_{UHPFRC}}{X_{matrix}} \quad (5.1)$$

where X_{UHPFRC} and X_{matrix} the key flexural properties of UHPFRC with and without steel fibres, respectively, such as first crack strength (σ_1), peak strength (σ_p), and toughness (T_f).

The reinforcing factors in terms of first crack strength, peak strength and toughness are presented in Table 5.5. The reinforcing factor in terms of first crack strength (η_{σ_1}) changes in a relatively low and narrow range between 1.085 and 1.246, which indicates that the first crack stress is not sensitive to the fibre type effect and is mainly determined by the UHPFRC matrix. The reinforcing factor in terms of peak strength (η_{σ_p}) is always clearly larger than that of first crack strength (η_{σ_1}) for the same UHPFRC matrix, which means that the steel fibres contribute more to the peak strength rather than the first crack strength. The fibre-to-matrix bonding force is triggered up to the maximum value during the strain hardening stage [143], which results in more efficient reinforcement and thus a larger reinforcing factor η_{σ_p} . The reinforcing factor in term of flexural toughness (η_{T_f}) is very considerable, namely dozens of times the flexural strengths. In other words, the flexural toughness or energy absorption ability of UHPFRC beam is mainly provided by the “bridge effect” of steel fibres, instead of the UHPFRC matrix. Compared with the reinforcing factors of different steel fibres, the 13 mm short straight fibres show the poorest reinforcement on both flexural strength and toughness. The 30 mm medium hook-ended fibres provide the best enhancement for UHPFRC with the finer aggregates ($D_{max} = 8$ mm), while the 60 mm long 5D fibres are more suitable than the medium ones for the UHPFRC with the coarser basalt aggregates ($D_{max} = 25$ mm).

Table 5.5: Fibre reinforcing factors for UHPFRC mixtures in Table 5.3.

Mix No.	η_{σ_1}	η_{σ_p}	η_{T_f}
A8F0	1.000	1.000	1.000
A8F13	1.092	1.120	28.36
A8F30	1.246	1.676	86.28
A8F60	1.204	1.592	86.52
A25F0	1.000	1.000	1.000
A25F13	1.085	1.154	30.46
A25F30	1.100	1.400	67.97
A25F60	1.154	1.500	71.68

To further characterize the steel fibre effect on strain hardening behaviour, the strain hardening factor ϕ , defined as a ratio of peak stress σ_p to first crack strength σ_1 [219], is introduced as,

$$\phi = \frac{\sigma_p}{\sigma_1} \quad (5.2)$$

The value of this factor is larger than 1.0 when a strain hardening phenomenon is triggered by the utilized steel fibres, and a larger value means a stronger strain hardening behaviour. The strain hardening factors of UHPFRC beams are shown in Figure 5.10. The strain hardening factors are very close to each other with different UHPFRC matrices incorporating the same type of steel fibres. UHPFRC incorporating the 13 mm short fibres shows a very slight strain hardening behaviour, with a factor ϕ around 1.04. UHPFRC with the 30 mm medium fibres acquires the strongest strain hardening behaviour incorporating the maximum basalt size of 8 mm ($\phi = 1.345$), followed by the 60 mm long 5D fibres ($\phi = 1.322$). On the one hand, the hook or 5D ends of steel fibres can provide an anchoring effect compared to

the straight fibres. On the other hand, longer fibres can enhance the flexural strength and energy absorption capacity by increasing the peak pull-out load and corresponding slip, due to the improvement on effective bonding area of fibres at crack surfaces and fibre orientation [213,220]. When coarser basalt aggregates are introduced, e.g. maximum size of 25 mm, the long steel fibres show a slightly larger strain hardening factor (1.300) than the medium fibre (1.291).

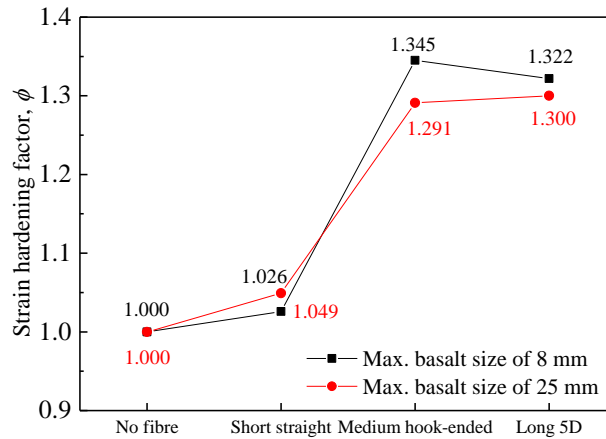


Figure 5.10: Fibre type effect on strain hardening factor.

5.3.3 Synergistic effect between aggregate and fibre

The order of reinforcement on flexural properties is as follows: 30 mm medium hook-ended fibre > 60 mm long 5D fibre > 13 mm short straight fibre for UHPFRC with the D_{max} of 8 mm, while 60 mm long 5D fibre > 30 mm medium hook-ended fibre > 13 mm short straight fibre for UHPFRC with the D_{max} of 25 mm. To reveal the interaction between aggregates and steel fibres, the relative size effect (ratio of fibre length to maximum aggregate size, L/D_{max}) on the fibre utilization factors (η_{σ_1} , η_{σ_p} , η_{T_f} and ϕ) are illustrated in Figure 5.11.

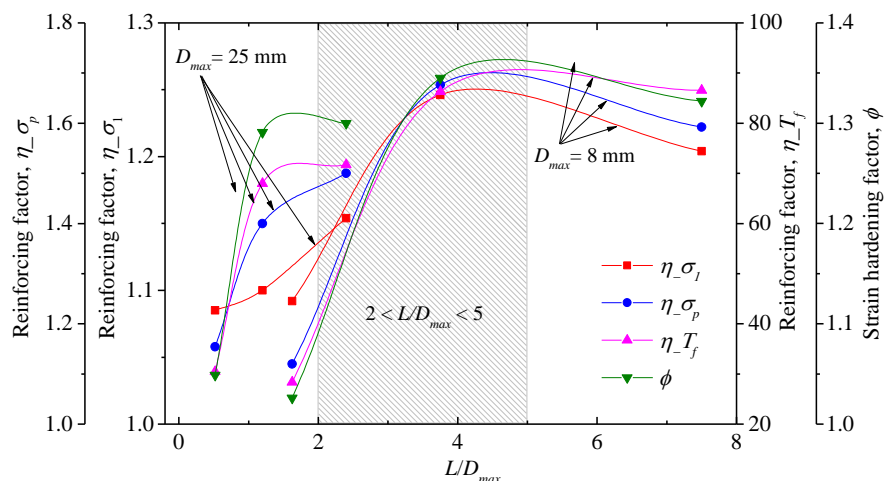


Figure 5.11: Correlation between L/D_{max} and fibre utilization.

The lowest utilization efficiency is obtained with the short steel fibres, which is in line with the results observed in the UHPFRC incorporating coarse aggregates [125]. Firstly, the straight fibres have weaker bond compared to other fibres with anchoring effect at ends. Additionally, the short fibres cannot completely overlay aggregates with a large size, thus

providing a limited fibre-bridging interlock stress. Furthermore, if the size of coarse aggregate is too large compared to the fibre length, the fibre distribution in matrix can be significantly disturbed, as shown in Figure 5.12. The non-random orientation of steel fibres adversely affects the reinforcement efficiency and decreases the compactness.

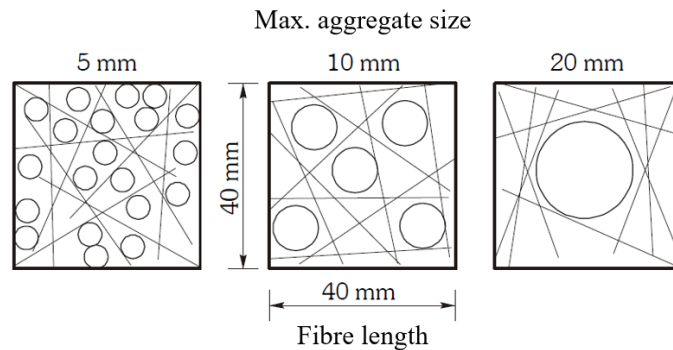


Figure 5.12: Interaction between aggregates and steel fibres on granular skeleton [214].

Preferential synergistic effects are observed between aggregates with the maximum size of 8 mm and 30 mm medium hook-ended fibres (A8F30), aggregates with the maximum size of 25 mm and 60 mm long 5D fibres (A25F60), considering all fibre utilization factors (η_{σ} , η_{σ_p} , η_{T_f} and ϕ) in Figure 5.11. Thus, a longer fibre is not always better, and an appropriate length of steel fibre is needed to match the size of coarse aggregate. On the one hand, longer fibres are beneficial to overlay coarse aggregates, enhance the interlock between fibres and coarse aggregates and then improve the flexural performance [213,218]. On the other hand, limiting the particle size to half the fibre length is recommended from the workability point of view [214], which can also decrease the probability of the ‘fibre balling’ phenomenon. Han et al. indicated that the rational range of the ratio of steel fibre length to coarse aggregate maximum size for steel fibre reinforced concrete is 1.25–3 by considering the reinforcements on splitting tensile strength and flexural properties [215]. Rui et al. summarized that the fibre length is mostly about 2-4 times of the maximum aggregate size in normal concrete, at least not shorter than the aggregate size [221]. Based on the results acquired here, the length of steel fibre (L) is recommended to be between 2 and 5 times the maximum size of aggregate (D_{max}) for UHPFRC systems, as illustrated in Figure 5.11.

5.4 Conclusions

This chapter studies the synergistic effect between steel fibres and aggregates on the mechanical properties of UHPFRC. The aggregate size effect, steel fibre type effect, and their interaction are analysed. The key conclusions can be summarized:

- Coarse basalt aggregates up to 25 mm can be successfully introduced in UHPFRC with a significantly lower cement consumption, designed by using a particle packing model, with limited influence on compressive and tensile splitting strengths. However, the negative influence of larger basalt size is more obvious on flexural toughness. The maximum size of coarse aggregate is suggested to be no more than 25 mm.
- The 13 mm short straight steel fibres show a good reinforcement on compressive strength due to the more homogenous distribution in UHPFRC matrix. While, the 30 mm medium

hook-ended or 60 mm long 5D fibres are more efficient in reinforcing tensile and flexural properties.

- Based on the analysis of fibre reinforcing factors, the flexural toughness is more sensitive to the steel fibres, followed by the flexural peak strength, while the first crack strength is mainly controlled by the UHPFRC matrix.
- The deflection or strain hardening behaviour can be acquired by utilizing 2 vol.% of 30 mm medium hook-ended or 60 mm long 5D steel fibres, while the 13 mm short straight fibres only trigger a very limited strain hardening behaviour.
- A preferential synergistic effect is observed between the coarser aggregates and the longer steel fibres. The length of steel fibre is suggested between 2 and 5 times the maximum size of aggregate. The order of reinforcement on flexural properties is: 30 mm hook-ended fibre > 60 mm 5D fibre > 13 straight fibre for UHPFRC with the D_{max} of 8 mm, while 60 mm 5D fibre > 30 mm hook-ended fibre > 13 straight fibre for UHPFRC with a D_{max} of 25 mm.

Chapter 6

Functionally graded UHPC beams

In this chapter, functionally graded ultra-high performance cementitious composite beams are developed by applying the composite concepts of Ultra-high Performance Concrete (UHPC), Two-stage Concrete (TSC) and Slurry-infiltrated Fibrous Concrete (SIFCON). The functionally graded composite beam (FGCB) is fabricated with a bottom layer of SIFCON and top layer of TSC, and the two layers are synchronously cast by using UHPC slurry. The novel concept of FGCB is proposed towards more economical and high performance structural systems, namely an excellent flexural bearing capacity and impact resistance, low cement consumption and high steel fibre utilization efficiency. The fresh and hardened properties of UHPC slurry, flexural properties of FGCB are measured (the impact resistance will be analysed in following chapter). The results reveal that the designed FGCB has superior flexural properties and energy absorption, without showing any interfacial bond problems. The fibre utilization efficiency of the designed FGCB is very high compared to the traditional UHPFRC and SIFCON beams. The 30 mm medium hook-ended steel fibres show the best utilization efficiency compared to the 13 mm short straight and 60 mm long 5D steel fibres, and 3 vol.% medium fibres are optimum to design FGCB.

This chapter is partially published elsewhere:

P.P. Li, M.J.C. Sluijsmans, H.J.H. Brouwers, Q.L. Yu. Functionally graded ultra-high performance cementitious composite with enhanced properties. *Composites Part B: Engineering*. 183 (2020) 107680.

6.1 Introduction

Concrete is one of the most widely used construction building materials in civil engineering. The brittle behaviour subjected to tensile or flexural loading is an adverse property, which causes negative influences, e.g. abrupt failure without warning, reduced service life due to crack formation and propagation. To overcome this shortcoming, fibre reinforced concrete was proposed by adding discrete steel fibres into the plain concrete matrix [222,223]. In the 1990s, UHPFRC was invented and further extended to the concept of fibre reinforced concrete, which is characterized by high dosages of steel fibres, large amounts of reactive powders without any coarse aggregate, and a very low water content [1,2,28]. Although UHPFRC already possesses excellent microstructure, strength, durability, ductility and impact resistance [10,224,225], its tensile and flexural strengths are still relatively low, especially compared to the compressive performance [6,79,226,227]. In addition, the high content of steel fibres and reactive powders in UHPFRC have adverse impacts, causing economic and environmental problems [27,228]. Thus, how to develop more eco-friendly UHPFRC materials and components is of great interest for both researchers and engineers.

The aggregate-to-powder ratio is a key factor to determine the powder consumption and control the cost of UHPC. Chapter 4 revealed that incorporating an appropriate amount of coarse aggregates with proper sizes can significantly reduce the powder content of UHPC, still possessing a comparable mechanical strength [125]. However, the coarse aggregates usually occupy a limited volume by normal mixing methods, less than 40% of total UHPC matrix. To further enlarge the volume of coarse aggregates and diminish the powder content, we applied the two-stage concrete (TSC) concept in UHPC system, i.e. we first place coarse aggregates in mould and subsequently inject ultra-high performance slurry into the voids by gravity pressure. The designed two-stage UHPC can significantly enhance the utilization potential of coarse aggregates, up to 55% - 60%, which consequently greatly decreases the powder demand and creates great economic benefits.

The high strength steel fibre is another key factor to remarkably address the brittle behaviour of UHPC, however it is much more expensive than the other ingredients. Thus, it is of great significance to improve the fibre utilization efficiency of ultra-high performance fibre reinforced concrete (UHPFRC). Meng et al. [229] studied the rheology to control fibre dispersion uniformity, which improved the flexural performance of UHPFRC. Yoo et al. [213] suggested to use long steel fibres to enhance flexural properties. Controlling fibre orientation [24,25] and using hybridization [26] are also efficient measures to increase the utilization efficiency, both static and dynamic. Another solution to efficiently utilize steel fibres is to position more steel fibres into the tensile zones instead of compressive areas, due to the more remarkable reinforcement of steel fibres on tensile behaviour rather than compressive behaviour. According to this design concept, multiple layered (or functionally graded) concrete composites have been developed with good flexural performance, fracture energy, penetration impact resistance, as well as economical benefit [211,230–232]. However, the functionally graded concrete composites have potential interfacial bond problems, namely weak bond or even delamination in the case of casting the top layer on the hardened bottom layer [233], or wavy layers and uneven thicknesses in the case of casting

the top layer onto the bottom layer, that is still not hardened due to gravity force from the top layer [230]. Furthermore, sometimes high dosages of steel fibres are needed to achieve stronger and energy absorptive UHPFRC beams, especially for protective structures subjected to impact and blast loadings. It is rather difficult or even impossible to add a high volume fraction of steel fibres in the bottom (tensile) layer because of the workability reduction and ‘balling’ phenomenon [7]. Thus, it is reasonable to use Slurry-infiltrated Fibre Concrete (SIFCON) in the tensile layer, which can easily achieve a fibre volume fraction up to 10 vol.% [234].

To develop a superior cementitious composite beam subjected to flexural and impact loadings, we propose a novel functionally graded composite beam (FGCB) concept by applying the combined concepts of UHPC, TSC and SIFCON. The bottom layer consists of SIFCON to withstand high tensile stress, while the top layer is designed by two-stage UHPC to achieve an excellent compressive strength with very low cement consumption. The UHPC slurry is injected into the voids of steel fibres (bottom layer) and coarse aggregates (top layer) simultaneously to acquire superior interfacial bond. The 13 mm straight, 30 mm hook-ended and 60 mm 5D steel fibres are investigated with volume fraction from 0 to 3 vol.%, in order to find an optimal type and content of steel fibres on the flexural properties. Furthermore, the superior performance, low cement consumption and high fibre utilization of FGCB are revealed by comparing them with conventional UHPFRC and SIFCON beams.

6.2 Materials and experiments

6.2.1 Materials

The UHPC slurry is composed of Portland cement CEM I 52.5 R (PC), micro-silica (mS), limestone powder (LP), fine sand (S), tap water (W) and PCE-type superplasticizer (SP3 from Chapter 2 is used). The physical and chemical properties of those raw materials can be found in Section 3.2.1, 3.3.1, 4.2.1 and 4.3.1. The coarse basalt aggregate (BA) with particle sizes between 16 and 25 mm is selected by considering its high inherent strength and passing ability of slurry based on our preliminary tests. Three types of steel fibres (SF) are used to investigate the type and dosage effect on the performance of FGCB, described in Section 5.2.1.

6.2.2 Fabrication of FGCB

As illustrated in Figure 6.1, the FGCB is fabricated by combining the bottom (SIFCON) and top (TSC) layers. The steel fibres are firstly placed in the steel mould, followed by coarse basalt aggregates on top of the steel fibres, then the UHPC slurry is injected into the voids by gravity pressure. Vibration is also applied to ensure a good quality of compactness. Because the steel fibres and coarse aggregates are well controlled and preplaced as a stiff skeleton, the phenomena of wavy layers and uneven thicknesses that usually occurs in the fresh state cast of conventional multi-layered concrete composites can be avoided. Furthermore, the slurry in both bottom and top layers is cast simultaneously, the interfacial bond strength should be much better than the cold bond in most multi-layered concrete composites.

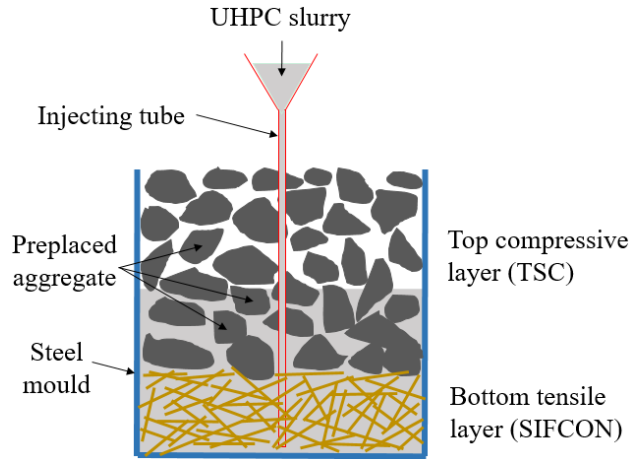


Figure 6.1: Schematic picture of casting procedure.

Besides the properties of coarse aggregates and steel fibres, the performance of FGCB is strongly dependent on the properties of the slurry. To acquire a superior FGCB, the slurry is designed based on the UHPC system, which has both excellent fresh and hardened properties. Table 6.1 shows the mix proportion of the designed UHPC slurry, based on the study in Chapter 4.3 with a slight adjustment. A PCE-type superplasticizer (SP3) is utilized to achieve a desired fluidity with a dosage of 2% by the weight of total powder [108]. The optimal proportion of powders is 5% of micro-silica and 20% of limestone powder by mass of the total powder, by considering the flow ability, mechanical strength and drying shrinkage of UHPC pastes. The fraction of fine sand is calculated based on the particle packing model (described in Section 4.2.2) to achieve a good packing density with a particle distribution q of 0.22. The total particle size distribution of UHPC slurry is shown in Figure 6.2.

Table 6.1: Mix proportion of UHPC slurry.

Materials	PC	mS	LP	S	water	SP
Volume fraction (%)	29.08	2.63	9.01	30.27	28.09	1.76
Mass proportion	0.75	0.05	0.20	0.66	0.23	0.02
Mass (kg/m ³)	916.1	61.1	244.3	808.1	280.9	21.1

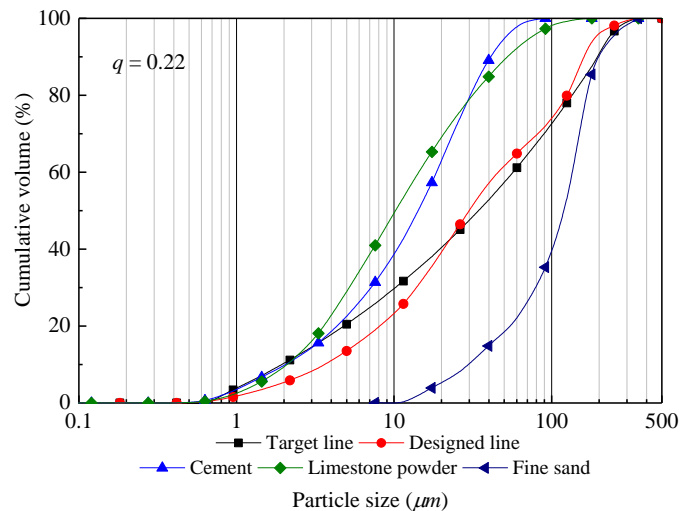


Figure 6.2: The PSDs of raw materials and designed UHPC slurry.

The recipes of the designed FGCB can be seen in Table 6.2. Although the first mixture is a two-stage UHPC without fibre, it is also abbreviated as FGCB as a special case without SIFCON layer. The research parameters include steel fibre dosage (from 0 to 3 vol.% by the total volume of FGCB) and type (13 mm straight (short), 30 mm hook-ended (medium), 60 mm 5D (long)). The binder (cement and micro-silica) consumption ranges approximately between 400 and 700 kg/m³, which is much lower than conventional UHPC [5,28]. The cross-sections of the designed FGCB are presented in Figure 6.3, which are cut from the hardened beams.

Table 6.2: Recipes of FGCB (UHPC slurry can be found in Table 6.1, BA is basalt aggregate with particle sizes between 16 mm and 25 mm in Section 4.2).

Mix No.	UHPC slurry (binder) (kg/m ³)	BA (kg/m ³)	Fibre average dosage (vol.) & type	Bottom layer to total beam ratio, β_{layer}
FGCB1	976.9 (408.9)	1825.9	0	0
FGCB2	1249.0 (522.7)	1427.8	2%, short	0.21
FGCB3	1447.3 (605.8)	1175.7	2%, medium	0.31
FGCB4	1357.6 (568.2)	1278.3	2%, long	0.25
FGCB5	1274.2 (533.3)	1414.0	1%, medium	0.12
FGCB6	1692.1 (708.2)	846.3	3%, medium	0.46

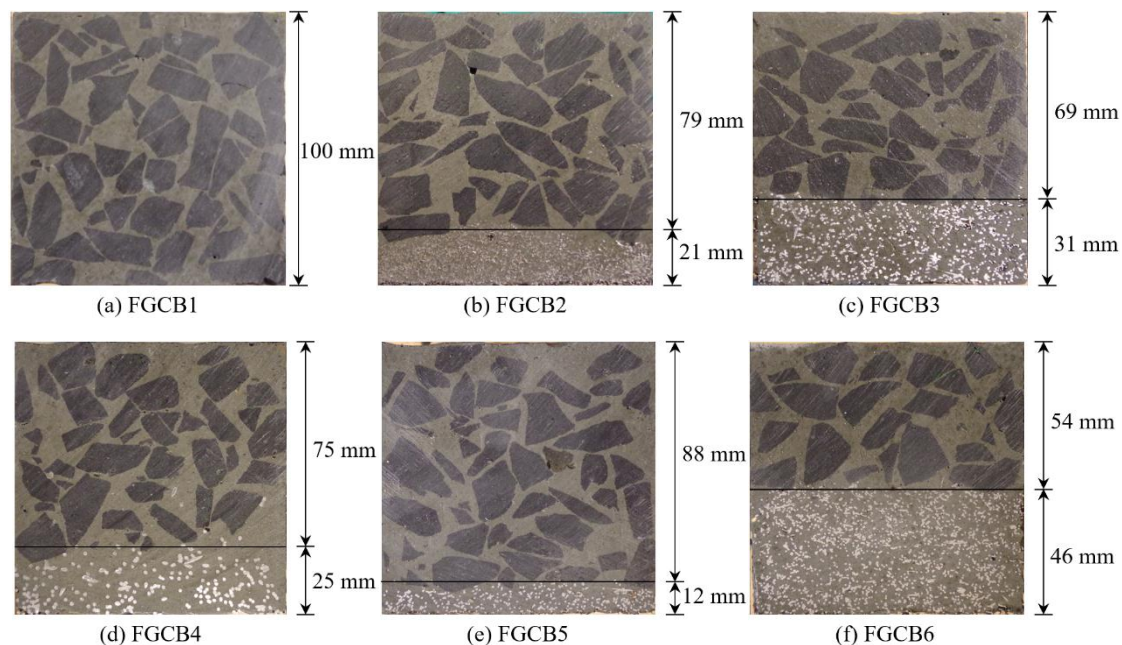


Figure 6.3: Cross-sections of FGCB (top layer is TSC, bottom layer is SIFCON).

6.2.3 Experimental methods

The fresh and strength tests of slurry are measured based on the methods as mentioned in Sections 2.22 and 3.23.

The central point flexural test is conducted for FGCB (100 × 100 × 500 mm³) with a span of 300 mm after 28 days, based on the EN 12390-5: 2009 [217]. Figure 6.4 shows the sample and set-up of the central point flexural test. Figure 6.5 illustrates the key parameters derived from the results of load-deflection curve. It can be divided into three stages, namely elastic

stage (I), deflection hardening stage (II) and deflection softening stage (III). The elastic strength (σ_e) and peak strength (σ_p) are calculated from the elastic (P_e) and peak loads (P_p) respectively. The flexural toughness (T) is defined as the area under the load-deflection curve, which represents the energy absorption ability. In comparison with Chapter 5,

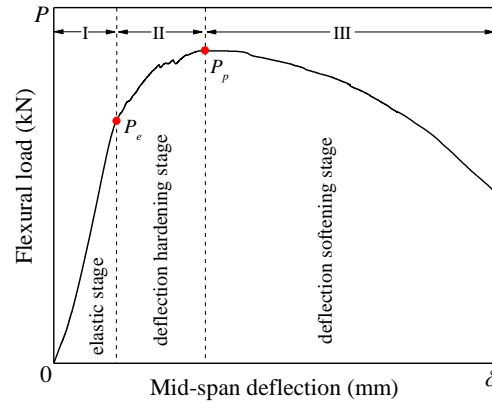
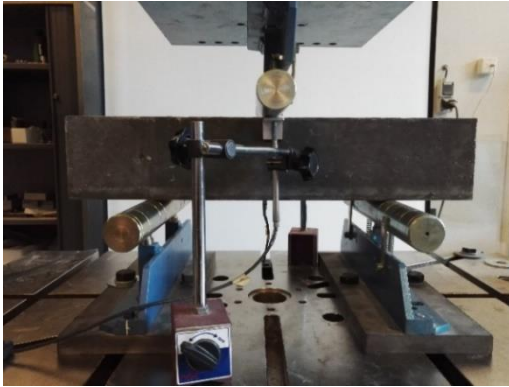


Figure 6.4: Three-point flexural test. Figure 6.5: Key parameters of flexural test.

6.3 Results and discussion

6.3.1 Fresh and hardened properties of slurry

The UHPC slurry is a critical factor for the overall performance of FGCB. The casting method and quality control of TSC and SIFCON are dependent on the excellent fresh behaviour of UHPC slurry. The fresh and hardened properties of UHPC slurry are presented in Table 6.3. In this study, the designed UHPC slurry has a mini slump flow of 39 cm (Hägermann cone) and mini V-funnel flow time of 7.1 s, which satisfy the requirement of self-compacting, namely slump flow larger than 24 cm and V-funnel time shorter than 11 s [100,101]. Based on our preliminary tests, a UHPC slurry possessing mini slump flow beyond 35 cm has enough passing ability to fill the voids of aggregates by checking the apparent and cross-section characters. The fresh density and 28d compressive strength are approximately 2.3 g/cm^3 and 144.6 MPa, respectively, which meet the required high strength of UHPC systems. To sum up, the UHPC slurry is successfully developed with both very good fresh and hardened properties, which will be utilized to design the FGCB.

Table 6.3: Fresh and hardened properties of UHPC slurry.

Mini slump flow (cm)	$T_{v\text{-funnel}}$ (s)	Fresh density (g/cm^3)	28d compressive strength (MPa)
39	7.1	2.3	144.6 ± 2.1

6.3.2 Flexural Load-deflection curves

Figure 6.6 presents the load-deflection curves of the designed FGCB based on central point flexural test. As illustrated in Figure 6.5, a cementitious composite usually undergoes three stages under a flexural loading till complete failure. The plain FGCB without SIFCON layer only shows an elastic stage and ruptures abruptly when reaching the maximum flexural load (20 kN). Other designed FGCBs almost experience three stages, including elastic, deflection/strain hardening, and deflection/strain soften stages. The first crack loads of

FGCB, defined as the elastic load in Figure 6.5, are not obvious. The elastic stage transits into the deflection hardening stage gradually after elastic load, which indicates that the ductility of the designed FGCB is good compared to other brittle cementitious composites. The 2 vol.% short and long fibres only provide limited deflection hardening behaviours compared to the medium fibres, and their residual bearing capacities remains until deflections of approximately 4 mm. For the medium hook-ended steel fibre, 2 vol.% can trigger a considerable deflection hardening behaviour, and 3 vol.% further improves this behaviour, and the residual bearing capacity can remain until the deflection of around 8 mm.

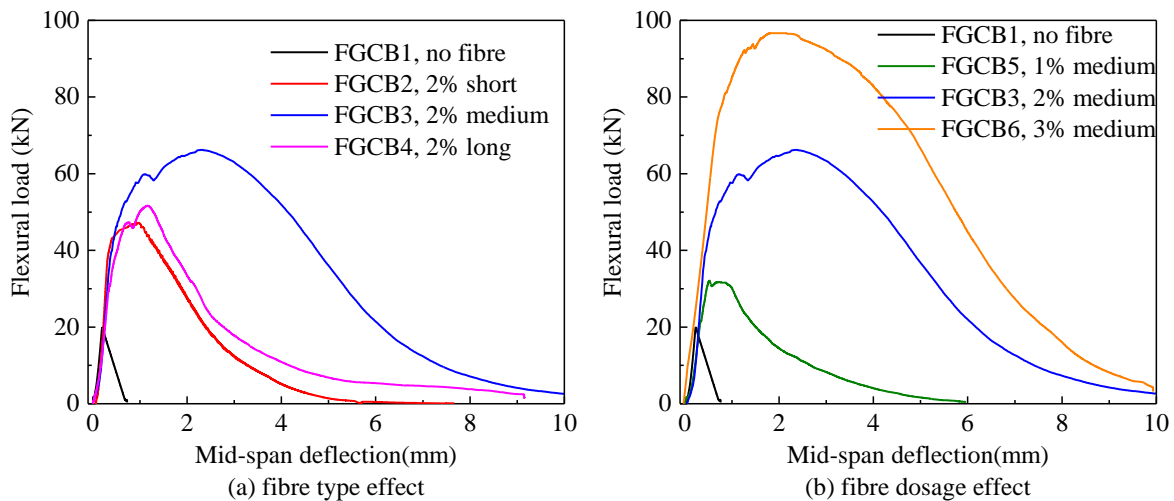


Figure 6.6: Flexural load vs. deflection curves of FGCB.

With the inclusion of 2 vol.% steel fibres, the load-deflection curves of FGCB can be significantly enhanced for both peak load and toughness, as shown in Figure 6.6(a). However, the different steel fibre types show great differences. The 13 mm short straight fibres provide the poorest enhancement, with about 2.4 times and 15.4 times of peak load and toughness, respectively, compared to the plain FGCB without fibres. Followed by the 60 mm long 5D fibres, they offer slightly higher reinforcements on both strength and toughness. The 30 mm medium hook-ended steel fibres have the best reinforcing effect, presenting approximately 3.3 times and 48.8 times of peak load and toughness, respectively, compared to the reference beam without fibre. The best reinforcing effect of medium fibres is attributed to the following aspects: (1) a good anchorage effect due to the hook-ended shape; (2) the highest aspect ratio that is usually positively linked to the reinforcement; (3) the largest distribution space because of the moderate length and number of fibres per kilogram, as shown in Figure 6.3(c), contributing to the largest tension resistant zone (SIFCON layer).

As analysed above, the 30 mm medium hook-ended steel fibres provide the best reinforcement on the flexural properties of FGCB. Hence, these steel fibres are chosen to investigate the fibre dosage effect. Figure 6.6(b) presents the load-deflection curves of FGCB with different medium steel fibre dosages. With the addition of fibre dosage from 1 vol.% to 3 vol.%, the maximum flexural strength of FGCB shows almost linear improvement of 1.6 times, 3.3 times and 4.9 times as plain FGCB, while the enhancement on the flexural toughness is much more remarkable, namely 9.5 times, 48.8 times and 79.0 times, respectively. The thickness of the bottom (SIFCON) layer ranges from 12 mm with 1 vol.%

fibres up to 46 mm with 3 vol.% fibres, so the bottom layer thickness ratio (β_{layer}) is increased from 0.12 to 0.46. The β_{layer} of approximately 0.5 was theoretically and experimentally confirmed to be the optimum by considering both flexural performance and fibre utilization, as illustrated in Figure 6.7 [199,211]. Thus, 3 vol.% medium hook-ended steel fibres almost achieve the optimum layer thickness ratio β_{layer} based on flexural properties and fibre utilization, which is suggested for designing FGCB in engineering applications.

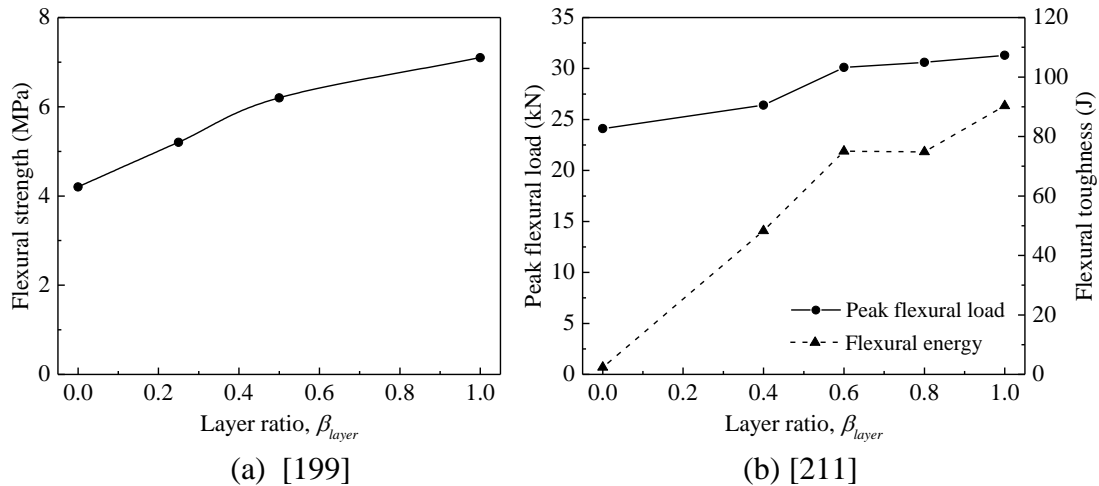


Figure 6.7: Flexural strength/load and energy with different layer ratios.

6.3.3 Damage pattern and bond characteristic

The brittleness of conventional concrete beam usually results in one dominant crack damage pattern subjected to flexural loading, which causes an abrupt failure of components or structures without warning. Hence, a multiple cracks damage pattern is more desired for cementitious composite beams, which is usually associated to the deflection or strain hardening stage [235]. Figure 6.8 illustrates the damage patterns of the designed FGCB. FGCB with 2 vol.% short or long steel fibres has only one dominant crack from the centre of beam, which is similar to plain FGCB. It agrees with the fact that the deflection hardening behaviour of this FGCB is not obvious, as shown in Figure 6.6. With the inclusion of 1 vol.% medium steel fibres, the multiple cracks damage pattern or deflection hardening behaviour cannot be triggered. While, a number of micro-cracks can be observed for the FGCB with 2 vol.% medium steel fibres, as plotted by the red lines in Figure 6.8. When 3 vol.% medium fibres are added, a much denser micro cracks on the surface occur, which is confirmed by the excellent deflection hardening behaviour and ductility.

The normal multiple layered or functionally graded concrete composites usually exhibit interfacial bond problems. The top layer is normally cast 24 hours after the cast of the bottom layer (so called cold cast), resulting in a weaker interfacial bonding strength or even delamination due to different shrinkages and poor old-to-new hydration production integration [233]. Casting the two layers simultaneously or within a very short time interval (so called hot cast) can achieve a higher interfacial bond than the cold cast [211]. But it is well possible that wavy layers and uneven thicknesses are generated, because of the gravity load from the top layer on the bottom layer [230]. Those adverse interfacial problems could possibly cause debond phenomenon (delamination) and influence the flexural bearing

capacity [236]. The delamination has never occurred during the flexural tests for all the designed FGCB in this study, as shown in Figure 6.8. The excellent interfacial bond of the designed FGCB is attributed to: (1) well controlled and preplaced stiff skeleton of the steel fibres and coarse aggregates; (2) very low shrinkage of both TSC and SIFCON; (3) same slurry and synchronous hydration for the two layers.

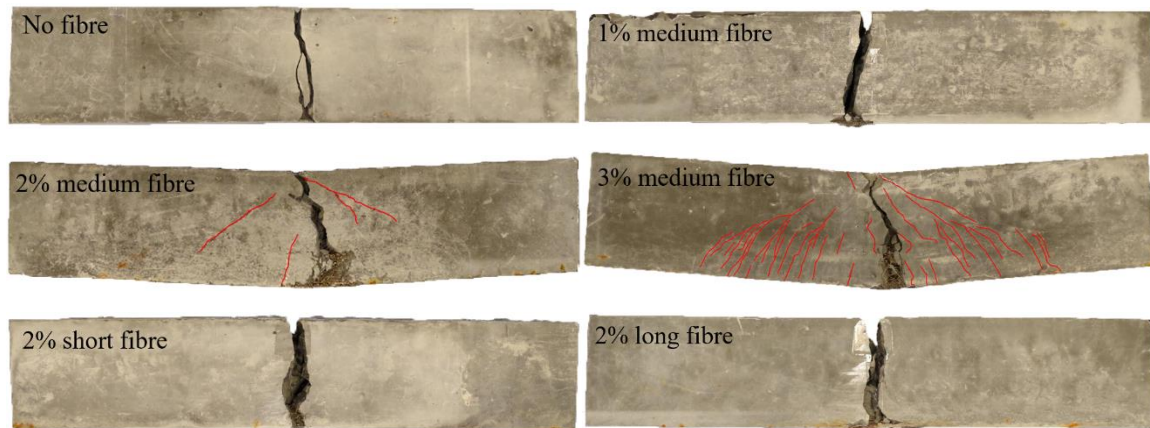


Figure 6.8: Damage patterns of FGCB after flexural tests.

6.3.4 Fibre utilization efficiency

As analysed above, the reinforcement degree of steel fibre on flexural properties is significantly influenced by the fibre characteristics, such as fibre content and shape [20,235,237,238]. Furthermore, the cost of 1 vol.% of fibre applied in concrete composites is generally higher than that of the plain matrix [212]. Thus, it is important to maximize the fibre utilization efficiency, or in other words, to minimize the amounts of fibre without sacrificing the superior performance of concrete composites. To study the steel fibre utilization efficiency on the flexural strength and toughness, a reinforcing factor η , defined as the normalized improvement ratio by steel fibre volume content is proposed,

$$\eta = \frac{X_{FGCB}}{X_{plain}} \cdot \frac{1}{V_{fibre}} \quad (6.1)$$

where X_{FGCB} and X_{plain} represents the flexural properties with fibres and without fibres, namely flexural strength and toughness in this study. V_{fibre} is the average volume content by the total volume of whole FGCB beam.

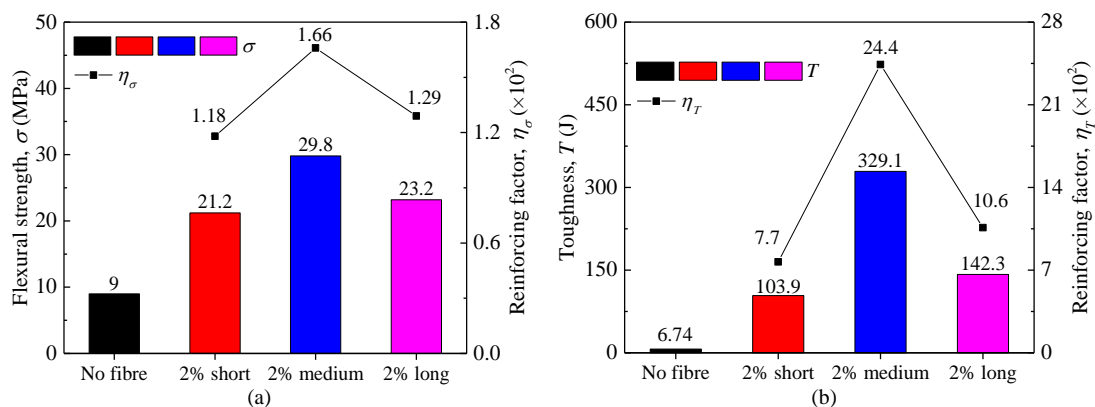


Figure 6.9: Steel fibre type effect on flexural strength and toughness of FGCB.

Figure 6.9 shows the steel fibre type effect on the flexural strength and toughness of the designed FGCB. The 2 vol.% medium steel fibres provide the largest flexural strength (29.8 MPa), followed by the long fibres (23.2 MPa) and short fibres (21.2 MPa). Based on the flexural strength of the plain beam (9.0 MPa), the reinforcing factors in term of strength (η_σ) are ordered as 1.66×10^2 , 1.29×10^2 and 1.18×10^2 , respectively. The fibre reinforcing effect on the flexural toughness has a similar trend to that of the flexural strength, while the reinforcing factors in terms of toughness (η_T) are much more remarkable, namely 24.4×10^2 , 10.6×10^2 and 7.7×10^2 , respectively. It indicates that both flexural and toughness are greatly dependent on the steel fibre types, while the contribution of fibres to toughness is more prominent. Furthermore, the 30 mm medium hook-ended steel fibres is appropriate and recommended to develop the FGCB, especially for the energy absorption ability.

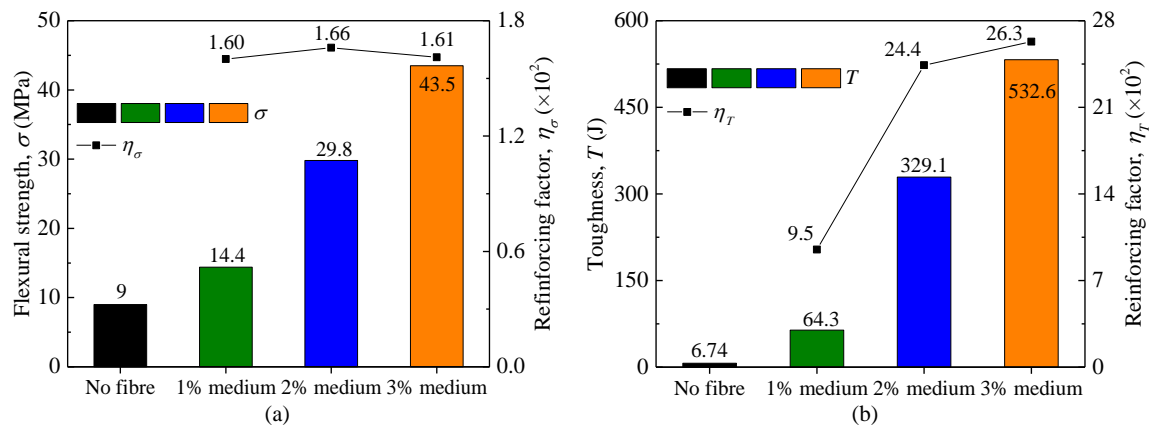


Figure 6.10: Steel fibre dosage effect on flexural strength and toughness of FGCB.

Figure 6.10 presents the dosage effect of 30 mm medium steel fibres on the flexural strength and toughness of the designed FGCB. 1 vol.% medium fibres addition can improve the flexural strength from 9 MPa to 14.4 MPa, while much more considerable flexural strength is achieved up to 43.5 MPa with 3 vol.% medium fibres. The flexural properties of the designed FGCB are more superior to those of most UHPFRC beams that usually have flexural strengths around 20-30 MPa [26,27,213]. Furthermore, the reinforcing factor η_σ keeps a stable level in the range of 1.6×10^2 - 1.66×10^2 , which indicates that the increased dosage of medium fibres continuously improves the flexural strength without sacrificing fibre utilization efficiency. As seen from the load-deflection curves in Figure 6.6, a much more significant improvement of medium fibres on toughness rather than strength is observed, with the reinforcing factor η_T increasing from 9.5×10^2 at 1 vol.% to 24.4×10^2 at 2 vol.%, then up to a slightly higher value of 26.3×10^2 at 3 vol.%. A higher dosage of medium steel fibres in the studied range always gives a higher fibre utilization efficiency on toughness. The 2 vol.% medium fibres increase the utilization efficiency significantly compared to the 1 vol.%, but 3 vol.% addition seems not to enlarge the fibre utilization efficiency much anymore. Yoo et al. also found that 3 vol.% steel fibre yielded the best mechanical properties, volume stability and fibre-to-matrix interfacial bond [239]. Thus, an average dosage between 2 vol.% and 3 vol.% medium fibres is recommended for designing FGCB.

As analysed above, 2 vol.% - 3 vol.% 30 mm medium hook-ended steel fibres are suggested to develop FGCB, considering both performance and fibre utilization efficiency. Because the steel fibres are added in the tension zone instead of the compression zone, the fibre utilization efficiency of the designed FGCB would be very high, which certainly contributes to the economic benefits and performance. To further demonstrate this advantage in FGCB, the fibre reinforcing factors η_σ of the designed FGCB are compared with other homogenous UHPFRC [23,27,240,241] and SIFCON [242] beams, as shown in Figure 6.11. Normally, with the increase of steel fibre dosage, the utilization efficiency of UHPFRC beam tends to decrease, from approximately 1.32×10^2 at 1 vol.% to 0.63×10^2 at 6 vol.%. Additionally, the mixing and workability usually would become an issue when the fibre addition is beyond 3 vol.% in UHPFRC. Although the SIFCON beams can utilize very high volumes of steel fibre without mixing and workability problems, usually more than 6 vol.%, they achieve even much lower utilization efficiencies. While, the utilization efficiency of the 30 mm medium hook-ended steel fibres is very high compared to the UHPFRC and SIFCON beams, beyond 1.6×10^2 without any diminishing trend with the increase of fibre dosage from 1 vol.% to 3 vol.%. Therefore, the designed FGCB not only has superior performance but also possesses excellent fibre utilization efficiency and economic benefits.

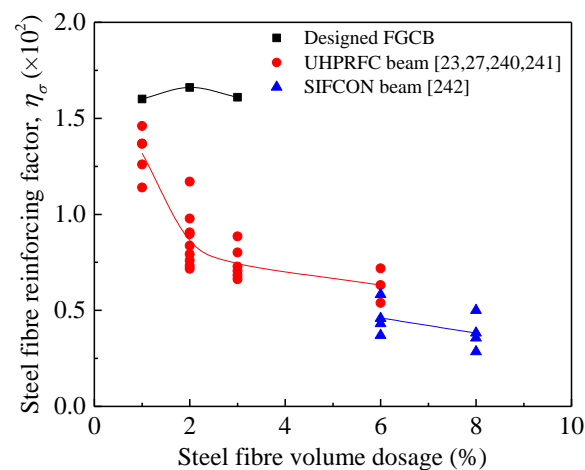


Figure 6.11: Steel fibre utilization efficiency in term of flexural strength.

6.4 Conclusions

The chapter aims to develop a novel functionally graded composite component towards superior flexural strength and toughness by applying the composite concepts of UHPC (slurry), TSC (top layer) and SIFCON (bottom layer). The fresh and hardened properties of UHPC slurry, flexural properties of the FGCB, cement consumption and steel fibre utilization efficiency are explored and discussed. The following main conclusions can be summarized based on the results:

- A novel FGCB is successfully developed by combining the concrete of UHPC (slurry), TSC (top layer) and SIFCON (bottom layer), which has superior flexural properties, strong interfacial bond, very low cement consumption and high steel fibre utilization efficiency.

- The UHPC slurry with excellent workability and strength is injected into the coarse basalt aggregates and steel fibres synchronously, avoiding uneven thicknesses phenomenon and weak interfacial bond problems that often occur in multi-layered concrete composites.
- The 30 mm medium hook-ended steel fibres show a better utilization efficiency than the 13 mm short straight and 60 mm long 5D steel fibres. 3 vol.% 30 mm hook-ended fibres are suggested to design FGCB with an optimum bottom-to-total layer ratio β of 0.46, considering both performance and fibre utilization efficiency.
- The binder consumption of FGCB is much lower than normal UHPFRC beam, ranging between 400 and 700 kg/m³. The steel fibre utilization efficiency of FGCB is beyond 1.6×10^2 , which is much higher compared to the homogenous UHPFRC and SIFCON beams. Both low binder consumption and high steel fibre efficiency contribute to economic benefits.

Chapter 7

Pendulum and drop-weight impact resistance of UHPFRC

This chapter addresses the low-velocity impact resistance of designed ultra-high performance cementitious materials under pendulum and drop-weight impacts. The effects of steel fibres and coarse aggregates, damage development and post-impact properties, and superiority of functionally graded composite components are investigated. The results again show that coarse basalt aggregates improve the impact resistance and reduce the powder content and cost. In the presence of coarse aggregates, the 30 mm medium hook-ended and 60 mm long 5D fibres are more efficient in reinforcing impact resistance than the 13 mm short straight ones. The residual strength of UHPFRC beams follows a ‘ $-e^x$ ’ law with the number of impacts, while the residual rigidity, toughness and impact resistance follow linear law. The novel concept of FGCB is has superior impact resistance, as well as very low cement consumption and high steel fibre utilization efficiency. Here, 3 vol.% 30 mm hook-ended fibres are suggested to design FGCB with an optimum bottom-to-top layer ratio β_{layer} of 0.46. The toughness is a good indicator to reflect the low-velocity impact resistance of UHPFRC beams. While, the impact resistance is also greatly influenced by the flexural strength when subjected to impacts with the impact energies below the threshold energy.

This chapter is partially published elsewhere:

P.P. Li, Y.Y.Y. Cao, M.J.C. Sluijsmans, H.J.H. Brouwers, Qingliang Yu. Synergistic effect of steel fibres and coarse aggregates on impact properties of ultra-high performance fibre reinforced concrete. Submitted.

P.P. Li, Q.L. Yu. Responses and post-impact properties of ultra-high performance fibre reinforced concrete under pendulum impact. *Composite Structures*. 208 (2019) 806-815.

P.P. Li, M.J.C. Sluijsmans, H.J.H. Brouwers, Q.L. Yu. Functionally graded ultra-high performance cementitious composite with enhanced properties. *Composites Part B: Engineering*. 183 (2020) 107680.

7.1 Introduction

UHPFRC is a relatively new building composite material, which has superior mechanical strength, impact resistance, fatigue resistance and durability [1,11,79,80,156,176]. Those excellent characters and properties make it suitable to be used in impact resistant components and structures, such as protective elements in military and municipal engineering.

The impact responses and post-impact properties of UHPFRC under low-velocity impact loading are of great significance and can provide insights on specific practical problems, such as vehicle impact on concrete infrastructure during a traffic accident, the ship collision on bridges' pillars or offshore structures, falling object impact on a concrete slab, wheel-rail interaction on concrete sleepers [243,244], etc. However, it is noticed that no standard low-velocity impact testing methods for UHPFRC are available currently. The drop-weight test and the modified Charpy system recommended by ACI Committee 544 are widely used [245–249]. However, these low-velocity impact testing methods are not appropriate for evaluating UHPFRC because of certain drawbacks. A high standard deviation and coefficient of variation from ACI repeated drop-weight impact test are usually observed, even more than 50% of coefficients of variation [246]. Furthermore, the number of impacts is too large for fibre reinforced concrete, sometimes as high as 1000 blows [247]. The Charpy type impact test can only measure small geometrical sizes of specimen containing short fibres [249]. The drop-weight impact test usually has a rebound and secondary impact effect, when the specimens do not completely damage [250]. Hence, it is necessary to develop a new low-velocity impact experimental method for UHPFRC.

Besides, the majority of current studies only place emphasis on investigating the total impact number and energy absorption under repeated low-velocity impact loading. Researches concerning impact responses and post-impact properties assessment are rather scarce. Both crack propagation and damage pattern are critical factors to interpret impact response and the resistant mechanism of UHPFRC. Furthermore, residual property (e.g. compressive strength after impact) is one of the most crucial parameters for damaged composite materials [251], which is widely used to evaluate the damage degree and health status of structures and components under extreme conditions, such as residual strength after fatigue loading, freeze-thaw cycles or high temperature exposure [252–254]. The investigation on post-impact properties (e.g. residual strength, stiffness, toughness, impact resistance) can provide key parameters and bases for the design of protective elements and components.

Nevertheless, impact resistance (energy absorption capacity) of UHPFRC is much more difficult to be determined than other static properties, due to the complexity of impact tests. Some researchers revealed that strength is associated with impact resistance (e.g. projectile penetration), while toughness is related to tension crack and scabbing [255]. The toughness reflecting the energy absorption capacity should have a relation with impact resistance. Another research tries to predict the initial impact behaviour (delamination damage) by economical static tests (e.g. shear stress) [256]. For these reasons, it is necessary to investigate the impact responses and post-impact properties of UHPFRC under repeated low-velocity impact loading, and to propose a reliable analytical model to predict the impact resistance by several key variables based on simple static tests.

The objective of this chapter is to develop a reliable repeated low-velocity impact testing device and method, investigate the impact responses and post-impact properties of UHPFRC designed in Chapters 4, 5, 6. The effects of coarse basalt aggregates and steel fibres, and the functionally graded composite component will be analysed. Furthermore, an analytical model is proposed to predict the impact resistance of UHPFRC based on the static flexural toughness, and successfully validated against the experimental data.

7.2 Specimens and impact methods

7.2.1 Pendulum impact test

Impact tests can be divided into three categories (qualitative, semi quantitative and quantitative), depending on the property measured by which the impact test is conducted. But quantitative interpretation of impact testing results to derive inherent physical material parameters has shown to be still quite difficult. Furthermore, impact tests should follow some primary criterion and achieve goals as: (1) simple to handle; (2) energy sufficient to fracture the specimen; and (3) number of blows to achieve a specified distress level [257].

A pendulum device is designed to investigate the low-velocity impact resistance of UHPFRC beams. The pendulum device has a flexible impact mass (22 - 40 kg) and height (0 - 4 m), as shown in Figure 7.1. First, the UHPFRC beam is hung by steel ropes with a specific span. Then, the hammer is released from a fixed position and perpendicularly impacted on the central point of UHPFRC beam at the lowest hammer position. Afterwards, both the highest positions of sample and hammer are recorded during the first post-impact swing by a high-speed camera, as well as the velocities of hammer and specimen before and after impact. The frame rate of high-speed camera is set at 5000 frames per second, and the displacement of movement is measured based on a white board background with centimetre grids drawn on it. The impact resistance of UHPFRC is described by the impact number and energy absorption E (J) for each impact is obtained by

$$E = \begin{cases} M_h g (H_h - h_h) - M_s g h_s \\ 1/2 M_h V_0^2 - 1/2 M_h V_r^2 - 1/2 M_s V_s^2 \end{cases} \quad (7.1)$$

where M_h and H_h are the mass and initial height of the hammer, the specimen mass M_s varies, gravity acceleration $g = 9.8 \text{ m/s}^2$, the maximum heights of hammer (h_h) and beam (h_s) are measured after impact, V_0 and V_r are the velocities of hammer before and after impact (m/s), V_s is the velocity of the concrete beam after impact (m/s). To obtain a moderate impact number, the pendulum hammer mass and its initial height in this study are chosen after preliminary trials. The impact is repeated till the complete failure (fracture) of UHPFRC beam, and the total absorbed energy E can be obtained.

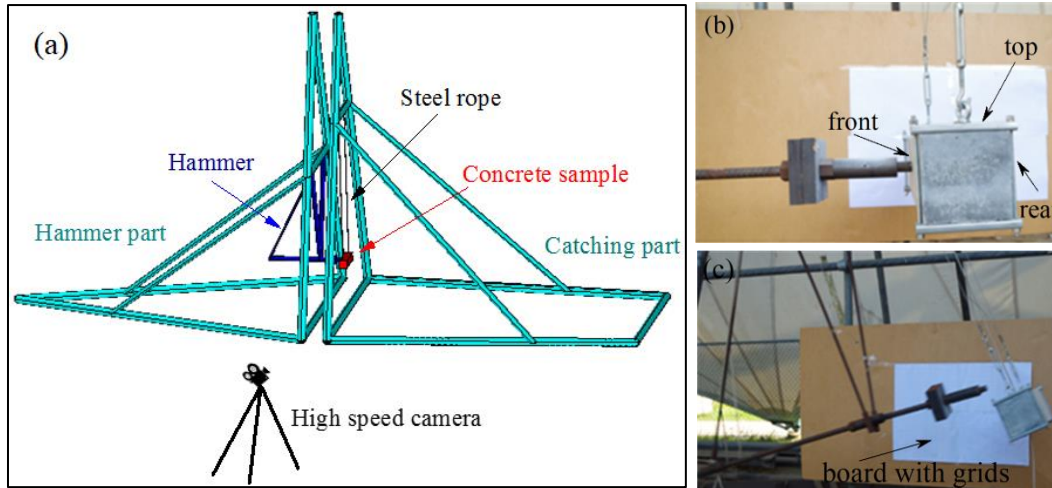


Figure 7.1: Pendulum impact set-up: scheme (a), before (b) and after (c) impact.

To evaluate the synergistic effect of steel fibres and coarse aggregates on impact properties of UHPFRC, the same mixtures and unnotched beams (size $150 \times 150 \times 550 \text{ mm}^3$ and span 450 mm) are utilized to conduct pendulum impact test, as mentioned in Chapter 5. The initial height of hammer (M_h) and the specimen mass (H_h) are 30.3 kg and 2.35 m, respectively. The total impact number and energy dissipation are measured.

To further analyse the post-impact properties of UHPFRC, one mixture (see Table 7.1) is used to measure the flexural behaviour of partially damaged beams after a certain impact number. Standard notched beams (size $150 \times 150 \times 550 \text{ mm}^3$ and span 450 mm) have been recommended by various organizations such as RILEM TC 162 [258] and EN 14651 [259] to test the impact resistance and post-impact flexural behaviour of UHPFRC [260]. The initial height of hammer (M_h) and the specimen mass (H_h) are 30.3 kg and 1.4 m, respectively.

Table 7.1: Mixture for post-impact properties research.

Materials	PC (kg/m^3)	mS (kg/m^3)	LP (kg/m^3)	S 0-2 (kg/m^3)	BA 2-5 (kg/m^3)	BA 5-8 (kg/m^3)	W (kg/m^3)	SP (kg/m^3)	SF vol.%
Quantity	588	39.2	156.8	839.9	413.2	232.3	187.8	12.6	2

7.2.2 Drop-weight impact test

To measure the low-velocity impact resistance of cementitious based composites, the drop-weight impact testing methods are also usually utilized. A drop-weight impact set-up is designed to research the impact resistance of FGCB, as presented in Figure 7.2. A steel ball weighted as approximately 4.01 kg is held up by a magnetic device, and released from the height of 3.16 m. Then, the steel ball impacts on the top surface in the centre of FGCB with a span of 300 mm. The drop-weight impact is repeated till the fracture of FGCB, and the impact resistance can be described by the total absorbed energy (E)

$$E = n \cdot mgh \quad (7.2)$$

where n is the total impact number till complete failure; m and h are the mass and impact height of steel ball, respectively; g is the gravity acceleration, 9.8 m/s^2 . The specimens of FGCB are same to those as mentioned in Chapter 6 (Table 6.2).

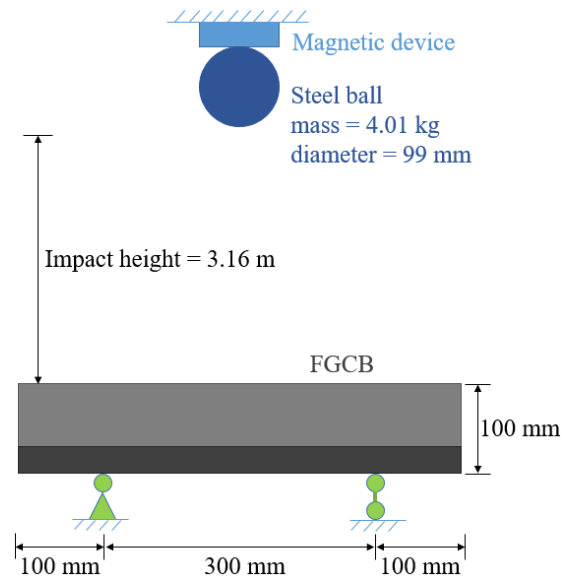


Figure 7.2: Scheme of drop-weight impact set-up.

7.3 Results of pendulum impact tests

7.3.1 Synergistic effect of steel fibres and coarse aggregates

The impact resistance of UHPFRC beams is represented by the impact number and absorbed energy. Table 7.2 shows the failure impact number and total absorbed energy calculated based on Eq. (7.1). The two plain concrete can only suffer from one pendulum impact, which indicates that they are very brittle and not suitable to be used for impact resistant elements or structures. Incorporating 2 vol.% of 13 mm short straight fibres, the energy dissipation ability of UHPFRC beams can be greatly enhanced, as high as about 5 to 6 times. The impact resistance is further significantly increased with the inclusion of 2 vol.% of 30 mm medium hook-ended or 60 long 5D steel fibres. Thus, the steel fibres are indispensable for UHPFRC subjected to impact loading, due to an increase in fibre pull-out load and strain capacity [10,213]. However, the improvement degrees are not the same for the different UHPFRC matrices. A similar synergistic effect as shown in flexural behaviour is observed, namely UHPFRC with the smaller basalt aggregates is preferred to the 30 mm medium hook-ended fibres to achieve the best impact resistant mixture (A8F30), while the coarser basalt aggregates need much longer steel fibres (60 mm long 5D) to acquire enough reinforcement (A25F60).

To further analyse the impact resistance mechanism and damage propagation, the development of energy absorption during each impact is investigated, as shown in Figure 7.3. In this study, the absorbed energy of UHPFRC beams during one impact usually ranges between 35% and 50% of the initial impact energy of hammer (approximately 698 J). For the UHPFRC beam reinforced with steel fibres, the energy absorption development suffers through three stages, firstly dissipating relatively low energy at the initial several impacts, afterwards keeping it at a higher and stable level at the following impacts, and then tending to a further higher energy absorption and complete failure at the last few impacts. The first stage is more like elastic collisions, transferring more gravitational potential energy into

kinetic energy of the UHPFRC beam, thus resulting in less energy absorption by the material itself. The second stage is mainly due to the fibre pull-out process. The partially damaged UHPFRC beam tends to be ‘soft’ because of degeneration of stiffness, which contributes to more impact energy transformation into the material deformation energy instead of the kinetic energy. The third stage is a failure acceleration stage where the damage degree develops faster and faster till the complete breakage from the centre occurs, and more impact energy is absorbed due to the large deformation. An example is shown in Figure 7.3(a), in which the three stages are indicated.

Table 7.2: Total impact number and energy dissipation.

Mix No.	Failure impact number, n	Energy dissipation, E (J)
A8F0	1	299
A8F13	6	1833
A8F30	93	27940
A8F60	17	5650
A25F0	1	325
A25F13	5	1561
A25F30	8	2519
A25F60	15	4759

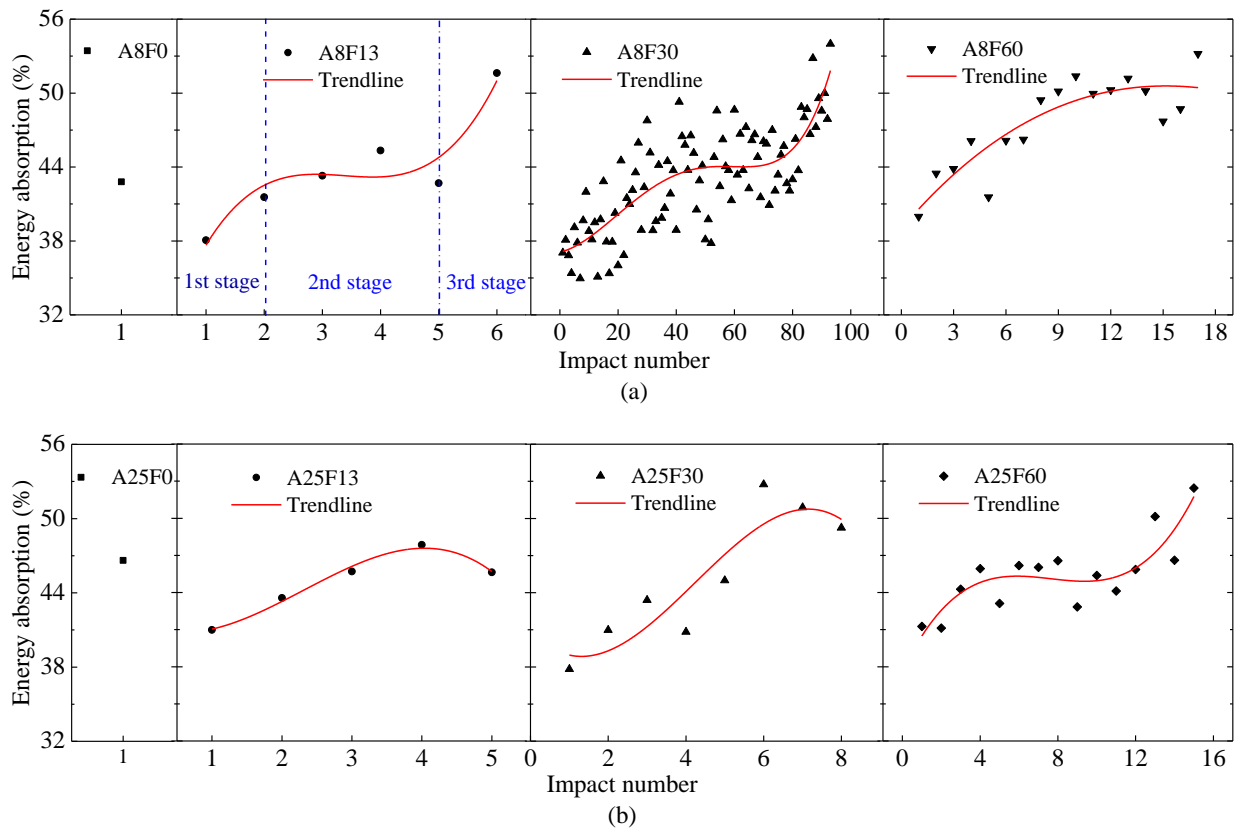


Figure 7.3: Development of energy absorption, in (a) an example of 3 impact stages are indicated.

7.3.2 Post-impact properties of UHPFRC beams

- **Crack propagation**

Figure 7.4 shows the crack propagation on the top surface. After the first impact, a long and thin crack can be observed, and it develops further after the second impact. An obvious macro crack can be seen after the third impact. It should be pointed out that the UHPFRC beams are complete failed (broke into two parts) after repeated impact of 4 times.

The comparative analysis on the values of crack length and width is shown in Figure 7.5. The crack depth and width of UHPFRC beam are not propagated simultaneously, which can be classified into three stages. At the first stage, the crack resistance is mainly depending on the brittle matrix of UHPFRC. Crack depth is developed more quickly at the initial impact, while the crack width only increases slightly. At the second stage, the fibre bridge effect begins to work and the crack resistance is highly dependent on the bonding force between fibre and matrix. Both crack length and depth have a further increase and a macro crack occurs with the further impact. At the third stage, the crack propagates rapidly till the complete damage, due to the pull-out of steel fibres and simultaneously a drastic degeneration of crack resistance. The sudden increase of crack width during the third impact can be regarded as a threshold point and a good indicator to the coming complete damage.

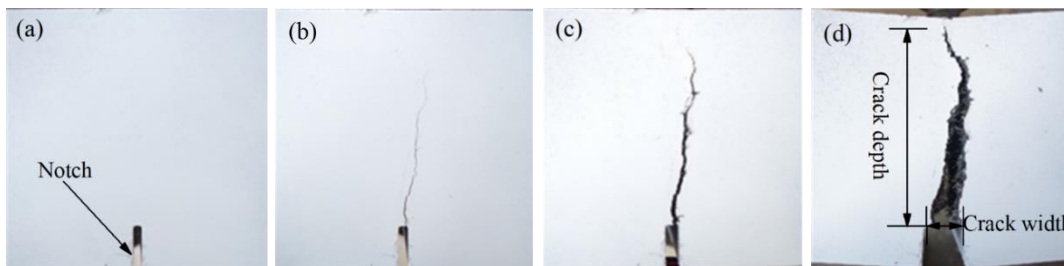


Figure 7.4: Crack propagation after impact number 0 (a), 1(b), 2(c) and 3(d) of UHPFRC mixture in Table 7.1.

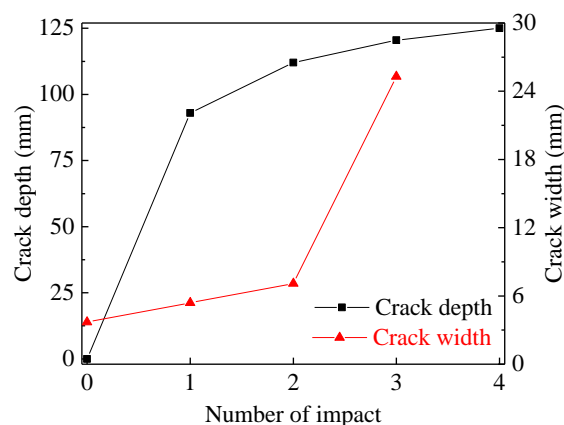


Figure 7.5: Crack values vs. impact number of 150 mm notched UHPFRC (Table 7.1) beams with notch of 25 mm.

- **Damage pattern**

The fracture pattern of a completely damaged beam is evaluated, as shown in Figure 7.6, to further understand the fracture mechanism of UHPFRC under low-velocity impact loading.

The UHPFRC beams show a flexural-like fracture, only one dominant macro crack occurs along the notch. There is almost no front face-crater and rear face-scabbing, punching fracture or delamination, which can probably be observed in other composite materials under impact, based on the different impact velocity and energy, size of specimen and impactor. The fracture pattern of UHPFRC beam indicates that the crack always initiates and propagates along the notch, contributing to reducing variations of testing results, which is in line with [261]. Therefore, a notched beam is proposed and suggested for impact test, attributed to certain fracture path along the notch plane. It can be concluded that the fracture of UHPFRC beam is only generated in a limited local area, nearby the position of maximum moment under impact loading.



Figure 7.6: Fracture pattern of completed damaged beams.

To explain the effect of steel fibres on impact resistance of UHPFRC, a qualitative comparison of steel fibres surface under static flexural and impact loading is performed, shown in Figure 7.7. It should be noted that fibres are pulled out from the matrix. Although the fibre-matrix bonding surface of this thin steel fibre is large enough, no cut-off is identified because of high intrinsic strength of the steel fibre, which proves that this type of high-strength thin fibre is suitable to design impact resistant UHPFRC. In addition, longitudinal scratches can be observed on the steel fibre surfaces, attributed to the abrasion caused by the particles during the pull-out process.

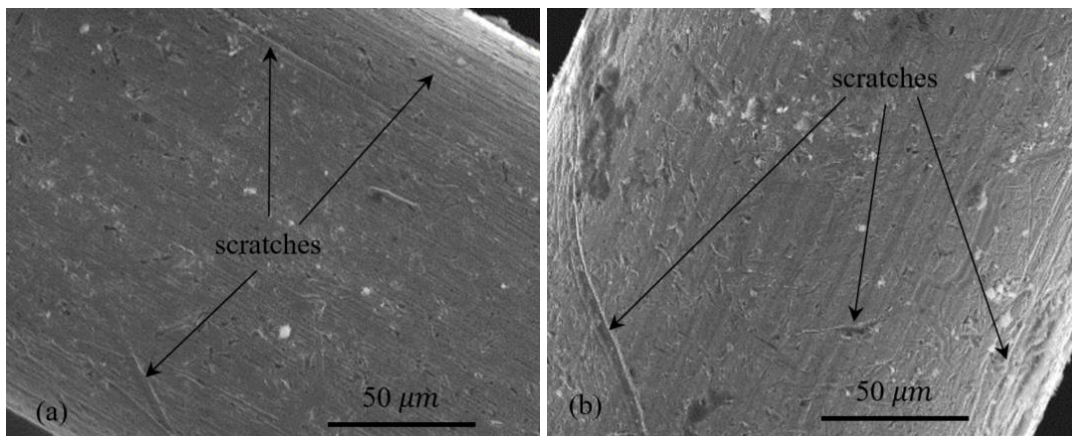


Figure 7.7: Fibre surface at static (a) and impact (b) loading.

The scratches subjected to impact loading are more extensive and severer than those under static loading, which can be attributed to the loading rate effect. Because the matrix is normally sensitive and enhanced under high loading rate, it leads to the increase of the friction between the fibre surface and UHPFRC matrix [162]. It means that the steel fibre works more efficient and is indispensable for UHPFRC subjected to impact loading.

A similar qualitative comparative analysis on coarse basalt aggregate fracture under static flexural and impact loading is presented in Figure 7.8. A great difference between the fracture patterns of coarse basalt aggregates under different loadings is clearly seen. Under static flexural loading, more unbroken coarse basalt aggregates (bright) can be observed, while more broken ones (dark, splitting into two parts) exist after impact loading. It is hypothesized that cracks initiate at the relatively weaker interfacial transition zone (ITZ) between coarse aggregate and UHPFRC matrix under static loading [162,262]. It does not have sufficient time to seek the weak ITZ under impact loading, and directly develops through the aggregates as the shortest fracture path, which is in line with [162]. This forced fracture pattern under a higher loading rate contributes to enhanced fracture energy absorption and corresponding higher impact resistance of UHPFRC in the presence of relatively stiffer and stronger coarse basalt aggregates.

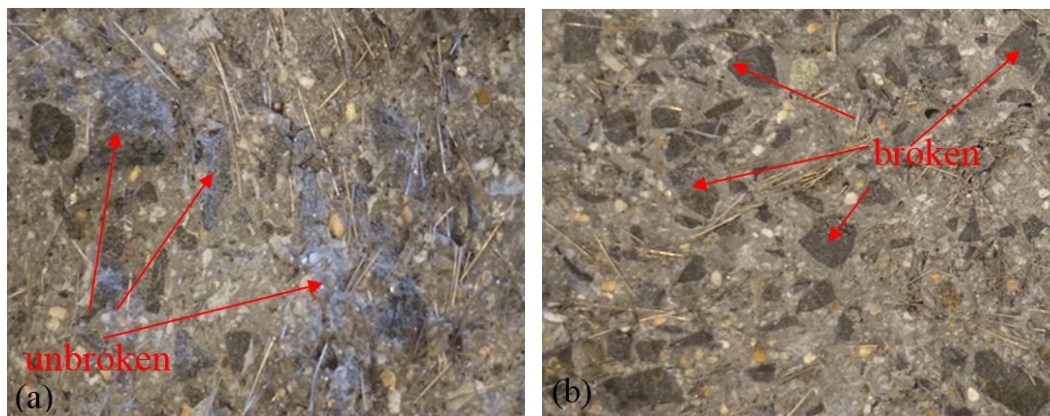


Figure 7.8: Aggregate under static (a) and impact (b) loading.

- **Energy dissipation**

The impact resistance of UHPFRC under pendulum impact can be defined as energy dissipation or energy absorption capacity. Figure 7.9 shows the absorbed energy of UHPFRC beam during each impact, calculated by Eq. (7.1). During the first three impacts, the UHPFRC beam can absorb approximately 160 J, which is about 46% of the total impact energy of hammer (346 J). After the first impact, the UHPFRC beam still has relatively high stiffness, which will be illustrated in the following analysis. The impact is more like an elastic collision, which leads more gravitational potential energy of hammer to transfer into kinetic energy of the UHPFRC beam. During the second impact, the stiffness of the partially damaged beam degenerates, more energy is dissipated by the deformation energy and fracture energy of concrete itself, leading to a slight increase of absorbed energy. With the further increase of damage degree, more and more fibres are pulled out and cracks of the matrix develop deeper and wider. The potential deformation energy and fracture energy decrease, which results in the decrease of energy dissipation of the UHPFRC beam.

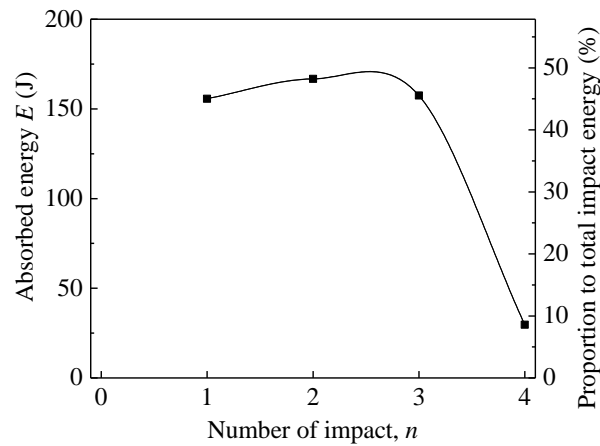


Figure 7.9: Absorbed energy during each impact.

- **Residual load-deflection relationship**

Residual properties are crucial parameters for damaged composite materials to evaluate the damage degree and structural health status. The load-deflection curves in Figure 7.10 highlight the differences in behaviour between the original (reference) beam and partially damaged beams. The curve of the reference beam can be divided into two phases of behaviour: the first phase is the elastic region, where linear behaviour is shown and no constituent materials are damaged; the second phase is the strain softening region, namely the post-peak period. There is a very wide strain softening region after crack initiation and propagation, due to the pull-out process of steel fibres without identification of any cut-off. The behaviour of the partially damaged beam can be divided into three phases. An extra short phase corresponds to the strain hardening region, which can be observed between elastic and strain softening regions, from the end of the linear elastic region to the peak flexural load. This extra strain hardening region indicates that the damaged beam undergoes some certain elastic-plastic deformation during the fibre pull-out process under bending load. The residual load-deflection curves of beams under the first and second impact still show a very good remaining load bearing capacity.

The envelopes (area covered by multiple curves) of the curves show the variation in results of repeated tests, which is likely due to local variations in fibre density and orientation [24,229]. It also should be noted that the strain hardening behaviour of the designed UHPFRC is not obvious, and a long load-deflection plateau does not occur. It is probably attributed to the utilized type and amount of steel fibres in this study [238]. Based on the analysis on the load-deflection curves, it can be concluded that the designed UHPFRC beam has an excellent ductility and residual bearing capacity, which indicates that it is suitable to be used as impact resistant composite material.

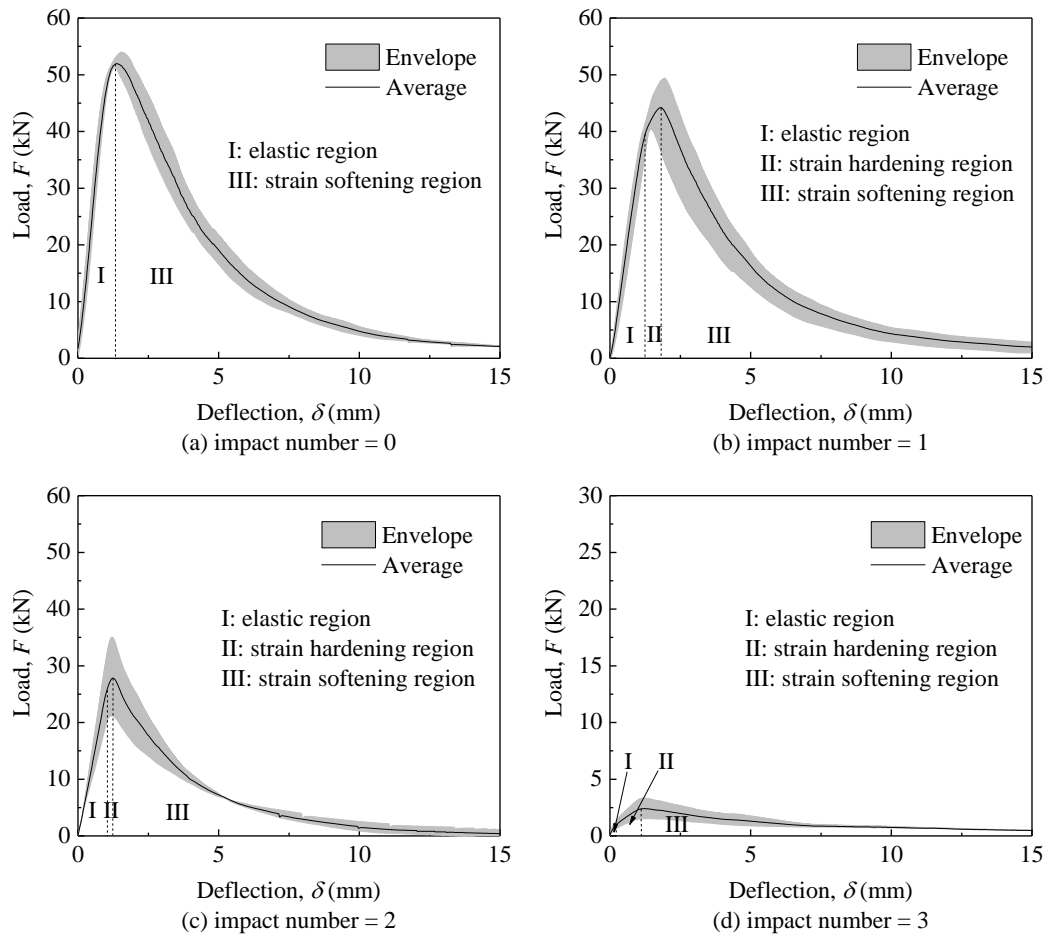


Figure 7.10: Load-deflection relationship after a certain impact number (I: elastic region, II: strain hardening region, III: strain softening region).

- **Residual strength, rigidity, toughness, impact resistance**

To further analyse and understand the post-impact properties, a number of key parameters are deduced based on the load-deflection curves, including residual ultimate strength (ultimate flexural bearing capacity), rigidity, toughness and impact resistance.

The ultimate strength or ultimate bearing capacity (F_u) is the peak load on the load-deflection curve, which is a basic and crucial parameter of UHPFRC. The residual ultimate bearing capacity is presented in Figure 7.11(a). An empirical relation is proposed by regression analysis, following ‘ $-e^x$ ’ law with the number of impacts. The strength of UHPFRC beam decreases slightly after the 2nd impact, which means the UHPFRC retain a large percentage of its bearing capacity at the first several impacts.

The flexural rigidity (EI) is defined as the force couple to bend a non-rigid structure or component in one unit of curvature, which can be deduced from the moment-curvature relation,

$$\frac{1}{\rho_r} = \frac{M(x)}{E_Y I} \quad (7.3)$$

where ρ_r is the radius of curvature, $M(x)$ is the bending moment at the position of x along the length, E_Y is the Young’s modulus, and I is the cross-section moment of inertia. The

parameters in this paper are all in SI units. Considering the Bernoulli hypothesis (plane cross-section assumption), the small deformation theory and the boundary condition in this study [263,264], the flexural rigidity can be determined from calculating the concentrated load and corresponding deflection,

$$E_Y I = \frac{FL_b^3}{48\delta} \quad (7.4)$$

where F is the concentrated load at the elastic region from central point bending test, L_b is the length of the beam, δ is the bending flexural deflection. A linear relation is obtained with the number of impacts, as shown in Figure 7.11(b). Unlike the residual strength, the residual flexural rigidity tends to decrease linearly.

The flexural toughness (T_f), representing energy absorption capacity, can be determined from the area under the load-deflection curve from the flexural test,

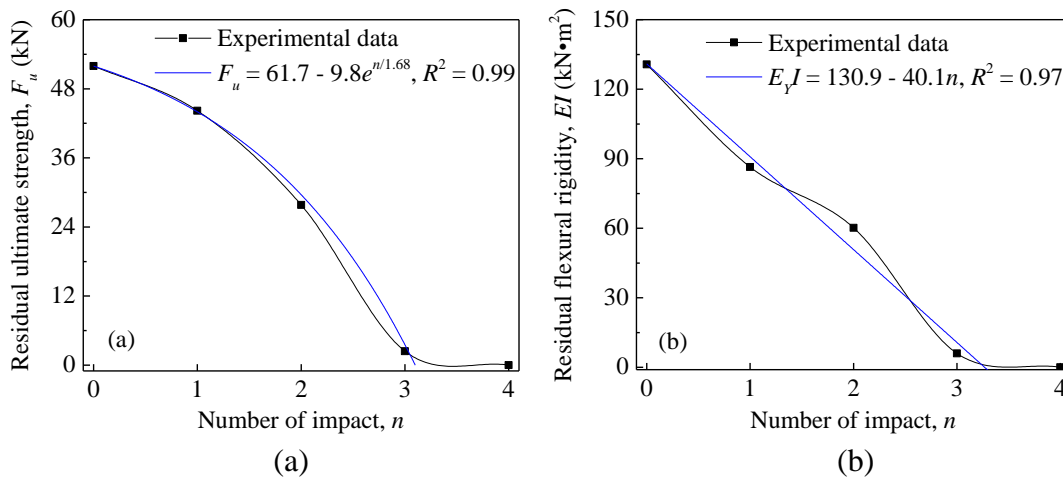
$$T_f = \int_0^{\delta_u} F(\delta)d\delta \quad (7.5)$$

where δ_u is the maximum deflection, $\delta_u = 15$ mm in this study. The residual flexural toughness can be expressed by a regressed linear relation, as illustrated in Figure 7.11(c). It is obvious that the residual toughness shares a similar decrease tendency as residual flexural rigidity, which indicates the residual toughness is more relevant to the rigidity rather than strength under low-velocity impact loading.

The residual impact resistance (E_r) can be represented by the remaining energy dissipation capacity, which is calculated as follows,

$$E_r = \sum_n^{n_u} E(n) \quad (7.6)$$

where $E(n)$ is the absorbed energy during the impact number of n , based on Eq. (7.1); n_u is the total impact number till to complete damage. The regressed relation shows an ideal linear decrease, as shown in Figure 7.11(d). The similar linear decreases indicate that it is possible to associate residual impact resistance with residual flexural rigidity and residual toughness.



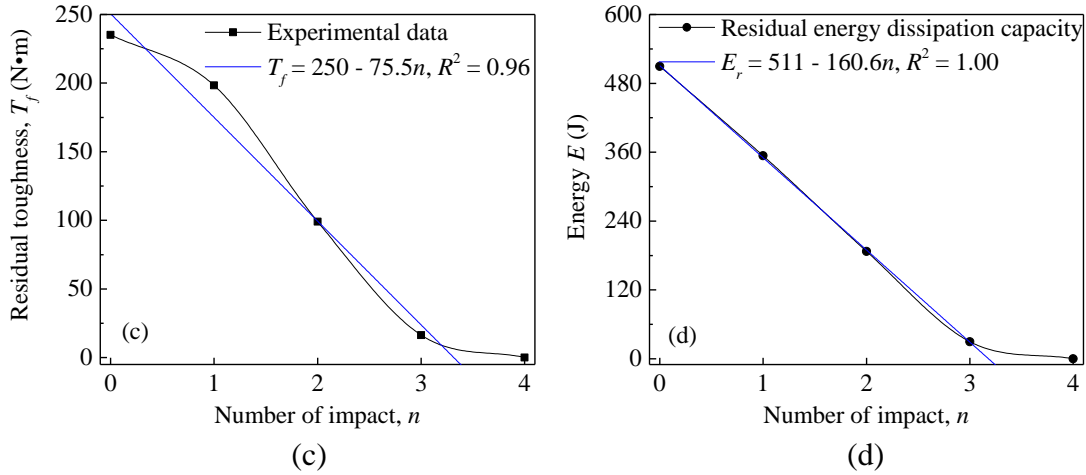


Figure 7.11: Residual strength (a), rigidity (b), toughness (c) and impact resistance (d).

- **Damage index and levels**

It is of great significance to evaluate the damage degree and health status of protective concrete structures or components after impact events. For instance, residual ultimate bearing load and impact resistance can provide insights on assessment of the service ability subjected to both static and impact loading. Hence, it is important to propose a damage index to describe the damage degrees and levels of UHPFRC under repeated low-velocity impact loading.

In order to analyse the damage degree development, regression analysis is used to develop empirical relations, based on the collected experimental database. Empirical models are proposed to predict the post-impact properties with the number of impacts (n) except for the last impact, including residual strength, flexural rigidity, flexural toughness, and impact resistance,

$$F_u(n) = 61.7 - 9.8e^{n/1.68} \quad (7.7)$$

$$E_y I(n) = 130.9 - 40.1n \quad (7.8)$$

$$T_f(n) = 250 - 75.5n \quad (7.9)$$

$$E_r(n) = 511 - 160.6n \quad (7.10)$$

A function of damage index is suggested to describe the damage degree in this study [265,266],

$$D(n) = 1 - \frac{A(n)}{A(0)} \quad (7.11)$$

where $A(n)$ represents a certain property of UHPFRC, such as ultimate bending load, flexural rigidity, flexural toughness or impact resistance. $A(0)$ is the initial property before any impact. According to Eqs. (7.7) - (7.11), the damage indexes of different post-impact properties can be written as,

$$D(n)|_{F_u} = 0.189(e^{n/1.68} - 1) \quad (7.12)$$

$$D(n)|_{E_{yI}} = 0.306n \quad (7.13)$$

$$D(n)|_{T_f} = 0.302n \quad (7.14)$$

$$D(n)|_{E_r} = 0.314n \quad (7.15)$$

Based on these damage indexes, the impact damage degree can be classified mainly into three levels [267]. The first level is light damage with a damage index of 0-0.5, corresponding to the first impact in this study. Only micro cracks occur in the UHPFRC beam at this stage. The UHPFRC beam is still usable, due to the large residual bearing capacity and impact resistance. The second level is medium damage with a damage index of 0.5-0.75, corresponding to the second impact in this study. The crack propagates longer and wider to a macro crack, and steel fibres slip from the matrix. The UHPFRC beam cannot be used or maybe still usable in some unimportant component, attributed to the degeneration of mechanical behaviour. The third level is severe damage with a damage index of 0.75-1, corresponding to the third and last impact in this study. The crack grows rapidly till the complete damage and steel fibres are pulled out. The UHPFRC beam cannot be used anymore because of almost entire loss of mechanical properties.

7.4 Results of drop-weight impact tests

The excellent flexural toughness shown by the designed FGCBs demonstrates that they possess excellent energy absorption capacities, which indicates that they are suitable to be applied in impact resistant components and structures. The impact resistance of the designed FGCB is described by the failure impact number and total energy dissipation under the drop-weight impact test, as seen in Table 7.3. The reference FGCB is very brittle and broken into two parts from the centre after only one impact (124 J), as shown in Figure 7.12(a). Nevertheless, the impact resistance of the designed FGCB is considerably improved and can withstand multiple impacts. An example of the failure pattern of FGCB with steel fibres is illustrated in Figure 7.12(b). The 30 mm medium hook-ended steel fibres provide the best reinforcement on the impact resistance of the designed FGCB, which is in line with the results of flexural properties. The FGCB incorporating 13 mm short straight and 60 mm long 5D steel fibres only provide about half the energy dissipation of the 30 mm medium hook-ended fibres in the case of 2 vol.% volume dosage. With the increase of medium steel fibres dosage from 1 vol.% to 3 vol.%, the failure impact number is enlarged from 8 times to 82 times. To sum up, the designed FGCB with 3 vol.% medium fibres has superior impact resistance and is appropriate for applications in protective materials and structures.

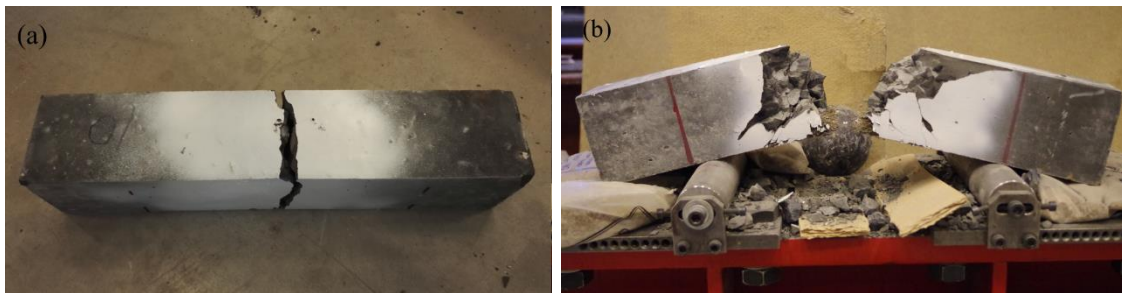


Figure 7.12: Failure after impact tests: (a) FGCB1 and (b) FGCB5 (Table 6.2).

Table 7.3: Failure impact number and total impact energy dissipation.

Mix No.	Fibre content and type	Failure impact number	Energy dissipation (J)
FGCB1	0	1	124
FGCB2	2 vol.%, short	30	3720
FGCB3	2 vol.%, medium	64	7936
FGCB4	2 vol.%, long	29	3596
FGCB5	1 vol.%, medium	8	992
FGCB6	3 vol.%, medium	82	10168

7.5 Predicting low-velocity impact resistance by static properties

It is widely accepted that it is much more difficult to determine dynamic properties (e.g. impact resistance or energy absorption capacity) of UHPFRC than its static properties, due to the complexity of the required test. Until now there is no standard impact method to measure the impact resistance of UHPFRC, most dynamic or impact testing methods reported in literature are too complex and costly compared to the static properties tests. Thus, it is of great significance if we can predict the impact resistance of UHPFRC by its static properties.

When we compare the flexural properties and energy dissipation of UHPFRC beams combined with steel fibres and coarse aggregates (as seen in Sections 7.3.1 and 5.3.2), the impact resistance is greatly dependent on the flexural behaviour. Therefore, it is postulated to predict the impact resistance by flexural properties, which is much easier and more economical to provide guidance for both researchers and engineers. Furthermore, in Section 7.3.2, it was shown that the residual impact resistance in Eq. (7.15) shares a similar damage index equation with residual rigidity and toughness by comparing with Eqs. (7.12) - (7.14), as the degeneration rates are almost the same. Hence, the flexural rigidity and toughness are more appropriate as indicators than ultimate bearing capacity, which can be used to predict the residual impact resistance of UHPFRC beams. Considering the fact that both impact resistance and flexural toughness reflect the energy absorption capacity, it is more reasonable to predict the impact resistance by flexural toughness. In addition, the impact resistance of the designed FGCBs are also associated to the flexural toughness, as shown in Sections 7.3.3 and 6.3.2. Hence, a linear empirical model is proposed to predict the impact resistance, based on the acquired experimental database,

$$E = k \cdot T_f \quad (7.16)$$

The correlation coefficient k should show a loading rate effect, which is mainly determined by the hammer (e.g. mass, velocity, texture), specimen (e.g. shape, size, texture), support and boundary condition. There are three different correlation coefficient values for the three different cases of impact tests, as illustrated in Figure 7.13. Because the toughness should vary at different impact conditions or loading rates [268], which could affect the energy absorption and consequently the value of k .

The value of k is approximately 7.6 ($R^2 = 0.96$) for the unnotched beam $150 \times 150 \times 550 \text{ mm}^3$ under pendulum impact energy of 698 J, which is much larger than the notched beam with

the same size but a smaller initial impact energy of 346 J, namely $k = 2.0$ ($R^2 = 0.96$). This enlarged k is probably due to the increased dynamic properties by the higher loading rates under much stronger impacts [162,269,270]. And, the correlation coefficient k is around 21.0 ($R^2 = 0.97$) for the unnotched FGCB beam under a drop-weight impact energy of 124 J. Although the correlation coefficient changes subjected to different low-velocity impact events, the proposed linear model always fits very well to the experimental results. Thus, the flexural toughness seems always to be a good indicator for the impact resistance of an ultra-high performance cementitious composite beam under different low-velocity impact tests, and a linear correlation exists.

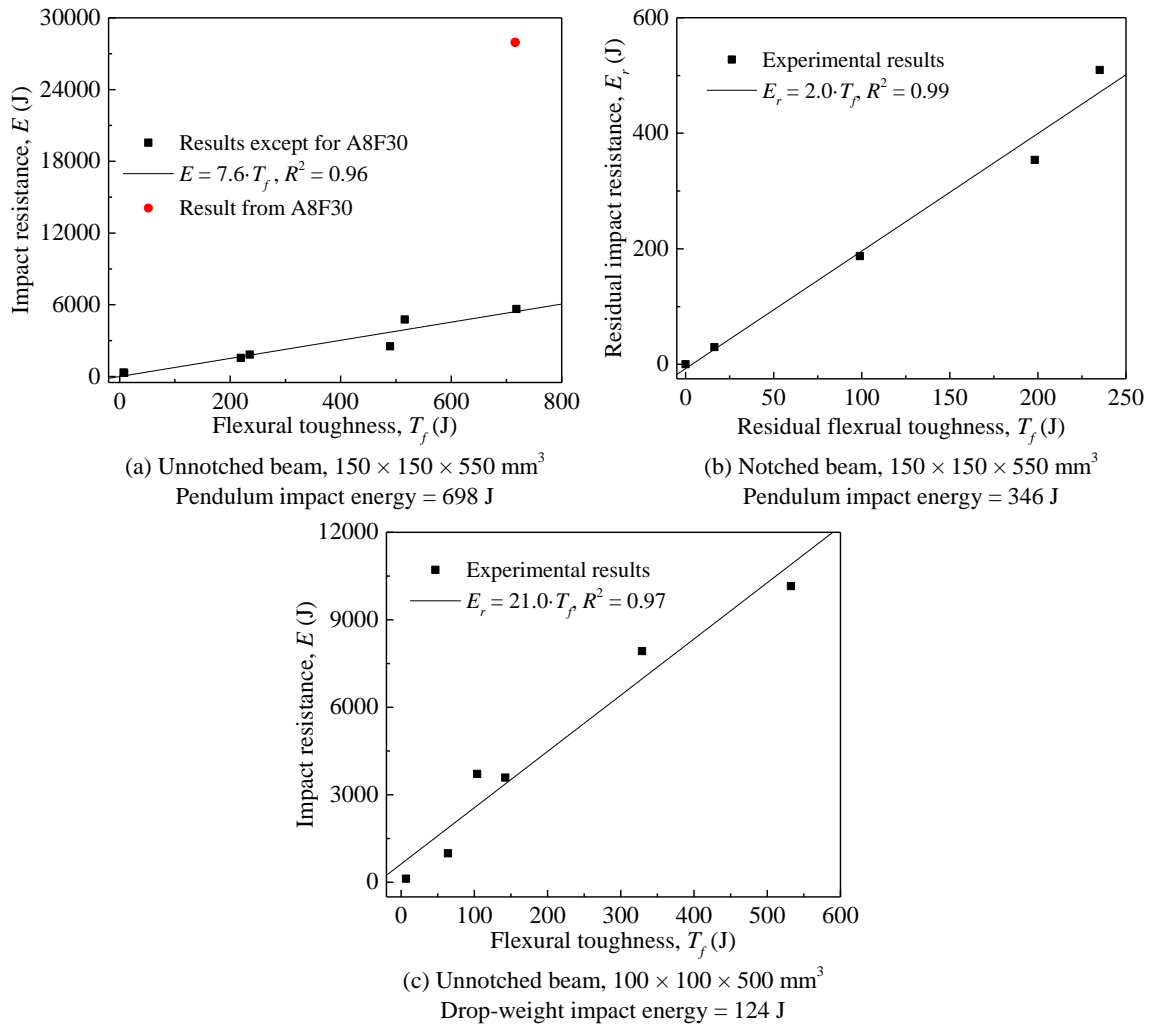


Figure 7.13: Correlation between impact energy and flexural toughness.

It should be noted that the result of specimen A8F30 does not fit to this linear model, which shows an impact resistance above the trend line. Because the beam of A8F30 possesses the highest flexural strength as shown in Figure 5.8, the stress induced by impacts is possibly below the elastic limits. Thus, the plastic deformation and damage is very limited, resulting in a relatively high residual strength and impact resistance. Figure 7.14(a) illustrates the residual strength of composites under different impact energy levels [271], with an obvious threshold value of impact energy. Below the threshold energy, the residual strength remains stable. Thus, there is almost no or only slight damage and the element can withstand many

repeated impacts. Figure 7.14(b) shows a parabolic relationship between the impact number and impact energy. Under the impact energy higher than the threshold, only a few impact number is observed. When the impact energy value is lower than the threshold, the impact responses behave elastically, resulting in a significant increase of impact numbers [251].

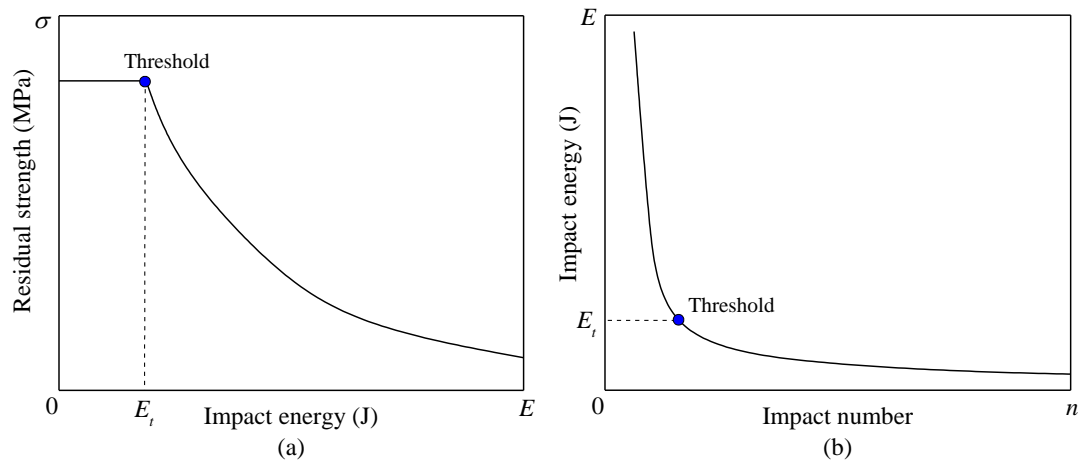


Figure 7.14: Effect of impact energy on (a) residual strength and (b) impact number.

Hence, the impact resistance of UHPFRC beam (absorbed energy or impact number) is greatly dependent on both flexural strength and toughness. It is mainly attributed to the flexural strength when subjected to impacts with impact energies below the threshold energy. While, flexural toughness determines the impact resistance and shows a linear correlation, if the impact energy is beyond the threshold.

7.6 Conclusions

This chapter researches the low-velocity impact resistance of designed UHPFRC by pendulum and drop-weight impact devices. The synergistic effect of steel fibres and coarse aggregates, damage development and post-impact properties, and superiority of functionally graded composite component are investigated and analysed. Finally, prediction of impact resistance by static properties is proposed. The key conclusions can be summarized as below:

- Coarse basalt aggregates up to 25 mm can be successfully introduced to reduce cement consumption and cost in UHPFRC for developing impact resistant construction materials. In the presence of coarse aggregates, the 30 mm medium hook-ended and 60 mm long 5D fibres are more efficient in reinforcing impact resistance than the 13 mm short straight ones.
- Damage of fibres and coarse aggregates under impact loading is severer than that under static loading. Most aggregates are broken at the fracture cross-section, which directly demonstrates that they contribute and improve the impact resistance under impact loading.
- Under the impact loading, the residual strength of UHPFRC beams follows ' $-e^x$ ' law with the number of impacts, while the residual rigidity, toughness and impact resistance follow a linear decrease. The residual impact resistance has a similar damage index as the residual flexural rigidity and toughness. The crack depth and width of UHPFRC

beam are not propagated simultaneously, crack depth is developed more quickly at the initial several impacts.

- The novel concept of FGCB is has superior impact resistance, as well as high cement and steel fibre utilization efficiencies. Here, 3 vol.% 30 mm hook-ended fibres are suggested for FGCB to design impact resistant component with an optimum bottom-to-total layer ratio β_{layer} of 0.46, considering both performance and fibre utilization efficiency.
- The toughness is a good indicator to reflect the low-velocity impact resistance of UHPFRC beams. A linear analytical model can be introduced to describe this correlation. While, the low-velocity impact resistance is also greatly influenced by the flexural strength when subjected to impacts with an impact energy below the threshold energy.

Chapter 8

Bullet impact resistance of UHPFRC

This chapter investigates the key parameters concerning high-velocity impact resistance of ultra-high performance fibre reinforced concrete (UHPFRC) by in-service bullet, with the aim to provide design guidance for the engineering applications. The effects of steel fibre type and dosage, matrix strength, coarse basalt aggregates, and target thickness are researched by subjecting the UHPFRC to a 7.62 mm bullet shooting with velocities of 843-926 m/s. The results show that the UHPFRC, designed by using a particle packing model with compressive strength around 150 MPa, is appropriate to develop protective elements considering both anti-penetration performance and cost-efficiency. The 13 mm short straight steel fibres show better anti-penetration than the 30 mm hook-ended ones, and the optimum volume dosage is approximately 2 vol.% by considering both the penetration and crack inhibition. Introducing coarse basalt aggregates with particle sizes up to 25 mm into UHPFRC reduces the powder consumption from 900 kg/m³ to 700 kg/m³, and results in slightly higher mechanical strength and significantly enhanced bullet impact resistance (14.5% reduction of penetration depth). The safe thicknesses (perforation limit) of the designed UHPFRC slabs are approximately 85 mm and 95 mm to withstand the 7.62×51 mm NATO armor-piercing bullet impact with velocity 843 mm/s and 926 mm/s, respectively.

This chapter is partially published elsewhere:

P.P. Li, H.J.H. Brouwers, Qingliang Yu. Influence of key design parameters of ultra-high performance fibre reinforced concrete on in-service bullet resistance. *Internal Journal of Impact Engineering*. 136 (2020) 103434.

8.1 Introduction

Extreme conditions or accidental loadings surrounding our human life have attracted more and more public attention, such as explosive or ballistic impact in terrorist attacks, natural earthquake or hurricane disasters, vehicle impact in traffic accidents, and ship collisions on offshore structures or bridges [7,8]. Concrete is one of the mostly widely utilized construction materials in both civil and defence engineering, and its projectile impact properties (e.g. penetration depth, perforation, crack propagation) are always an important concern. Among the diverse types of concretes, ultra-high performance fibre reinforced concrete (UHPFRC) has great potential for civil and military applications, owing to its superior workability, mechanical strength, toughness and energy absorption capacity [6,9–13]. UHPFRC has been developed since the 1990s, and its mix design and basic static properties have been extensively investigated [1,2,28,79,160]. However, the phase composition, microstructure and response behave very differently under impact loadings compared to static load [14–17]. Furthermore, the dynamic properties and damage patterns exhibit large differences when subjected to different impact loadings, such as drop-weight or pendulum impact, seismic effect, projectile impact, blast, etc. [7,18]. Hence, the material or even structural design principles should differ based on the different specific loading type, instead of simply considering static performance. This study aims to optimize the mix design of UHPFRC and research the influence of key parameters on ballistic impact properties subjected to the in-service 7.62×51 mm NATO armor-piercing bullets.

The matrix strength class greatly influences the anti-penetration of concrete under the high-velocity projectile impact. Many experimental results and analytical models indicated that the depth of penetration (DOP) under projectile impact has an inverse relationship with the compressive strength [272,273], which means that concrete with a higher compressive strength contributes to a better bullet impact resistance. Currently, the compressive strength of UHPFRC is usually achieved within a large range from about 120 MPa to 200 MPa [6,160]. The high strength of UHPFRC can be obtained by using some special design principles, such as a low water amount with a high dosage of superplasticizer, a large amount of cement, steel fibre addition, thermal and chemical activation, and extra pressurization treatment before final setting [1,274]. All those methods tend to enlarge the cost of UHPFRC. Thus, a better ballistic impact resistance normally goes with the sacrifice of economic benefits. How to keep a balance between impact performance and strength/cost of UHPFRC is of great significance for its wider engineering application. This study attempts to research the effect of matrix strength on the projectile impact resistance, and suggests an appropriate efficient matrix strength of UHPFRC in protective elements and structures.

Steel fibres are another key ingredient in UHPFRC to strengthen the bullet impact resistance. They are considerably efficient to enhance the stress transfer capability beyond elastic state and improve the energy absorption capacity [7,211]. The ‘bridge effect’ by the steel fibres contributes to restraining crack propagation and benefits the multiple bullet striking bearing capacity. Furthermore, steel fibres significantly reduce the fragments induced by the scabbing and spalling, which consequently decreases the secondary harm by the concrete fragments. Meanwhile, the enhanced crack inhibition capacity by steel fibres helps to

maintain the integrity of concrete targets, which provides a certain confinement on the impact position by the surrounding material, and ease the inner local impact damage. However, the steel fibre reinforcement is greatly dependent on the fibre content and shape [20,23]. Moreover, the utilized high-strength steel fibres in UHPFRC are much more expensive compared to other raw materials. Therefore, steel fibres should be optimized in UHPFRC in terms of type and content by comprehensively considering the DOP, crack resistance and steel utilization efficiency, to achieve a cost-efficient protective component and structure.

Conventional UHPFRC is usually developed without applying coarse aggregates to achieve a better homogeneity and avoid inherent stress concentrations [1,2]. Coarse aggregates were introduced into UHPC system, in order to reduce the cost and powder consumption, increase volume stability and even mechanical strength. Furthermore, some researchers found that concrete containing coarse aggregates contributes to enhanced high-velocity projectile impact resistance, attributing to the mass abrasion and trajectory deviation of the projectile by coarse aggregates with high hardness index [272]. Zhang et al. [273] reported that coarse granite aggregates addition could reduce the DOP and crater diameter of high strength concrete by a 12.6 mm ogive-nosed projectile. Wu et al. [166,168] investigated the effects of coarse basalt and corundum aggregates on the impact resistance of UHPFRC by reduce-scaled (25.3 mm) ogive-nosed projectiles, and suggested that aggregate sizes should be 1.5 times larger than the diameter of projectile. However, the ballistic impact resistance of UHPFRC with coarse aggregates by smaller projectiles (e.g. the in-service 7.62 mm NATO armor-piercing bullet) should be more sensitive to the aggregates' sizes and contents, due to the high variability when hitting the mortar matrix or a coarse aggregate. Thus, the effect of coarse aggregates on small bullet impact resistance should be researched and identified.

The objective of this study is to explore the influence of key parameters on impact resistance of UHPFRC subjected to the in-service 7.62×51 mm NATO armor-piercing bullet with velocities of 843-926 m/s, and propose a design guideline for relevant engineering applications. Five UHPFRC matrixes are designed by using a particle packing model, and 37 cylindrical targets are prepared to study the effects of steel fibre type and dosage, matrix strength, coarse basalt aggregate, and target thickness. The mechanical strength, penetration depth and damage pattern are measured and analysed. The appropriate strength class, steel fibre type and content, coarse aggregates addition are attained by comprehensively considering penetration depth, crack inhibition and cost-efficiency. Furthermore, safety thicknesses (perforation limit) of the designed UHPFRC slabs are suggested in order to withstand the in-service 7.62×51 mm NATO armor-piercing bullet impact, which provides guidance and reference to the future design of protective components and structures.

8.2 Materials and testing methods

8.2.1 Materials and mix design

The ingredients of UHPFRC mixtures include Portland cement (PC), limestone powder (LP), micro-silica (mS), normal sand (S), coarse basalt aggregates (BA) with different sizes, steel fibres with different types (SF), superplasticizer (SP3 from Chapter 2 is used) and tap water

(W). The detailed physical and chemical properties of powders can be found in Section 3.2.1, 3.3.1, 4.2.1 and 4.3.1. Two different steel fibres are used, namely 13 mm (short) straight fibre and 30 mm (long) hook-ended fibre, as described in Section 5.2.1.

Five UHPFRC matrixes are designed with the maximum aggregate size (D_{\max}) ranging from 2 mm up to 25 mm, as presented in Table 8.1. 20% limestone powder and 5% micro-silica are added to partially replace the cement by mass, considering both sustainability and performance. The powder content is reduced from 900 kg/m³ to 700 kg/m³ with D_{\max} increasing from 2 mm to 25 mm, due to the fact that coarse aggregates contribute to less demand of powder in concrete [125,209,216]. The fractions of aggregates are determined based on the particle packing model, as described in Section 4.2.2. UHPC incorporating coarser aggregates tends to a smaller distribution modulus q in Chapter 4, and the specific q values and PSD curves of designed UHPFRC matrixes are shown in Figure 8.1(b). The match of the target lines and designed lines confirms the packing quality of the designed mixes. The water and superplasticizer amounts are adjusted to achieve self-compacting.

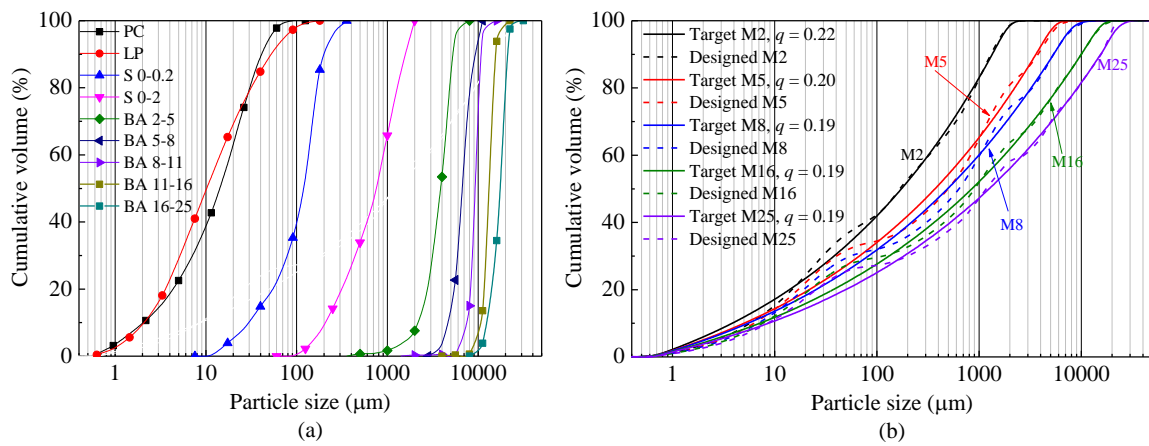


Figure 8.1: Particle size distributions of (a) ingredients and (b) designed mixtures.

Table 8.1: Recipes of designed UHPFRC matrixes (kg/m³).

Mix.	PC	mS	LP	S	S	BA	BA	BA	BA	BA	W	SP
				0-0.2	0-2	2-5	5-8	8-11	8-16	16-25		
M2	675.0	45.0	180	276	1067	-	-	-	-	-	182.0	9.0
M5	637.5	42.5	170	-	988	488	-	-	-	-	174.3	8.5
M8	600.0	40.0	160	-	911	410	249	-	-	-	168.0	8.0
M16	562.5	37.5	150	-	743	390	195	127	192	-	161.3	7.5
M25	525.0	35.0	140	-	667	367	173	121	64	365	154.0	7.0

8.2.2 Specimens preparation

To investigate the effects of steel fibre type and dosage, matrix strength, coarse aggregate size, slab thickness, and impact velocity on the ballistic resistance, 37 cylindrical specimens are prepared, as listed in Table 8.2. Some targets are duplicate to check the experimental variation. The diameter of all targets are fixed at 300 mm, which is much more than 30 times the projectile diameter, thus achieving negligible boundary effects [166]. All the samples are cast in mould and covered by a plastic film, and demoulded after 24 hours. After curing for another 27 days (see details in Table 8.2), the ballistic tests on all targets are conducted.

Table 8.2: UHPFRC recipes and hardening.

Groups	Matrix No.	Thickness (mm)	Impact velocity, V (m/s)	Fiber type & dosage (vol.)	Curing regime
Matrix strength effect	M2	120	843, 926	2% straight	1 d heat curing (60 °C/80 RH), 26 d water curing. 5 d heat curing (60 °C/80 RH), 22 d water curing.
Fibre effect	M2	120	843	0 1%, 2%, 3%, 5% straight 1%, 2%, 3% hook-ended	27 d water curing
Aggregate size effect	M5 M8 M16 M25	100	843, 926	2% straight	27 d water curing
Thickness effect	M2	60 ~ 140	843, 926	2% straight	27 d water curing

8.2.3 Testing methods

The tensile splitting and compressive strengths of each UHPFRC mix are based on the methods described in Section 4.2.3.

The in-service 7.62×51 mm NATO armor-piercing bullets are used for the ballistic impact test on UHPFRC targets, as shown in Figure 8.2. Two striking velocities of the projectile, recorded by a radar velocity system, are utilized in this study by changing the powder amount in the shell case. The projectile consists of outside brass jacket (2.5 g) and inside hard steel core (5.9 g). The 7.62 mm calibre launching device and target supporting frame are presented in Figure 8.3. The distance between UHPFRC target and the launching device is around 30 m, based on the standard of NATO STANAG 2280 [276]. The target supporting frame is fixed on the ground to avoid any variation or movement. A white paper board is placed behind the supporting frame to witness any probable perforation.

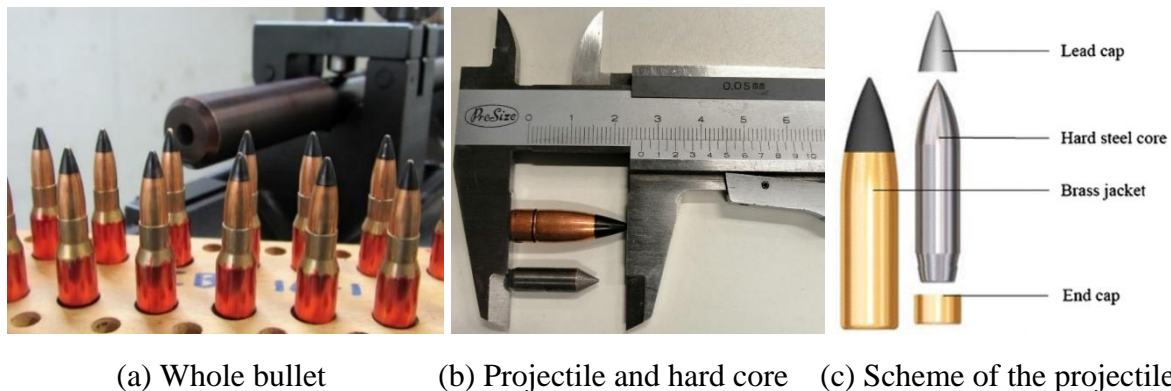
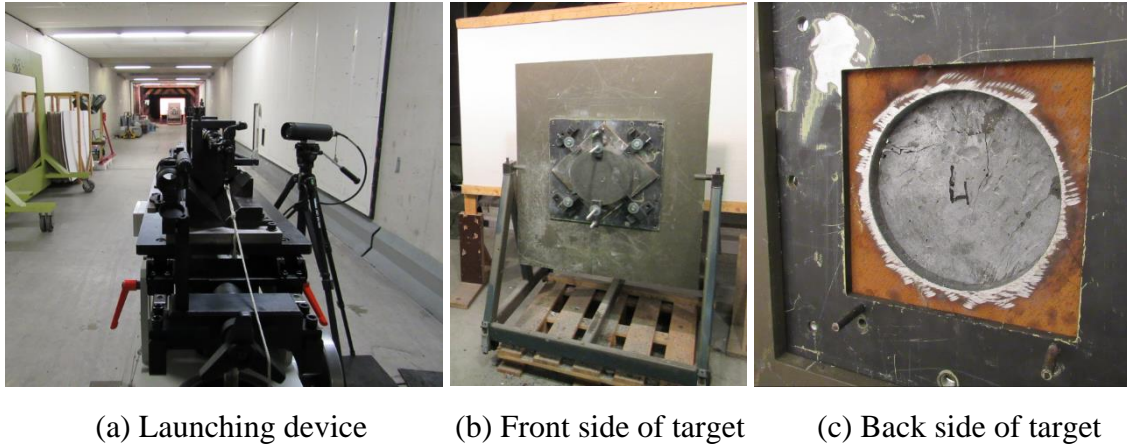


Figure 8.2: 7.62×51 mm NATO armor-piercing bullet.



(a) Launching device (b) Front side of target (c) Back side of target

Figure 8.3: Launching device (a), and front (b) and rear (c) side of target.

After the ballistic test, the UHPFRC target is cut from the centre of impact point along its longitudinal direction (as semi-cylinder), in order to observe the cross-section damage pattern and measure the penetration depth, as illustrated in Figure 8.4. In general, a crater is observed on the impact side, while spalling and scabbing occurred on the rear side. The outside brass jacket is usually destroyed and peeled off during the cratering process, subsequently the hard steel core penetrates deeper and creates a tunnel. The depth of penetration (DOP) of UHPFRC targets includes both crater depth and tunnel depth. The projectile could perforate a target completely depending on the quality of concrete and speed of bullet.

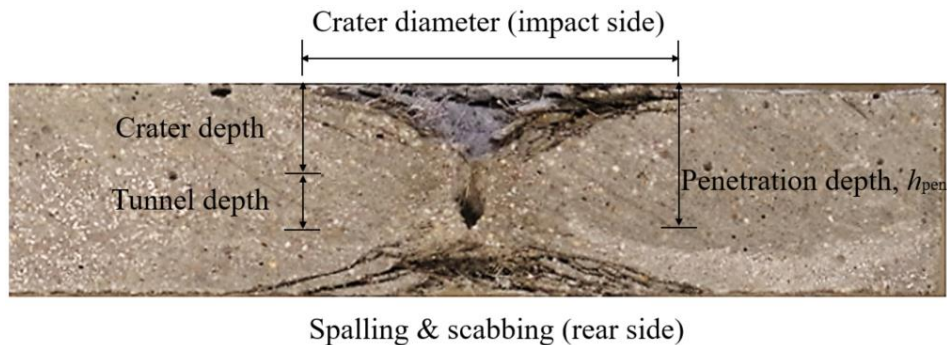


Figure 8.4: Typical damage pattern of UHPFRC target.

8.3 Results and discussion

8.3.1 Effect of matrix strength

The DOP is one of the most critical responses of UHPFRC under high-velocity projectile impact, which is adversely related to the compressive strength. To identify the effect of matrix strength, the different matrix strength classes of UHPFRC targets are achieved by different curing regimes without changing other key parameters of the recipes, as illustrated in Table 8.2. The correlations between DOP and UHPFRC compressive strength are shown in Figure 8.5. For a reference UHPFRC mixture (M2 with 2 vol.% straight fibres) with normal 27 d water curing after demoulding, the compressive strength reaches 143.3 MPa. While, the compressive strength is enhanced to 154.3 MPa with 1-day extra thermal curing

(60 °C/80% RH), and further increased up to 162.9 MPa applying the same thermal curing after demoulding but with a duration of 5 days.

For the mixtures with different strength classes, the DOP varies from around 62 mm to 57 mm at the striking velocity of 843 m/s, and between 76 mm and 73 mm under the striking velocity of 926 m/s. Generally, a higher compressive strength tends to a better anti-penetration capacity (smaller DOP), which is in line with other investigations about high-velocity projectile penetration of concretes [232,277,278]. Furthermore, many representative DOP prediction models, such as U.S. Army Corps Engineers model, the National Defence Research Committee model, and Li and Chen's model, have indicated that DOP is correlated to the square root of compressive strength [272,273,279]. Therefore, the trend lines are regressed and plotted in Figure 8.5, as followed by

$$\text{DOP} = k/\sqrt{\sigma_c} + d_p \quad (8.1)$$

where k is a content value, d_p is the diameter of projectile. According to the fitting trend lines, the values of DOP can be further reduced to as low as 55 mm and 69.4 mm with a compressive strength of 180 MPa under the low and high striking velocities, respectively. The improvement degrees of penetration resistance of UHPFRC are very limited, compared to the UHPFRC mixture with the compressive strength of around 150 MPa. It also should be noted that it is relatively easy to develop a ~150 MPa UHPFRC, while a higher strength (e.g. 200 MPa) usually considerably sacrifices the cost and needs extra special treatments, such as a very low water amount with a very high dosage of superplasticizer, a large amount cement, high steel fibre addition, thermal and chemical activation, and extra pressurization treatment before final setting. Hence, it is not efficient to use too high-strength UHPFRC to develop protective elements by comprehensively considering both cost and anti-penetration performance. Based on the analysis above, a compressive strength of around 150 MPa for the bullet impact resistant UHPFRC is recommended.

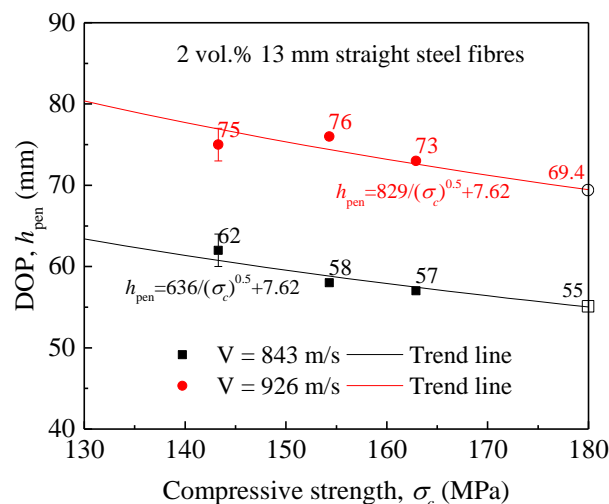


Figure 8.5: Correlation between DOP and M2 matrix strength.

8.3.2 Effect of steel fibre type and content

- **Mechanical strengths**

The mechanical strengths of UHPFRC are influenced by the steel fibre types and contents, thus affecting the impact resistance [280–282]. Figure 8.6 shows the compressive and splitting tensile strength of UHPFRC mixture with different types and contents of steel fibres. Normally, hook-ended steel fibres with appropriate length are more suitable to reinforce the mechanical properties especially for flexural strength, compared to shorter straight ones [27,213]. While, UHPFRC incorporating short straight fibres possesses a slightly higher compressive and splitting tensile strengths. This is probably attributed to the more homogenous distribution of the smaller fibres in the matrix, thus providing a better reinforcement. The compressive strength continuously increases from 130.9 MPa to 177.2 MPa when adding a straight fibre content from 0 to 5 vol.%, while the splitting tensile strength ranges between 9.5 MPa and 25.7 MPa. Namely, the improvement ratios in the presence of 5 vol.% straight fibres are 35.4% and 170.5% for compressive and splitting tensile strengths, respectively. The different reinforcing effects on compressive and tensile strengths probably indicate that the steel fibre addition preferably improves the crack inhibition capacity rather than anti-penetration resistance, which will be discussed in the following sections.

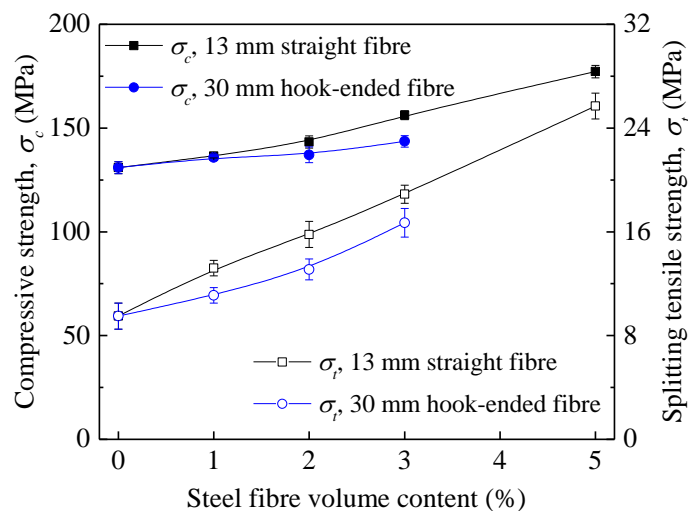


Figure 8.6: Mechanical strengths of UHPFRC with different steel fibres.

- **Depth of penetration**

The steel fibres in UHPFRC enhance the bullet impact resistance by inhibiting crack propagation, diminishing the secondary harm induced by scabbing and spalling fragments, and providing confinement on the inner local impact position. Figure 8.7 presents the DOP of the designed UHPFRC targets with two kinds of high-strength steel fibres at the bullet impact velocity of 843 m/s. The DOP of the plain target without fibre is very large, namely 78 mm. While, it sharply decreases to 66 mm and 62 mm when adding 1 vol.% 30 mm hook-ended and 13 mm straight steel fibres, namely a 15.4% and a 20.5% reduction, respectively. After that, the penetration resistance can be further gradually improved with the increase of steel fibres' dosage, e.g. a DOP of 61 mm is achieved with 3 vol.% hook-ended fibres and

58 mm with 5 vol.% straight ones. But, steel fibre addition beyond 1 vol.% seems to have limited contribution to decrease the DOP, especially in the case of the 13 mm straight fibres.

It should be pointed out that the utilization of 13 mm straight fibres seems to be more efficient to reinforce the bullet penetration resistance than the 30 mm hook-ended ones, although a long and hook shape in some cases results in better mechanical properties (e.g. flexural strength) in UHPFRC in Chapter 5. Yu et al. also revealed a similar high-velocity projectile experimental result, where the DOP is smaller with hybrid fibres (0.5 vol.% small and 1.5 vol.% large) compared to the pure 2 vol.% large ones [283]. On the one hand, the smaller DOP for UHPFRC targets with straight fibres is attributed to the higher reinforcement on both compressive and tensile strengths, as illustrated in Figure 8.6. On the other hand, the quantity density (number of fibres per kg) of straight fibre is much larger and the fibres can be distributed more homogeneously. It means that the projectile has a higher probability to strike the high-strength fibres, and consequently being subjected to heavier mass abrasion and penetration resistance. Thus, the 13 mm straight fibres are recommended for bullet resistant UHPFRC.

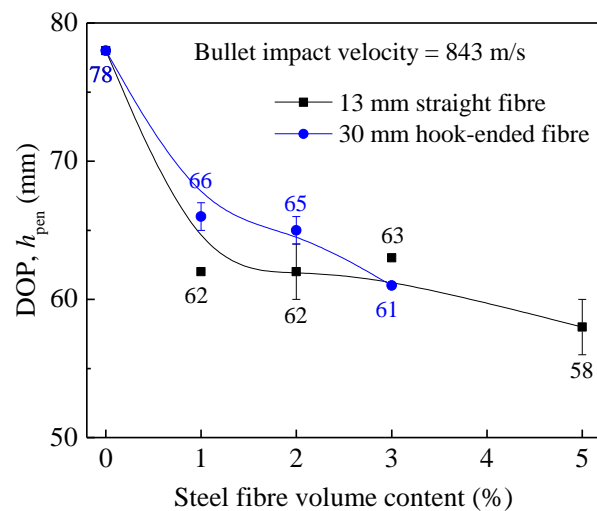


Figure 8.7: DOP of UHPFRC (M2) targets with different steel fibres.

- **Damage patterns**

As analysed above, 1 vol.% 13 mm straight steel fibres are able to provide enough reinforcement on the penetration resistance of the designed UHPFRC targets. A protective UHPFRC element also needs to possess a good crack resistance, in order to remain sufficient residual bearing capacity and relieve second harm induced by scabbing and spalling fragments. Therefore, the damage patterns of UHPFRC are observed with different straight steel fibre contents, through spraying the damage surfaces with white paint to make cracks more visible, as illustrated in Figure 8.8.

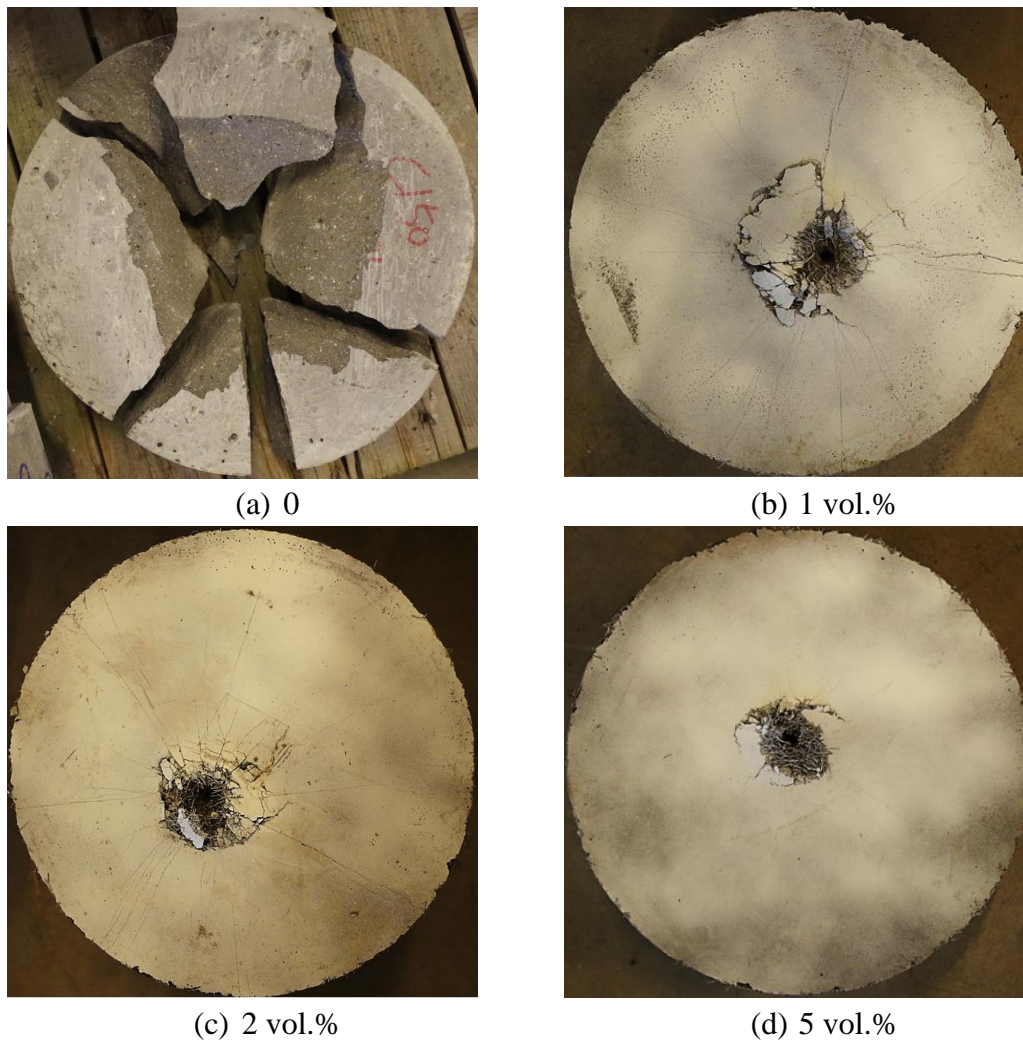


Figure 8.8: Damage patterns with different straight fibre contents.

The plain target is extremely brittle and splits into several pieces, which indicates that it cannot withstand the bullet impact. 1 vol.% steel fibres result in an integral specimen and no obvious scabbing on the rear side, but a relatively large crater and many macro cracks are observed on the impact side, as shown in Figure 8.8(b). 2 vol.% steel fibres considerably diminish the crater diameter and only some hairline cracks are visible. Continuously increasing the utilized fibre content can further improve the crack inhibition capacity, e.g. almost no visible crack is seen with fibres up to 5 vol.%, and however the crater diameter remains similar.

To sum up, the steel fibres are indispensable and play a critical role in UHPFRC towards both penetration and crack resistance when subjected to high-velocity bullet impact. 2 vol.% 13 mm straight steel fibres are suggested by comprehensively considering DOP, damage pattern and fibre utilization efficiency.

8.3.3 Effect of coarse aggregates

- **Mechanical strengths**

Figure 8.9 shows the mechanical strengths of UHPFRC incorporating different D_{\max} in the presence of 2 vol.% 13 mm straight steel fibres. For the UHPFRC with D_{\max} of 2 mm (sands),

the 28 d compressive and splitting tensile strengths attain 143.3 MPa and 15.8 MPa, respectively. The strengths fluctuate between 155.5 - 165.6 MPa and 17.5 - 19.1 MPa, respectively, when coarse basalt aggregates are introduced with D_{max} from 5 mm to 25 mm. The coarser aggregates utilization in UHPFRC usually tends to a slightly lower mechanical strength in Chapter 4. The enhanced mechanical properties probably owe to the lower absolute water amount, as presented in Table 8.1, which tends to reduce the porosity and consequently increases the packing density.

Based on the packing theory of particle size distribution, a lower fines content is needed for a mixture with coarser particles. In this study, the powder content decreases from 900 kg/m³ to 700 kg/m³ with the increase of D_{max} from 2 mm to 25 mm. Although the active binders are diluted, the mechanical strength of UHPFRC is not sacrificed. Apart from the increased packing density as mentioned above, the higher water-to-binder ratio for UHPFRC incorporating coarser aggregates contributes to improving the binder hydration degree, and thus compensating the reduction effect of absolute powder amount. Hence, introducing high-strength coarse aggregates could improve the cement utilization and economic benefits, without sacrificing or even strengthening mechanical strength.

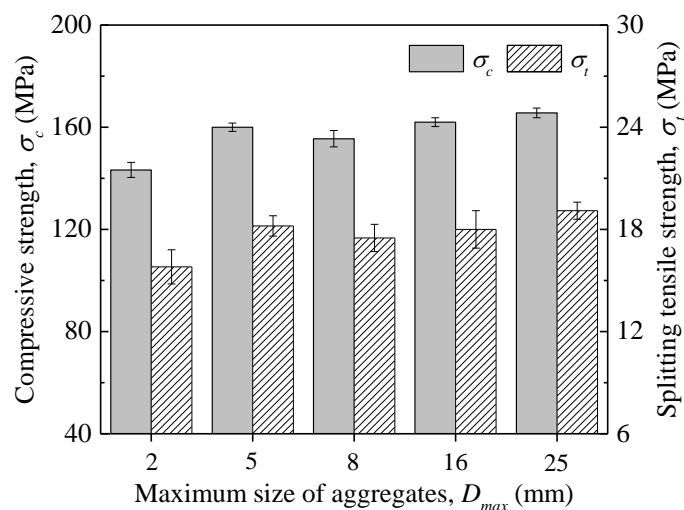


Figure 8.9: Mechanical strengths of UHPFRC with different D_{max} .

- **Depth of penetration**

Many researchers believed that high-strength coarse aggregates are beneficial for diminishing the DOP under high-velocity projectile impact, due to mass abrasion, trajectory deviation of the projectile [166,168,232,273,284]. Furthermore, in the presence of hard coarse aggregates in UHPFRC under impact loading, more fracture energy is dissipated because more cracks going through the aggregates instead of initiating along the interfacial transition zones [10,162]. But some researchers pointed out that this finding is questionable when the projectile is very small (e.g. 7.62 mm [161,285]) relative to the size of aggregates [286], because of the high variability of striking whether an aggregate or the mortar [272]. Figure 8.10 shows the DOP of UHPFRC targets with different D_{max} by the in-service 7.62×51 mm NATO armor-piercing bullets. When increasing D_{max} from 2 mm to 25 mm, the values of DOP reduce from about 62 mm to 53 mm and from 75 mm to 64.5 mm under

843 m/s and 926 m/s, respectively. Namely, the reduction ratios are approximately 14.5%, which is more efficient and cost-effective compared to the measure of fibre addition, as illustrated in Figure 8.7. The enhanced anti-penetration capacity of UHPFRC is attributed to both the enlarged D_{max} and the increased volume content of hard basalt aggregates. Wu et al. [168] suggested the hard coarse aggregate size should be larger than 1.5 times of the projectile diameter. Wang et al. [272] demonstrated critical contribution of the coarse aggregate volume fraction and the hardness. Both the volume fraction and the hardness contribute to the total effective hardness index, and this index has adversely linear relationship with the DOP. The basalt aggregates usually have much higher hardness than cementitious based mortar, which means that introducing coarse basalt aggregates contributes to total effective hardness index and then reduces DOP. Thus, UHPFRC incorporating D_{max} of 25 mm is suggested to develop protective elements by considering positive effects of both size and volume fraction of basalt aggregates.

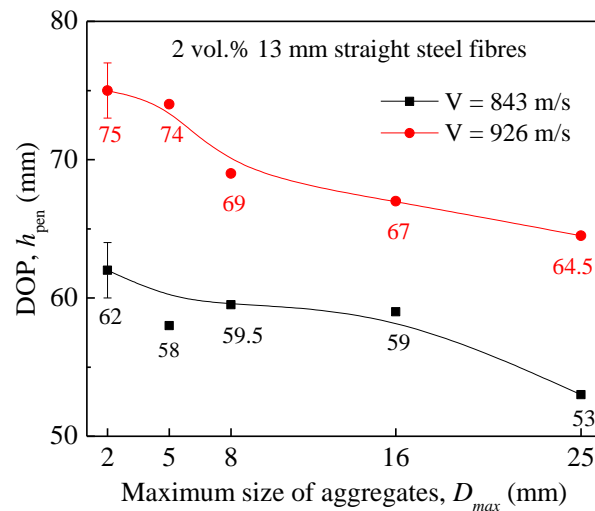


Figure 8.10: DOP of UHPFRC targets with different D_{max} .

8.3.4 Effect of target thickness

- **Perforation limit**

The perforation limit is defined as the minimum safe thickness of a target to avoid the perforation under a specific projectile impact with a given striking velocity [278,287]. The perforation limit has great significance for developing protective structures, which provides guidance to engineers to design the safe and cost-efficient structures [288–290]. In this paper, the perforation limit of the designed UHPFRC is determined from the damage observations of the targets with different thicknesses. Figure 8.11 presents the DOP of UHPFRC targets with thicknesses from 60 mm to 140 mm under striking velocities of 843 m/s and 926 m/s. For a lower striking velocity of 843 m/s, the DOP is slightly enlarged from about 59 mm to 63 mm with the decrease of the target thickness from 130 mm to 90 mm. After that, the UHPFRC target is perforated in the case of a thickness down to 80 mm, as represented by the dash line. For a higher striking velocity of 926 m/s, the DOP experiences a similar decreasing tendency, and the perforation phenomenon occurs at the thickness of 90 mm. The accurate perforation limit cannot be directly measured due to the testing thickness interval

of being 10 mm. Thus, the perforation limit is calculated as the average thicknesses of the thickest perforated target and the thinnest unperforated target. In this study, the perforation limits of the designed UHPFRC mixtures subjected to the in-service 7.62×51 mm NATO armor-piercing bullet are derived as 85 mm and 95 mm for a given striking velocity of 843 m/s and 926 m/s, respectively.

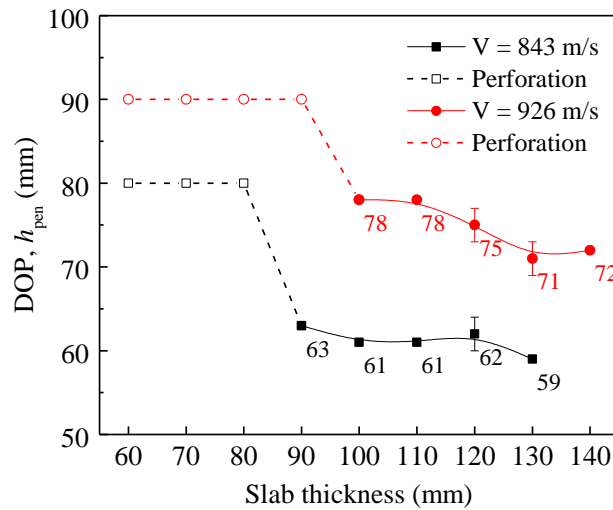


Figure 8.11: DOP and perforation limit with different target thicknesses (M2 with 2 vol.% 13 mm straight steel fibres).

- **Damage patterns**

To reveal the mechanism of target thickness effect on high-velocity bullet impact resistance, the cross-section damage patterns of UHPFRC targets with different thicknesses are observed by cutting the tested samples into semi-cylinders. Because the effects of target thickness on damage patterns at 843 m/s and 926 m/s share the same tendency, we only present those at the higher striking velocity in this paper, as illustrated in Figure 8.12.

The targets with the thickness of both 80 mm and 90 mm are all perforated. While, the damage of the thinner target is much severer, namely larger crater diameter and larger depth on the impact side, and more spalling and scabbing on the rear side. When the target thickness increases up to 100 mm, the inner hard core of projectile is stopped inside the target. There is no obvious spalling and scabbing on the back side, but two dominant macro cracks like inverted funnels are still observed inside the target. The crack resistance can be further improved with the increase of the thickness, for example a much smaller crater and no obvious macro cracks are observed in the case of a 110 mm target. The diminished damage degree of a thicker UHPFRC target is attributed to a more remarkable confinement of surrounding concrete on the inner local damage part. The impact bearing capacity of concrete can be enhanced with confinement [291–293], which consequently reduces the concrete damage degree, as well as the DOP shown in Figure 8.11.

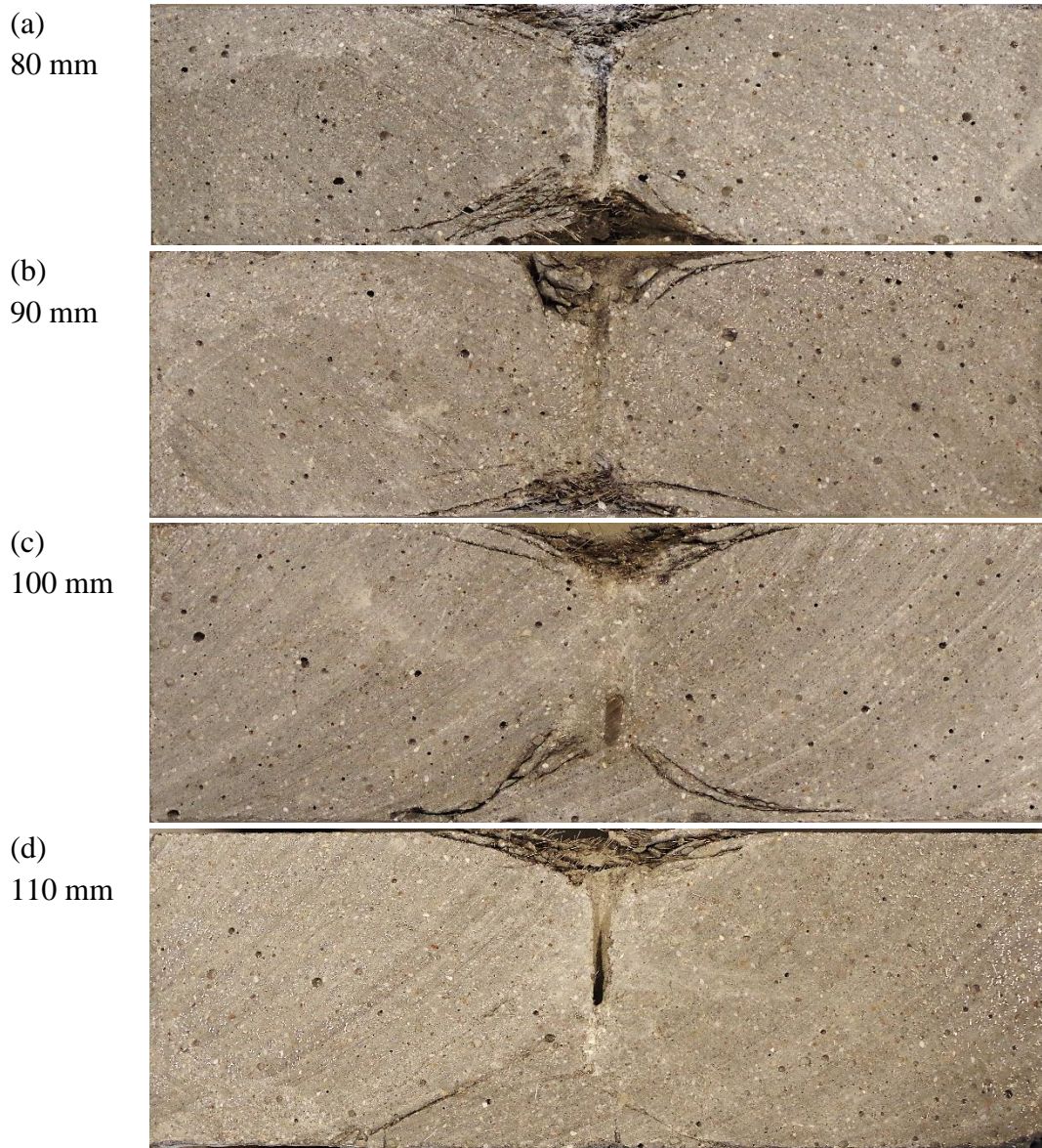


Figure 8.12: Cross-sections damage with different target thicknesses at 926 m/s (M2 with 2 vol.% 13 mm straight steel fibres).

8.4 Conclusions

This chapter investigates the key parameters of UHPFRC towards high-velocity impact resistance by in-service 7.62×51 mm NATO armor-piercing bullet. The main key parameters on penetration and crack resistance are studied, including matrix strength, steel fibre type and content, aggregate size and target thickness. The present findings contribute to providing reference and guidance to design the protective elements and structures. Based on the obtained results, the following conclusions can be summarized:

- The designed UHPFRC with the compressive strength at 140 -170 MPa by using a particle packing model shows excellent high-velocity bullet impact resistance, and the compressive strength class of 150 MPa is recommended for UHPFRC to design

protective structures by considering both cost efficiency and anti-penetration performance.

- Steel fibres are indispensable and play a critical role in UHPFRC towards bullet impact resistance, and 13 mm straight steel fibres show better contributions than 30 mm hook-ended ones. 2 vol.% is recommended as the optimum content to design impact resistant UHPFRC by further concerning the crack inhibition.
- Coarse basalt aggregates with particle size up to 25 mm are successfully introduced into protective UHPFRC system, which results in a lower powder consumption (i.e. from 900 kg/m³ to 700 kg/m³) and lower cost, higher mechanical strength and stronger bullet impact resistance. The DOP reduction is about 14.5% with the increase of the D_{\max} from 2 mm to 25 mm.
- A UHPFRC target with a larger thickness tends to have a smaller DOP, attributed to the better confinement by the surrounding material on the local damaged concrete. Perforation limits (safe thicknesses) of the designed UHPFRC (M2 with 2 vol.% 13 mm short steel fibres) are about 85 mm and 95 mm to withstand the 7.62×51 mm NATO armor-piercing bullet at striking velocities of 843 m/s and 926 m/s, respectively.

Chapter 9

Conclusions and recommendations

9.1 Conclusions

Ultra-high performance fibre reinforced concrete (UHPFRC) is a relatively new building material, which has superior workability, mechanical properties, energy dissipation capacity and durability. Those excellent characteristics and properties give it a great potential to be used in impact resistant components and structures, such as protective elements in military and civil engineering. However, the high cement consumption, large dosage of superplasticizer and high content of steel fibre unitization cause some disadvantages, such as high costs and a large embodied energy. Hence, optimization on UHPFRC mixtures is needed to make them cheaper, more eco-friendly and higher impact resistance to broaden the applications, and the static mechanical properties and impact resistance of UHPFRC are necessary to be investigated to reveal the impact resistant mechanism and provide guidance in the design of protective elements and structures. This research aims to optimize the mix design of UHPFRC towards high impact resistance, cost-effectiveness and eco-friendliness, and investigate its mechanical properties and impact resistance.

To approach the research targets, the most important and indispensable chemical additive (superplasticizer) is researched during the early-age of UHPC. Then, the binder for UHPC system is optimized by using high-volume limestone powder and developing quaternary blends with cement-slag-silica-limestone. To further reduce the powder content and costs, and to improve its properties, coarse aggregates are introduced in the UHPC system by applying both a normal mixing method and a two-stage casting method. After that, the homogeneous beams combined with steel fibres and coarse aggregates, and functionally graded composite beams, are investigated to enhance the fibre utilization efficiency and maximize mechanical and impact performances. Lastly, the impact resistance of the designed UHPFRC mixtures and components are evaluated by low-velocity pendulum and drop-weight impact tests, as well as high-velocity in-service bullet impact tests.

The main conclusions of this work drawn, based on the performed study, are summarized in the following sections.

9.1.1 Superplasticizer effect on early-age behaviour

UHPC is developed after the invention of superplasticizer, which greatly influences the dispersing, fluid-retaining and retardation performance. The dispersing ability of PCE-type SP is determined by its chemical structure, which features an exponential relationship between the flow ability of pastes and SP dosages. The fluid-retaining abilities of UHPC mixtures are sensitive to the water-to-powder ratio, while the further addition of SP will not enhance the slump life after reaching the saturation dosage. Both the adsorbed PCE and the PCE remaining in the aqueous phase contribute to retardation effect. A linear correlation between the final setting time (T_{final}) and the time of maximum heat flow rate ($t_{\dot{q}=max}$) is

derived. The types and dosages of SP primarily influence the absolute chemical shrinkage of pastes within 1 day, and have a great effect on the autogenous shrinkage due to different physical coagulation and chemical process.

9.1.2 Binder optimization towards low clinker content

The high cement clinker consumption is one of the most critical factors to limit the practical applications, because it brings an environmental burden and cost problems. In the meanwhile, a large proportion of binders cannot be completely hydrated under the relatively low water-to-binder ratio (usually less than 0.2) prevailing in a UHPC system. Thus, cheaper and more sustainable mineral admixtures could be utilized to partly replace the cement clinker. Two methods are used to modify the binder system, namely using high-volume limestone powder and developing quaternary blends with cement-slag-silica-limestone.

The limestone powder shows a positive mineral plasticization effect that should be considered in designing UHPC. The degree of secondary pozzolanic hydration is more intensive than C_3S/C_2S hydration, which will enhance the later-age strength development. The optimum content of limestone powder appears to be 50 vol.% of the total powder content in UHPC, and contributes to a higher strength, denser pore structure, diminished total free shrinkage and higher sustainability efficiency. Quaternary blends with cement-slag-limestone-silica in UHPC pastes have a considerable advantage of reducing embodied energy and improving sustainability. Furthermore, positive synergies in term of strength, fibre-to-matrix bond and total free shrinkage are observed in UHPC pastes with quaternary binders compared to binary and ternary ones.

9.1.3 Introduction of coarse aggregates

Currently, most UHPC has been designed without coarse aggregates to ensure the homogeneity. Introducing coarse aggregates into UHPC system could reduce the powder content and cost, improve the volume stability and penetration impact resistance, etc.

Coarse basalt aggregates can be successfully introduced by applying the modified Andreasen and Andersen model. The utilization volume of coarse basalt aggregates is up to 35% with a reduced powder content. With the increase of particle size of basalt aggregate, the mechanical strengths tend to decrease. Nevertheless, the maximum decrease degrees of compressive and tensile strengths are very limited, namely 8.3% and 16.3%, respectively. The optimal powder content of UHPC in this study is about 800 kg/m^3 and 700 kg/m^3 with maximum basalt aggregate size of 8 mm and 16 mm, respectively. In addition, a distribution modulus q of 0.19 is recommended for the modified Andreasen and Andersen model.

The new concept of TS-UHPC with coarse basalt volume around 55% has a low binder amount (e.g. 364 kg/m^3) and high binder efficiency (e.g. $0.417 \text{ MPa}\cdot\text{m}^3/\text{kg}$), possessing excellent compressive strength of up to 151.8 MPa at 91 days. New formulas are proposed to describe correlation between compressive and splitting tensile strength of TS-UHPC, and to predict the strength of TS-UHPC by its grout strength.

9.1.4 Efficient utilization of steel fibres

Medium and long fibres contribute to an excellent deflection/strain hardening behaviour instead of short ones. A preferential synergistic effect on flexural properties is observed between the medium fibres and the finer aggregates, while the longer fibres are more compatible to the coarser aggregates. The length of steel fibre is recommended between 2 and 5 times as the D_{max} (maximum size of aggregate).

The novel concept of functionally graded composite beam (FGCB) further improves steel fibre utilization efficiency. It also has superior flexural properties and energy absorption, without showing any interfacial bond problem. The fibre utilization efficiency of the designed FGCB is much higher compared to the traditional UHPC and SIFCON beams. The 30 mm medium hook-ended steel fibres show the best utilization efficiency compared to the 13 mm short straight and 60 mm long 5D steel fibres, and 3 vol.% medium fibres are optimum to design FGCB.

9.1.5 Resistance under low and high-velocity impact loadings

Both low-velocity and high-velocity impact tests are conducted in this study, including pendulum, drop-weight and in-service bullet impacts.

Coarse basalt aggregates up to 25 mm can be successfully introduced to reduce cement consumption and cost in UHPFRC for developing an impact resistant construction material. In the presence of coarse aggregates, the 30 mm medium hook-ended and 60 mm long 5D fibres are more efficient in improving the impact resistance than the 13 mm short straight ones. The novel concept of FGCB results in superior impact resistance, as well as very low cement consumption and a high steel fibre utilization efficiency. Hence, 3 vol.% 30 mm hook-ended fibres are suggested for FGCB to design an impact resistant component with an optimum bottom-to-top layer ratio β_{layer} of 0.46, considering both performance and fibre utilization efficiency. The toughness can be used as a good indicator to reflect the low-velocity impact resistance of UHPFRC beams. A linear analytical model is proposed to describe this correlation. While, the low-velocity impact resistance is also greatly influenced by the flexural strength when subjected to impacts with an impact energy below the threshold energy.

The compressive strength class of 150 MPa is recommended for UHPFRC to design protective structures by considering both cost efficiency and anti-penetration performance. Steel fibres are indispensable and play a critical role towards bullet impact resistance, and 13 mm straight steel fibres show better contributions than 30 mm hook-ended ones. Hence, 2 vol.% is recommended as the optimum content to design impact resistant UHPFRC by further concerning the crack inhibition. The DOP reduction is about 14.5% with the increase of the maximum size of coarse aggregates from 2 mm to 25 mm. A UHPFRC target with a larger thickness tends to show a smaller DOP, attributed to the better confinement of outer material to the local damaged concrete. Perforation limits of the designed slabs are about 85 mm and 95 mm to withstand the 7.62×51 mm NATO armor-piercing bullet at the striking velocity of 843 m/s and 926 m/s, respectively.

9.2 Recommendations for future research

This thesis focuses on the development of impact resistant ultra-high performance fibre reinforced concrete (UHPFRC), from material design to component optimization to properties evaluation. The presented results positively confirm the hypothesis of the performed research. Nevertheless, further study is still needed on a number of issues and remaining open questions. The following work is proposed as recommendations for the future research.

- The properties of UHPFRC are greatly dependent on the packing density or particle size distribution. The distribution modulus q of the packing model for designing UHPFRC should be further optimized and demonstrated, incorporating different maximum particle sizes of aggregates.
- Currently, there is no standard impact test to easily compare the impact resistance of different UHPFRC materials. Cost-efficient and reliable impact testing methods are necessary to be proposed and systematically validated.
- The dynamic constitutive model under different strain-rates should be further understood, for example seeking further research on impact resistance by applying the split Hopkinson press bar tests. Then, one could propose dynamic compressive and tensile strength-strain relations, which could be used to analytical and/or numerical calculation on large-scale components or structures under impact loadings.
- When the stress induced by especially repeated impact event is below the elastic limit of UHPFRC, probably a so-called ‘fatigue-impact’ phenomenon occurs. Thus, the service life and damage pattern of UHPFRC material and structure should receive enough attention if they are subjected fatigue-impact loadings.
- Impact resistance of UHPFRC under real service conditions is another very important concern, because mostly impact event occurs to concrete structures in combination with other service loadings, e.g. axial compression for bridge pillar.

Bibliography

- [1] Richard P, Cheyrezy M. Composition of reactive powder concretes. *Cem Concr Res* 1995;25:1501–11.
- [2] de Larrard F, Sedran T. Optimization of ultra-high-performance concrete by the use of a packing model. *Cem Concr Res* 1994;24:997–1009.
- [3] Eide MB, Hisdal J-M. Ultra High Performance Fibre Reinforced Concrete (UHPFRC) – State of the art : FA 2 Competitive constructions : SP 2.2 Ductile high strength concrete. COIN Projet report (44); 2012.
- [4] Schmidt M, Fehling E, Geisenhanslüke C. Ultra High Performance Concrete (UHPC). Proceedings of the International Symposium on Ultra High Performance Concrete. Kassel, Germany: 2004.
- [5] Stengel T, Schießl P. Life cycle assessment (LCA) of ultra high performance concrete (UHPC) structures. Woodhead Publishing Limited; 2014.
- [6] Wang D, Shi C, Wu Z, Xiao J, Huang Z, Fang Z. A review on ultra high performance concrete: Part II. Hydration, microstructure and properties. *Constr Build Mater* 2015;96:368–77.
- [7] Soufeiani L, Raman SN, Jumaat MZ Bin, Alengaram UJ, Ghadyani G, Mendis P. Influences of the volume fraction and shape of steel fibers on fiber-reinforced concrete subjected to dynamic loading – A review. *Eng Struct* 2016;124:405–17.
- [8] Tran NT, Tran TK, Jeon JK, Park JK, Kim DJ. Fracture energy of ultra-high-performance fiber-reinforced concrete at high strain rates. *Cem Concr Res* 2015;79:169–84.
- [9] Yu R, Spiesz P, Brouwers HJH. Static properties and impact resistance of a green Ultra-High Performance Hybrid Fibre Reinforced Concrete (UHPHFRC): Experiments and modeling. *Constr Build Mater* 2014;68:158–71.
- [10] Li PP, Yu QL. Responses and post-impact properties of ultra-high performance fibre reinforced concrete under pendulum impact. *Compos Struct* 2019;208:806–15.
- [11] Kang S-T, Lee Y, Park Y-D, Kim J-K. Tensile fracture properties of an Ultra High Performance Fiber Reinforced Concrete (UHPFRC) with steel fiber. *Compos Struct* 2010;92:61–71.
- [12] Liu J, Wu C, Su Y, Li J, Shao R, Chen G, et al. Experimental and numerical studies of ultra-high performance concrete targets against high-velocity projectile impacts. *Eng Struct* 2018;173:166–79.
- [13] Feng J, Sun W, Liu Z, Cui C, Wang X. An armour-piercing projectile penetration in a double-layered target of ultra-high-performance fiber reinforced concrete and armour steel: Experimental and numerical analyses. *Mater Des* 2016;102:131–41.
- [14] Feng J, Li W, Wang X, Song M, Ren H, Li W. Dynamic spherical cavity expansion analysis of rate-dependent concrete material with scale effect. *Int J Impact Eng* 2015;84:24–37.
- [15] Su H, Xu J. Dynamic compressive behavior of ceramic fiber reinforced concrete under impact load. *Constr Build Mater* 2013;45:306–13.
- [16] Zhang X, Ruiz G, Abd Elazim AM. Loading rate effect on crack velocities in steel fiber-reinforced concrete. *Int J Impact Eng* 2015;76:60–6.
- [17] Ren F, Mattus CH, Wang JJA, DiPaolo BP. Effect of projectile impact and penetration on the phase composition and microstructure of high performance concretes. *Cem Concr Compos* 2013;41:1–8.
- [18] Lai J, Guo X, Zhu Y. Repeated penetration and different depth explosion of ultra-high performance concrete. *Int J Impact Eng* 2015;84:1–12.
- [19] Wille K, Boisvert-Cotulio C. Material efficiency in the design of ultra-high performance concrete. *Constr Build Mater* 2015;86:33–43.
- [20] Yoo D-Y, Lee J-H, Yoon Y-S. Effect of fiber content on mechanical and fracture properties of ultra high performance fiber reinforced cementitious composites. *Compos Struct* 2013;106:742–53.
- [21] Lee JH. Influence of concrete strength combined with fiber content in the residual flexural strengths of fiber reinforced concrete. *Compos Struct* 2017;168:216–25.

- [22] Kim H, Kim G, Nam J, Kim J, Han S, Lee S. Static mechanical properties and impact resistance of amorphous metallic fiber-reinforced concrete. *Compos Struct* 2015;134:831–44.
- [23] Wu Z, Shi C, He W, Wu L. Effects of steel fiber content and shape on mechanical properties of ultra high performance concrete. *Constr Build Mater* 2016;103:8–14.
- [24] Yoo DY, Banthia N, Kang ST, Yoon YS. Effect of fiber orientation on the rate-dependent flexural behavior of ultra-high-performance fiber-reinforced concrete. *Compos Struct* 2016;157:62–70.
- [25] Yu R, Song Q, Wang X, Zhang Z, Shui Z, Brouwers HJH. Sustainable development of Ultra-High Performance Fibre Reinforced Concrete (UHPFRC): Towards to an optimized concrete matrix and efficient fibre application. *J Clean Prod* 2017;162:220–33.
- [26] Wu Z, Shi C, He W, Wang D. Static and dynamic compressive properties of ultra-high performance concrete (UHPC) with hybrid steel fiber reinforcements. *Cem Concr Compos* 2017;79:148–57.
- [27] Yu R, Spiesz P, Brouwers HJH. Development of Ultra-High Performance Fibre Reinforced Concrete (UHPFRC): Towards an efficient utilization of binders and fibres. *Constr Build Mater* 2015;79:273–82.
- [28] Shi C, Wu Z, Xiao J, Wang D, Huang Z, Fang Z. A review on ultra high performance concrete: Part I. Raw materials and mixture design. *Constr Build Mater* 2015;96:368–77.
- [29] Flatt RJ, Schober I. Superplasticizers and rheology of concrete. Woodhead Publishing Limited; 2011.
- [30] Li CZ, Feng NQ, Li Y De, Chen RJ. Effects of polyethylene oxide chains on the performance of polycarboxylate-type water-reducers. *Cem Concr Res* 2005;35:867–73.
- [31] Li Y, Yang C, Zhang Y, Zheng J, Guo H, Lu M. Study on dispersion, adsorption and flow retaining behaviors of cement mortars with TPEG-type polyether kind polycarboxylate superplasticizers. *Constr Build Mater* 2014;64:324–32.
- [32] Chandra S, Björnström J. Influence of superplasticizer type and dosage on the slump loss of Portland cement mortars - Part II. *Cem Concr Res* 2002;32:1613–9.
- [33] Zhang Y, Kong X. Correlations of the dispersing capability of NSF and PCE types of superplasticizer and their impacts on cement hydration with the adsorption in fresh cement pastes. *Cem Concr Res* 2015;69:1–9.
- [34] Nkinamubanzi P-C, Mantellato S, Flatt RJ. Superplasticizers in practice. Elsevier Ltd; 2016.
- [35] Yamada K, Takahashi T, Hanehara S, Matsuhisa M. Effects of the chemical structure on the properties of polycarboxylate-type superplasticizer. *Cem Concr Res* 2000;30:197–207.
- [36] Winnefeld F, Becker S, Pakusch J, G??tz T. Effects of the molecular architecture of comb-shaped superplasticizers on their performance in cementitious systems. *Cem Concr Compos* 2007;29:251–62.
- [37] Schmidt W, Brouwers HJH, Kuehne H-C, Meng B. Effects of the characteristics of high range water reducing agents and the water to powder ratio on rheological and setting behavior of Self-Consolidating Concrete. *Adv Civ Eng Mater* 2015;3:1–15.
- [38] Bentz DP. A review of early-age properties of cement-based materials. *Cem Concr Res* 2008;38:196–204.
- [39] Felekoğlu B, Sarikahya H. Effect of chemical structure of polycarboxylate-based superplasticizers on workability retention of self-compacting concrete. *Constr Build Mater* 2008;22:1972–80.
- [40] Shin JY, Hong JS, Suh JK, Lee YS. Effects of polycarboxylate-type superplasticizer on fluidity and hydration behavior of cement paste. *Korean J Chem Eng* 2008;25:1553–61.
- [41] Hallal A, Kadri EH, Ezziane K, Kadri A, Khelafi H. Combined effect of mineral admixtures with superplasticizers on the fluidity of the blended cement paste. *Constr Build Mater* 2010;24:1418–23.
- [42] Schröfl C, Gruber M, Plank J. Preferential adsorption of polycarboxylate superplasticizers on cement and silica fume in ultra-high performance concrete (UHPC). *Cem Concr Res* 2012;42:1401–8.
- [43] Zhang L, Lu Q, Xu Z, Liu Q, Zeng H. Effect of polycarboxylate ether comb-type polymer on viscosity and interfacial properties of kaolinite clay suspensions. *J Colloid Interface Sci* 2012;378:222–31.

- [44] Lei L, Plank J. A concept for a polycarboxylate superplasticizer possessing enhanced clay tolerance. *Cem Concr Res* 2012;42:1299–306.
- [45] Ng S, Plank J. Interaction mechanisms between Na montmorillonite clay and MPEG-based polycarboxylate superplasticizers. *Cem Concr Res* 2012;42:847–54.
- [46] Lei L, Plank J. A study on the impact of different clay minerals on the dispersing force of conventional and modified vinyl ether based polycarboxylate superplasticizers. *Cem Concr Res* 2014;60:1–10.
- [47] Zhang YR, Kong XM, Lu ZB, Lu ZC, Hou SS. Effects of the charge characteristics of polycarboxylate superplasticizers on the adsorption and the retardation in cement pastes. *Cem Concr Res* 2015;67:184–96.
- [48] Jiang SP, Mutin JC, Nonat A. Studies on mechanism and physico-chemical parameters at the origin of the cement setting. I. The fundamental processes involved during the cement setting. *Cem Concr Res* 1995;25:779–89.
- [49] Jiang SP, Mutin JC, Nonat A. Studies on mechanism and physico-chemical parameters at the origin of the cement setting II. Physico-chemical parameters determining the coagulation process. *Cem Concr Res* 1996;26:491–500.
- [50] Bentz DP, Garboczi EJ, Haecker CJ, Jensen OM. Effects of cement particle size distribution on performance properties of Portland cement-based materials. *Cem Concr Res* 1999;29:1663–71.
- [51] Bentz DP. Cement hydration: building bridges and dams at the microstructure level. *Mater Struct* 2007;40:397–404.
- [52] Yoo D-Y, Park J-J, Kim S-W, Yoon Y-S. Early age setting, shrinkage and tensile characteristics of ultra high performance fiber reinforced concrete. *Constr Build Mater* 2013;41:427–38.
- [53] Brooks J. *Shrinkage of Concrete*. Butterworth-Heinemann; 2015.
- [54] Schmidt W, Brouwers HJH, Kühne HC, Meng B. Influences of superplasticizer modification and mixture composition on the performance of self-compacting concrete at varied ambient temperatures. *Cem Concr Compos* 2014;49:111–26.
- [55] Elakneswaran Y, Nawa T, Kurumisawa K. Zeta potential study of paste blends with slag. *Cem Concr Compos* 2009;31:72–6.
- [56] Srinivasan S, Barbhuiya SA, Charan D, Pandey SP. Characterising cement-superplasticiser interaction using zeta potential measurements. *Constr Build Mater* 2010;24:2517–21.
- [57] He Y, Zhang X, Hooton RD. Effects of organosilane-modified polycarboxylate superplasticizer on the fluidity and hydration properties of cement paste. *Constr Build Mater* 2017;132:112–23.
- [58] Neubauer CM, Yang M, Jennings HM. Interparticle Potential and Sedimentation Behavior of Cement Suspensions: Effects of Admixtures. *Adv Cem Based Mater* 1998;8:17–27.
- [59] Zhang T, Shang S, Yin F, Aishah A, Salmiah A, Ooi TL. Adsorptive behavior of surfactants on surface of Portland cement. *Cem Concr Res* 2001;31:1009–15.
- [60] Nägele E, Schneider U. From cement to hardened paste - an elektrokinetic study. *Cem Concr Res* 1989;19:978–86.
- [61] Yoshioka K, Tazawa EI, Kawai K, Enohata T. Adsorption characteristics of superplasticizers on cement component minerals. *Cem Concr Res* 2002;32:1507–13.
- [62] Zingg A, Winnefeld F, Holzer L, Pakusch J, Becker S, Gauckler L. Adsorption of polyelectrolytes and its influence on the rheology, zeta potential, and microstructure of various cement and hydrate phases. *J Colloid Interface Sci* 2008;323:301–12.
- [63] Hajime Okamura, Ouchi M. Self-Compacting concrete. *J Adv Concr Technol* 2003;1:5–15.
- [64] Brouwers HJH, Radix HJ. Self-compacting concrete: Theoretical and experimental study. *Cem Concr Res* 2005;35:2116–36.
- [65] Quercia G, Hüsken G, Brouwers HJH. Water demand of amorphous nano silica and its impact on the workability of cement paste. *Cem Concr Res* 2012;42:344–57.
- [66] Yu QL, Brouwers HJH. Microstructure and mechanical properties of β -hemihydrate produced gypsum: An insight from its hydration process. *Constr Build Mater* 2011;25:3149–57.
- [67] Bessaies-Bey H, Baumann R, Schmitz M, Radler M, Roussel N. Organic admixtures and cement particles: Competitive adsorption and its macroscopic rheological consequences. *Cem*

- Concr Res 2016;80:1–9.
- [68] Kirby G, Lewis JA, Matsuyama H, Morissette S, Young JF. Polyelectrolyte effects on the rheological properties of concentrated cement suspensions. *J Am Ceram Soc* 2000;83:1905–13.
- [69] Jeknavorian AA, Jardine L, Ou CC, Koyata H, Folliard K. Interaction of superplasticizers with clay-bearing aggregates. *Proc Seventh CANMET/ACI Int Conf Superplast Other Chem Admixtures Concr* 2003;SP-217:143–60.
- [70] Mardani-Aghabaglou A, Tuyan M, Yilmaz G, Ariöz Ö, Ramyar K. Effect of different types of superplasticizer on fresh, rheological and strength properties of self-consolidating concrete. *Constr Build Mater* 2013;47:1020–5.
- [71] Papayianni I, Tsohos G, Oikonomou N, Mavria P. Influence of superplasticizer type and mix design parameters on the performance of them in concrete mixtures. *Cem Concr Compos* 2005;27:217–22.
- [72] Bonen D, Sarkar SL. The superplasticizer adsorption capacity of cement pastes, pore solution composition, and parameters affecting flow loss. *Cem Concr Res* 1995;25:1423–34.
- [73] Chen Y, Odler I. On the origin of portland cement setting. *Cem Concr Res* 1992;22:1130–40.
- [74] Mollah MY a., Adams WJ, Schennach R, Cocke DL. A review of cement-superplasticizer interactions and their models. *Adv Cem Res* 2000;12:153–61.
- [75] Schmidt W. Design concepts for the robustness improvement of self-compacting concrete: effect of admixtures and mixture components on the rheology and early hydration at varying temperatures. Eindhoven university of technology, 2014.
- [76] Shen W, Li X, Gan G, Cao L, Li C, Bai J. Experimental investigation on shrinkage and water desorption of the paste in high performance concrete. *Constr Build Mater* 2016;114:618–24.
- [77] Mihashi H, Leite JPDB. State-of-the-Art Report on Control of Cracking in Early Age Concrete. *J Adv Concr Technol* 2004;2:141–54.
- [78] Li Y, Li J. Capillary tension theory for prediction of early autogenous shrinkage of self-consolidating concrete. *Constr Build Mater* 2014;53:511–6.
- [79] Yoo DY, Banthia N. Mechanical properties of ultra-high-performance fiber-reinforced concrete: A review. *Cem Concr Compos* 2016;73:267–80.
- [80] Wang W, Liu J, Agostini F, Davy CA, Skoczylas F, Corvez D. Durability of an Ultra High Performance Fiber Reinforced Concrete (UHPFRC) under progressive aging. *Cem Concr Res* 2014;55:1–13.
- [81] Zhong R, Wille K, Viegas R. Material efficiency in the design of UHPC paste from a life cycle point of view. *Constr Build Mater* 2018;160:505–13.
- [82] Wang D, Shi C, Farzadnia N, Shi Z, Jia H. A review on effects of limestone powder on the properties of concrete. *Constr Build Mater* 2018;192:153–66.
- [83] Wang D, Shi C, Farzadnia N, Shi Z, Jia H, Ou Z. A review on use of limestone powder in cement-based materials: Mechanism, hydration and microstructures. *Constr Build Mater* 2018;181:659–72.
- [84] Burroughs JF, Shannon J, Rushing TS, Yi K, Gutierrez QB, Harrelson DW. Potential of finely ground limestone powder to benefit ultra-high performance concrete mixtures. *Constr Build Mater* 2017;141:335–42.
- [85] Abdulkareem OM, Ben Fraj A, Bouasker M, Khelidj A. Mixture design and early age investigations of more sustainable UHPC. *Constr Build Mater* 2018;163:235–46.
- [86] Bentz DP, Ferraris CF, Jones SZ, Lootens D, Zunino F. Limestone and silica powder replacements for cement: Early-age performance. *Cem Concr Compos* 2017;78:43–56.
- [87] Zhang Z, Wang Q, Chen H. Properties of high-volume limestone powder concrete under standard curing and steam-curing conditions. *Powder Technol* 2016;301:16–25.
- [88] De Weerd K, Haha M Ben, Le Saout G, Kjellsen KO, Justnes H, Lothenbach B. Hydration mechanisms of ternary Portland cements containing limestone powder and fly ash. *Cem Concr Res* 2011;41:279–91.
- [89] Kang SH, Jeong Y, Tan KH, Moon J. The use of limestone to replace physical filler of quartz powder in UHPFRC. *Cem Concr Compos* 2018;94:238–47.
- [90] Shi C, Wang D, Wu L, Wu Z. The hydration and microstructure of ultra high-strength concrete with cement–silica fume–slag binder. *Cem Concr Compos* 2015;61:44–52.

- [91] Edwin RS, Mushthofa M, Gruyaert E, De Belie N. Quantitative analysis on porosity of reactive powder concrete based on automated analysis of back-scattered-electron images. *Cem Concr Compos* 2019;96:1–10.
- [92] Koutný O, Snoeck D, Van Der Vurst F, De Belie N. Rheological behaviour of ultra-high performance cementitious composites containing high amounts of silica fume. *Cem Concr Compos* 2018;88:29–40.
- [93] Edwin RS, De Schepper M, Gruyaert E, De Belie N. Effect of secondary copper slag as cementitious material in ultra-high performance mortar. *Constr Build Mater* 2016;119:31–44.
- [94] Dave N, Kumar A, Srivastava A, Kumar S. Experimental analysis of strength and durability properties of quaternary cement binder and mortar. *Constr Build Mater* 2016;107:117–24.
- [95] Dave N, Kumar A, Srivastava A, Kumar A, Kumar S. Study on quaternary concrete microstructure, strength, durability considering the influence of multi-factors. *Constr Build Mater* 2017;139:447–57.
- [96] Makhloufi Z, Bouziani T, Hadjoudja M, Bederina M. Durability of limestone mortars based on quaternary binders subjected to sulfuric acid using drying – immersion cycles. *Constr Build Mater* 2014;71:579–88.
- [97] Makhloufi Z, Aggoun S, Benabed B, Kadri EH, Bederina M. Effect of magnesium sulfate on the durability of limestone mortars based on quaternary blended cements. *Cem Concr Compos* 2016;65:186–99.
- [98] El-chabib H, Ibrahim A. The performance of high-strength flowable concrete made with binary, ternary, or quaternary binder in hot climate. *Constr Build Mater* 2013;47:245–53.
- [99] Van den Heede P, De Belie N. A service life based global warming potential for high-volume fly ash concrete exposed to carbonation. *Constr Build Mater* 2014;55:183–93.
- [100] EFNARC. Specification and Guidelines for Self-Compacting Concrete. Rep from EFNARC 2002;44:32.
- [101] Coo M, Pheeraphan T. Effect of sand, fly ash, and coarse aggregate gradation on preplaced aggregate concrete studied through factorial design. *Constr Build Mater* 2015;93:812–21.
- [102] Yu R, Spiesz P, Brouwers HJH. Effect of nano-silica on the hydration and microstructure development of Ultra-High Performance Concrete (UHPC) with a low binder amount. *Constr Build Mater* 2014;65:140–50.
- [103] Yuan B, Yu QL, Dainese E, Brouwers HJH. Autogenous and drying shrinkage of sodium carbonate activated slag altered by limestone powder incorporation. *Constr Build Mater* 2017;153:459–68.
- [104] Brunauer S, Emmett PH, Teller E. Adsorption of Gases in Multimolecular Layers. *J Am Chem Soc* 1938;60:309–19.
- [105] Barrett EP, Joyner LG, Halenda PP. The Determination of Pore Volume and Area Distributions in Porous Substances. I. Computations from Nitrogen Isotherms. *J Am Chem Soc* 1951;73:373–80.
- [106] De Belie N, Kratky J, Van Vlierberghe S. Influence of pozzolans and slag on the microstructure of partially carbonated cement paste by means of water vapour and nitrogen sorption experiments and BET calculations. *Cem Concr Res* 2010;40:1723–33.
- [107] EN 12390-3. Testing hardened concrete - Part 3: Compressive strength of test specimens. Br Stand Institution-BSI CEN Eur Comm Stand 2009.
- [108] Li PP, Yu QL, Brouwers HJH. Effect of PCE-type superplasticizer on early-age behaviour of ultra-high performance concrete (UHPC). *Constr Build Mater* 2017;153:740–50.
- [109] Sekkal W, Zaoui A. Nanoscale analysis of the morphology and surface stability of calcium carbonate polymorphs. *Sci Rep* 2013;3:1587.
- [110] Mikanovic N, Jolicoeur C. Influence of superplasticizers on the rheology and stability of limestone and cement pastes. *Cem Concr Res* 2008;38:907–19.
- [111] Nehdi M RM. Why some carbonate fillers cause rapid increases of viscosity in dispersed cement-based materials. *Cem Concr Res* 2000;30:1663–9.
- [112] Huang W, Kazemi-Kamyab H, Sun W, Scrivener K. Effect of cement substitution by limestone on the hydration and microstructural development of ultra-high performance concrete (UHPC). *Cem Concr Compos* 2017;77:86–101.
- [113] Wu Z, Shi C, Khayat KH. Influence of silica fume content on microstructure development

- and bond to steel fiber in ultra-high strength cement-based materials (UHSC). *Cem Concr Compos* 2016;71:97–109.
- [114] Jain J, Neithalath N. Analysis of calcium leaching behavior of plain and modified cement pastes in pure water. *Cem Concr Compos* 2009;31:176–85.
- [115] Taylor HFW. *Cement chemistry*. 2nd ed. London: Thomas Telford; 1997.
- [116] Lothenbach B, Scrivener K, Hooton RD. Supplementary cementitious materials. *Cem Concr Res* 2011;41:1244–56.
- [117] Rossen JE, Lothenbach B, Scrivener KL. Composition of C-S-H in pastes with increasing levels of silica fume addition. *Cem Concr Res* 2015;75:14–22.
- [118] Cook RA, Hover KC. Mercury porosimetry of hardened cement pastes. *Cem Concr Res* 1999;29:933–43.
- [119] Mehta PK, Monteiro PJM. *Concrete: Microstructure, Properties, and Materials*. 3rd ed. McGraw-Hill; 2006.
- [120] Yajun J, Cahyadi JH. Effects of densified silica fume on microstructure and compressive strength of blended cement pastes. *Cem Concr Res* 2003;33:1543–8.
- [121] Jennings HM, Kumar A, Sant G. Quantitative discrimination of the nano-pore-structure of cement paste during drying: New insights from water sorption isotherms. *Cem Concr Res* 2015;76:27–36.
- [122] Hou D, Li D, Hua P, Jiang J, Zhang G. Statistical modelling of compressive strength controlled by porosity and pore size distribution for cementitious materials. *Cem Concr Compos* 2018;96:11–20.
- [123] Wang L, Yang HQ, Dong Y, Chen E, Tang SW. Environmental evaluation, hydration, pore structure, volume deformation and abrasion resistance of low heat Portland (LHP) cement-based materials. *J Clean Prod* 2018;203:540–58.
- [124] Wu Z, Shi C, He W. Comparative study on flexural properties of ultra-high performance concrete with supplementary cementitious materials under different curing regimes. *Constr Build Mater* 2017;136:307–13.
- [125] Li PP, Yu QL, Brouwers HJH. Effect of coarse basalt aggregates on the properties of Ultra-high Performance Concrete (UHPC). *Constr Build Mater* 2018;170:649–59.
- [126] Wang Y, Shui Z, Gao X, Huang Y, Yu R, Li X, et al. Utilizing coral waste and metakaolin to produce eco-friendly marine mortar: Hydration, mechanical properties and durability. *J Clean Prod* 2019;219:763–74.
- [127] King D. The effect of silica fume on the properties of concrete as defined in concrete society report 74, cementitious materials. 37th Conf Our World Concr Struct 2012:1–23.
- [128] Justnes H. Thaumassite formed by sulfate attack on mortar with limestone filler. *Cem Concr Compos* 2003;25:955–9.
- [129] EN-1097-3. Tests for mechanical and physical properties of aggregates- Part 3: Determination of loose bulk density and voids. Br Stand Institution-BSI CEN Eur Comm Stand 1998.
- [130] Li LG, Kwan AKH. Packing density of concrete mix under dry and wet conditions. *Powder Technol* 2014;253:514–21.
- [131] C 307-03. Standard Test Method for Tensile Strength of Chemical-Resistant Mortar, Grouts, and Monolithic Surfacing. ASTM Stand 2004.
- [132] Arora A, Aguayo M, Hansen H, Castro C, Federspiel E, Mobasher B, et al. Microstructural packing- and rheology-based binder selection and characterization for Ultra-high Performance Concrete (UHPC). *Cem Concr Res* 2018;103:179–90.
- [133] Domone P, Hsi-wen C. Testing of binders for high performance concrete. *Cem Concr Res* 1997;27:1141–7.
- [134] Lei DY, Guo LP, Sun W, Liu J, Shu X, Guo XL. A new dispersing method on silica fume and its influence on the performance of cement-based materials. *Constr Build Mater* 2016;115:716–26.
- [135] Bouasker M, Khalifa NEH, Mounanga P, Ben Kahla N. Early-age deformation and autogenous cracking risk of slag-limestone filler-cement blended binders. *Constr Build Mater* 2014;55:158–67.
- [136] Yu R, Spiesz P, Brouwers HJH. Development of an eco-friendly Ultra-High Performance

- Concrete (UHPC) with efficient cement and mineral admixtures uses. *Cem Concr Compos* 2015;55:383–94.
- [137] Li W, Huang Z, Zu T, Shi C, Duan WH, Shah SP. Influence of Nanolimestone on the Hydration, Mechanical Strength, and Autogenous Shrinkage of Ultrahigh-Performance Concrete. *J Mater Civ Eng* 2015;28:04015068.
- [138] Kakali G, Tsivilis S, Aggeli E, Bati M. Hydration products of C3A, C3S and Portland cement in the presence of CaCO₃. *Cem Concr Res* 2000;30:1073–7.
- [139] Nili M, Ehsani A. Investigating the effect of the cement paste and transition zone on strength development of concrete containing nanosilica and silica fume. *Mater Des* 2015;75:174–83.
- [140] Hosseini P, Booshehrian A, Madari A. Developing concrete recycling strategies by utilization of nano-SiO₂ particles. *Waste and Biomass Valorization* 2011;2:347–55.
- [141] Hong SY, Glasser FP. Phase relations in the CaO-SiO₂-H₂O system to 200 °C at saturated steam pressure. *Cem Concr Res* 2004;34:1529–34.
- [142] Yazici H, Yiğiter H, Karabulut AŞ, Baradan B. Utilization of fly ash and ground granulated blast furnace slag as an alternative silica source in reactive powder concrete. *Fuel* 2008;87:2401–7.
- [143] Cao YYY, Yu QL. Effect of inclination angle on hooked end steel fiber pullout behavior in ultra-high performance concrete. *Compos Struct* 2018;201:151–60.
- [144] Robins P, Austin S, Jones P. Pull-out behaviour of hooked steel fibres. *Mater Struct* 2002;35:434–42.
- [145] Yoo DY, Park JJ, Kim SW. Fiber pullout behavior of HPFRCC : Effects of matrix strength and fiber type. *Compos Struct* 2017;174:263–76.
- [146] Hun S, Sung G, Taek K, Joo D. Effect of shrinkage reducing agent on pullout resistance of high-strength steel fibers embedded in ultra-high-performance concrete. *Cem Concr Compos* 2014;49:59–69.
- [147] Hu X, Shi Z, Shi C, Wu Z, Tong B, Ou Z, et al. Drying shrinkage and cracking resistance of concrete made with ternary cementitious components. *Constr Build Mater* 2017;149:406–15.
- [148] Yang W. *Fatal Factor for Durability: Drying Shrinkage*. Springer, Berlin, Heidelberg; 2015.
- [149] Li W, Huang Z, Hu G, Hui Duan W, Shah SP. Early-age shrinkage development of ultra-high-performance concrete under heat curing treatment. *Constr Build Mater* 2017;131:767–74.
- [150] Mackenzie JK. The Elastic Constants of a Solid containing Spherical Holes. *Proc Phys Soc Sect B* 2002;63:2–11.
- [151] Wongkeo W, Thongsanitgarn P, Chaipanich A. Compressive strength and drying shrinkage of fly ash-bottom ash-silica fume multi-blended cement mortars. *Mater Des* 2012;36:655–62.
- [152] Van den Heede P, De Belie N. 9 - Sustainability assessment of potentially 'green' concrete types using life cycle assessment. In: Savastano Junior H, Fiorelli J, dos Santos SFBT-S and NCM using IBFC, editors., Woodhead Publishing; 2017, p. 235–63.
- [153] Damineli BL, Kemeid FM, Aguiar PS, John VM. Measuring the eco-efficiency of cement use. *Cem Concr Compos* 2010;32:555–62.
- [154] Banthia N, Majdzadeh F, Wu J, Bindiganavile V. Fiber synergy in Hybrid Fiber Reinforced Concrete (HyFRC) in flexure and direct shear. *Cem Concr Compos* 2014;48:91–7.
- [155] Banthia N, Gupta R. Hybrid fiber reinforced concrete (HyFRC): Fiber synergy in high strength matrices. *Mater Struct Constr* 2004;37:707–16.
- [156] Yu R, van Beers L, Spiesz P, Brouwers HJH. Impact resistance of a sustainable Ultra-High Performance Fibre Reinforced Concrete (UHPFRC) under pendulum impact loadings. *Constr Build Mater* 2016;107:203–15.
- [157] Rozalija K, Darwin D. *Effects of aggregate type, size, and content on concrete strength and fracture energy*. Lawrence, Kansas: 1997.
- [158] Ma J, Orgass M, Dehn F, Schmidt D, Tue N V. Comparative Investigations on Ultra-High Performance Concrete with or without Coarse Aggregates. *Proc Int Symp Ultra High Perform Concr Kassel* 2004:205–12.
- [159] Collepardi S, Coppola L, Troli R, Collepardi M. Mechanical properties of modified reactive powder concrete. *ACI Spec Publ* 1997;173:1–22.
- [160] Wille K, Naman AE, Parra-Montesinos GJ. Ultra-High Performance Concrete with

- Compressive Strength Exceeding 150 MPa (22ksi): A Simpler Way. *ACI Mater J* 2011;108:46–53.
- [161] Peng Y, Wu H, Fang Q, Liu JZ, Gong ZM. Impact resistance of basalt aggregated UHP-SFRC/fabric composite panel against small caliber arm. *Int J Impact Eng* 2016;88:201–13.
- [162] Tai YS, El-Tawil S, Chung TH. Performance of deformed steel fibers embedded in ultra-high performance concrete subjected to various pullout rates. *Cem Concr Res* 2016;89:1–13.
- [163] Vermeulen B. Ultra High Performance Concrete in Action. 2nd Grad Lab AE Conf 2013.
- [164] Nikbin IM, Beygi MHA, Kazemi MT, Vaseghi Amiri J, Rabbanifar S, Rahmani E, et al. A comprehensive investigation into the effect of water to cement ratio and powder content on mechanical properties of self-compacting concrete. *Constr Build Mater* 2014;57:69–80.
- [165] Domone PL. A review of the hardened mechanical properties of self-compacting concrete. *Cem Concr Compos* 2007;29:1–12.
- [166] Wu H, Fang Q, Chen XW, Gong ZM, Liu JZ. Projectile penetration of ultra-high performance cement based composites at 510–1320m/s. *Constr Build Mater* 2015;74:188–200.
- [167] Pyo S, Kim HK, Lee BY. Effects of coarser fine aggregate on tensile properties of ultra high performance concrete. *Cem Concr Compos* 2017;84:28–35.
- [168] Wu H, Fang Q, Gong J, Liu JZ, Zhang JH, Gong ZM. Projectile impact resistance of corundum aggregated UHP-SFRC. *Int J Impact Eng* 2015;84:38–53.
- [169] Abdelgader HS. How to design concrete produced by a two-stage concreting method. *Cem Concr Res* 1999;29:331–7.
- [170] Najjar MF, Soliman AM, Nehdi ML. Critical overview of two-stage concrete: Properties and applications. *Constr Build Mater* 2014;62:47–58.
- [171] Abdelgader HS, Górski J. Stress-Strain Relations and Modulus of Elasticity of Two-Stage Concrete. *J Mater Civ Eng* 2003;15:329–34.
- [172] Nehdi ML, Najjar MF, Soliman AM, Azabi TM. Novel steel fibre-reinforced preplaced aggregate concrete with superior mechanical performance. *Cem Concr Compos* 2017;82:242–51.
- [173] Rajabi AM, Omid Moaf F. Simple empirical formula to estimate the main geomechanical parameters of preplaced aggregate concrete and conventional concrete. *Constr Build Mater* 2017;146:485–92.
- [174] Najjar MF, Soliman AM, Nehdi ML. Two-stage concrete made with single, binary and ternary binders. *Mater Struct* 2014;49:317–27.
- [175] Najjar MF, Soliman AM, Nehdi ML. Grouts incorporating supplementary cementitious materials for two-stage concrete. *J Mater Civ Eng* 2017;29:1–9.
- [176] Makita T, Brühwiler E. Tensile fatigue behaviour of Ultra-High Performance Fibre Reinforced Concrete combined with steel rebars (R-UHPFRC). *Int J Fatigue* 2014;59:145–52.
- [177] Habel K, Viviani M, Denarié E, Brühwiler E. Development of the mechanical properties of an Ultra-High Performance Fiber Reinforced Concrete (UHPFRC). *Cem Concr Res* 2006;36:1362–70.
- [178] Mahmud GH, Yang Z, Hassan AMT. Experimental and numerical studies of size effects of Ultra High Performance Steel Fibre Reinforced Concrete (UHPFRC) beams. *Constr Build Mater* 2013;48:1027–34.
- [179] Meng W, Valipour M, Khayat KH. Optimization and performance of cost-effective ultra-high performance concrete. *Mater Struct* 2017;50:29.
- [180] Alkaysi M, El-Tawil S, Liu Z, Hansen W. Effects of silica powder and cement type on durability of ultra high performance concrete (UHPC). *Cem Concr Compos* 2016;66:47–56.
- [181] Gu CP, Ye G, Sun W. Ultrahigh performance concrete-properties, applications and perspectives. *Sci China Technol Sci* 2015;58:587–99.
- [182] Funk JE, Dinger DR. Predictive Process Control of Crowded Particulate Suspensions: Applied to Ceramic Manufacturing. Kluwer Academic Publishers; 1994.
- [183] Yu QL, Spiesz P, Brouwers HJH. Development of cement-based lightweight composites - Part 1: Mix design methodology and hardened properties. *Cem Concr Compos* 2013;44:17–29.
- [184] Yu QL, Brouwers HJH. Development of a self-compacting gypsum-based lightweight

- composite. *Cem Concr Compos* 2012;34:1033–43.
- [185] Hunger M. An integral design concept for ecological self-compacting concrete. PhD thesis. Eindhoven, the Netherland: Eindhoven Universtiy of Technology; 2010.
- [186] Yu R. Development of sustainable protective Ultra-High Performance Fibre Reinforced Concrete (UHPRFC). PhD thesis. Eindhoven, the Netherland: Eindhoven Universtiy of Technology; 2015.
- [187] EN 12390-6. Testing hardened concrete - Part 6: Tensile splitting strength of test specimens. Br Stand Institution-BSI CEN Eur Comm Stand 2009.
- [188] Fennis SAAM. Design of Ecological Concrete by Particle Packing Optimization. PhD thesis. Delft, the Netherlands: Delft University of Technology; 2009.
- [189] Ferraris CF, de Larrard F. Testing and Modelling of Fresh Concrete Rheology. Maryland, United States: NISTIR 6094; 1998.
- [190] Van Der Putten J, Dils J, Minne P, Boel V, De Schutter G. Determination of packing profiles for the verification of the compressible packing model in case of UHPC pastes. *Mater Struct* 2017;50:118.
- [191] Brouwers HJH. Particle-size distribution and packing fraction of geometric random packings. *Phys Rev E* 2006;74:031309.
- [192] Madandoust R, Ranjbar MM, Ghavidel R, Fatemeh Shahabi S. Assessment of factors influencing mechanical properties of steel fiber reinforced self-compacting concrete. *Mater Des* 2015;83:284–94.
- [193] Coo M, Pheeraphan T. Effect of sand, fly ash and limestone powder on preplaced aggregate concrete mechanical properties and reinforced beam shear capacity. *Constr Build Mater* 2016;120:581–92.
- [194] Shen W, Dong R, Li J, Zhou M, Ma W, Zha J. Experimental investigation on aggregate interlocking concrete prepared with scattering-filling coarse aggregate process. *Constr Build Mater* 2010;24:2312–6.
- [195] Wang C, Yang C, Liu F, Wan C, Pu X. Preparation of Ultra-High Performance Concrete with common technology and materials. *Cem Concr Compos* 2012;34:538–44.
- [196] Abdelgader HS, Elgalhud AA. Effect of grout proportions on strength of two-stage concrete. *Struct Concr* 2008;9:163–70.
- [197] Abdelgader HS, Ben-Zeitun AE. Tensile strength of two-stage concrete measured by double-punch and split tests, In: *Global Construction. Role of Concrete in Nuclear Facilities. Proceedings of International Conference, University of Dundee, Scotland, UK: 2005*, p. 43–50.
- [198] Neville AM. Properties of concrete. 4 edition. Prentice Hall; 2002.
- [199] Zhang J, Leung CKY, Cheung YN. Flexural performance of layered ECC-concrete composite beam. *Compos Sci Technol* 2006;66:1501–12.
- [200] Hassan AMT, Jones SW, Mahmud GH. Experimental test methods to determine the uniaxial tensile and compressive behaviour of ultra high performance fibre reinforced concrete (UHPRFC). *Constr Build Mater* 2012;37:874–82.
- [201] Yang SL, Millard SG, Soutsos MN, Barnett SJ, Le TT. Influence of aggregate and curing regime on the mechanical properties of ultra-high performance fibre reinforced concrete (UHPRFC). *Constr Build Mater* 2009;23:2291–8.
- [202] Toledo Filho RD, Koenders EAB, Formagini S, Fairbairn EMR. Performance assessment of Ultra High Performance Fiber Reinforced Cementitious Composites in view of sustainability. *Mater Des* 2012;36:880–8.
- [203] Wu K, Shi H, Xu L, Ye G, De Schutter G. Microstructural characterization of ITZ in blended cement concretes and its relation to transport properties. *Cem Concr Res* 2016;79:243–56.
- [204] Bentur A, Cohen MD. Effect of Condensed Silica Fume on the Microstructure of the Interfacial Zone in Portland Cement Mortars. *J Am Ceram Soc* 1987;70:738–43.
- [205] Erdem S, Dawson AR, Thom NH. Influence of the micro- and nanoscale local mechanical properties of the interfacial transition zone on impact behavior of concrete made with different aggregates. *Cem Concr Res* 2012;42:447–58.
- [206] Wang XH, Jacobsen S, He JY, Zhang ZL, Lee SF, Lein HL. Application of nanoindentation testing to study of the interfacial transition zone in steel fiber reinforced mortar. *Cem Concr*

- Res 2009;39:701–15.
- [207] Schultz RA. Comparative rock mass strengths of basalt and tuff and some planetological implications. 25th Lunar Planet. Sci. Conf., Houston: 1994, p. 1217–8.
- [208] Wang Y, Liew JYR, Lee SC. Theoretical models for axially restrained steel-concrete-steel sandwich panels under blast loading. *Int J Impact Eng* 2015;76:221–31.
- [209] Dittmer T, Beushausen H. The effect of coarse aggregate content and size on the age at cracking of bonded concrete overlays subjected to restrained deformation. *Constr Build Mater* 2014;69:73–82.
- [210] Jiang C, Wu YF, Jiang JF. Effect of aggregate size on stress-strain behavior of concrete confined by fiber composites. *Compos Struct* 2017;168:851–62.
- [211] Cao YYY, Li PP, Brouwers HJH, Sluijsmans M, Yu QL. Enhancing flexural performance of ultra-high performance concrete by an optimized layered-structure concept. *Compos Part B Eng* 2019;171:154–65.
- [212] Kim DJ, Park SH, Ryu GS, Koh KT. Comparative flexural behavior of Hybrid Ultra High Performance Fiber Reinforced Concrete with different macro fibers. *Constr Build Mater* 2011;25:4144–55.
- [213] Yoo DY, Kang ST, Yoon YS. Enhancing the flexural performance of ultra-high-performance concrete using long steel fibers. *Compos Struct* 2016;147:220–30.
- [214] Johnston CD. Proportioning, mixing and placement of fibre-reinforced cements and concretes, *Production Methods and Workability of Concrete*, London: E & FN Spon; 1996, p. 155–80.
- [215] Han J, Zhao M, Chen J, Lan X. Effects of steel fiber length and coarse aggregate maximum size on mechanical properties of steel fiber reinforced concrete. *Constr Build Mater* 2019;209:577–91.
- [216] Banyhussan QS, Yıldırım G, Bayraktar E, Demirhan S, Şahmaran M. Deflection-hardening hybrid fiber reinforced concrete: The effect of aggregate content. *Constr Build Mater* 2016;125:41–52.
- [217] EN 12390-5. Testing hardened concrete Part 5: Flexural strength of test specimens. Br Stand Institution-BSI CEN Eur Comm Stand 2009.
- [218] Liu J, Han F, Cui G, Zhang Q, Lv J, Zhang L, et al. Combined effect of coarse aggregate and fiber on tensile behavior of ultra-high performance concrete. *Constr Build Mater* 2016;121:310–8.
- [219] Park SH, Kim DJ, Ryu GS, Koh KT. Tensile behavior of ultra high performance hybrid fiber reinforced concrete. *Cem Concr Compos* 2012;34:172–84.
- [220] Yoo DY, Kang ST, Yoon YS. Effect of fiber length and placement method on flexural behavior, tension-softening curve, and fiber distribution characteristics of UHPFRC. *Constr Build Mater* 2014;64:67–81.
- [221] Grünewald S. Performance-based design of self-compacting fibre reinforced concrete. Delft University of Technology, 2004.
- [222] Rossi P, Coussy O, Boulay C, Acker P, Malier Y. Comparison between plain concrete toughness and steel fibre reinforced concrete toughness. *Cem Concr Res* 1986;16:303–13.
- [223] Olivito RS, Zuccarello FA. An experimental study on the tensile strength of steel fiber reinforced concrete. *Compos Part B Eng* 2010;41:246–55.
- [224] Su Y, Li J, Wu C, Wu P, Li ZX. Influences of nano-particles on dynamic strength of ultra-high performance concrete. *Compos Part B Eng* 2016;91:595–609.
- [225] Yoo DY, Banthia N, Yoon YS. Predicting service deflection of ultra-high-performance fiber-reinforced concrete beams reinforced with GFRP bars. *Compos Part B Eng* 2016;99:381–97.
- [226] Shafieifar M, Farzad M, Azizinamini A. A comparison of existing analytical methods to predict the flexural capacity of Ultra High Performance Concrete (UHPC) beams. *Constr Build Mater* 2018;172:10–8.
- [227] Nguyen DL, Ryu GS, Koh KT, Kim DJ. Size and geometry dependent tensile behavior of ultra-high-performance fiber-reinforced concrete. *Compos Part B Eng* 2014;58:279–92.
- [228] Randl N, Steiner T, Ofner S, Baumgartner E, Mészöly T. Development of UHPC mixtures from an ecological point of view. *Constr Build Mater* 2014;67:373–8.
- [229] Meng W, Khayat KH. Improving flexural performance of ultra-high-performance concrete by rheology control of suspending mortar. *Compos Part B Eng* 2017;117:26–34.

- [230] Shen B, Hubler M, Paulino GH, Struble LJ. Functionally-graded fiber-reinforced cement composite: Processing, microstructure, and properties. *Cem Concr Compos* 2008;30:663–73.
- [231] Park K, Paulino GH, Roesler J. Cohesive fracture model for functionally graded fiber reinforced concrete. *Cem Concr Res* 2010;40:956–65.
- [232] Lai J, Wang H, Yang H, Zheng X, Wang Q. Dynamic properties and SPH simulation of functionally graded cementitious composite subjected to repeated penetration. *Constr Build Mater* 2017;146:54–65.
- [233] Qin R, Hao H, Rousakis T, Lau D. Effect of shrinkage reducing admixture on new-to-old concrete interface. *Compos Part B Eng* 2019;167:346–55.
- [234] Rao HS, Ghorpade VG, Ramana N V., Gnaneswar K. Response of SIFCON two-way slabs under impact loading. *Int J Impact Eng* 2010;37:452–8.
- [235] Nguyen DL, Kim DJ, Ryu GS, Koh KT. Size effect on flexural behavior of ultra-high-performance hybrid fiber-reinforced concrete. *Compos Part B Eng* 2013;45:1104–16.
- [236] El-Hacha R, Chen D. Behaviour of hybrid FRP-UHPC beams subjected to static flexural loading. *Compos Part B Eng* 2012;43:582–93.
- [237] Hannawi K, Bian H, Prince-Agbodjan W, Raghavan B. Effect of different types of fibers on the microstructure and the mechanical behavior of Ultra-High Performance Fiber-Reinforced Concretes. *Compos Part B Eng* 2016;86:214–20.
- [238] Gesoglu M, Güneyisi E, Muhyaddin GF, Asaad DS. Strain hardening ultra-high performance fiber reinforced cementitious composites: Effect of fiber type and concentration. *Compos Part B Eng* 2016;103:74–83.
- [239] Yoo DY, Shin HO, Yang JM, Yoon YS. Material and bond properties of ultra high performance fiber reinforced concrete with micro steel fibers. *Compos Part B Eng* 2014;58:122–33.
- [240] Yu R, Tang P, Spiesz P, Brouwers HJH. A study of multiple effects of nano-silica and hybrid fibres on the properties of Ultra-High Performance Fibre Reinforced Concrete (UHPFRC) incorporating waste bottom ash (WBA). *Constr Build Mater* 2014;60:98–110.
- [241] Abbas S, Soliman AM, Nehdi ML. Exploring mechanical and durability properties of ultra-high performance concrete incorporating various steel fiber lengths and dosages. *Constr Build Mater* 2015;75:429–41.
- [242] Yazici H, Yiğiter H, Aydin S, Baradan B. Autoclaved SIFCON with high volume Class C fly ash binder phase. *Cem Concr Res* 2006;36:481–6.
- [243] Kaewunruen S, Remennikov AM. Dynamic flexural influence on a railway concrete sleeper in track system due to a single wheel impact. *Eng Fail Anal* 2009;16:705–12.
- [244] Bambach MR, Jama H, Zhao XL, Grzebieta RH. Hollow and concrete filled steel hollow sections under transverse impact loads. *Eng Struct* 2008;30:2859–70.
- [245] ACI Committee 544. Measurement of properties of fiber reinforced concrete. *Aci* 5442R-89 1999;89:1–12.
- [246] Badr A, Ashour AF, Platten AK. Statistical variations in impact resistance of polypropylene fibre-reinforced concrete. *Int J Impact Eng* 2006;32:1907–20.
- [247] Alavi Nia A, Hedayatian M, Nili M, Sabet VA. An experimental and numerical study on how steel and polypropylene fibers affect the impact resistance in fiber-reinforced concrete. *Int J Impact Eng* 2012;46:62–73.
- [248] Myers JJ, Tinsley M. Impact Resistance of Blast Mitigation Material Using Modified ACI Drop-Weight Impact Test. *ACI Mater J* 2014:339–48.
- [249] Xu B, Toutanji HA, Gilbert J. Impact resistance of poly(vinyl alcohol) fiber reinforced high-performance organic aggregate cementitious material. *Cem Concr Res* 2010;40:347–51.
- [250] Yoo D-Y, Banthia N, Kim S-W, Yoon Y-S. Response of ultra-high-performance fiber-reinforced concrete beams with continuous steel reinforcement subjected to low-velocity impact loading. *Compos Struct* 2015;126:233–45.
- [251] Akatay A, Bora MÖ, Çoban O, Fidan S, Tuna V. The influence of low velocity repeated impacts on residual compressive properties of honeycomb sandwich structures. *Compos Struct* 2015;125:425–33.
- [252] Caous D, Bois C, Wahl JC, Palin-Luc T, Valette J. A method to determine composite material residual tensile strength in the fibre direction as a function of the matrix damage state after

- fatigue loading. *Compos Part B Eng* 2017;127:15–25.
- [253] Lopresto V, Papa I, Langella A. Residual strength evaluation after impact tests in extreme temperature conditions. New equipment for CAI tests. *Compos Part B Eng* 2017;127:44–52.
- [254] Schubel PM, Luo J-J, Daniel IM. Impact and post impact behavior of composite sandwich panels. *Compos Part A Appl Sci Manuf* 2007;38:1051–7.
- [255] Kim H, Kim G, Gucunski N, Nam J, Jeon J. Assessment of flexural toughness and impact resistance of bundle-type polyamide fiber-reinforced concrete. *Compos Part B Eng* 2015;78:431–46.
- [256] Sutherland LS, Guedes Soares C. The use of quasi-static testing to obtain the low-velocity impact damage resistance of marine GRP laminates. *Compos Part B Eng* 2012;43:1459–67.
- [257] Zhou X, Ghaffar SH, Dong W, Oladiran O, Fan M. Fracture and impact properties of short discrete jute fibre-reinforced cementitious composites. *Mater Des* 2013;49:35–47.
- [258] RILEM TC 162-TDF. Test and design methods for steel fibre reinforced concrete: bending test. *Mater Struct* 2002;35:579–82.
- [259] EN 14651. Test method for metallic fibred concrete - Measuring the flexural tensile strength (limit of proportionality (LOP), residual). *Br Stand Institution-BSI CEN Eur Comm Stand* 2005.
- [260] Zhang XX, Abd Elazim AM, Ruiz G, Yu RC. Fracture behaviour of steel fibre-reinforced concrete at a wide range of loading rates. *Int J Impact Eng* 2014;71:89–96.
- [261] Sivakumar A, Sounthararajan VM. Toughness characterization of steel fibre reinforced concrete A review on various international standards. *J Civ Eng Constr Technol* 2013;4:65–9.
- [262] Erdem S, Blankson MA. Fractal-fracture analysis and characterization of impact-fractured surfaces in different types of concrete using digital image analysis and 3D nanomap laser profilometry. *Constr Build Mater* 2013;40:70–6.
- [263] Truong BT, Bui TT, Limam A, Si Larbi A, Le Nguyen K, Michel M. Experimental investigations of reinforced concrete beams repaired/reinforced by TRC composites. *Compos Struct* 2017;168:826–39.
- [264] Safdar M, Matsumoto T, Kakuma K. Flexural behavior of reinforced concrete beams repaired with ultra-high performance fiber reinforced concrete (UHPRC). *Compos Struct* 2016;157:448–60.
- [265] Knab LI, Clifton JR. Cumulative damage of reinforced concrete subjected to repeated impact. *Cem Concr Res* 1982;12:359–70.
- [266] Hashin Z. Cumulative damage theory for composite materials: Residual life and residual strength methods. *Compos Sci Technol* 1985;23:1–19.
- [267] Kaewunruen S, Remennikov AM. Progressive failure of prestressed concrete sleepers under multiple high-intensity impact loads. *Eng Struct* 2009;31:2460–73.
- [268] Dey V, Bonakdar A, Mobasher B. Low-velocity flexural impact response of fiber-reinforced aerated concrete. *Cem Concr Compos* 2014;49:100–10.
- [269] Cao YYY, Yu QL, Brouwers HJH, Chen W. Predicting the rate effects on hooked-end fiber pullout performance from Ultra-High Performance Concrete (UHPC). *Cem Concr Res* 2019;120:164–75.
- [270] Caverzan A, Cadoni E, Di Prisco M. Tensile behaviour of high performance fibre-reinforced cementitious composites at high strain rates. *Int J Impact Eng* 2012;45:28–38.
- [271] Mouhoubi S, Azouaoui K. Residual properties of composites based on glass fiber cloth of satin 8 weaving under impact-fatigue loading. 22ème Congrès Français de Mécanique, Lyon: 2015.
- [272] Wang S, Le HTN, Poh LH, Feng H, Zhang MH. Resistance of high-performance fiber-reinforced cement composites against high-velocity projectile impact. *Int J Impact Eng* 2016;95:89–104.
- [273] Zhang MH, Shim VPW, Lu G, Chew CW. Resistance of high-strength concrete to projectile impact. *Int J Impact Eng* 2005;31:825–41.
- [274] Li PP, Cao YYY, Brouwers HJH, Chen W, Yu QL. Development and properties evaluation of sustainable ultra-high performance pastes with quaternary blends. *J Clean Prod* 2019;240:118124.

- [275] Li PP, Yu QL, Brouwers HJH, Chen W. Conceptual design and performance evaluation of two-stage ultra-low binder ultra-high performance concrete. *Cem Concr Res* 2019;125:105858.
- [276] STANAG 2280. Test procedures and classification of the effects of weapons on structures. North Atlantic Treaty Organization (NATO); 2009.
- [277] Mao L, Barnett S, Begg D, Schleyer G, Wight G. Numerical simulation of ultra high performance fibre reinforced concrete panel subjected to blast loading. *Int J Impact Eng* 2014;64:91–100.
- [278] Hanchak SJ, Forrestal MJ, Young ER, Ehrgott JQ. Perforation of concrete slabs with 48 MPa (7 ksi) and 140 MPa (20 ksi) unconfined compressive strengths. *Int J Impact Eng* 1992;12:1–7.
- [279] Li QM, Chen XW. Dimensionless formulae for penetration depth of concrete target impacted by a non-deformable projectile. *Int J Impact Eng* 2003;28:93–116.
- [280] Ong KCG, Basheerkhan M, Paramasivam P. Behaviour of fibre reinforced concrete slabs under low velocity projectile impact. *ACI Spec Publ* 1999;172:993–1011.
- [281] Feng J, Gao X, Li J, Dong H, He Q, Liang J, et al. Penetration resistance of hybrid-fiber-reinforced high-strength concrete under projectile multi-impact. *Constr Build Mater* 2019;202:341–52.
- [282] Feng J, Gao X, Li J, Dong H, Yao W, Wang X, et al. Influence of fiber mixture on impact response of ultra-high-performance hybrid fiber reinforced cementitious composite. *Compos Part B Eng* 2019;163:487–96.
- [283] Yu R, Spiesz P, Brouwers HJH. Energy absorption capacity of a sustainable Ultra-High Performance Fibre Reinforced Concrete (UHPFRC) in quasi-static mode and under high velocity projectile impact. *Cem Concr Compos* 2016;68:109–22.
- [284] Liu J, Wu C, Li J, Fang J, Su Y, Shao R. Ceramic balls protected ultra-high performance concrete structure against projectile impact—A numerical study. *Int J Impact Eng* 2019;125:143–62.
- [285] Sovják R, Vavříník T, Zatloukal J, Máca P, Mičunek T, Frydrýn M. Resistance of slim UHPFRC targets to projectile impact using in-service bullets. *Int J Impact Eng* 2015;76:166–77.
- [286] Peng Y, Wu H, Fang Q, Gong ZM. Geometrical scaling effect for penetration depth of hard projectiles into concrete targets. *Int J Impact Eng* 2018;120:46–59.
- [287] Dancygier AN, Katz A, Benamou D, Yankelevsky DZ. Resistance of double-layer reinforced HPC barriers to projectile impact. *Int J Impact Eng* 2014;67:39–51.
- [288] Peng Y, Wu H, Fang Q, Liu JZ, Gong ZM. Residual velocities of projectiles after normally perforating the thin ultra-high performance steel fiber reinforced concrete slabs. *Int J Impact Eng* 2016;97:1–9.
- [289] Li J, Zhang YX. Evolution and calibration of a numerical model for modelling of hybrid-fibre ECC panels under high-velocity impact. *Compos Struct* 2011;93:2714–22.
- [290] Tai YS. Flat ended projectile penetrating ultra-high strength concrete plate target. *Theor Appl Fract Mech* 2009;51:117–28.
- [291] Chi Y, Xu L, Mei G, Hu N, Su J. A unified failure envelope for hybrid fibre reinforced concrete subjected to true triaxial compression. *Compos Struct* 2014;109:31–40.
- [292] Song D, Tan Q, Zhan H, Liu F, Jiang Z. Experimental investigation on the cellular steel-tube-confined concrete targets against projectile impact. *Int J Impact Eng* 2019;131:94–110.
- [293] Meng C, Tan Q, Jiang Z, Song D, Liu F. Approximate solutions of finite dynamic spherical cavity-expansion models for penetration into elastically confined concrete targets. *Int J Impact Eng* 2018;114:182–93.

Abbreviations and symbols

Abbreviations

BA	Basalts aggregate
BET	Brunauer-Emmett-Teller
BJH	Barrett-Joyner-Hallenda
bvop	By the volume of powder
CH	Calcium hydroxide
C-S-H	Calcium silicate hydrate
DOP	Depth of penetration
DTG	Differential thermal grvimetric
FGCB	Functionally graded composite beam
FTIR	Fourier transform infrared spectroscopy
GGBS	Ground granulated blast furnace slag
GPC	Gel permeation chromatography
ITZ	Interfacial transition zone
LP	Limestone powder
MHF	Maximum heat flow
MIP	Mercury intrusion porosimetry
mS	Micro-silica
MS	Micro-sand
NATO	North Atlantic Treaty Organization
nS	Nano-silica
PC	Portland cement
PCE	Polycarboxylic ethers
RH	Relative humidity
PSD	Particle size distribution
RPC	Reactive powder concrete
S	Sand
SC	Slag cement
SCC	Self-compacting concrete
SCM	Supplementary cementitious material
SEM	Scanning electron microscope
SF	Steel fibre
SIFCON	Slurry-infiltrated fibrous concrete
SP	Superplasticizer
TG	Thermal gravimetric
TRMP	Time to reach the maximum peak
TSC	Two-stage concrete
TS-UHPC	Two-stage ultra-high performance concrete
UHPC	Ultra-high performance concrete
UHPRFC	Ultra-high performance fibre reinforced concrete
vol.	Volume fraction
W	Water
w/b	Water-to-binder ratio by mass
w/p	Water-to-powder ratio by mass
XRF	X-ray Fluorescence

Roman symbols

a_{ij}	Interaction coefficient of loosening effect	[-]
$A(n)$	A certain property of UHPFRC	[-]
b_{ij}	Interaction coefficient of wall effect	[-]
d	Spread flow diameter	[cm]
D	Particle size	[mm]
d_0	The cone base diameter	[cm]
d_f	Diameter of fibre	[mm]
d_j	Average particle diameter of j -class particle	[mm]
D_{max}	Maximum particle size	[mm]
D_{min}	Minimum particle size	[mm]
$D(n)$	Damage index after impact number of n	[-]
d_p	Diameter of projectile	[mm]
E	Energy absorption	[J]
$E(n)$	Absorbed energy during the impact number of n	[J]
E_p	Deformation coefficient on the water demand	[-]
E_r	Residual impact resistance	[J]
E_Y	Young's modulus	[GPa]
F	Concentrated load	[kN]
g	Gravity	[m/s ²]
h	Height of drop-weight ball	[m]
h_h	Maximum height of hammer after impact	[m]
H_h	Initial height of impact hammer	[m]
h_s	Maximum height of specimen after impact	[m]
I	Cross-section moment of inertia	[m ⁴]
k	Correlation coefficient	[-]
K	Bulk modulus of the whole matrix	[MPa]
K_s	Bulk modulus of the solid material	[MPa]
K_r	Compaction index to determine the real packing density	[-]
L	Fibre length	[mm]
L_b	Length of beam	[mm]
m	Mass of drop-weight ball	[kg]
M_w	Molecular weight	[g/mol]
m_{BA}	Mass of basalt aggregate	[kg]
m_{binder}	Mass of binder	[kg]
M_{CH}	Molar mass of calcium hydroxide	[g/mol]
M_{C-S-H}	Molar mass of calcium silicate hydrate gel	[g/mol]
m_{CO_2}	Mass of embedded CO ₂ emission	[kg]
m_d	Mass of sample in air after oven drying	[kg]
M_h	Mass of impact hammer	[kg]
M_H	Molar mass of water	[g/mol]
m_i	Mass of material i	[kg]
m_{i_grout}	Mass of material i in grout	[kg]
m_s	Mass of sample in air after water saturation	[kg]
M_s	Mass of beam	[kg]
m_w	Mass of sample in water after water saturation by vacuum	[kg]
$M(x)$	Bending moment at the position of x along the length	[m]

n	Impact number	[-]
n_u	Total impact number till to complete damage	[-]
P_1	First crack load	[kN]
$P(D)$	Cumulative fraction of total solids being smaller than D	[-]
P_{mix}	Designed mix	[-]
P_p	Peak load	[kN]
P_{tar}	Target grading	[-]
q	Particle distribution modulus	[-]
$\dot{Q}(t)$	Heat flow	[J/s]
$\ddot{Q}(t)$	Heat flow rate	[J/s ²]
R	Ideal gas constant	[-]
R^2	Coefficient of determination	[-]
r_{grout}	Volume fraction of grout	[-]
r_i	Mass fraction of material i	[-]
t	Time	[s]
T	Temperature	[°C]
T_f	Flexural toughness	[J]
t_{final}	Final setting time	[s]
$t_{\dot{Q}=max}$	Time of maximum heat flow rate	[s]
$T_{v-funnel}$	Mini V-funnel flow time	[s]
V_0	Velocity of hammer before impact	[m/s]
$V_{container}$	Volume of testing container	[m ³]
V_{fibre}	Volume content of fibre	[%]
V_p	Volume of powder	[m ³]
V_r	Velocity of hammer after impact	[m/s]
V_s	Velocity of specimen after impact	[m/s]
V_{solids}	Solid volume	[m ³]
V_w	Volume of water	[m ³]
X	Binder efficiency	[MPa/(kg/m ³)]
X_B	Property in binary binder	[-]
X_Q	Property in quaternary binder	[-]
X_{ref}	Property in reference	[-]
X_T	Property in ternary binder	[-]

Greek symbols

α_j	Packing density of j -class particle	[-]
β	Virtual packing density of total mixture	[-]
β_{CO2}	Binder sustainability efficiency	[MPa/(kg/m ³)]
β_j	Virtual packing density of the j -class particle	[-]
β_{layer}	Bottom layer to total beam thickness ratio	[-]
β_p	Water demand	[-]
Γ_p	Relative slump	[-]
δ	Deflection	[mm]
δ_u	Maximum deflection	[mm]
Δm_{C-S-H}	TG mass loss of calcium silicate hydrate gel	[%]
Δm_{CH}	TG mass loss of calcium hydroxide	[%]
η	Fibre reinforced factor	[-]
η_T	Fibre reinforced factor in terms of toughness	[-]
η_σ	Fibre reinforced factor in terms of flexural strength	[-]

ρ	Density	[kg/m ³]
ρ_{bulk}	Bulk density	[kg/m ³]
ρ_r	Radius of curvature	[m]
$\rho_{specific}$	Specific density	[kg/m ³]
σ_1	First crack stress	[MPa]
σ_c	Compressive strength	[MPa]
σ_{cap}	Capillary tensile stress	[MPa]
$\sigma_{c_concrete}$	Compressive strength of TSC	[MPa]
σ_{c_grout}	Compressive strength of grout	[MPa]
σ_e	Elastic strength	[MPa]
σ_p	Peak stress	[MPa]
σ_t	Splitting tensile strength	[MPa]
$\sigma_{t_concrete}$	Splitting tensile strength of TSC	[MPa]
φ	Water permeable porosity	[%]
$\varphi_{concrete}$	Water permeable porosity of TSC	[%]
φ_{grout}	Water permeable porosity of grout	[%]
$\varphi_{ITZ_induced}$	ITZ-induced water permeable porosity	[%]
ϕ	Strain hardening factor	[-]
ϕ_p	Wet packing density	[-]

Acknowledgements

I started this PhD research on 1 September 2015 in the Building Materials group at the Department of Built Environment, Eindhoven University of Technology (TU/e), the Netherlands. When the end of my PhD research is approaching, I am really realizing that the work presented in this thesis should not have been completed without the support and help of a lot of institutions and people. I would like to express my sincere appreciation to all those who contributed to this research both directly and indirectly.

Firstly, I would like to sincerely express my gratitude to my supervisor and promotor Prof.dr.ir. H.J.H. Brouwers, who gave me the chance to join his group and did my PhD research. Thank you very much to support me to apply for the funding from China Scholar Council. During the last four years, you gave me valuable guidance, suggestions, discussions and trust on my research project. You also provided me adequate testing and working conditions, and supported me to participate in lots of international conferences and academic communications. It is my great honour and pleasure to work in your group.

Furthermore, I want to extend my appreciation to my daily supervisor and co-promotor Dr. Qingliang Yu. I am grateful to your help, effort and dedication on supervising my daily research. You were always ready to offer your patient and timely help even though you were very busy to handle the supervision for many other PhD students. I still remember that you often helped to modify our draft papers late at night, even in weekends. The attitude towards research and life that I learned from you will definitely benefit my future career.

Additionally, I would like to thank all the teachers in my education career. Among those, I am especially grateful to my master supervisor Prof. Zhigang Ren, who taught and helped me a lot. It was you that encouraged me to go abroad and continue my PhD study. Also I wish to thank some other professors from Wuhan University of Technology, e.g. Prof. Zhean Lu, Prof. Qiankun Wang, Prof. Zhonghe Shui, Prof. Wei Chen. You offered lots of assistance and support to me for my research.

I would like to express my appreciation to Prof.dr. W. Chen (Wuhan University of Technology, China), Prof.dr. H. Justnes (Norwegian University of Science and Technology, Norway), Prof.ir. S.N.M. Wijte (Eindhoven University of Technology, the Netherlands), Prof.dr.-ing. P.M. Teuffel (Eindhoven University of Technology, the Netherlands), Dr.dipl.-ing. G. Hüsken (Bundesanstalt für Materialforschung und -prüfung, Germany) for your comments on my PhD thesis and for agreeing to be the member of my defence committee.

I also greatly thank the China Scholarship Council and all sponsors of the Building Materials research group at TU/e, which provided the financial supports for my living and research during the last four years. I also appreciate the companies for supplying the cement (ENCI), steel fibres (Bekaert) and superplasticizer (Sika and BASF). Appreciations are expressed to the Dutch Defense Academy and the Knowledge Centre Weapon System, and Ammunition from the Dutch Ministry of Defense for conducting the ballistic tests. I am also grateful to the Management and Secretary departments at TU/e, who gave a lot of assistance beside the research, and made the life and work environment much easier and more convenient.

Special appreciation is expressed to late Ing. Ad. Verhagen for sharing his experience about impact resistant concrete and designing the pendulum impact device at TU/e. I am grateful for the help of Ing. D. Krabbenborg during the ballistic tests. I also would like to thank Dr. P. Spiesz and Prof.dr. Rui Yu for sharing their experience and providing guidance on ultra-high performance concrete. Also thank my previous colleagues Dr. Pei Tang, Dr. Xu Gao, Dr. Bo Yuan to teach me how to use various testing devices in the lab. It is my pleasure to cooperate with Gang Liu, Yangyueye Cao, Chengping Chung and Maarten Sluijsmans, we were very happy to discuss and help each other about our research. I also thank the technicians in BPS lab and Structural lab for their support and assistance on my tests, as well as Dr. Lihua Shen, Yi Qin and Xinglong Pan for the selfless helps and contributions to my experiments.

Many other people I want to thank without whom my PhD life would be less fun and meaningful. Thanks to all my colleagues in the Building Materials research group, all the poker group members and my Chinese friends in the Netherlands. I enjoyed the talks, travelling, parties and games with you, which were definitely pleasant times and experiences in the last four years.

Finally, I must express my appreciations to my family, my father, mother, brother, sister-in-law, sister, girlfriend, and my little cute niece and nephew. I owe you a lot, and could not stay around to take care of you during these years. I am grateful to have you as my family member and love you forever. I wish all of you a happy and healthy life in the future.

Summary

Extreme conditions or accidental loadings surrounding our human life have attracted more and more public attention. Examples are explosive or ballistic impact in terrorist attacks, natural earthquakes or hurricanes, vehicle impact in traffic accidents, and ship collisions on offshore structure or bridge. Ultra-high performance fibre reinforced concrete (UHPFRC) is a relatively new building material, which has superior workability, mechanical properties, energy dissipation capacity and durability. Those excellent characteristics and properties give it a great potential to be used in impact resistant components and structures, such as protective elements in military and civil engineering. However, the high cement consumption, large dosage of superplasticizer and high content of steel fibre unitization cause some disadvantages, such as high costs and a large embodied energy. Hence, optimization of UHPFRC mixtures is needed to make them cheaper, more eco-friendly and higher impact resistant to broaden the applications, and the static mechanical properties and impact resistance of UHPFRC are necessary to be investigated to reveal the impact resistant mechanism and provide guidance in the design of protective elements and structures.

To develop impact resistant UHPFRC mixtures, the key parameters in the mix design of UHPFRC are investigated and further optimized. As an indispensable chemical additive, superplasticizers are firstly studied in Chapter 2, including the effect of dispersing, fluid-retaining and retardation on the early-age properties of ultra-high performance concrete (UHPC). Then, the optimal type and dosage of superplasticizer can be obtained. Secondly, the binder system in UHPC is further optimized towards low cement clinker consumption in Chapter 3. Two methods are proposed, namely utilizing high-volume limestone powder to replace cement and developing quaternary binders containing cement-slag-limestone-silica. After that, coarse aggregates are introduced in the UHPC system in Chapter 4, to reduce the powder content and cost, improve the volume stability and penetration impact resistance, etc. UHPC mixtures incorporating coarse aggregates are successfully developed by applying a particle packing model. And a novel concept of two-stage UHPC is proposed for maximum volume of coarse aggregate utilization and ultra-low binder consumption. Furthermore, the influence of steel fibres on the properties of UHPC are explored in Chapter 5. Three types of steel fibres are studied in terms of the utilization efficiencies. Additionally, functionally graded composite beams (FGCB) are developed in Chapter 6, to further increase impact resistance and steel fibre utilization efficiency. They are designed by applying the composite concepts of UHPC, two-stage concrete and slurry-infiltrated fibrous concrete.

To evaluate the impact resistance of the designed UHPFRC and get a better understanding on the impact resistant mechanism, both low-velocity and high-velocity impact experiments are conducted in Chapter 7 & Chapter 8, including pendulum, drop-weight and in-service bullet impacts. The low-velocity impact testing results show that coarse basalt aggregates up to 25 mm can be successfully introduced in developing an impact resistant UHPFRC. The 30 mm medium hook-ended are more efficient in improving the impact resistance than the other ones. The novel concept of FGCB results in a superior impact resistance, as well as a high cement and steel fibre utilization efficiency. The toughness can be used as a good

indicator to reflect the low-velocity impact resistance of UHPFRC beams, while the flexural strength also affects impact resistance when the impact energy is below the threshold energy. The bullet testing results indicate that a compressive strength class of 150 MPa is recommended for UHPFRC to design protective structures by considering both cost efficiency and anti-penetration performance. And 2 vol.% 13 mm straight steel fibres are recommended to design impact resistant UHPFRC by concerning the depth of penetration (DOP) and crack inhibition. The DOP reduction is about 14.5% with the increase of the maximum size of coarse aggregates from 2 mm to 25 mm. Perforation limits of the designed slabs are about 85 mm and 95 mm to withstand the 7.62×51 mm NATO armor-piercing bullet at the striking velocity of 843 m/s and 926 m/s, respectively.

List of publications

Peer-reviewed journal papers

- [1] **P.P. Li**, Q.L. Yu, H.J.H. Brouwers. Effect of PCE-type superplasticizer on early-age behaviour of ultra-high performance concrete (UHPC). *Construction and Building Materials*. 153 (2017) 740-750.
- [2] **P.P. Li**, Q.L. Yu, H.J.H. Brouwers. Effect of coarse basalt aggregates on the properties of Ultra-high Performance Concrete (UHPC). *Construction and Building Materials*. 170 (2018) 649-659.
- [3] **P.P. Li**, Q.L. Yu. Responses and post-impact properties of ultra-high performance fibre reinforced concrete under pendulum impact. *Composite Structures*. 208 (2019) 806-815.
- [4] Y.Y.Y. Cao, **P.P. Li**, H.J.H. Brouwers, M.J.C. Sluijsmans, Q.L. Yu. Enhancing flexural performance of ultra-high performance concrete by an optimized layered-structure concept. *Composites Part B: Engineering*. 171 (2019) 154-165. (**Equivalent first author**)
- [5] **P.P. Li**, Y.Y.Y. Cao, H.J.H. Brouwers, W. Chen, Q.L. Yu. Development and properties evaluation of sustainable ultra-high performance pastes with quaternary blends. *Journal Cleaner Production*. 240 (2019) 118124.
- [6] **P.P. Li**, Q.L. Yu, H.J.H. Brouwers, W. Chen. Conceptual design and performance evaluation of two-stage ultra-low binder ultra-high performance concrete. *Cement and Concrete Research*. 125 (2019) 105858.
- [7] **P.P. Li**, H.J.H. Brouwers, Qingliang Yu. Influence of key design parameters of ultra-high performance fibre reinforced concrete on in-service bullet resistance. *Internal Journal of Impact Engineering*. 136 (2020) 103434.
- [8] **P.P. Li**, M.J.C. Sluijsmans, H.J.H. Brouwers, Q.L. Yu. Functionally graded ultra-high performance cementitious composite with enhanced properties. *Composites Part B: Engineering*. 183 (2020) 107680.
- [9] **P.P. Li**, H.J.H. Brouwers, W. Chen, Qingliang Yu. Optimization and characterization of high-volume limestone powder in sustainable ultra-high performance concrete. Submitted.
- [10] **P.P. Li**, Y.Y.Y. Cao, M.J.C. Sluijsmans, H.J.H. Brouwers, Qingliang Yu. Synergistic effect of steel fibres and coarse aggregates on impact properties of ultra-high performance fibre reinforced concrete. Submitted.

Conference proceedings

- [1] **P.P. Li**, Q.L. Yu, H.J.H. Brouwers, R. Yu. Fresh behaviour of ultra-high performance concrete (UHPC): an investigation of the effect of superplasticizers and steel fibres. *Proceedings of the 9th International Concrete Conference 2016, Environment, Efficiency and Economic Challenges for Concrete, Dundee, Scotland*, p. 635-644.

- [2] **P.P. Li**, Q.L. Yu, C.P. Chung, H.J.H. Brouwers. Mix design and performance evaluation of ultra-high performance concrete (UHPC) with basalt aggregate. 6th International Conference on Non-Traditional Cement and Concrete 2017, Brno, Czech Republic, p. 202-209.
- [3] **P.P. Li**, Q.L. Yu, H.J.H. Brouwers. Damage mechanism of ultra-high performance fiber reinforced concrete under repeated low-velocity impact. The 9th International Symposium on Cement and Concrete (ISCC 2017), Wuhan, China, p. 1-7.
- [4] **P.P. Li**, Q.L. Yu, H.J.H. Brouwers. Strength and bond characteristic of UHPC pastes with quaternary binders. Proceedings of the 2nd International Conference on UHPC Materials and Structures UHPC 2018, Fuzhou, China, p. 337-343.
- [5] **P.P. Li**, Q.L. Yu, H.J.H. Brouwers. Recent development on sustainable ultra-high performance concrete design with low cement consumption: a review. 2nd International Conference on Sustainable Building Materials 2019, Eindhoven, Netherlands, p. 353-362.

Curriculum vitae

Peipeng Li was born in Guangshui City, Hubei Province, China on September 26, 1988. After finishing his primary, middle and high school educations in Guangshui City, he started to study at Wuhan University of Technology (WHUT) in September 2008. In June 2012, he received his Bachelor's degree from the Department of Transportation, majored in Engineering Structural Analysis. Then he continued his graduate study at WHUT and got the Master's degree from the Department of Civil Engineering and Architecture, majored in Structural Engineering under the supervision of Prof. Zhigang Ren. His research interests included composite structures (e.g. concrete-filled steel tube), numerical simulation analysis and structural health monitoring. In September 2015, he began the PhD study under the supervision of Prof. H.J.H. Brouwers and Dr. Qingliang Yu in the Netherlands. The PhD research was funded by the China Scholarship Council and Eindhoven University of Technology (TU/e). His PhD research involved ultra-high performance concrete, fibre reinforced concrete, sustainable and green building materials, protective and defence materials and structures.

Bouwstenen is een publicatiereeks van de Faculteit Bouwkunde, Technische Universiteit Eindhoven. Zij presenteert resultaten van onderzoek en andere activiteiten op het vakgebied der Bouwkunde, uitgevoerd in het kader van deze Faculteit.

Bouwstenen en andere proefschriften van de TU/e zijn online beschikbaar via:
<https://research.tue.nl/>

Kernredactie
MTOZ

Reeds verschenen in de serie

Bouwstenen

nr 1

Elan: A Computer Model for Building Energy Design: Theory and Validation

Martin H. de Wit

H.H. Driessen

R.M.M. van der Velden

nr 2

Kwaliteit, Keuzevrijheid en Kosten: Evaluatie van Experiment Klarendal, Arnhem

J. Smeets

C. le Nobel

M. Broos

J. Frenken

A. v.d. Sanden

nr 3

Crooswijk: Van 'Bijzonder' naar 'Gewoon'

Vincent Smit

Kees Noort

nr 4

Staal in de Woningbouw

Edwin J.F. Delsing

nr 5

Mathematical Theory of Stressed Skin Action in Profiled Sheeting with Various Edge Conditions

Andre W.A.M.J. van den Bogaard

nr 6

Hoe Berekenbaar en Betrouwbaar is de Coëfficiënt k in x -ksigma en x -ks?

K.B. Lub

A.J. Bosch

nr 7

Het Typologisch Gereedschap: Een Verkennende Studie Omtrent Typologie en Omtrent de Aanpak van Typologisch Onderzoek

J.H. Luiten

nr 8

Informatievoorziening en Beheerprocessen

A. Nauta

Jos Smeets (red.)

Helga Fassbinder (projectleider)

Adrie Proveniers

J. v.d. Moosdijk

nr 9

Strukturering en Verwerking van Tijdgegevens voor de Uitvoering van Bouwwerken

ir. W.F. Schaefer

P.A. Erkelens

nr 10

Stedebouw en de Vorming van een Speciale Wetenschap

K. Doevendans

nr 11

Informatica en Ondersteuning van Ruimtelijke Besluitvorming

G.G. van der Meulen

nr 12

Staal in de Woningbouw, Korrosie-Bescherming van de Begane Grondvloer

Edwin J.F. Delsing

nr 13

Een Thermisch Model voor de Berekening van Staalplaatbetonvloeren onder Brandomstandigheden

A.F. Hamerlinck

nr 14

De Wijkgedachte in Nederland: Gemeenschapsstreven in een Stedebouwkundige Context

K. Doevendans

R. Stolzenburg

nr 15

Diaphragm Effect of Trapezoidally Profiled Steel Sheets:

Experimental Research into the Influence of Force Application

Andre W.A.M.J. van den Bogaard

nr 16

Versterken met Spuit-Ferrocement: Het Mechanische Gedrag van met Spuit-Ferrocement Versterkte Gewapend Betonbalken

K.B. Lubir

M.C.G. van Wanroy

nr 17

**De Tractaten van
Jean Nicolas Louis Durand**
G. van Zeyl

nr 18

**Wonen onder een Plat Dak:
Drie Opstellen over Enkele
Vooronderstellingen van de
Stedebouw**
K. Doevendans

nr 19

**Supporting Decision Making Processes:
A Graphical and Interactive Analysis of
Multivariate Data**
W. Adams

nr 20

**Self-Help Building Productivity:
A Method for Improving House Building
by Low-Income Groups Applied to Kenya
1990-2000**
P. A. Erkelens

nr 21

**De Verdeling van Woningen:
Een Kwestie van Onderhandelen**
Vincent Smit

nr 22

**Flexibiliteit en Kosten in het Ontwerpproces:
Een Besluitvormingondersteunend Model**
M. Prins

nr 23

**Spontane Nederzettingen Begeleid:
Voorwaarden en Criteria in Sri Lanka**
Po Hin Thung

nr 24

**Fundamentals of the Design of
Bamboo Structures**
Oscar Arce-Villalobos

nr 25

Concepten van de Bouwkunde
M.F.Th. Bax (red.)
H.M.G.J. Trum (red.)

nr 26

Meaning of the Site
Xiaodong Li

nr 27

**Het Woonmilieu op Begrip Gebracht:
Een Speurtocht naar de Betekenis van het
Begrip 'Woonmilieu'**
Jaap Ketelaar

nr 28

Urban Environment in Developing Countries
editors: Peter A. Erkelens
George G. van der Meulen (red.)

nr 29

**Stategische Plannen voor de Stad:
Onderzoek en Planning in Drie Steden**
prof.dr. H. Fassbinder (red.)
H. Rikhof (red.)

nr 30

Stedebouwkunde en Stadsbestuur
Piet Beekman

nr 31

**De Architectuur van Djenné:
Een Onderzoek naar de Historische Stad**
P.C.M. Maas

nr 32

Conjoint Experiments and Retail Planning
Harmen Oppewal

nr 33

**Strukturformen Indonesischer Bautechnik:
Entwicklung Methodischer Grundlagen
für eine 'Konstruktive Pattern Language'
in Indonesien**
Heinz Frick arch. SIA

nr 34

**Styles of Architectural Designing:
Empirical Research on Working Styles
and Personality Dispositions**
Anton P.M. van Bakel

nr 35

**Conjoint Choice Models for Urban
Tourism Planning and Marketing**
Benedict Dellaert

nr 36

Stedelijke Planvorming als Co-Productie
Helga Fassbinder (red.)

nr 37

Design Research in the Netherlands

editors: R.M. Oxman
M.F.Th. Bax
H.H. Achten

nr 38

Communication in the Building Industry

Bauke de Vries

nr 39

**Optimaal Dimensioneren van
Gelaste Plaatliggers**

J.B.W. Stark
F. van Pelt
L.F.M. van Gorp
B.W.E.M. van Hove

nr 40

Huisvesting en Overwinning van Armoede

P.H. Thung
P. Beekman (red.)

nr 41

**Urban Habitat:
The Environment of Tomorrow**

George G. van der Meulen
Peter A. Erkelens

nr 42

A Typology of Joints

John C.M. Olie

nr 43

**Modeling Constraints-Based Choices
for Leisure Mobility Planning**

Marcus P. Stemerding

nr 44

Activity-Based Travel Demand Modeling

Dick Ettema

nr 45

**Wind-Induced Pressure Fluctuations
on Building Facades**

Chris Geurts

nr 46

Generic Representations

Henri Achten

nr 47

**Johann Santini Aichel:
Architectuur en Ambiguiteit**

Dirk De Meyer

nr 48

**Concrete Behaviour in Multiaxial
Compression**

Erik van Geel

nr 49

Modelling Site Selection

Frank Witlox

nr 50

Ecolemma Model

Ferdinand Beetstra

nr 51

**Conjoint Approaches to Developing
Activity-Based Models**

Donggen Wang

nr 52

On the Effectiveness of Ventilation

Ad Roos

nr 53

**Conjoint Modeling Approaches for
Residential Group preferences**

Eric Molin

nr 54

**Modelling Architectural Design
Information by Features**

Jos van Leeuwen

nr 55

**A Spatial Decision Support System for
the Planning of Retail and Service Facilities**

Theo Arentze

nr 56

Integrated Lighting System Assistant

Ellie de Groot

nr 57

Ontwerpend Leren, Leren Ontwerpen

J.T. Boekholt

nr 58

**Temporal Aspects of Theme Park Choice
Behavior**

Astrid Kemperman

nr 59

**Ontwerp van een Geïndustrialiseerde
Funderingswijze**

Faas Moonen

nr 60

Merlin: A Decision Support System for Outdoor Leisure Planning

Manon van Middelkoop

nr 61

The Aura of Modernity

Jos Bosman

nr 62

Urban Form and Activity-Travel Patterns

Daniëlle Snellen

nr 63

Design Research in the Netherlands 2000

Henri Achten

nr 64

Computer Aided Dimensional Control in Building Construction

Rui Wu

nr 65

Beyond Sustainable Building

editors: Peter A. Erkelens
Sander de Jonge
August A.M. van Vliet

co-editor: Ruth J.G. Verhagen

nr 66

Das Globalrecyclingfähige Haus

Hans Löfflad

nr 67

Cool Schools for Hot Suburbs

René J. Dierkx

nr 68

A Bamboo Building Design Decision Support Tool

Fitri Mardjono

nr 69

Driving Rain on Building Envelopes

Fabien van Mook

nr 70

Heating Monumental Churches

Henk Schellen

nr 71

Van Woningverhuurder naar Aanbieder van Woongenot

Patrick Dogge

nr 72

Moisture Transfer Properties of Coated Gypsum

Emile Goossens

nr 73

Plybamboo Wall-Panels for Housing

Guillermo E. González-Beltrán

nr 74

The Future Site-Proceedings

Ger Maas

Frans van Gassel

nr 75

Radon transport in Autoclaved Aerated Concrete

Michel van der Pal

nr 76

The Reliability and Validity of Interactive Virtual Reality Computer Experiments

Amy Tan

nr 77

Measuring Housing Preferences Using Virtual Reality and Belief Networks

Maciej A. Orzechowski

nr 78

Computational Representations of Words and Associations in Architectural Design

Nicole Segers

nr 79

Measuring and Predicting Adaptation in Multidimensional Activity-Travel Patterns

Chang-Hyeon Joh

nr 80

Strategic Briefing

Fayez Al Hassan

nr 81

Well Being in Hospitals

Simona Di Cicco

nr 82

Solares Bauen: Implementierungs- und Umsetzungs-Aspekte in der Hochschulausbildung in Österreich

Gerhard Schuster

nr 83

Supporting Strategic Design of Workplace Environments with Case-Based Reasoning

Shauna Mallory-Hill

nr 84

ACCEL: A Tool for Supporting Concept Generation in the Early Design Phase

Maxim Ivashkov

nr 85

Brick-Mortar Interaction in Masonry under Compression

Ad Vermeltfoort

nr 86

Zelfredzaam Wonen

Guus van Vliet

nr 87

Een Ensemble met Grootstedelijke Allure

Jos Bosman

Hans Schippers

nr 88

On the Computation of Well-Structured Graphic Representations in Architectural Design

Henri Achten

nr 89

De Evolutie van een West-Afrikaanse Vernaculaire Architectuur

Wolf Schijns

nr 90

ROMBO Tactiek

Christoph Maria Ravesloot

nr 91

External Coupling between Building Energy Simulation and Computational Fluid Dynamics

Ery Djunaedy

nr 92

Design Research in the Netherlands 2005

editors: Henri Achten

Kees Dorst

Pieter Jan Stappers

Bauke de Vries

nr 93

Ein Modell zur Baulichen Transformation

Jalil H. Saber Zaimian

nr 94

Human Lighting Demands: Healthy Lighting in an Office Environment

Myriam Aries

nr 95

A Spatial Decision Support System for the Provision and Monitoring of Urban Greenspace

Claudia Pelizaro

nr 96

Leren Creëren

Adri Proveniers

nr 97

Simlandscape

Rob de Waard

nr 98

Design Team Communication

Ad den Otter

nr 99

Humaan-Ecologisch Georiënteerde Woningbouw

Juri Czabanowski

nr 100

Hambase

Martin de Wit

nr 101

Sound Transmission through Pipe Systems and into Building Structures

Susanne Bron-van der Jagt

nr 102

Het Bouwkundig Contrapunt

Jan Francis Boelen

nr 103

A Framework for a Multi-Agent Planning Support System

Dick Saarloos

nr 104

Bracing Steel Frames with Calcium Silicate Element Walls

Bright Mweene Ng'andu

nr 105

Naar een Nieuwe Houtskeletbouw

F.N.G. De Medts

nr 106 and 107
Niet gepubliceerd

nr 108
Geborgenheid
T.E.L. van Pinxteren

nr 109
Modelling Strategic Behaviour in Anticipation of Congestion
Qi Han

nr 110
Reflecties op het Woondomein
Fred Sanders

nr 111
On Assessment of Wind Comfort by Sand Erosion
Gábor Dezsö

nr 112
Bench Heating in Monumental Churches
Dionne Limpens-Neilen

nr 113
RE. Architecture
Ana Pereira Roders

nr 114
Toward Applicable Green Architecture
Usama El Fiky

nr 115
Knowledge Representation under Inherent Uncertainty in a Multi-Agent System for Land Use Planning
Liyang Ma

nr 116
Integrated Heat Air and Moisture Modeling and Simulation
Jos van Schijndel

nr 117
Concrete Behaviour in Multiaxial Compression
J.P.W. Bongers

nr 118
The Image of the Urban Landscape
Ana Moya Pellitero

nr 119
The Self-Organizing City in Vietnam
Stephanie Geertman

nr 120
A Multi-Agent Planning Support System for Assessing Externalities of Urban Form Scenarios
Rachel Katoshevski-Cavari

nr 121
Den Schulbau Neu Denken, Fühlen und Wollen
Urs Christian Maurer-Dietrich

nr 122
Peter Eisenman Theories and Practices
Bernhard Kormoss

nr 123
User Simulation of Space Utilisation
Vincent Tabak

nr 125
In Search of a Complex System Model
Oswald Devisch

nr 126
Lighting at Work: Environmental Study of Direct Effects of Lighting Level and Spectrum on Psycho-Physiological Variables
Grazyna Górnicka

nr 127
Flanking Sound Transmission through Lightweight Framed Double Leaf Walls
Stefan Schoenwald

nr 128
Bounded Rationality and Spatio-Temporal Pedestrian Shopping Behavior
Wei Zhu

nr 129
Travel Information: Impact on Activity Travel Pattern
Zhongwei Sun

nr 130
Co-Simulation for Performance Prediction of Innovative Integrated Mechanical Energy Systems in Buildings
Marija Trčka

nr 131
Niet gepubliceerd

nr 132

Architectural Cue Model in Evacuation Simulation for Underground Space Design

Chengyu Sun

nr 133

Uncertainty and Sensitivity Analysis in Building Performance Simulation for Decision Support and Design Optimization

Christina Hopfe

nr 134

Facilitating Distributed Collaboration in the AEC/FM Sector Using Semantic Web Technologies

Jacob Beetz

nr 135

Circumferentially Adhesive Bonded Glass Panes for Bracing Steel Frame in Façades

Edwin Huveners

nr 136

Influence of Temperature on Concrete Beams Strengthened in Flexure with CFRP

Ernst-Lucas Klamer

nr 137

Sturen op Klantwaarde

Jos Smeets

nr 139

Lateral Behavior of Steel Frames with Discretely Connected Precast Concrete Infill Panels

Paul Teewen

nr 140

Integral Design Method in the Context of Sustainable Building Design

Perica Savanović

nr 141

Household Activity-Travel Behavior: Implementation of Within-Household Interactions

Renni Anggraini

nr 142

Design Research in the Netherlands 2010

Henri Achten

nr 143

Modelling Life Trajectories and Transport Mode Choice Using Bayesian Belief Networks

Marloes Verhoeven

nr 144

Assessing Construction Project Performance in Ghana

William Gyadu-Asiedu

nr 145

Empowering Seniors through Domotic Homes

Masi Mohammadi

nr 146

An Integral Design Concept for Ecological Self-Compacting Concrete

Martin Hunger

nr 147

Governing Multi-Actor Decision Processes in Dutch Industrial Area Redevelopment

Erik Blokhuis

nr 148

A Multifunctional Design Approach for Sustainable Concrete

Götz Hüsken

nr 149

Quality Monitoring in Infrastructural Design-Build Projects

Ruben Favié

nr 150

Assessment Matrix for Conservation of Valuable Timber Structures

Michael Abels

nr 151

Co-simulation of Building Energy Simulation and Computational Fluid Dynamics for Whole-Building Heat, Air and Moisture Engineering

Mohammad Mirsadeghi

nr 152

External Coupling of Building Energy Simulation and Building Element Heat, Air and Moisture Simulation

Daniel Cóstola

nr 153

**Adaptive Decision Making In
Multi-Stakeholder Retail Planning**

Ingrid Janssen

nr 154

Landscape Generator

Kymo Slager

nr 155

Constraint Specification in Architecture

Remco Niemeijer

nr 156

**A Need-Based Approach to
Dynamic Activity Generation**

Linda Nijland

nr 157

**Modeling Office Firm Dynamics in an
Agent-Based Micro Simulation Framework**

Gustavo Garcia Manzato

nr 158

**Lightweight Floor System for
Vibration Comfort**

Sander Zegers

nr 159

Aanpasbaarheid van de Draagstructuur

Roel Gijsbers

nr 160

'Village in the City' in Guangzhou, China

Yanliu Lin

nr 161

Climate Risk Assessment in Museums

Marco Martens

nr 162

Social Activity-Travel Patterns

Pauline van den Berg

nr 163

**Sound Concentration Caused by
Curved Surfaces**

Martijn Vercammen

nr 164

**Design of Environmentally Friendly
Calcium Sulfate-Based Building Materials:
Towards an Improved Indoor Air Quality**

Qingliang Yu

nr 165

**Beyond Uniform Thermal Comfort
on the Effects of Non-Uniformity and
Individual Physiology**

Lisje Schellen

nr 166

Sustainable Residential Districts

Gaby Abdalla

nr 167

**Towards a Performance Assessment
Methodology using Computational
Simulation for Air Distribution System
Designs in Operating Rooms**

Mônica do Amaral Melhado

nr 168

**Strategic Decision Modeling in
Brownfield Redevelopment**

Brano Glumac

nr 169

**Pamela: A Parking Analysis Model
for Predicting Effects in Local Areas**

Peter van der Waerden

nr 170

**A Vision Driven Wayfinding Simulation-System
Based on the Architectural Features Perceived
in the Office Environment**

Qunli Chen

nr 171

**Measuring Mental Representations
Underlying Activity-Travel Choices**

Oliver Horeni

nr 172

**Modelling the Effects of Social Networks
on Activity and Travel Behaviour**

Nicole Ronald

nr 173

**Uncertainty Propagation and Sensitivity
Analysis Techniques in Building Performance
Simulation to Support Conceptual Building
and System Design**

Christian Struck

nr 174

**Numerical Modeling of Micro-Scale
Wind-Induced Pollutant Dispersion
in the Built Environment**

Pierre Gousseau

nr 175

**Modeling Recreation Choices
over the Family Lifecycle**

Anna Beatriz Grigolon

nr 176

**Experimental and Numerical Analysis of
Mixing Ventilation at Laminar, Transitional
and Turbulent Slot Reynolds Numbers**

Twan van Hooff

nr 177

**Collaborative Design Support:
Workshops to Stimulate Interaction and
Knowledge Exchange Between Practitioners**

Emile M.C.J. Quanjel

nr 178

Future-Proof Platforms for Aging-in-Place

Michiel Brink

nr 179

**Motivate:
A Context-Aware Mobile Application for
Physical Activity Promotion**

Yuzhong Lin

nr 180

**Experience the City:
Analysis of Space-Time Behaviour and
Spatial Learning**

Anastasia Moiseeva

nr 181

**Unbonded Post-Tensioned Shear Walls of
Calcium Silicate Element Masonry**

Lex van der Meer

nr 182

**Construction and Demolition Waste
Recycling into Innovative Building Materials
for Sustainable Construction in Tanzania**

Mwita M. Sabai

nr 183

**Durability of Concrete
with Emphasis on Chloride Migration**

Przemysław Spiesz

nr 184

**Computational Modeling of Urban
Wind Flow and Natural Ventilation Potential
of Buildings**

Rubina Ramponi

nr 185

**A Distributed Dynamic Simulation
Mechanism for Buildings Automation
and Control Systems**

Azzedine Yahiaoui

nr 186

**Modeling Cognitive Learning of Urban
Networks in Daily Activity-Travel Behavior**

Şehnaz Cenani Durmazoğlu

nr 187

**Functionality and Adaptability of Design
Solutions for Public Apartment Buildings
in Ghana**

Stephen Agyefi-Mensah

nr 188

**A Construction Waste Generation Model
for Developing Countries**

Lilliana Abarca-Guerrero

nr 189

**Synchronizing Networks:
The Modeling of Supernetworks for
Activity-Travel Behavior**

Feixiong Liao

nr 190

**Time and Money Allocation Decisions
in Out-of-Home Leisure Activity Choices**

Gamze Zeynep Dane

nr 191

**How to Measure Added Value of CRE and
Building Design**

Rianne Appel-Meulenbroek

nr 192

**Secondary Materials in Cement-Based
Products:
Treatment, Modeling and Environmental
Interaction**

Miruna Florea

nr 193

**Concepts for the Robustness Improvement
of Self-Compacting Concrete:**

**Effects of Admixtures and Mixture
Components on the Rheology and Early
Hydration at Varying Temperatures**

Wolfram Schmidt

nr 194

Modelling and Simulation of Virtual Natural Lighting Solutions in Buildings

Rizki A. Mangkuto

nr 195

Nano-Silica Production at Low Temperatures from the Dissolution of Olivine - Synthesis, Tailoring and Modelling

Alberto Lazaro Garcia

nr 196

Building Energy Simulation Based Assessment of Industrial Halls for Design Support

Bruno Lee

nr 197

Computational Performance Prediction of the Potential of Hybrid Adaptable Thermal Storage Concepts for Lightweight Low-Energy Houses

Pieter-Jan Hoes

nr 198

Application of Nano-Silica in Concrete

George Quercia Bianchi

nr 199

Dynamics of Social Networks and Activity Travel Behaviour

Fariya Sharmeen

nr 200

Building Structural Design Generation and Optimisation including Spatial Modification

Juan Manuel Davila Delgado

nr 201

Hydration and Thermal Decomposition of Cement/Calcium-Sulphate Based Materials

Ariën de Korte

nr 202

Republiek van Beelden: De Politieke Werkingen van het Ontwerp in Regionale Planvorming

Bart de Zwart

nr 203

Effects of Energy Price Increases on Individual Activity-Travel Repertoires and Energy Consumption

Dujuan Yang

nr 204

Geometry and Ventilation: Evaluation of the Leeward Sawtooth Roof Potential in the Natural Ventilation of Buildings

Jorge Isaac Perén Montero

nr 205

Computational Modelling of Evaporative Cooling as a Climate Change Adaptation Measure at the Spatial Scale of Buildings and Streets

Hamid Montazeri

nr 206

Local Buckling of Aluminium Beams in Fire Conditions

Ronald van der Meulen

nr 207

Historic Urban Landscapes: Framing the Integration of Urban and Heritage Planning in Multilevel Governance

Loes Veldpaus

nr 208

Sustainable Transformation of the Cities: Urban Design Pragmatics to Achieve a Sustainable City

Ernesto Antonio Zumelzu Scheel

nr 209

Development of Sustainable Protective Ultra-High Performance Fibre Reinforced Concrete (UHPFRC): Design, Assessment and Modeling

Rui Yu

nr 210

Uncertainty in Modeling Activity-Travel Demand in Complex Urban Systems

Soora Rasouli

nr 211

Simulation-based Performance Assessment of Climate Adaptive Greenhouse Shells

Chul-sung Lee

nr 212

Green Cities: Modelling the Spatial Transformation of the Urban Environment using Renewable Energy Technologies

Saleh Mohammadi

nr 213

A Bounded Rationality Model of Short and Long-Term Dynamics of Activity-Travel Behavior

Ifigeneia Psarra

nr 214

Effects of Pricing Strategies on Dynamic Repertoires of Activity-Travel Behaviour

Elaheh Khademi

nr 215

Handstorm Principles for Creative and Collaborative Working

Frans van Gassel

nr 216

Light Conditions in Nursing Homes: Visual Comfort and Visual Functioning of Residents

Marianne M. Sinoo

nr 217

**Woonsporen:
De Sociale en Ruimtelijke Biografie van een Stedelijk Bouwblok in de Amsterdamse Transvaalbuurt**

Hüseyin Hüsnü Yegenoglu

nr 218

Studies on User Control in Ambient Intelligent Systems

Berent Willem Meerbeek

nr 219

Daily Livings in a Smart Home: Users' Living Preference Modeling of Smart Homes

Erfaneh Allameh

nr 220

Smart Home Design: Spatial Preference Modeling of Smart Homes

Mohammadali Heidari Jozam

nr 221

**Wonen:
Discoursen, Praktijken, Perspectieven**

Jos Smeets

nr 222

Personal Control over Indoor Climate in Offices:

Impact on Comfort, Health and Productivity

Atze Christiaan Boerstra

nr 223

Personalized Route Finding in Multimodal Transportation Networks

Jianwe Zhang

nr 224

The Design of an Adaptive Healing Room for Stroke Patients

Elke Daemen

nr 225

Experimental and Numerical Analysis of Climate Change Induced Risks to Historic Buildings and Collections

Zara Huijbregts

nr 226

Wind Flow Modeling in Urban Areas Through Experimental and Numerical Techniques

Alessio Ricci

nr 227

Clever Climate Control for Culture: Energy Efficient Indoor Climate Control Strategies for Museums Respecting Collection Preservation and Thermal Comfort of Visitors

Rick Kramer

nr 228

Fatigue Life Estimation of Metal Structures Based on Damage Modeling

Sarmediran Silitonga

nr 229

A multi-agents and occupancy based strategy for energy management and process control on the room-level

Timilehin Moses Labeodan

nr 230

Environmental assessment of Building Integrated Photovoltaics: Numerical and Experimental Carrying Capacity Based Approach

Michiel Ritzen

nr 231

Performance of Admixture and Secondary Minerals in Alkali Activated Concrete: Sustaining a Concrete Future

Arno Keulen

nr 232

World Heritage Cities and Sustainable Urban Development: Bridging Global and Local Levels in Monitoring the Sustainable Urban Development of World Heritage Cities

Paloma C. Guzman Molina

nr 233

Stage Acoustics and Sound Exposure in Performance and Rehearsal Spaces for Orchestras: Methods for Physical Measurements

Remy Wenmaekers

nr 234

Municipal Solid Waste Incineration (MSWI) Bottom Ash: From Waste to Value Characterization, Treatments and Application

Pei Tang

nr 235

Large Eddy Simulations Applied to Wind Loading and Pollutant Dispersion

Mattia Ricci

nr 236

Alkali Activated Slag-Fly Ash Binders: Design, Modeling and Application

Xu Gao

nr 237

Sodium Carbonate Activated Slag: Reaction Analysis, Microstructural Modification & Engineering Application

Bo Yuan

nr 238

Shopping Behavior in Malls

Widiyani

nr 239

Smart Grid-Building Energy Interactions: Demand Side Power Flexibility in Office Buildings

Kennedy Otieno Aduda

nr 240

Modeling Taxis Dynamic Behavior in Uncertain Urban Environments

Zheng Zhong

nr 241

Gap-Theoretical Analyses of Residential Satisfaction and Intention to Move

Wen Jiang

nr 242

Travel Satisfaction and Subjective Well-Being: A Behavioral Modeling Perspective

Yanan Gao

nr 243

Building Energy Modelling to Support the Commissioning of Holistic Data Centre Operation

Vojtech Zavrel

nr 244

Regret-Based Travel Behavior Modeling: An Extended Framework

Sunghoon Jang

nr 245

Towards Robust Low-Energy Houses: A Computational Approach for Performance Robustness Assessment using Scenario Analysis

Rajesh Reddy Kotireddy

nr 246

Development of sustainable and functionalized inorganic binder-biofiber composites

Guillaume Doudart de la Grée

nr 247

A Multiscale Analysis of the Urban Heat Island Effect: From City Averaged Temperatures to the Energy Demand of Individual Buildings

Yasin Toparlar

nr 248

Design Method for Adaptive Daylight Systems for buildings covered by large (span) roofs

Florian Heinzelmann

nr 249

Hardening, high-temperature resistance and acid resistance of one-part geopolymers

Patrick Sturm

nr 250

Effects of the built environment on dynamic repertoires of activity-travel behaviour

Aida Pontes de Aquino

nr 251

Modeling for auralization of urban environments: Incorporation of directivity in sound propagation and analysis of a framework for auralizing a car pass-by

Fotis Georgiou

nr 252

Wind Loads on Heliostats and Photovoltaic Trackers

Andreas Pfahl

nr 253

Approaches for computational performance optimization of innovative adaptive façade concepts

Roel Loonen

nr 254

Multi-scale FEM-DEM Model for Granular Materials: Micro-scale boundary conditions, Statics, and Dynamics

Jiadun Liu

nr 255

Bending Moment - Shear Force Interaction of Rolled I-Shaped Steel Sections

Rianne Willie Adriana Dekker

nr 256

Paralympic tandem cycling and hand-cycling: Computational and wind tunnel analysis of aerodynamic performance

Paul Fionn Mannion

nr 257

Experimental characterization and numerical modelling of 3D printed concrete: Controlling structural behaviour in the fresh and hardened state

Robert Johannes Maria Wolfs

nr 258

Requirement checking in the building industry: Enabling modularized and extensible requirement checking systems based on semantic web technologies

Chi Zhang

nr 259

A Sustainable Industrial Site Redevelopment Planning Support System

Tong Wang

nr 260

Efficient storage and retrieval of detailed building models: Multi-disciplinary and long-term use of geometric and semantic construction information

Thomas Ferdinand Krijnen

nr 261

The users' value of business center concepts for knowledge sharing and networking behavior within and between organizations

Minou Weijs-Perrée

nr 262

Characterization and improvement of aerodynamic performance of vertical axis wind turbines using computational fluid dynamics (CFD)

Abdolrahim Rezaeiha

nr 263

In-situ characterization of the acoustic impedance of vegetated roofs

Chang Liu

nr 264

Occupancy-based lighting control: Developing an energy saving strategy that ensures office workers' comfort

Christel de Bakker

nr 265

Stakeholders-Oriented Spatial Decision Support System

Cahyono Susetyo

nr 266

Climate-induced damage in oak museum objects

Rianne Aleida Luimes

nr 267

Towards individual thermal comfort: Model predictive personalized control of heating systems

Katarina Katic

nr 268

Modelling and Measuring Quality of Urban Life: Housing, Neighborhood, Transport and Job

Lida Aminian

nr 269

Optimization of an aquifer thermal energy storage system through integrated modeling of aquifer, HVAC systems and building

Basar Bozkaya

nr 270

Numerical modeling for urban sound propagation: developments in wave-based and energy-based methods

Raúl Pagán Muñoz

nr 271

Lighting in multi-user office environments: improving employee wellbeing through personal control

Sanae van der Vleuten-Chraibi

nr 272

A strategy for fit-for-purpose occupant behavior modelling in building energy and comfort performance simulation

Isabella I. Gaetani dell'Aquila d'Aragona

nr 273

Een architectuurhistorische waardestelling van naoorlogse woonwijken in Nederland: Het voorbeeld van de Westelijke Tuinsteden in Amsterdam

Eleonore Henriette Marie Mens

nr 274

Job-Housing Co-Dependent Mobility Decisions in Life Trajectories

Jia Guo

nr 275

A user-oriented focus to create healthcare facilities: decision making on strategic values

Emilia Rosalia Catharina Maria Huisman

nr 276

Dynamics of plane impinging jets at moderate Reynolds numbers – with applications to air curtains

Adelya Khayrullina

nr 277

Valorization of Municipal Solid Waste Incineration Bottom Ash - Chemical Nature, Leachability and Treatments of Hazardous Elements

Qadeer Alam

nr 278

Treatments and valorization of MSWI bottom ash - application in cement-based materials

Veronica Caprai

nr 279

Personal lighting conditions of office workers - input for intelligent systems to optimize subjective alertness

Juliëtte van Duijnhoven

nr 280

Social influence effects in tourism travel: air trip itinerary and destination choices

Xiaofeng Pan

nr 281

Advancing Post-War Housing: Integrating Heritage Impact, Environmental Impact, Hygrothermal Risk and Costs in Renovation Design Decisions

Lisanne Claartje Havinga

Ultra-high performance fibre reinforced concrete (UHPFRC) is a relatively new building material, which has superior workability, mechanical properties, energy dissipation capacity and durability. Those excellent characteristics and properties give it a great potential to be used in impact resistant components and structures, such as protective elements in military and civil engineering. However, the high cement consumption, large dosage of superplasticizer and high content of steel fibre unitization cause some disadvantages, such as high costs and a large embodied energy. Hence, optimization on UHPFRC mixtures is needed to make them cheaper, more eco-friendly and higher impact resistance to broaden the applications, and the static mechanical properties and impact resistance of UHPFRC are necessary to be investigated to reveal the impact resistant mechanism and provide guidance in the design of protective elements and structures. This research aims to optimize the mix design of UHPFRC towards high impact resistance, cost-effectiveness and eco-friendliness, and investigate its mechanical properties and impact resistance.

DEPARTMENT OF THE BUILT ENVIRONMENT